



**GDAŃSK UNIVERSITY
OF TECHNOLOGY**

FACULTY OF ELECTRONICS, TELECOMMUNICATIONS
AND INFORMATICS



The author of the PhD dissertation: **Adrian Kajetan Bekasiewicz**
Scientific discipline: **electronics**

DOCTORAL DISSERTATION

Title of PhD dissertation: **Design of Wideband Antennas By Means of Fast Multi-Objective Optimization**

Title of PhD dissertation (in Polish): **Projektowanie Anten Szerokopasmowych z Użyciem Szybkich Metod Optymalizacji Wielokryterialnej**

Supervisor	Auxiliary supervisor
<i>signature</i>	<i>signature</i>
PhD, DSc, Włodzimierz Zieniutycz	PhD, Sławomir Kozieł

Gdańsk, year 2016

To Alexandra and Igor, the most important individuals of my life.



STATEMENT

The author of the PhD dissertation: **Adrian Kajetan Bekasiewicz**

I, the undersigned, agree/~~do not agree~~* that my PhD dissertation entitled:
Design of wideband antennas by means of fast multi-objective optimization
may be used for scientific or didactic purposes.¹

Gdańsk,.....
signature of the PhD student

Aware of criminal liability for violations of the Act of 4th February 1994 on Copyright and Related Rights (Journal of Laws 2006, No. 90, item 631) and disciplinary actions set out in the Law on Higher Education (Journal of Laws 2012, item 572 with later amendments),² as well as civil liability, I declare, that the submitted PhD dissertation is my own work.

I declare, that the submitted PhD dissertation is my own work performed under and in cooperation with the supervision of Włodzimierz Zieniutycz and the auxiliary supervision of Sławomir Kozieł.

This submitted PhD dissertation has never before been the basis of an official procedure associated with the awarding of a PhD degree.

All the information contained in the above thesis which is derived from written and electronic sources is documented in a list of relevant literature in accordance with art. 34 of the Copyright and Related Rights Act.

I confirm that this PhD dissertation is identical to the attached electronic version.

Gdańsk,.....
signature of the PhD student

I, the undersigned, agree/~~do not agree~~* to include an electronic version of the above PhD dissertation in the open, institutional, digital repository of Gdańsk University of Technology, Pomeranian Digital Library, and for it to be submitted to the processes of verification and protection against misappropriation of authorship.

Gdańsk,.....
signature of the PhD student

*) strikethrough where appropriate.

¹ Decree of Rector of Gdansk University of Technology No. 34/2009 of 9th November 2009, TUG archive instruction addendum No. 8.
² Act of 27th July 2005, Law on Higher Education: Chapter 7, Criminal responsibility of PhD students, Article 226.



DESCRIPTION OF DOCTORAL DISSERTATION

The Author of the PhD dissertation: Adrian Kajetan Bekasiewicz

Title of PhD dissertation: Design of wideband antennas by means of fast multi-objective optimization

Title of PhD dissertation in Polish: Projektowanie anten szerokopasmowych z użyciem szybkich metod optymalizacji wielokryterialnej

Language of PhD dissertation: English

Supervision: Włodzimierz Zieniutycz

Auxiliary supervision: Sławomir Kozieł

Date of doctoral defense:.....

Keywords of PhD dissertation in Polish: algorytmy metaheurystyczne, kriging, metody surrogatowe, modele interpolacyjne, optymalizacja wielokryterialna, projektowanie anten, projektowanie wspomagane komputerowo, redukcja przestrzeni zmiennych projektowych.

Keywords of PhD dissertation in English: antenna design, computer-aided design (CAD), design space reduction, kriging interpolation, metaheuristic algorithms, multi-objective optimization, response surface approximation, surrogate-based optimization.

Summary of PhD dissertation in Polish: W rozprawie omówiono metodę szybkiej optymalizacji wielokryterialnej realistycznych modeli współczesnych struktur antenowych przy użyciu technik redukcji przestrzeni zmiennych projektowych, modeli interpolacyjnych, populacyjnych algorytmów metaheurystycznych i algorytmów surrogatowych. Centralnym elementem procedury jest optymalizacja modelu interpolacyjnego z wykorzystaniem algorytmu ewolucyjnego. Model interpolacyjny buduje się na podstawie danych uzyskanych w wyniku symulacji modelu elektromagnetycznego struktury o obniżonej dokładności. Symulacje przeprowadza się w obszarze przestrzeni projektowej zidentyfikowanym dzięki technikom redukcji. W pracy opisano pięć algorytmów do redukcji przestrzeni oraz zbadano ich wpływ na wzrost kosztu optymalizacji wielokryterialnej wraz ze zwiększaniem wymiarowości problemu projektowego. Metodę zweryfikowano numerycznie. W tym celu zaprojektowano siedem anten szerokopasmowych, zminiaturyzowany transformator impedancji oraz antenę z rezonatorem dielektrycznym względem dwóch lub trzech sprzecznych kryteriów. Liczba parametrów geometrycznych rozważanych układów waha się od trzech do dwudziestu czterech. Omówiony algorytm pozwala uzyskać rozwiązania stanowiące najlepszy możliwy kompromis względem stawianych wymagań projektowych przy niewielkim koszcie obliczeniowym w porównaniu do bezpośredniej wielokryterialnej optymalizacji dokładnych modeli elektromagnetycznych struktur. Dwa wybrane projekty anten (sześć kompromisowych rozwiązań) zostały pomyślnie zweryfikowane poprzez wykonanie pomiarów.



**GDAŃSK UNIVERSITY
OF TECHNOLOGY**

FACULTY OF ELECTRONICS, TELECOMMUNICATIONS
AND INFORMATICS



Summary of PhD dissertation in English: In this work, a multi-objective framework for fast optimization of modern antenna structures has been discussed. The approach is based on space reduction, response surface approximation modeling and variable-fidelity electromagnetic simulations. The design process involves optimization of the interpolation model constructed from the low-fidelity model data using a multi-objective evolutionary algorithm. The obtained initial Pareto-optimal set is then corrected by means of surrogate-based optimization. The interpolation model is set up within a region of the design space confined using a suitable reduction technique. Five reduction methods have been described and extensively compared against each other. The influence of the reduction method on the scalability properties of the optimization framework with respect to the dimensionality of the design space has also been investigated. The algorithm has been validated through optimization of high-fidelity electromagnetic models of nine antenna structures in two- or three-objective setups. Design examples include seven wideband antenna structures, an ultra-wideband compact impedance transformer and a dielectric resonator antenna. The number of geometrical parameters for the considered structures range from three to twenty four. The discussed algorithm allows for obtaining comprehensive information about the possible trade-offs between conflicting objectives at a fraction of time required by direct multi-objective optimization. In case of two antenna structures, the numerical results have been confirmed by experimental validation.

ACKNOWLEDGEMENTS

This work would not have been possible without constant support of people who helped me overcome research failures, interpersonal difficulties and disapproval. I would like to acknowledge people and institutions that have had the greatest impact on my work.

In the first place, I would like to express deep gratitude to prof. Sławomir Koziół, my mentor and supervisor of this doctoral work. His constant support, patience and guidance have allowed me to vastly develop my research skills and understand secrets of modern surrogate-assisted optimization techniques.

I would like to express my recognition of prof. Włodzimierz Zieniutycz for supervision during my doctoral studies. Owing to his forbearance, intercession and support, I was able to conduct my research abroad.

I would like to acknowledge prof. Marek Kitliński for supervision during the first year of doctoral studies.

Last but not least, I would like to express my deepest gratitude to my wife for her endless patience, agreeing to relocate to Iceland and unconditional support from the beginning to the very end of my studies.

I would like to thank Computer Simulation Technology AG, Darmstadt, Germany, for making CST Microwave Studio available.

This work was supported in part by the Icelandic Centre for Research (RANNIS) Grant 130450051, and by National Science Centre of Poland Grants 2013/11/B/ST7/04325, 2014/12/ST7/00045 and 2014/15/B/ST7/04683.

LIST OF SYMBOLS AND ACRONYMS

SYMBOLS

A^*	– diagonal correction matrix	$\ln(L)$	– concentrated ln-likelihood function
D	– total number of design variables	n	– design sample count
F	– multi-objective function	r	– random number in 0 to 1 range
K	– total number of design objectives	s_d	– correlation smoothness factor
N	– total number of design samples	\mathbf{u}	– upper bounds vector
\mathbf{R}	– model of the structure	u	– element of vector \mathbf{u}
SF	– sharing function	\mathbf{x}	– vector of design parameters
U	– objective function	x	– element of vector \mathbf{x}
X	– a set of samples \mathbf{x}	Ψ	– correlation matrix
X_C	– design space region obtained using confinement method	α	– regression coefficient
X_D	– design space region obtained by Pareto-dominance-based method	β	– penalty coefficient of objective function
X_I	– feasible design space	γ	– sharing function factor
X_P	– a set of Pareto-optimal designs	δ	– distance between individuals in feature space
X_R	– design space region obtained using rotational technique	δ_p	– average minimum distance between training points
X_S	– design space region obtained by sequential algorithm	θ_d	– correlation parameters
X_{Sr}	– design space region obtained using enhanced sequential algorithm	ρ	– maximum likelihood estimation
d	– dimension count	σ^2	– estimated variance of the kriging model
k	– design objective count	σ_m	– mutation radius
\mathbf{l}	– lower bounds vector	σ_r	– sharing radius
l	– element of vector \mathbf{l}	χ	– volume-wise design space reduction ratio
$\ln(L)$	– concentrated ln-likelihood function	ω	– frequency points vector

ACRONYMS

DAA	– Detect and Avoid	OSM	– output space mapping
DoE	– design of experiment	PSO	– particle swarm optimization
EA	– evolutionary algorithm	RF	– radio frequency
EM	– electromagnetic	RMS	– root mean square
FD	– factorial design	RSA	– response surface approximation
FCC	– Federal Communications Commission	SBO	– surrogate-based optimization
LHS	– latin hypercube sampling	SM	– space mapping
MOEA	– multi-objective evolutionary algorithm	UWB	– ultra-wideband
MIMO	– multiple-input-multiple-output		

CONTENTS

1 INTRODUCTION.....	12
1.1 The State of the Art	13
1.2 The Aim and Theses of the Work.....	16
1.3 Dissertation Outline.....	17
2 SURROGATE-BASED MODELING AND OPTIMIZATION.....	18
2.1 Surrogate-Based Optimization Concept	19
2.2 Surrogate Models.....	20
2.2.1 Physics-Based Surrogates	20
2.2.2 Function Approximation Surrogates	21
2.2.2.1 Design of Experiments.....	22
2.2.2.2 Kriging Interpolation	24
2.2.2.3 Model Validation	25
2.2.2.4 Cost of RSA Model Construction.....	26
2.2.3 Variable-Fidelity Modeling.....	27
2.2.3.1 Correction of Training Data Using Space Mapping	27
2.2.3.2 Co-kriging Modeling	29
2.3 Exploitation versus Exploration	30
3 MULTI-OBJECTIVE OPTIMIZATION.....	32
3.1 Problem Formulation.....	33
3.2 Solution Approaches to Multi-Objective Optimization.....	33
3.3 Multi-Objective Evolutionary Algorithms.....	37
3.3.1 Algorithm Description.....	37
3.3.1.1 Assessment of Individuals	39
3.3.1.2 Fitness Sharing.....	39
3.3.1.3 Selection.....	40
3.3.1.4 Recombination	41
3.3.1.5 Mutation.....	41
3.3.1.6 Elitism.....	42
3.3.1.7 Mating Restrictions.....	42
3.3.1.8 Stopping Criteria.....	42
4 MULTI-OBJECTIVE ANTENNA DESIGN.....	44
4.1 Problem Formulation	44
4.2 Optimization Algorithm.....	45
4.2.1 Optimization Algorithm Overview	45
4.3 Design Space Reduction	47
4.3.1 Pareto-Dominance Design Space Reduction.....	50
4.3.2 Sequential Single-Objective Optimizations	51
4.3.3 Rotational Design Space Reduction.....	54
4.3.4 Design Space Confinement	56
4.3.5 Space Reduction Using High-Fidelity Model Data.....	58
4.4 Pareto Set Refinement	61

4.4.1 Pareto Set Refinement Using Response Correction.....	61
4.4.2 Pareto Set Refinement Using Co-Kriging.....	61
4.5 Comparison of the Methods	64
4.5.1 Simulation Model Setup	65
4.5.2 UWB Monocone – Design and Optimization Setup.....	65
4.5.2.1 Design Space Reduction.....	66
4.5.2.2 Data Acquisition.....	68
4.5.2.3 MOEA Optimization	69
4.5.2.4 Pareto Set Refinement	71
4.5.2.5 Optimization Algorithm – Computational Cost	73
4.5.3 UWB Dipole – Design and Optimization Setup.....	73
4.5.3.1 Design Space Reduction.....	74
4.5.3.2 Data Acquisition.....	76
4.5.3.3 MOEA Optimization	77
4.5.3.4 Pareto Set Refinement	78
4.5.3.5 Optimization Algorithm – Computational Cost	79
4.5.4 UWB Monopole – Design and Optimization Setup	79
4.5.4.1 Design Space Reduction.....	81
4.5.4.2 Data Acquisition.....	83
4.5.4.3 MOEA Optimization	84
4.5.4.4 Pareto Set Refinement	85
4.5.4.5 Optimization Algorithm – Computational Cost	85
4.5.5 Scalability of Multi-Objective Antenna Optimization Algorithm	85
4.6 Summary and Algorithm Limitations	89
5 DESIGN EXAMPLES.....	91
5.1 UWB Monopole Antenna.....	91
5.2 UWB MIMO Antenna.....	93
5.3 Planar Quasi-Yagi-Uda Antenna.....	97
5.4 Planar Yagi-Uda antenna	99
5.5 Quasi-Isotropic Dielectric Resonator Antenna.....	101
5.6 Compact UWB Impedance Transformer.....	106
6 EXPERIMENT.....	110
6.1 UWB Monopole Antenna.....	110
6.2 Quasi-Yagi-Uda Antenna	111
7 DISCUSSION AND RECOMMENDATIONS	116
7.1 Quantitative Discussion of Algorithm Components	116
7.2 Discussion and Recommendations.....	118
8 SUMMARY	119
8.1 Conclusions.....	120
8.2 Future Work	120
REFERENCES	122
APPENDICES.....	131
APPENDIX 1 STATISTICAL ANALYSIS OF MOEA.....	132

1 INTRODUCTION

Rapid development of global communication systems in the past decades has had a significant influence on nearly all aspects of human life. The means of information exchange have evolved from the stationary model to the wireless one where mobility of the end user is the key feature. Nowadays, the development of communication systems is focused on increasing the capacity of structural networks and advancements in data management mechanisms, but also on providing the means for fast and reliable wireless connectivity.

Currently, the wireless user connection is realized through RF/microwave communication systems. Their inherent components, which allow obtaining direct access to wireless medium through RF frontend, are antennas. The antenna plays a role of an interface between two different mediums. In other words, it transforms the signal in the form of an electromagnetic energy guided by the transmission lines to a radiated field, which can be used as information carrier, in a free space. In other words, the antenna may be considered as a matching transformer converting the impedance of the transmission line—usually 50 ohm in the microwave technology—to the 377 ohm impedance of the free space.

Contemporary antennas are often characterized by sophisticated electrical and field properties such as wideband or multiband operation, or unconventional radiation patterns, to name just a few. In many cases, rigorous design specifications can be fulfilled only by geometrically complex structures. Unfortunately, their evaluation usually requires utilization of general purpose electromagnetic (EM) solvers. Although EM simulations can provide accurate responses even for complex antenna geometries, their fundamental drawback is high computational cost. Depending on the complexity of the problem, a single evaluation may take from dozens of minutes to many hours. The problem is further complicated by the fact that real-world antenna designs are supposed to fulfill multiple requirements so as to allow them to operate within strictly specified electrical and field conditions. The necessity for simultaneous accounting for various requirements makes their design an extremely challenging task that requires careful selection of appropriate tools, optimization techniques, as well as the engineering experience. At the same time, the process is subjected to various constraints (e.g., maximum footprint or volume of the antenna) as well as the computational budget (determined by available resources and the timeframe of the design cycle).

Despite its significance, the problem of fast antenna design with respect to multiple requirements remains unsolved. The process cannot be performed by manual adjustment of geometrical parameters and thus suitable optimization techniques are the only reliable design tools. These, however, require numerous evaluations of electromagnetic models which makes numerical optimization inefficient from computational standpoint. This dissertation is an attempt to develop a comprehensive solution that enables expedited design of contemporary antenna structures with

respect to multiple performance requirements. The stated problem is addressed using fast and accurate antenna models, advanced optimization algorithms, as well as methods for correcting the obtained design solutions.

1.1 The State of the Art

Since the late 80s of the XIX century when the experiments by Hertz [1, 2] verified the electromagnetic theory formulated by Maxwell [3], design and implementation of wireless communication systems, including antennas as their key components, have been of great interest for academic community [4-7], industry [8-11] and army [12-15]. An extensive research programs on wideband pulse radio systems for the development of novel radar, imaging and communication techniques have been initiated in 1960s in both US and former Soviet Union [16-19]. Some of these systems became available for commercial and military applications in 1970s [19-22]. At the same time, the interest in wideband system design was rather limited across the academic institutions. The situation changed as a consequence of a Federal Commission for Communications (FCC) regulations. In 2002, FCC released a specification for the unlicensed use of ultra-wideband (UWB) frequency for short-range indoor communication with high-data rates [23]. Perhaps, the term ultra-wideband was first used in 1989 in the context of wideband antennas [19, 24]; it is commonly accepted today. The regulation defines a 7.5 GHz bandwidth for the systems designated to operate from 3.1 GHz to 10.6 GHz [23]. The decision of FCC pushed other countries and international communities to release UWB frequencies for non-licensed use; however, specifications vary considerably between the regions of the world [25]. For instance, a regulation of the European Commission from 2007 released the frequencies from 6 GHz to 8.5 GHz for the unlicensed use [26]. The UWB bandwidth can be extended to the bands from 3.1 GHz to 4.8 GHz and from 8.5 GHz to 9 GHz when Detect and Avoid (DAA) mitigation techniques are utilized [27]. In 2014, the European regulation from 2007 has been modified to provide harmonized conditions for utilization of UWB spectrum [28].

Following the FCC definition, a wireless system has to exceed either 20% of the carrier frequency or exhibit at least 500 MHz bandwidth to be considered as UWB [23, 29]. This is in contrast to narrowband systems that usually offer no more than 10% bandwidth. At first, even old-fashioned low-frequency antennas seem to match UWB definition formulated by FCC, since their overall operational bandwidth often exceeds 100% (e.g., from 535 kHz to 1705 kHz [30]). However, the aforementioned structures are tuned to the desired frequency channel that is usually narrower than 2% of the effective bandwidth. Thus, they are rather multi-narrowband systems suited to operate within a limited spectrum at a time [30]. This example illustrates the key difference between the UWB (as capable to independently operate within entire band) and the narrowband antennas. Other features of UWB structures include immunity to multipath interferences [31, 32], relatively simple RF frontend [33, 34], or low power consumption [19, 33].

The properties of UWB antennas make them attractive for variety of applications that include, but are not limited to, radar [35, 36] and military communication systems [37, 38], wireless sensor networks for health monitoring [38, 39], energy harvesting [40, 41], indoor surveillance [42, 43], personal area networks [44, 45], high data-rate communication [46, 47], and many others. Undoubtedly, medical imaging is one of the most interesting application areas of the UWB structures [39, 48, 49]. The imaging techniques can be used for detection of breast cancer by transmitting short microwave pulses and analyzing the scattering variations between the healthy and malignant tissues [49]. On the hardware level, functionality of an UWB system strictly depends on the antenna operational and/or geometrical properties. The former comprises, among others, acceptable in-band reflection response [50, 51], phase stability [52, 53], specific radiation pattern [44, 54], high radiation efficiency [55, 56], gain [57, 58], and polarization [59, 60], whereas the latter refer to antenna footprint [61, 62] (or volume [63]), lateral size [64], specific shape [46], curvature [65, 66] or even structure flexibility [67, 68]. Moreover, budget-related requirements such as cheap fabrication, low cost of construction materials, or simple integration with other electronic components of the microwave system [38] should also be accounted for.

To date, a number of UWB antenna configurations have been proposed. More conventional geometries include both three-dimensional and planar realizations of spiral [69, 70], bi-conical [71, 72], conical [73, 74], log-periodic [75, 76], and horn [77, 78] antennas that satisfy the principle for frequency independent antennas formulated by Rumsey [38, 79]. Although mentioned structures ensure UWB operation, relatively large dimensions—especially of volumetric realizations—limit their applications to rather stationary systems. This problem is mitigated in modern antennas such as Vivaldi [80, 81], monopole [82, 83], dipole [50, 84], bow-tie [67, 85], or even some Yagi-based [86, 87] designs which provide UWB operation together with relatively compact and mostly planar topology.

The antenna has to be large enough to couple to a free space wave and thus its miniaturization is subject to fundamental limitation [88]. More precisely, reduction of the size below the threshold for which its electrical length corresponds to the free space wave results in unacceptable electrical characteristics [89]. Also, miniaturization comes at the expense of the increased complexity with large number of geometrical parameters (often more than ten) [31, 50, 82, 85]. The number of variables may be larger (even more than 20 [86, 90]) for structures with sophisticated features such as the ones that feature band-notch behavior [45, 57, 91], multiple-input-multiple-output properties [31, 32, 55] or compact size [61, 62, 82] to name just a few. Furthermore, the antenna design process often requires a realistic setup that comprises not only the radiator together with its feeding network, but also housing [92, 93], connectors [82, 94], and/or the nearest environment of the structure [95, 96]. Reliable evaluation of such antennas can only be achieved by means of full-wave electromagnetic (EM) analysis.

The aforementioned considerations indicate that design of contemporary UWB antennas is hindered by two fundamental difficulties: (i) unconventional and complex geometries with multiple adjustable parameters, and (ii) the necessity to fulfill multiple—and often conflicting—design requirements. The first implicates complicated relationships between the design variables and the antenna performance. Therefore, hands-on design or tuning strategies based on repetitive parameter sweeps driven by engineering experience are of limited use for modern structures [51, 72, 90, 97, 98]. At the same time, suitably developed optimization techniques seem to be the only useful tools for their reliable design [34, 50, 60, 82, 99, 100]. The second refers to the multi-objective nature of antenna design problem, which is more challenging than single-objective one [59, 60, 80, 101-103].

In multi-objective problems, determination of optimal design solutions is not straightforward. A popular approach is to seek for a set of solutions representing the best possible trade-offs between the considered objectives. Following the theory of Pareto [104], the optimal solutions are those for which improvement of the design with respect to any given objective is not possible without degradation of the others [105, 106]. These solutions form a so-called Pareto-optimal set, a representation of which is the outcome of the multi-objective optimization [102, 103, 106]. At first, finding multiple optimal solutions to the stated problem seems to be redundant. From practical point of view, only one design is required regardless of multi- or single-objective nature of the problem [105]. On the other hand, comprehensive information about the trade-offs between various requirements may be indispensable for making application-dependent decisions. In other words, having knowledge about the Pareto set, an experienced engineer can introduce some higher-level information to the problem in order to select the most appropriate antenna design for a given application [105, 106].

Popular approaches for solving multi-objective optimization problems are based on scalarization of design requirements (using, e.g., a weighted sum method [100] with the aggregated objective optimized using conventional methods [102], [103]) or utilization of metaheuristic algorithms [82, 105]. Metaheuristic algorithms are optimization techniques that gained considerable attention over the past decades due to their usefulness for solving complex design tasks where no explicit knowledge about the problem is available [107]. One of their advantages is relatively straightforward implementation of mechanisms for handling multiple objectives.

Metaheuristics are simple and universal strategies that mimic certain biological [108-110] or social [111-113] phenomena. Among them, population-based methods are especially useful for solving multi-objective problems due to their ability to process and outcome the entire set of

solutions in a single run [80, 103, 105, 106, 114], in particular, representations of the Pareto fronts upon implementing appropriate selection and recombination procedures [105, 114-116]. The most popular schemes, widely applied in many engineering areas [117-119], are evolutionary algorithms [103, 120-122] and particle swarm optimizers (PSOs) [80, 123-125]. Both are often utilized for optimization of antenna structures [57, 92, 124, 125], even in multi-objective sense [102, 103, 123, 126]. Although population-based metaheuristics are useful for multi-objective optimization, they also suffer from a fundamental drawback, which is a very high computational cost [60, 80, 106]. As mentioned before, a single simulation of contemporary antenna structure is a matter of minutes or even hours [50, 80, 82, 127]. Therefore, direct optimization by means of population-based metaheuristic algorithms can be performed if either (i) computational cost of the process is not of primary concern or (ii) optimization is conducted at the level of a simplified (and, presumably fast) antenna representation.

The number model evaluations necessary to complete the multi-objective optimization driven by population-based metaheuristic algorithm usually varies from a few thousands [128, 129] to tens of thousands [60, 103]. Consequently, multi-objective optimization of real-world antenna design may be computationally prohibitive unless massive computational resources (e.g., supercomputers or distributed-computing platforms) with multiple electromagnetic software licenses are available. Unfortunately, the literature usually lacks detailed information on the numerical cost of the optimization process. However, in [103], optimization of the Yagi-Uda antenna with respect to three objectives required 300,000 model evaluations to yield the Pareto-optimal set. In [60], the trade-off solutions for an antenna model (typical simulation time of only 30s) with respect to the three design requirements have been obtained at a cost of 20,000 simulations, with a total optimization time of over 166 hours (almost 7 days). In [80], multi-objective antenna optimization required only 800 simulations, yet fairly high evaluation time of 15 min resulted in the total design cost of 200 hours (over 8 days). While the aforementioned examples are related to rather simple antenna models, they imply that optimization cost of more complex structures would be incomparably higher [106, 120]. Consequently, direct optimization of full-wave electromagnetic models of contemporary antennas in a multi-objective setup is virtually impractical.

Although the number of model evaluations required by population-based methods to converge cannot be substantially decreased without a risk of obtaining non-optimal solutions, the design cost can be reduced by substituting electromagnetic models with their simplified empirical representations [89]. Empirical models are fast and can be efficient in handling multiple independent variables. For example, in [59], an array of dual-feed patch antennas has been successfully optimized with respect to two design objectives, whereas in [130] multi-objective optimization of a planar 2×2 antenna array with a total of 22 parameters has been successfully performed. Despite promising results, utilization of the empirical models is limited to rather old-fashioned antenna structures that cannot operate in ultra-wideband range. Furthermore, the results obtained by optimization of empirical antenna models are inaccurate and thus their further tuning using EM simulators is necessary [59, 130, 131].

Surrogate-based optimization (SBO) is another approach that can be applied to reduce the cost of multi-objective optimization [132-134]. The SBO techniques (e.g., space mapping [135, 136], manifold mapping [137, 138], shape preserving response prediction [139, 140], etc.) are promising and potentially efficient in dealing with computationally expensive design problems [34, 61, 82]. The main idea behind SBO is that the direct optimization of the high-fidelity (a so-called fine) EM antenna model is replaced by iterative correction and re-optimization of the surrogate model [133, 135, 140]. The latter is a computationally cheap low-fidelity (also referred to as a coarse) representation of the antenna and it is typically constructed using coarsely-discretized EM simulations [50, 93, 120]. Although the surrogate can be significantly faster [106, 141] than its high-fidelity counterpart, it is still computationally too expensive to be directly subjected to multi-objective optimization in a reasonable timeframe [64, 106]. The design cost of SBO may be further reduced using response surface approximations (RSA) constructed using the data acquired within a defined region of the design variable space [133, 134, 142]. The RSA-based techniques proved to be useful auxiliary tools for solving a variety of problems in,

e.g., microwave [143, 144] and aerospace engineering [133, 145]. Short evaluation times make the RSA models attractive for multi-objective optimization [106, 133, 143].

In [64], an SBO technique for multi-objective optimization of ultra-wideband antennas has been presented. The method utilizes an RSA surrogate of the antenna constructed from coarsely-discretized EM simulation data which is optimized using an evolutionary algorithm. The obtained Pareto front is then refined in a point-by-point manner using the response correction methods. The technique of [64] allows obtaining the Pareto front representation at a small cost compared to the direct multi-objective optimization of the high-fidelity EM model, yet its difficulty lies in the number of EM simulations required for a construction of an accurate RSA model. This is particularly troublesome for contemporary antennas since the cost of training data acquisition for RSA model construction grows exponentially with the number of parameters [106, 146]. In [64], the problem is mitigated by decomposition of many-variable antenna into sub-problems that are solved using separate RSAs. However, such an approach is restricted only to decomposable structures [147, 148]. In practice, applicability of the approximation techniques is limited to problems with only a few design variables [64, 142]. For structures with a large number of parameters, the cost of RSA model preparation may even exceed the number of evaluations required by direct multi-objective optimization [106].

Design of real-world antenna structures is a challenging task involving simultaneous handling of multiple and often conflicting objectives [101, 126, 130, 146]. This class of problems can be handled using multi-objective implementations of population-based metaheuristic algorithms. Unfortunately, metaheuristics require a very large number of model simulations to converge [50, 82, 127]. Consequently, their applicability for direct optimization of expensive EM antenna models is limited. The optimization cost can be reduced by replacing direct EM-driven design with a combination of response surface approximations and suitable surrogate-assisted techniques [64]. Utilization of approximation models for multi-objective optimization seems to be a promising approach but their setup cost grows quickly with the problem dimensionality. Contemporary antennas are often characterized by multi-parameter geometries which make construction of their approximation models difficult [64, 146].

1.2 The Aim and Theses of the Work

This study describes procedures for expedited multi-objective optimization of contemporary ultra-wideband antennas. The main contribution of the work is the development of methods for fast multi-objective optimization of multi-parameter antenna structures. Significant part of the study is focused on detailed investigation of the applicability of RSA models for solving the design problems with multiple independent variables. The number of data samples required for a construction of an accurate RSA model is limited by narrowing down the search space to the region of interest using suitable reduction techniques. The methods are based on the observation that the Pareto-optimal solutions—particularly those that satisfy certain minimum performance requirements—occupy a very small fraction of the design space. At the same time, its allocation within the search space is unknown beforehand. Reduction techniques identifies and narrows down the space to the smallest possible region that still contains all (or at least majority of) the Pareto-optimal solutions. Therefore, they are considered critical for construction of reliable RSA model using a reasonable amount of data. The design strategies considered in this dissertation have been extensively examined, compared against each other and verified using a set of carefully selected antenna structures. The obtained results have not only proven the usefulness of the discussed techniques but also their generality in the context of fast multi-objective optimization of contemporary ultra-wideband structures and other microwave/antenna designs.

The main goal of this dissertation was to show that accurate response surface approximation models of geometrically complex ultra-wideband antennas can be constructed and then utilized for multi-objective optimization driven by population-based metaheuristic algorithm. This was achieved by the development of methodologies that allow for identification of the search space region containing the Pareto front. The discussed procedures are applicable to structures with up to a few dozens of parameters and, from this point of view, they are considered generic. The

developed algorithms were verified based on the design cases of modern wideband antennas and favorably compared with state-of-the-art techniques. A secondary objective of the work was the design and experimental verification of selected ultra-wideband antenna structures.

The aforementioned goals have been achieved by positively verifying the following theses of the work:

1. Variable-fidelity EM simulations, approximation models, surrogate methods and evolutionary algorithms are useful tools for multi-objective optimization of modern antennas.
2. Design space reduction enhances applicability of approximation models to many-dimensional structures.
3. Interpolation models allow for reducing the multi-objective design cost by at least an order of magnitude in comparison to direct optimization of EM antenna models.

1.3 Dissertation Outline

The dissertation is organized as follows. In Chapter 2, the methods and algorithms for expedited modeling and optimization are discussed. The emphasis is put on the description of surrogate-based optimization concept, antenna surrogate models and response correction techniques. Chapter 3 discusses the concept of multi-objective design optimization. It contains formulation of the design problem, description of solution approaches for multi-objective optimization and explanation of utilized multi-objective algorithm.

Chapter 4 describes the methods and algorithms for fast multi-objective optimization of antenna structures. A significant part of the chapter is focused on explaining the fast multi-objective optimization algorithm and formulating design space reduction techniques. Detailed comparison of the developed techniques is also provided. The chapter is summarized with a discussion on the utilized multi-objective optimization approach and its limitations.

In Chapter 5, numerical verification of the considered optimization technique is performed. The method is validated using four antenna structures designed with respect to two objectives. Moreover, two additional problems that include a three-objective-oriented design of a narrow-band dielectric resonator antenna and optimization of a compact microstrip impedance transformer with respect to two requirements are also considered. The number of parameters of the structures range from six to over twenty.

In Chapter 6, two selected antenna designs are experimentally validated. Recommendations and discussion of the multi-objective optimization procedure are provided in Chapter 7. Chapter 8 concludes the dissertation and discusses possible directions for the future work.

2 SURROGATE-BASED MODELING AND OPTIMIZATION

Full-wave electromagnetic analysis belongs to the most important antenna design tools. In the past, application of EM simulations has been limited only to design verification. Typically, simulation-driven design approaches are based on manual adjustment of selected parameters, most often realized through parameter sweeps [97, 98]. Unfortunately, these methods require considerable engineering experience and cannot provide truly optimum results. Alternatively, optimum dimensions of antenna can be obtained through numerical optimization [34, 50, 82]. However, optimization may involve a large number of model evaluations. Other challenges of EM-driven optimization include possible discontinuity or even non-differentiability of objective functions, as well as numerical noise [141].

High cost of antenna design can be reduced, to some extent, by utilization of adjoint sensitivities which allow obtaining derivatives of the antenna responses at small computational overhead [93, 100, 138, 141]. Their combination with gradient-based algorithms allows for speeding up convergence of the optimization process. However, adjoints are available only in certain commercial software packages such as CST Microwave Studio [149] and Ansys HFSS [150]. Derivatives of the antenna response can be estimated using finite differentiation [151]. However, it involves multiple EM simulations per design.

Computational cost of antenna optimization can be also reduced by means of surrogate-based optimization techniques. To date, SBO found applications in various engineering fields, including microwave and antenna engineering [34, 82, 135, 143]. The main concept behind SBO is to replace direct handling of the expensive simulation model by an iterative process that involves construction, optimization and correction of its computationally cheap counterpart, a so-called surrogate. In such a scheme, the optimum values of the antenna design parameters are predicted by optimizing the surrogate which is iteratively corrected and updated using high-fidelity model data. The surrogate is supposed to be a cheap and—at least locally—reasonably accurate representation of the structure under design. The computational advantage of SBO over conventional (direct optimization) methods stems from casting most of the operations into the fast surrogate, while utilizing occasional references to the original (high-fidelity) model for the sake of design verification only. As demonstrated in the literature, design speedup offered by SBO may be

significant [82]. So far surrogate-assisted antenna optimization has been mostly performed in single-objective setups [34, 50].

This chapter reviews the basic principles of surrogate-based optimization and modeling. The SBO concept is introduced in Section 2.1. Fundamentals of surrogate modeling are presented in Section 2.2. Section 2.3 concludes the chapter with discussion of the challenges related to balancing between global and local accuracy of the surrogate model.

2.1 Surrogate-Based Optimization Concept

Design optimization of contemporary antenna structures is predominantly realized using electromagnetic simulations. Simulation-driven design can be formulated as a non-linear minimization problem of the form [152]

$$\mathbf{x}^* = \arg \min_{\mathbf{x}} U(\mathbf{R}_f(\mathbf{x})) \quad (2.1)$$

Here, vector \mathbf{x} represents a set of design parameters of the structure at hand, $\mathbf{R}_f(\mathbf{x})$ is the response of an accurate high-fidelity (or fine) model of the antenna obtained by means of CPU-intensive EM simulations and U is an objective function. Optimum design to be found is denoted by \mathbf{x}^* . Direct solving of (2.1) using high-fidelity EM simulations may be impractical from the point of view of numerical cost [153].

Surrogate-based optimization can be formulated as follows [152]

$$\mathbf{x}^{(i+1)} = \arg \min_{\mathbf{x}} U(\mathbf{R}_s^{(i)}(\mathbf{x})) \quad (2.2)$$

The SBO scheme (2.2) iteratively generates a series of approximate solutions $\mathbf{x}^{(i)}$, $i = 1, 2, \dots$, to the original problem (2.1). The vector $\mathbf{x}^{(i+1)}$ is obtained by optimizing the surrogate model $\mathbf{R}_s^{(i)}(\mathbf{x})$. The surrogate is a faster, yet less accurate representation of high-fidelity model that can be utilized to speed up the antenna design. It is constructed by means of suitable correction of an underlying low-fidelity or functional antenna model \mathbf{R}_c (also referred to as coarse). The aim of the correction process is to reduce discrepancies between $\mathbf{R}_s^{(i)}$ and \mathbf{R}_f at least in the vicinity of the current design $\mathbf{x}^{(i)}$. Under certain conditions (such as a good generalization capability of the surrogate), the process (2.2) may quickly converge to the optimum design \mathbf{x}^* . Thus, the cost of SBO may be substantially lower than for majority of conventional optimization techniques, such as gradient-based methods with numerical derivatives [154], or derivative-free algorithms [155].

The most popular SBO techniques exploit either simplified EM or functional approximation models [141, 153]. Both types are briefly described in Section 2.2. The surrogate is utilized as a prediction tool for identifying the values of adjustable parameters that lead to a better design. The candidate design obtained with the aid of the surrogate is validated by evaluating the high-fidelity model. The latter is also utilized to update the surrogate. In the subsequent iteration, the prediction of the optimal design is carried out by the corrected surrogate. Generally, the operation of the majority of SBO algorithms is as follows (see Figure 2.1 for a flow diagram):

1. Construct the initial surrogate model;
2. Find a design $\mathbf{x}^{(i+1)}$ by optimizing $\mathbf{R}_s^{(i)}$ as in (2.2);
3. Evaluate \mathbf{R}_f at the candidate design solution $\mathbf{x}^{(i+1)}$;
4. If the termination condition is fulfilled, then set $\mathbf{x}^* = \mathbf{x}^{(i+1)}$ and stop; otherwise update the surrogate model and go to Step 2.

The surrogate model update is the fundamental step of the above algorithm which, similarly as its construction, is handled by means of appropriate correction mechanisms. Selection of the most suitable method is essential for successful operation of SBO. In this work, the construction and enhancement of the surrogate is handled by means of space mapping (cf. Section 2.2.3.1) and co-kriging (cf. Section 2.2.3.2).

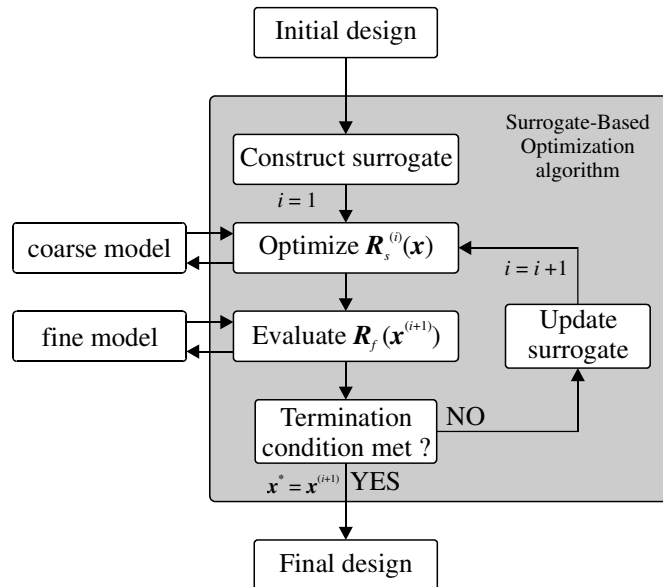


Figure 2.1: Algorithm flow of the surrogate-based optimization process [153].

2.2 Surrogate Models

A surrogate model is a key component of any SBO procedure. It should be fast, sufficiently accurate, and preferably continuous and differentiable [153]. There are two classes of surrogate models that can be distinguished: physics-based and functional (or function approximation) models [141]. Both classes can be utilized in this work for fast design optimization of antennas.

2.2.1 Physics-Based Surrogates

Expedited design of contemporary antennas is usually performed using physics-based surrogates constructed from underlying low-fidelity models. On one hand, evaluation of physical models may involve EM simulations and thus is numerically more expensive compared to the approximation ones. On the other hand, they embed knowledge on the design problem and thus allow obtaining better generalization than functional models.

In microwave engineering, the low-fidelity models are often constructed using empirical or analytical formulas [89, 156]. As mentioned before, such a description is hardly available for modern antennas [86, 95], thus their coarse models—similarly to high-fidelity ones—are constructed entirely within the EM simulation environment. Moreover, both are usually evaluated using the same solver [50, 93]. A conceptual illustration of low-fidelity antenna modeling by means of EM simulations is shown in Figure 2.2.

Simulation speedup of the low-fidelity model is primarily achieved by reducing the discretization density of the structure [141] but also by neglecting certain phenomena that are normally accounted for in the high-fidelity EM model. Possible simplifications include, among others, modeling of metallization as infinitely thin sheet, neglecting dielectric losses, or utilization of perfect electrical conductor instead of metallization with finite conductivity [141]. The simulation cost of low-fidelity antenna model may be also decreased by reducing its computational domain or by neglecting the influence of the structure environment [153]. The latter can be achieved by removing from the model any neighboring subsystems and adjacent components such as connectors or housing [106]. The above simplifications may limit the cost of model evaluation by a factor of 10 up to 50 with respect to the high-fidelity one [141, 153]. Clearly, model simplifications also decrease its accuracy and thus appropriate balance between them has to be ensured to maintain the reliability of the SBO process.

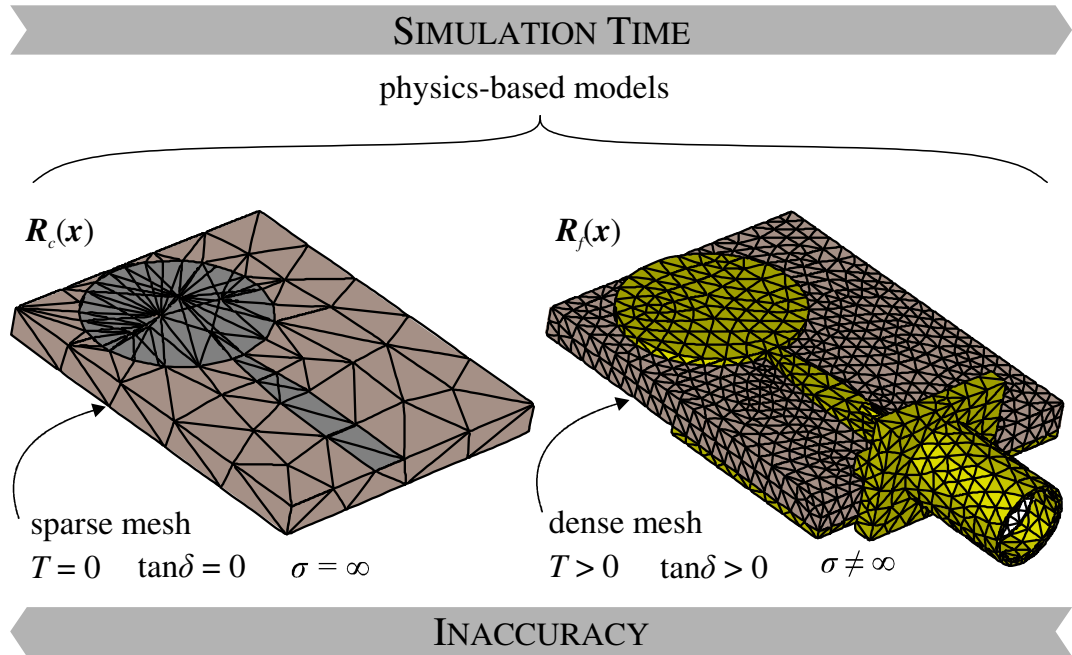


Figure 2.2: EM simulation models of an exemplary antenna structure [106]. The low-fidelity EM model is usually 10 to 50 times faster than the high-fidelity one. Simplifications introduced in the former may include: coarse discretization of a structure, zero thickness metallization ($T = 0$), perfect conductivity of metallization ($\sigma = \infty$), and lossless dielectric ($\tan\delta = 0$). Complexity of the model can be also reduced e.g., by excluding antenna connector from simulation. It should be noted that the computational cost is reduced at the expense of degraded accuracy of the $R_c(x)$ model.

As of now, the low-fidelity model setup is normally obtained based on engineering experience [82, 141, 157]. The process is as follows. Initially, a series of EM model simulations for meshes with various (usually gradually increasing) densities is performed at one or a few designs. Subsequently, appropriate antenna representations on both (high and low) levels of fidelity are selected based on visual inspection of the characteristics.

Automated setup of a fast yet reasonably accurate low-fidelity model, although more desired for SBO, is considerably more challenging. The main difficulty is finding a suitable measure of discrepancy between the antenna models of various fidelities [141]. Standard measures, such as a norm are inadequate because they cannot account for discrepancies between the models that could be easily corrected (e.g., frequency shifts for narrowband designs). A few promising techniques aimed at handling this problem have been developed so far. These include the feature selective validation technique and a procedure based on analysis of correlations between response features of the structure at hand [158, 159].

2.2.2 Function Approximation Surrogates

Functional models, also known as response surface approximation or data-driven models, utilize simulation and/or measurement data to mimic the behavior of the system within a defined region of the search space [142]. RSA models are generic in a sense that they are applicable to variety of problems. The RSA model is constructed by identifying its parameters so that the model fits the available training data. Coefficients of the model are often obtained through solving of a separate optimization problem (e.g., for kriging or neural networks) [153]. Functional models are very fast, but they do not embed any knowledge about the problem and, consequently, their extrapolation capabilities are normally poor. Moreover, the cost of RSA setup may be very high because considerable amount of data is normally required to ensure reasonable accuracy.

A general procedure for RSA model construction may be summarized as follows [153]:

1. Allocate training samples using a suitable design of experiments technique;

2. Acquire training data by simulating the high-fidelity model at the designs pre-selected in Step 1;
3. Identify the RSA model using a selected approximation technique;
4. Validate the model;
5. If the target accuracy is achieved then stop; otherwise generate infill points and go to Step 2;

The block diagram of the above procedure is shown in Figure 2.3. In the first step of the process, appropriate Design of Experiment (DoE) strategy is utilized for allocating the training data within the search space (cf. Section 2.2.2.1). The number of required samples mostly depends on the complexity of problem (dimensionality of the design space, parameter ranges, and non-linearity of the system responses) and selected DoE. Subsequently, the training data is acquired at selected locations (here, using EM simulations). In the next step, the RSA model is identified. Techniques for RSA construction include, among others polynomial regression [133], radial basis functions [142, 153], and neural networks [153, 160]. Here, the approximation models are generated using kriging (cf. Section 2.2.2.2). Finally, the accuracy of the RSA is verified using an appropriate validation technique (see Section 2.2.2.3). Both approximation and generalization capability of the model are of interest (cf. Section 2.3). In case of insufficient accuracy, model generalization may be improved by incorporating additional (infill) samples. The latter can be allocated using a suitable DoE technique [134]. Figure 2.4 illustrates the concept of RSA model generation. For simplicity, it is explained using the exemplary antenna structure with only two design parameters. More detailed discussion on each step of the model construction process is provided in the following subsections.

2.2.2.1 Design of Experiments

The term design of experiments refers to strategies for allocation of training data samples—here, the vectors of antenna geometry parameters—within the search space. The goal of DoE is to allocate the training samples according to given requirements (e.g., uniformly). In this work, the search space is defined by the lower and upper bounds (denoted as \mathbf{l} and \mathbf{u} , respectively) for design parameters [146]. Later on, the surrogate model is constructed using the EM model data acquired at the points assigned by DoE (cf. Section 2.2.2.2).

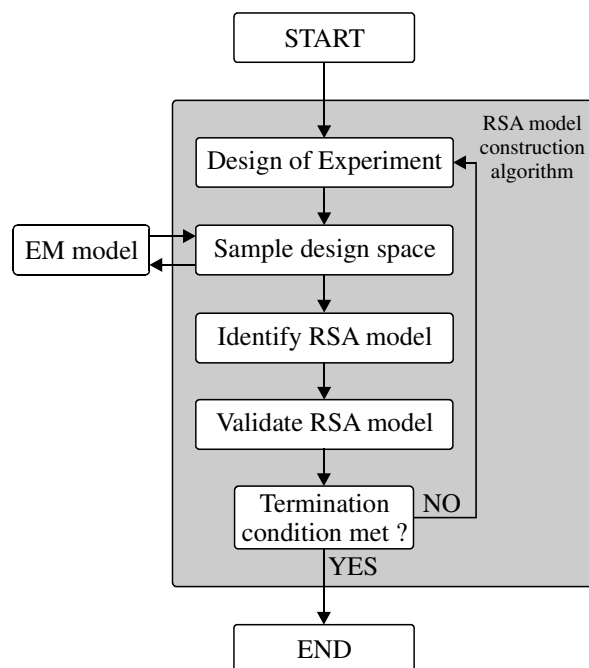


Figure 2.3: Design flow of RSA model construction.

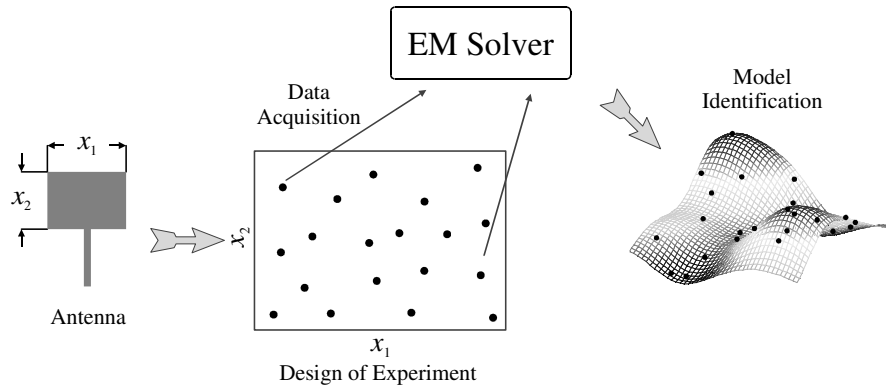


Figure 2.4: Visualization of RSA modeling process [106]. Two-dimensional ($D = 2$) search space of an exemplary planar antenna is sampled and the EM antenna model is evaluated at the selected designs. The EM data is utilized for identification of the RSA model that represents the behavior of the structure.

Factorial designs and Latin hypercube sampling belong to the most popular DoE methods for antenna design [134, 153]. Both are utilized in this dissertation. Other commonly used DoE include quasi-Monte Carlo [161], orthogonal array sampling [133], and pseudo-random sampling [153]. More detailed discussion on DoE techniques can be found in the literature [133, 151, 161].

Basic implementation of the first mentioned DoE—full factorial designs—allocates $N = p^D$ samples on a rectangular grid, where p stands for the number of points along each dimension whereas D is the number of design variables. Better control of the number of samples along each dimension is ensured by fractional factorial designs

$$N = \prod_{k=1}^D p_k \quad (2.3)$$

Appropriate number of points along each dimension can be determined by means of sensitivity analysis [133]. Nonetheless, the number of samples N in factorial designs techniques grows quickly with the dimensionality of the problem, which is a bottleneck for numerically demanding antenna designs with multiple parameters (i.e., for 10-parameter structure with only two points along each dimension, $N = 1024$). Alternative fractional factorial designs, commonly used in microwave/antenna engineering, is a star-distribution scheme that generates $N = 2D + 1$ designs located at the center of the selected search space region and at the center of each of its faces [82, 106]. Selected factorial designs-based sample allocation techniques are illustrated in Figure 2.5.

Selection of suitable DoE is especially important when design problems with many parameters are considered. For instance, conventional implementations of factorial designs generate abundance of sample points which translates to high cost of data acquisition. From this perspective, an approach for generating a possibly uniform distribution for a given number of samples N is preferred. This can be partially addressed by means of stratified methods such as Latin Hypercube Sampling (LHS) [133]. The technique is based on division of each dimension into N regions so that in D dimensional space a total number of D^N regions—with equal selection probability of $1/D^N$ —are obtained. Subsequently, the N test points are determined within the search space in the following manner: (i) each point is allocated within a randomly selected region, and (ii) for all one-dimensional projections of N regions and points, in each region there is exactly one point [153]. It should be noted that LHS can produce highly non-uniform distributions of points (e.g., diagonally allocated set) which still fulfill conditions (i) and (ii). This difficulty can be mitigated by improvements which enforce more uniform allocation of samples [162-164]. Figure 2.6 illustrates different sample distributions that can be produced by conventional LHS scheme.

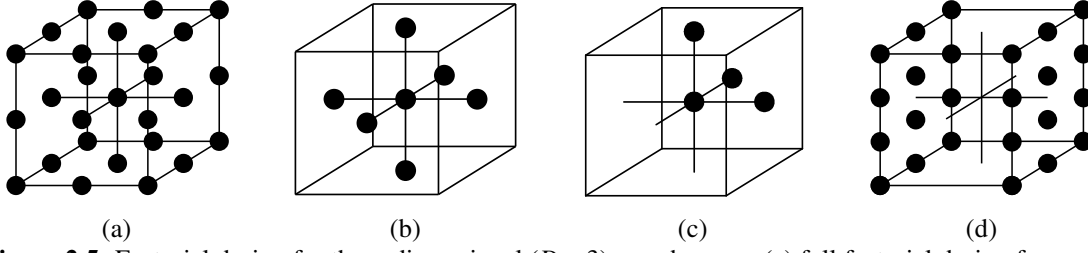


Figure 2.5: Factorial design for three-dimensional ($D = 3$) search space: (a) full factorial design for $p = 3$; (b) star-distribution; and (c) half-star-distribution factorial design [153]; (d) fractional design defined by (2.3) with different density of samples along each dimension: $p = [2 \ 3 \ 4]^T$.

2.2.2.2 Kriging Interpolation

The points allocated using DoE are utilized, upon acquiring the corresponding EM simulation data, for RSA model construction. A particular modeling technique discussed in this section is kriging interpolation. Although, the term ‘kriging’ originates from the South African mining engineer Krige [165], the method was formally developed by Matheron [166]. Kriging surrogates are characterized, among others, by low computational cost [146], smooth response surface [151], and relatively simple implementation as well as several third-party toolboxes available (e.g., [167, 168]). The method proved to be useful in the context of antenna design [106, 146] but also other engineering problems [133, 145]. The kriging model is a composition of a trend function implemented as a low-order polynomial (zero-, first- or second-order) and a systematic departure representing local deviations of the model [133, 142]. A brief formulation of the kriging model is presented below.

Let $X = \{\mathbf{x}^1, \mathbf{x}^2, \dots, \mathbf{x}^N\}^T$ be a set of training points and $\mathbf{R}_f(X) = \{\mathbf{R}_f(\mathbf{x}^1), \mathbf{R}_f(\mathbf{x}^2), \dots, \mathbf{R}_f(\mathbf{x}^N)\}^T$ be the corresponding set of high-fidelity model responses. The goal of kriging is to fit the regression function to available data samples. In its basic form (often referred to as ordinary kriging [133]), the kriging predictor can be defined as [169]

$$\mathbf{R}_{KR}(\mathbf{x}) = M\alpha + r^T(\mathbf{x}) \cdot \Psi^{-1}(\mathbf{R}_f(X) - F\alpha) \quad (2.4)$$

where $\mathbf{R}_{KR}(\mathbf{x})$ is the unknown response of the surrogate model for the given non-sampled location \mathbf{x} . The regression coefficient α is determined by the generalized least squares (unknown model parameters), $r(\mathbf{x})$ is a $1 \times N$ vector of correlations between the point \mathbf{x} and the base set X , whereas Ψ is an $N \times N$ correlation matrix, $M = 1$ and $F = [1 \ 1 \ \dots \ 1]^T$. They are defined as [151]

$$\alpha = \frac{F^T \Psi^{-1} \mathbf{R}_f(X)}{F^T \Psi^{-1} F} \quad (2.5)$$

$$r(\mathbf{x}) = [\Psi(\mathbf{x}, \mathbf{x}^1) \ \dots \ \Psi(\mathbf{x}, \mathbf{x}^N)] \quad (2.6)$$

$$\Psi = \begin{bmatrix} \Psi(\mathbf{x}^1, \mathbf{x}^1) & \dots & \Psi(\mathbf{x}^1, \mathbf{x}^N) \\ \vdots & \ddots & \vdots \\ \Psi(\mathbf{x}^N, \mathbf{x}^1) & \dots & \Psi(\mathbf{x}^N, \mathbf{x}^N) \end{bmatrix} \quad (2.7)$$

Correlation function is a key component of the kriging model. Here, the following correlation function is utilized

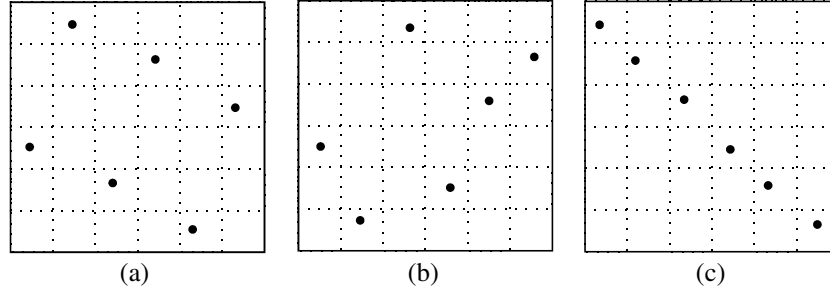


Figure 2.6: Different realizations of conventional LHS distributions ($N = 6$) in two-dimensional search space: (a) fairly uniform realization; (b) non-uniform realization; and (c) highly non-uniform realization with diagonally allocated samples.

$$\Psi(\mathbf{x}, \mathbf{x}') = \exp\left(\sum_{k=1}^D -\theta_k |x^k - x'^k|^{s_k}\right) \quad (2.8)$$

The correlation between two points \mathbf{x} and \mathbf{x}' (x^k and x'^k denote vector components along k th dimension) is controlled by smoothness factor s_k and correlation parameters θ_k . The former can be utilized to adjust (2.8) so that it reflects expected properties of the response surface. For engineering problems the system response is usually smooth and continuous and thus Gaussian correlation with $s_k = 2$ can be utilized [170]. However for sharp responses, the exponential correlation function ($s_k = 1$) or the one with $s_k < 1$ may be more suitable [170]. The parameter θ_k determine a range of influence of a sample point on its neighbors in k th dimension [151]. It is determined by maximizing the likelihood estimation of available training samples [170]. The concentrated ln-likelihood function $\ln(L)$ can be reformulated as a minimization problem of the form

$$\ln(L) \approx -\frac{N}{2} \ln(\sigma^2) - \frac{1}{2} \ln(|\Psi|) \quad (2.9)$$

$$\sigma^2 = \frac{(\mathbf{R}_f(X) - F\alpha)^T \Psi^{-1} (\mathbf{R}_f(X) - F\alpha)}{N} \quad (2.10)$$

where σ^2 is estimated variance of the model. The kriging model, on the top of predicting the systems response, also provided information about the prediction variance [142]. Consequently, prediction error of the model (expressed in terms of correlation between samples) can be estimated at any point of the design space. Since kriging is the interpolative technique, the correlation at the training points is one [170]. In this work, implementation of kriging available in DACE toolbox is used [167].

Generally, kriging is interpolation method. However, its modifications (e.g., blind kriging [142]) may be used for extrapolation beyond the sampled region of the design space. Such extensions may be especially useful if certain regions of the search space lack sufficient sampling. It should be noted that other basis functions methods are also available in the literature. These include radial basis functions [171], support vector regression [172], or Gaussian process regression [173] to name just a few. For more detailed description of kriging, see, e.g., [133, 142, 151, 170].

2.2.2.3 Model Validation

Validation is the last step related to RSA construction. It is important because approximation models are always biased to some extent. Error estimation allows the user to decide whether the model is sufficiently accurate for a particular purpose or requires incorporation of additional training data. Model accuracy can be determined using suitable validation routines that, in gen-

eral, divide available data into two subsets. The first one is utilized for RSA construction, whereas the second serves as the reference (testing) data. The most popular techniques, i.e., split sample and cross validation are discussed below. It should be noted that model validation can be fed back into the model construction procedure for automatic generation of the model with desired accuracy [146].

The concept of the split sample method is illustrated in Figure 2.7(a). The available data is split into training and test sets. The former comprises majority of samples and it is utilized for the model construction. The model error is estimated by comparing its prediction at the testing points with the true values at these points. A disadvantage of the split sample method is its high variance (i.e., dependence of the predicted error on the allocation of test samples). Distortion of the results caused by constructing the model using only a portion of available samples—excluding the test set (cf. Section 2.2.2.2)—is another weakness of the split sample method. On the other hand, it is easy to implement and useful for fast estimation of the RSA quality [153].

Cross validation may be considered as an extension of the split sample method that utilizes all available nodes for both RSA model construction and estimation of its error. The method divides the data samples into L subsets of equal (or approximately equal) sizes. Each of these subsets is sequentially utilized as test data for the RSA model constructed using remaining $L - 1$ subsets. Similarly to the split sample method, cross validation estimates generalization error by comparing the approximated and the actual responses at the test points [133]. The difference lies in the amount of information utilized for error estimation. The scheme provides L partial error estimations that are collectively less biased than the single model assessment. The obtained results can be utilized for approximation of the model average error or its standard deviation. It should be mentioned here, that the split sample method outperforms cross validation in terms of the computational cost [153]. This might be important if the RSA model is constructed using large number of samples. The method is schematically illustrated in Figure 2.7(b).

2.2.2.4 Cost of RSA Model Construction

The main difficulty related to application of RSA to a design of contemporary antenna structures lies in the tremendous computational cost of data acquisition (large number of high-fidelity EM simulations) required to achieve sufficient model accuracy. As mentioned before, the cost of data acquisition grows quickly with dimensionality of the problem. It means that applicability of RSA for constructing antenna models in a setup involving multi-parameter spaces (say, with over a dozen of variables) or computationally expensive models (characterized by simulation times being orders of many minutes or hours) is limited. These difficulties may be partially alleviated using techniques of Section 2.2.3.

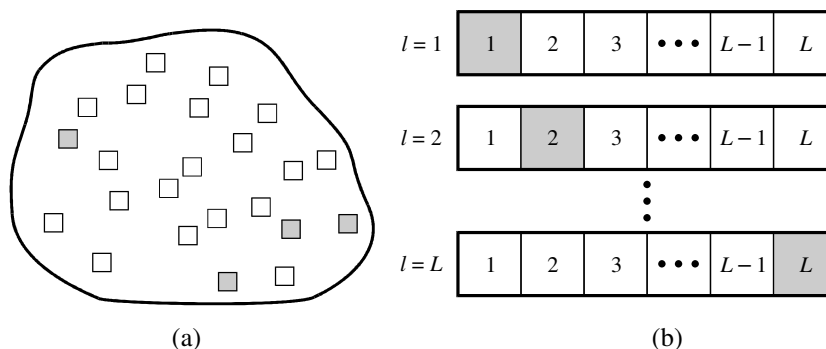


Figure 2.7: Conceptual visualization of RSA validation methods: (a) split sample; (b) cross validation. The gray squares represent the testing data, whereas the training samples are marked as the white ones. Error estimated by the split sample depends on the location of the test samples. Here, the test samples represent only a fraction of the search space. Cross validation method sequentially utilizes all data subsets for RSA construction and validation, thus the error estimation is less biased.

2.2.3 Variable-Fidelity Modeling

Data acquisition may be prohibitively expensive when high-fidelity model is used for RSA model construction. Cost reduction can be achieved by utilizing low-fidelity data instead. However, an important issue is discrepancy between the EM models, which should be reasonably small in order to ensure sufficient generalization of the response surface approximation surrogate. Nevertheless, the low-fidelity RSA model has to be corrected—at some stage of the design process using high-fidelity data—because the optimization results are eventually sought at the high-fidelity model level.

Correction of the RSA model can be realized using variable-fidelity surrogate-based optimization techniques. The basic concept is to utilize sparsely allocated high-fidelity data to enhance the RSA model and, consequently, increase its accuracy. This can be realized by means of space mapping (cf. Section 2.2.3.1) or co-kriging (cf. Section 2.2.3.2). In space mapping, the transformations utilized for model correction are normally parameterized and the parameters are extracted through nonlinear regression. In co-kriging prediction accuracy of the model is enhanced by blending together the low- and high-fidelity model data into one surrogate. Discussed variable-fidelity modeling concepts are illustrated in Figure 2.8.

2.2.3.1 Correction of Training Data Using Space Mapping

Space mapping (SM), initially proposed by Bandler *et al.* in 1994 [174], is one of the most popular techniques for accelerated simulation-driven design in microwave engineering. The original concept is based on making adjustments at the level of design variables of the low-fidelity model (input SM) [174]. However, alternative SM methods which exploit parameters independent from the design variables (implicit SM) [175], correct the low-fidelity model response (output SM) [152], or utilize parameters specific to the problem at hand (frequency SM) [176] have been also developed.

Common misalignments between reflection responses of the high- and the low-fidelity antenna models which should be accounted for to ensure reliability of the design process are frequency shifts and vertical discrepancies. Good model alignment is especially important when the design response is close to the boundary of acceptable performance. This is often the case for compact structures, where the in-band reflection of the optimized design is just below the acceptable level of -10 dB [34, 82]. Such discrepancies can be corrected using frequency and output space mapping, which are briefly described below [82, 106, 146].

The frequency-scaled antenna model is defined as

$$\mathbf{R}_s(\mathbf{x}) = \mathbf{R}_c(\mathbf{x}, \omega_f) \quad (2.11)$$

where $\mathbf{R}_c(\mathbf{x}, \omega_f)$ denotes explicit dependence of the low-fidelity model \mathbf{R}_s on frequency (here, changes of reflection response for a discrete range of frequencies ω_f). Frequency space mapping can be realized as an affine transformation of the following form [176]

$$\omega_f = F_0^* + \omega F_1^* \quad (2.12)$$

where $\omega = [\omega^1 \dots \omega^m]^T$ denote the original frequency sweep. Additive and multiplicative scaling coefficients are denoted by F_0^* and F_1^* , respectively. The scaling parameters are found by solving the nonlinear regression problem of the form [177]

$$[F_0^*, F_1^*] = \arg \min_{[F_0^*, F_1^*]} \sum_{n=1}^N \left\| \mathbf{R}_f(\mathbf{x}^n) - \mathbf{R}_c(\mathbf{x}^n, F_0^* + \omega F_1^*) \right\| \quad (2.13)$$

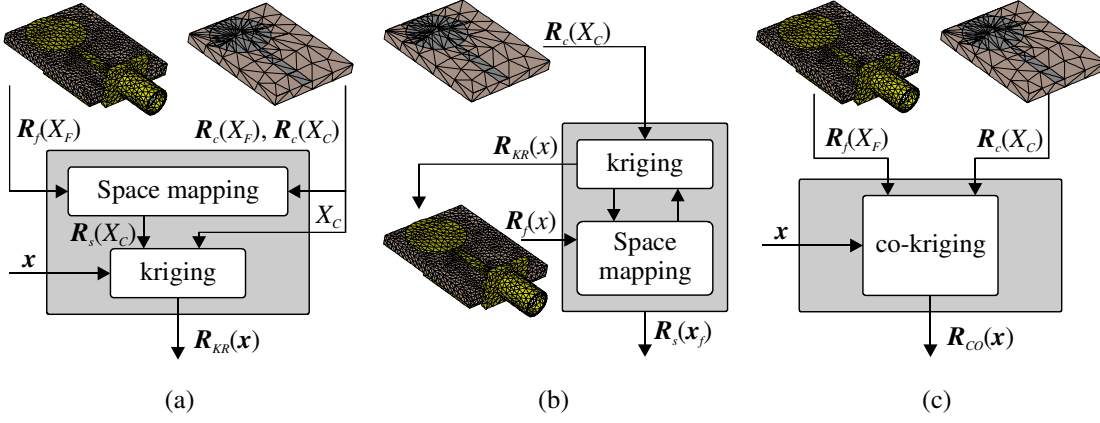


Figure 2.8: Various variable-fidelity modeling concepts: (a) pre-refinement of data for RSA model construction; (b) post-refinement of the RSA model constructed using low-fidelity samples; (c) co-kriging surrogate constructed using blended high- and low-fidelity model samples. For explanation of abbreviations see Sections 2.2.3.1 and 2.2.3.2.

Here, \mathbf{x}^n ($n = 1, 2, \dots, N$) denote the reference designs. The method (2.11) is a convenient approach for reducing frequency misalignment between models of various fidelities.

Vertical misalignment between the high- and low-fidelity model responses can be reduced by means of output space mapping (OSM) [178]. This can be realized, among others, by means of multiplicative correction given by [177]

$$\mathbf{R}_s(\mathbf{x}) = \mathbf{A}^* \cdot \mathbf{R}_c(\mathbf{x}) \quad (2.14)$$

where \mathbf{R}_s is a OSM-corrected model and \mathbf{A}^* stands for a diagonal correction matrix

$$\mathbf{A}^* = \text{diag}([a_1 \cdots a_m]) \quad (2.15)$$

The matrix elements $a_1 \dots a_m$ can be obtained as

$$\mathbf{A}^* = \arg \min_A \sum_{n=1}^N \left\| \mathbf{R}_f(\mathbf{x}^{(n)}) - \mathbf{A} \cdot \mathbf{R}_c(\mathbf{x}^{(n)}) \right\|^2 \quad (2.16)$$

where $n = 1, \dots, N$, denote the number of points utilized for correction. Output space mapping can be also realized as additive correction of the form [179]

$$\mathbf{R}_s(\mathbf{x}) = \mathbf{R}_c(\mathbf{x}) + \mathbf{D}^* \quad (2.17)$$

where the vector $\mathbf{D}^* = [d_1 \ d_2 \ \dots \ d_m]^T$ can be obtained as

$$\mathbf{D}^* = \arg \min_D \sum_{n=1}^N \left\| \mathbf{R}_f(\mathbf{x}^{(n)}) - [\mathbf{R}_c(\mathbf{x}^{(n)}) + \mathbf{D}] \right\|^2 \quad (2.18)$$

Here, $n = 1, \dots, N$, stands for the number of training points. Both (2.16) and (2.18) are, in fact, equivalent to linear regression problems that can be solved analytically. Another possibility is a combination of additive and multiplicative correction [179]

$$\mathbf{R}_s(\mathbf{x}) = \mathbf{A}^* \cdot \mathbf{R}_c(\mathbf{x}) + \mathbf{D}^* \quad (2.19)$$

The quality of the surrogate model constructed using OSM depends on correlation between \mathbf{R}_c and \mathbf{R}_f , as well as on the allocation and the number of high-fidelity samples utilized for correction. Selection of high-fidelity samples can be performed based on engineering experience or by means of appropriate DoE techniques [106]. It should be noted that discussed correction approaches can be used separately or in combination with frequency SM. The latter is realized by substituting the low-fidelity model in (2.14), (2.17), or (2.20) by their corresponding frequency scaled surrogate (2.11). Moreover, frequency SM and OSM corrections can be applied directly to the \mathbf{R}_c model prior to construction of the RSA surrogate (pre-refinement), as well as to correct the RSA model responses (post-refinement).

In the optimization context, OSM correction is usually realized as a single-point model enhancement of the form [178]

$$\mathbf{R}_s^{(i)}(\mathbf{x}) = \mathbf{R}_c(\mathbf{x}) + \left[\mathbf{R}_f(\mathbf{x}^{(i)}) - \mathbf{R}_c(\mathbf{x}^{(i)}) \right] \quad (2.20)$$

where $\mathbf{R}_s^{(i)}(\mathbf{x})$, $i = 1, 2, \dots$, is the surrogate model response at the given design \mathbf{x} (cf. Section 2.2.2.2). The correction term $[\mathbf{R}_f(\mathbf{x}^{(i)}) - \mathbf{R}_c(\mathbf{x}^{(i)})]$ ensures zero-order consistency between the high-fidelity and RSA model responses at design $\mathbf{x}^{(i)}$, which means that $\mathbf{R}_s^{(i)}(\mathbf{x}^{(i)}) = \mathbf{R}_f(\mathbf{x}^{(i)})$ at the beginning of each iteration [152, 180]. A more detailed survey of space mapping can be found in [135, 136, 152].

2.2.3.2 Co-kriging Modeling

Co-kriging is an extension of kriging that exploits multi-fidelity data to increase the accuracy of the surrogate model. The method incorporates the Markov assumption that inaccuracies of the RSA are introduced only by low-fidelity samples. High-fidelity data provide exact information about the problem at hand [151]. The formulation of co-kriging presented here is based on the autoregressive model of Kennedy and O'Hagan [181].

Consider the two training sets of the high- and low-fidelity model samples, i.e., $X_F = \{\mathbf{x}_f^1, \mathbf{x}_f^2, \dots, \mathbf{x}_f^N\}^T$ and $X_C = \{\mathbf{x}_c^1, \mathbf{x}_c^2, \dots, \mathbf{x}_c^N\}^T$. Then, let $\mathbf{R}_f(X_F)$ and $\mathbf{R}_c(X_C)$ be the sets of the high- and low-fidelity model responses, respectively. Co-kriging is essentially a sequential process involving construction of two kriging interpolation models. The first model, denoted as \mathbf{R}_γ is constructed using the low-fidelity samples $\mathbf{R}_c(X_C)$. The second model \mathbf{R}_δ is constructed on residuals between the low- and high-fidelity samples. The residuals \mathbf{R}_δ are defined as [142]

$$\mathbf{R}_\delta = \mathbf{R}_f(X_F) - \rho \cdot \mathbf{R}_c(X_C) \quad (2.21)$$

Here, ρ stands for maximum likelihood estimation of the \mathbf{R}_δ model [182]. If, for some reason, the responses $\mathbf{R}_c(X_C)$ are unavailable, they can be approximated using the first kriging model

$$\mathbf{R}_c(X_C) \approx \mathbf{R}_\gamma(X_C) \quad (2.22)$$

The important feature of co-kriging modeling is the possibility for separate adjustments of correlation and/or regression functions for the low-fidelity data \mathbf{R}_c and the residuals \mathbf{R}_δ . Both considered models use the correlation function (2.8). The co-kriging interpolant is given by [169]

$$\mathbf{R}_{CO}(\mathbf{x}) = \mathbf{M}\alpha + r^T(\mathbf{x}) \cdot \Psi^{-1} \cdot (\mathbf{R}_\delta - F\alpha) \quad (2.23)$$

Here, α is obtained from (2.5), whereas the parameters M , F , $r(\mathbf{x})$ and Ψ denote block matrices of the two underlying kriging models \mathbf{R}_γ and \mathbf{R}_δ [151]

$$r(\mathbf{x}) = \left[\rho \cdot \sigma_\gamma^2 \cdot r_\gamma(\mathbf{x}), \quad \rho^2 \cdot \sigma_\gamma^2 \cdot r_\gamma(\mathbf{x}, X_F) + \sigma_\delta^2 \cdot r_\delta(\mathbf{x}) \right] \quad (2.24)$$

$$\Psi = \begin{bmatrix} \sigma_\gamma^2 \Psi_\gamma(X_C, X_C) & \rho \sigma_\gamma^2 \Psi_\gamma(X_C, X_F) \\ \rho \sigma_\gamma^2 \Psi_\gamma(X_F, X_C) & \rho^2 \sigma_\gamma^2 \Psi_\gamma(X_F, X_F) + \sigma_\delta^2 \Psi_\delta(X_F, X_F) \end{bmatrix} \quad (2.25)$$

$$F = \begin{bmatrix} F_\gamma & 0 \\ \rho \cdot F_\delta & F_\delta \end{bmatrix}, \quad M = \begin{bmatrix} \rho \cdot M_\gamma & M_\delta \end{bmatrix} \quad (2.26)$$

Matrices Ψ_γ , Ψ_δ , σ_γ , σ_δ are obtained from \mathbf{R}_γ and \mathbf{R}_δ models, respectively. Moreover, parameters F_γ , F_δ and M_γ , M_δ are set constant. Process variances σ_γ^2 and σ_δ^2 are obtained from (2.10). The optimized set of parameters θ_k (cf. Section 2.2.2.2) and the correlation functions of \mathbf{R}_γ and \mathbf{R}_δ are determined by the correlation matrices Ψ_γ and Ψ_δ defined as in (2.8). The correlation vectors r_γ , r_δ are defined as in (2.6). It should be noted that the covariance matrix Ψ of (2.25) is the key component of \mathbf{R}_{CO} , because it includes correlation information between the high- and low-fidelity model responses. In this work, implementation of co-kriging from SUMO (SURrogate MOdeling) toolbox is used [168].

Figure 2.9 illustrates the co-kriging concept using an analytical function example [183]. The kriging interpolant based on sparsely allocated high-fidelity samples does not provide accurate response prediction. Although kriging precisely interpolates the low-fidelity samples, the obtained results are distant from the high-fidelity response because the samples are inaccurate. The high-fidelity function behavior can be captured more accurately if high- and low-fidelity model data are blended into a co-kriging surrogate. As it can be seen, co-kriging provides more precise response than kriging constructed merely using either low- or high-fidelity model samples. More detailed survey of co-kriging can be found in [142, 151].

2.3 Exploitation versus Exploration

Surrogate-assisted design is an iterative process that involves construction and optimization of the corrected low-fidelity model. The high-fidelity model data accumulated in the course of the process can be used either to improve the global accuracy of the surrogate (design space exploration) or to identify the optimum design in the promising regions of the design space found beforehand (design space exploitation). Allocation of these points (also referred to as infill points [142]) depends on a particular purpose. For exploration, the points are situated in the areas corresponding to the largest estimated model error [142]. For exploitation, local or global surrogate model optima are utilized. In general, finding a working balance between exploration and exploitation is important (see also [142, 184] for more in-depth discussion of the subject).

It should be emphasized that pure exploration by means of dense sampling of the design space and construction of a globally accurate surrogate model is impractical when expensive EM simulations are utilized for antenna evaluation [153]. A workaround is initial restriction of the design space using certain criteria such as design feasibility (e.g., with respect to acceptable antenna responses) or Pareto-optimality (e.g., optimum designs with respect to individual design objectives). The optimization methods presented in this work are largely based on this concept (cf. Chapter 4).

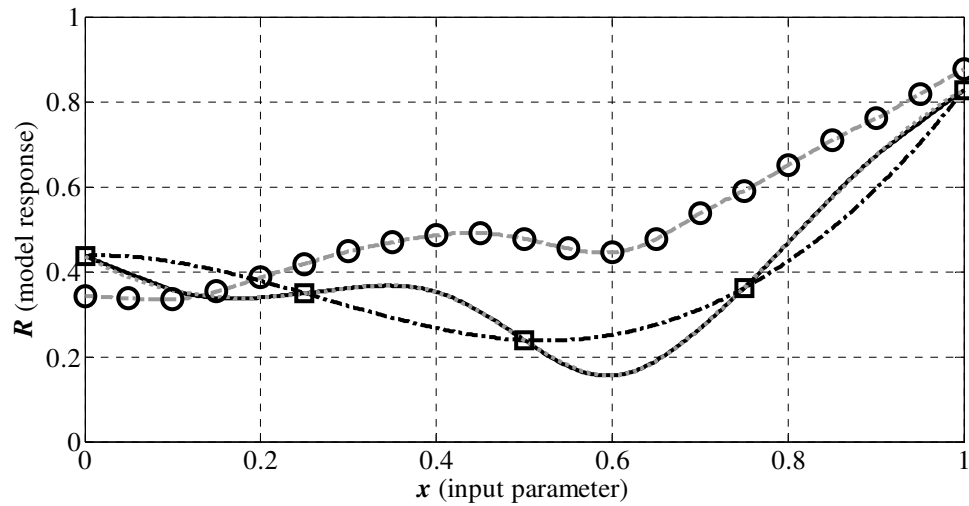


Figure 2.9: Illustration of the co-kriging concept [183]: high-fidelity model (—), low-fidelity model (gray dashed line), high-fidelity model samples (\square), low-fidelity model samples (\circ). Kriging interpolation of the high-fidelity model samples ($- \cdot -$) is not an adequate representation of the high-fidelity model (due to the limited data set size). Co-kriging interpolation (gray dotted line) of blended low- and high-fidelity model data provides much better accuracy at low computational cost.

3 MULTI-OBJECTIVE OPTIMIZATION

In this work, optimization is understood as solving the problem (2.1). In many cases, (2.1) is considered with a scalar objective function where comparison of designs is straightforward (lower value of the objective function corresponds to a better design). Unfortunately, majority of real-world design problems are of multi-objective nature, i.e., require simultaneous handling of several criteria. In antenna engineering, design requirements usually refer to structure performance (reflection response [50], gain [106], radiation pattern [185], side-lobe level [147]) as well as its geometry (size [82] or volume [185]). If the priorities concerning the design goals are established, the optimization problem can be simplified to single-objective one, e.g., by selecting the primary objective and controlling the remaining ones through appropriately defined constraints. Other methods are based on utilization of a weighted sum approach or penalty functions in order to aggregate objectives into a scalar cost function [105]. However, in some situations, acquiring knowledge about possible design alternatives might be necessary, in particular, designs that represent the best trade-offs between conflicting criteria [114]. This calls for genuine multi-objective optimization. From numerical point of view, solving multi-objective optimization problems is considerably more challenging than single-objective ones [105].

In practice, only one solution is needed as a final outcome of the optimization process, regardless the type of considered problem. On the other hand, the knowledge of the trade-offs between design requirements may be indispensable to make application-dependent design decisions. In other words, having a set of alternative solutions, an experienced engineer can utilize some higher-level information to select the design that is the most suitable for a specific application (this is referred to as a decision making process) [114]. Another potential benefit of having compromise designs is their reusability. From this perspective, multi-objective optimization may reduce the cumulative computational cost related to the development of a group of systems with similar (but not the same) performance characteristics.

The most popular algorithms for solving multi-objective design tasks are population-based metaheuristics [102, 103, 123, 126]. They are stochastic algorithms that mimic certain biological, social or physical phenomena [186]. The main feature of population-based metaheuristics, which makes them useful for solving multi-objective problems, is the ability to process and outcome the entire set of solutions in a single run [80, 103, 106, 114]. Nonetheless, they require thousands or even tens of thousands of objective function evaluations to complete the optimization process. Therefore, direct multi-objective optimization of EM antenna models using population-based metaheuristics is numerically very expensive.

This chapter provides formulation of the multi-objective optimization problem and outlines the most popular solution approaches. The emphasis is put on evolutionary methods which are presented in more detail because of their subsequent use in this work.

3.1 Problem Formulation

A multi-objective optimization can be formulated as simultaneous minimization of several cost functions [114]

$$\mathbf{x}^* \in \arg \min_{\mathbf{x} \in X_I} F(\mathbf{x}) = \begin{bmatrix} F_1(\mathbf{x}) \\ \vdots \\ F_K(\mathbf{x}) \end{bmatrix} \quad (3.1)$$

where \mathbf{x} stands for vector of decision variables: $\mathbf{x} = [x_1, x_2, \dots, x_D]^T$, X_I is a feasible space (or, objective function domain) and $F(\mathbf{x})$ is a vector of given objective functions $F_k(\mathbf{x})$, $k = 1, \dots, K$. Vector \mathbf{x}^* denotes the optimal design [114], whereas $F(X_I)$ is the design space image (through F) embedded in the feature space. Note that (3.1) is formulated as minimization-only problem. However, without loss of generality maximization of a function $F_k(\mathbf{x})$ can be considered as minimization of $-F_k(\mathbf{x})$.

Conventional notion of optimality used in single-objective optimization is not applicable for multi-objective design [105]. If $K > 1$, any two designs $\mathbf{x}^{(1)}$ and $\mathbf{x}^{(2)}$ that satisfy relations $F_k(\mathbf{x}^{(1)}) < F_k(\mathbf{x}^{(2)})$ and $F_l(\mathbf{x}^{(2)}) < F_l(\mathbf{x}^{(1)})$ for at least one pair $k \neq l$ ($l = 1, \dots, K$) are non-commensurable which means that none of them is better than the other in multi-objective sense [105, 114]. A convenient and widely used way of comparing the solutions is a Pareto-dominance relation formulated as follows [105, 114]: for any two designs \mathbf{x} and \mathbf{y} in X_I , the design \mathbf{x} dominates over \mathbf{y} (or $\mathbf{x} \prec \mathbf{y}$) if $F_k(\mathbf{x}) \leq F_k(\mathbf{y})$ for all design objectives and $F_k(\mathbf{x}) < F_k(\mathbf{y})$ for at least one k [114]. The domination concept can be utilized to define optimality in the multi-objective sense: the vector \mathbf{x} is Pareto-optimal in X_I if it is non-dominated by any $\mathbf{y} \in X_I$. The goal of multi-objective optimization is to find a representation of a Pareto front X_P consisting of non-dominated designs from the search space X_I , such that for any $\mathbf{x} \in X_P$, there is no $\mathbf{y} \in X_I$ for which $\mathbf{y} \prec \mathbf{x}$ [105, 114].

A conceptual illustration of Pareto optimality is shown in Figure 3.1, whereas the difference between Pareto front and Pareto set is explained in Figure 3.2. Except degenerated design problems (see below), the Pareto front has infinite number of solutions (marked using red line in Figure 3.2) [105]. The Pareto set (denoted using squares) is a discrete representation of the Pareto front.

Clearly, it is desirable to obtain not just any Pareto-optimal solutions but a set of solutions that are (preferably uniformly) spread along the front. This allows for finding the actual relationships between the trade-off designs as well as the shape of the Pareto front (cf. Figure 3.2). It should be noted that the multi-optimization problem is non-trivial if the design objectives are partially conflicting. In the two extreme cases, i.e., totally conflicting or totally non-conflicting objectives, the problem simplifies considerably [114]. For the first case, the search space is identical with the Pareto front, whereas in the second case, multi-objective problem reduces to a single-objective one (as minimization of one objective implies minimization of the remaining ones). For more detailed survey of the formulation of multi-objective optimization problem see, e.g., [105, 114, 187, 188].

3.2 Solution Approaches to Multi-Objective Optimization

According to classification by Cohon and Marks [189], there are three fundamental approaches to multi-objective optimization, different by a relationship between identifying Pareto-optimal solutions and a decision making process aimed at selecting a single final design [114, 189]:

- *a priori*,
- progressive,
- *a posteriori*.

A priori preference articulation is appropriate especially if the relative importance of the objectives is clearly defined before the optimization process. Then, the multi-objective problem can be converted to a single-objective task by aggregating the objectives with respect to their importance. Typically, such aggregation is realized by means of weighted sum methods [105]. The progressive preference articulation is usually applied if the knowledge of the problem at hand is rather limited. In such a case, the objectives can be modified during the optimization run based on information gained on the way (the search process is intertwined with the decision making one). The method is useful when the defined objectives are heavily conflicting and therefore difficult to be fulfilled [114]. *A posteriori* preference articulation separates optimization from a decision making process. It is realized in two stages. Initially, a set of solutions representing the Pareto front are found. Decision making process is performed afterwards.

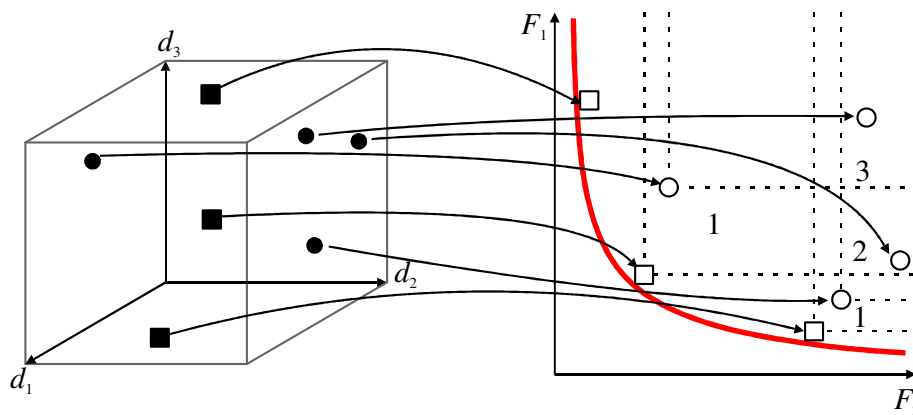


Figure 3.1: Conceptual illustration of the mapping between design variables ($D = 3$) and the feature space (here, for $K = 2$). The goal of multi-objective optimization is to seek for non-dominated designs that are a representation of the Pareto front (here marked as red curve). The non-dominated designs are denoted as (\square), whereas the designs (\circ) are dominated. The set X_p is denoted as (\blacksquare). The feasible solutions of the design space X_l are denoted as (\bullet, \blacksquare), thus $X_p \in X_l$. Numbers denote rank (or a so-called level of domination) of designs [114], i.e., the number of designs that dominate over a particular (\circ).

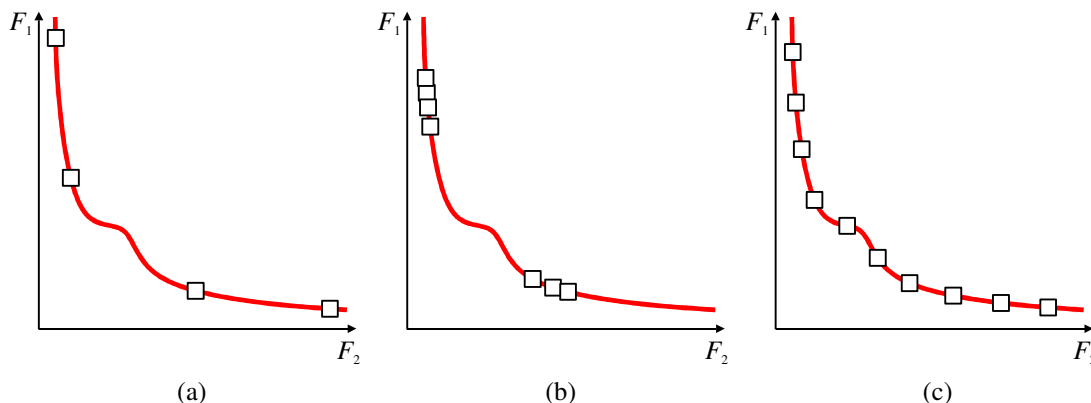


Figure 3.2: Conceptual illustration of the importance of spreading the Pareto-optimal solutions along the front. Here, non-convex front is considered: (a) too small number of diverse solutions; (b) responses are clustered in two regions of the front; (c) decent number of diverse solutions. It should be noted that the shape of the Pareto front (red line) is not well represented in (a) and (b), whereas allocation of solutions in (c) allows estimating the shape of the Pareto front and provides more detailed insight into the relationships between compromise designs.

The weighted sum approach (also referred to as linear function aggregation) [190] belongs to the family of conventional *a priori* routines for multi-objective optimization. The importance of each objective is defined before the optimization process which is realized by their aggregation into a sum prefixed by appropriate weighting factors. The goal is to solve [114]

$$F(\mathbf{x}) = \min \sum_{k=1}^K a_k F_k(\mathbf{x}) \quad (3.2)$$

where a_k denotes positive weighting coefficients that are adjusted depending on the priority of a particular design objective. Although the method is easy to implement, the optimization outcome of such linearly aggregated objective is sensitive to variations of the scaling factors [191]. At the same time, determination of the appropriate scaling factors for the optimization process is a difficult problem. The reason is that, typically, change of antenna design parameters has different influence on each of its performance figures. Therefore, the coefficients are mostly selected based on engineering experience [192]. It should be noted that this method allows for finding only one solution at a single algorithm run. However, global optimum obtained for the given set of scaling coefficients is always the Pareto optimal solution [193]. Consequently, different Pareto designs can be identified iteratively by means of multiple optimizations with varying weighting factors. On the other hand, the weighting sum approach cannot identify designs allocated in the concave regions of the Pareto front. Other methods based on the scaling concept include lexicographic ordering [114], Chebyshev approach [105], or non-linear aggregating functions [114]. Some of them can handle non-convex Pareto fronts. Conceptual visualization of the weighted sum method is shown in Figure 3.3. More detailed discussion on *a priori* techniques can be found in [105, 114].

Progressive preference articulation is realized as a two stage procedure where optimization algorithm is interfered by the decision making process. First, the optimizer identifies the Pareto front regions representing acceptable trade-offs between the design requirements. Then, the decision making process alters the objective functions, so that the search is shifted to the region of the Pareto front that contains solutions of interest [194]. The method may be useful for real-world design problems where certain trade-off designs are unacceptable from practical standpoint (i.e., for antennas, the search can be limited to solutions with maximum in-band reflection below -10 dB). A popular approach to progressive preference articulation is based on holding goal information as an additional objective [194]. The method can be utilized together with a so-called goal attainment approach [195] which allows for update trade-offs between objectives. It provides an intuitive interpretation of the problem at hand which can be solved using conventional SOO algorithms. The method can be formulated as the following minimization problem [195]

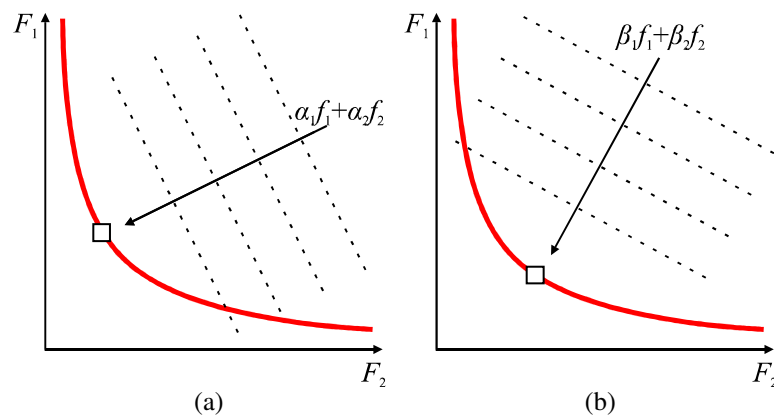


Figure 3.3: Weighting sum method – a conceptual explanation. Modification of the weighting coefficients alters the objective function and changes the functional landscape leading the optimization process to a different Pareto-optimal solution. Optimization process carried out using: (a) certain weighting factors α_i ; (b) other set of coefficients β . The method can be exploited to determine Pareto front (red line) representation by performing multiple optimizations with different values of scaling factors.

$$\arg \min_{\substack{\zeta \in \mathbb{R} \\ \mathbf{x} \in X_f}} \zeta \quad (3.3)$$

so that

$$F_k(\mathbf{x}) - a_k \zeta \leq F_k^* \quad (3.4)$$

Here, ζ is a scalar real-valued variable, $F_k(\mathbf{x})$ stands for the set of design objectives and F_k^* are their associated design goals. Moreover, a_k denote normalized vector of weights [114]

$$\sum_{k=1}^K |a_k| = 1 \quad (3.5)$$

The goal attainment technique allows generating non-dominated solutions even for non-convex regions of the Pareto front. It should be noted that ζ provides the information about feasibility of the goal for the decision making process. If $\zeta < 0$, an improved solution can be obtained; otherwise, the goal cannot be attained [114]. The concept of the progressive preference articulation is illustrated in Figure 3.4. A more detailed description of the method can be found in, e.g., [114, 195].

A posteriori techniques—where the decision making process is performed after the optimization stage—are preferable in many multi-objective problems [59, 80, 103]. The reason is that they can provide comprehensive information about possible trade-offs between the requirements so that the most suitable solution can be selected [114]. The aim of *a posteriori* methods is to perform search in a possibly large region of the design space and provide multiple solutions. Therefore, they exploit algorithms which allow for explicit search of the Pareto front [114]. The most popular techniques utilize population-based metaheuristic algorithms.

It should be reiterated that utilization of population-based methods for direct multi-objective optimization of EM antenna models is extremely expensive [106, 146]. On the other hand, population-based algorithms allow for obtaining close-to-uniform coverage of the Pareto front which makes them useful for solving problems considered here. It should be mentioned that an important stage of multi-objective design is a decision making process leading to a selection of (usually) single final design. However, this stage is not considered in this work. In other words, multi-objective optimization is understood here merely as a process of finding the Pareto set.

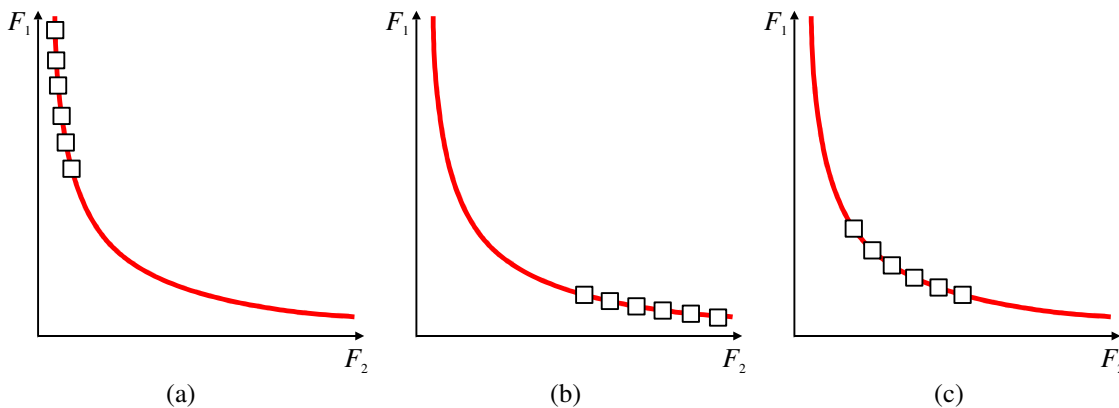


Figure 3.4: Preference articulation – a conceptual illustration: (a) objective F_1 is of less importance, F_2 is minimized; (b) objective F_1 is of less importance, F_1 is minimized; and (c) both objectives are of similar importance and thus they are minimized simultaneously. Requirements related to objectives can be iteratively changed by the decision making process (hence, progressive). The Pareto front is represented by red line.

3.3 Multi-Objective Evolutionary Algorithms

Population-based metaheuristics belong to the most popular methods for solving multi-objective optimization problems [114]. Among them, evolutionary algorithms are, perhaps, the most often utilized metaheuristics. Potential usefulness of EA for multi-objective design was already suggested—albeit not implemented—by Rosenberg in the late 1960’s [196]. The first multi-objective implementation of EA (a so-called vector evaluation genetic algorithm – VEGA) was proposed by Shaffer in 1984 [197]. The usefulness of EAs for solving multi-objective optimization problems mostly comes from their ability to process multiple solutions. However, they also benefit from being rather insensitive to discontinuities of the Pareto front, as well as its shape (EAs can handle non-convex fronts). The general structure of multi-objective evolutionary algorithm (MOEA) is similar to the single-objective one yet its selection mechanisms and evaluation procedures are different to promote non-dominated individuals. It should be noted that other population-based metaheuristic algorithms, such as particle swarm optimizers [126], ant colony approaches [111], or, recently popular, firefly algorithm [110] also have their multi-objective implementations.

According to the so-called *no free lunch* theorems, MOEA cannot be considered as an universal method for solving all optimization problems [198]. Empirical studies indicate that certain realizations of MOEAs seem to be more appropriate for solving specific benchmark functions, whereas others are better suited for real-world design problems [114]. In this work, a MOEA implementation with dynamic fitness sharing, Pareto-dominance-based tournament selection, mating restrictions and elitism is utilized [199]. The detailed description of the algorithm—and its components—is provided in the next section. More detailed survey of MOEA used here and other implementations can be found in [105, 114, 188, 197, 200].

It should be emphasized that selection of certain MOEA realization (or utilization of MOEA at all) is not of primary importance from the point of view of this dissertation. One of the reasons is that the shape of the Pareto front is typically much simpler for multi-objective antenna optimization problems than for standard functions utilized for MOEA testing. Moreover, MOEA optimization is just an intermediate step of the optimization procedure used in this work, so that possible inaccuracies (e.g., due to inappropriate setup) can be corrected to some extent by means of appropriate techniques.

3.3.1 Algorithm Description

Multi-objective evolutionary algorithms seek for a Pareto set by processing populations of potential solutions to the given optimization problem (also known as individuals or agents). Optimization process involves selection, recombination and mutation operators that yield a new—and hopefully better—population in each iteration [187]. Other mechanisms, typical for MOEAs, include Pareto-based assessment of individuals and domination-based elitism (archiving) [199].

A general structure of the single- and multi-objective evolutionary algorithms is comparable. Both utilize similar mechanisms for generating an initial population and constructing new individuals using recombination and mutation operators.

The MOEA utilized in this work is based on implementation described in [200]. The structure of the algorithm is the same as in standard evolutionary methods [107]. Nonetheless, majority of its operations (ranking, domination, etc.) is Pareto-based [200]. Its general flow is as follows (see Figure 3.5 for the flow diagram):

1. Initialize population;
2. Assess individuals;
3. Generate the offspring population using evolutionary operators;
4. Assess individuals;
5. Archive the best individuals;
6. Stop if the termination condition is fulfilled; otherwise go to Step 3.

The algorithm utilizes floating point representation of data, preferred for continuous optimization problems [187]. The optimization process begins with randomly generated population. In the next step, individuals in the population are evaluated and their fitness is determined (assessment). Subsequently, an offspring population is generated by applying selection, recombination and mutation mechanisms to the parent population.

As mentioned before, one aims at finding a Pareto set that uniformly covers the Pareto front. This can be achieved implementing mechanisms for pushing individuals towards the front (a so-called normal pressure) and avoiding clustering of solutions (referred to as tangent pressure) as shown in Figure 3.6. The first one is enforced by giving preference to non-dominated individuals in the selection process. The second can be implemented by means of so-called fitness sharing that penalizes clustered individuals.

More detailed description of the considered algorithm components is provided in the following sections.

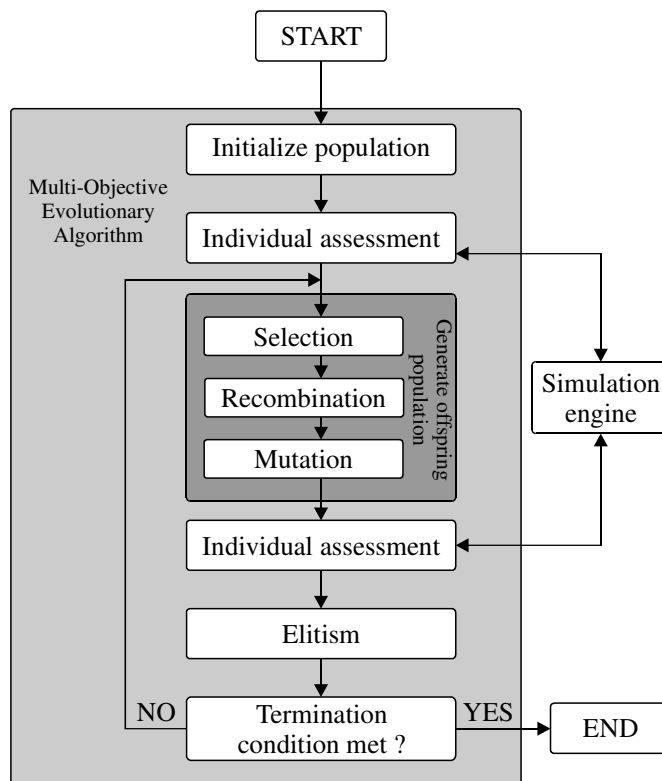


Figure 3.5: A general flowchart of a multi-objective evolutionary algorithm.

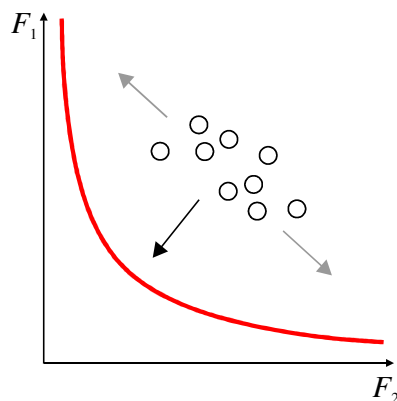


Figure 3.6: Conceptual illustration of normal (black arrow) and tangent (gray arrows) pressure. Both are implemented using appropriate mechanisms of the MOEA to obtain uniform Pareto set.

3.3.1.1 Assessment of Individuals

Assessment of individuals is realized through Pareto-dominance relation (cf. Section 3.1) used to determine the level of domination q_i for the i th individual, i.e., the number of designs that dominate over it (see Figure 3.1). This is realized through Pareto ranking [105]

$$r_i = 1 + q_i \quad (3.6)$$

where, r_i stands for a rank of q_i . Ranking can be utilized for determination of a so-called fitness f_i of the individual [114]

$$f_i = \frac{1}{r_i} \quad (3.7)$$

3.3.1.2 Fitness Sharing

Fitness sharing enforces uniform allocation of individuals along Pareto front by penalizing individuals located too close to each other [105]. The sharing function $SF^{(i,j)}$ can be defined as [201]

$$SF^{(i,j)} = \begin{cases} 1 - \left(\frac{\delta^{(i,j)}}{\sigma_r} \right)^\gamma & \text{if } \delta^{(i,j)} < \sigma_r \\ 0 & \text{if } \delta^{(i,j)} \geq \sigma_r \end{cases} \quad (3.8)$$

where γ determines the shape of the sharing function (usually linear; $\gamma = 1$) and $\delta^{(i,j)}$ stands for the distance between i th and j th individual in the feature space. The latter can be calculated as the following Euclidean norm [199]

$$\delta^{(i,j)} = \left\| F(\mathbf{x}^{(i)}) - F(\mathbf{x}^{(j)}) \right\|_2 \quad (3.9)$$

The radius σ_r (a so-called niche size) for which sharing between individuals is non-zero can be calculated dynamically as [199]

$$\sigma_r = \frac{\delta_k}{2} P_s^{\frac{1}{1-K}} \quad (3.10)$$

where P_s is the population size. The parameter δ_k can be estimated as follows. Let $F_x = [F_{x1} F_{x2} \dots F_{xK}]^T$ and $F_y = [F_{y1} F_{y2} \dots F_{yK}]^T$ denote objective vectors of the most distant individuals in a current Pareto-optimal set. Then let F_z be the vector of the minimum of objectives of both vectors, i.e., $F_z = [\min(F_{x1}, F_{y1}) \min(F_{x2}, F_{y2}) \dots \min(F_{xK}, F_{yK})]^T$. Then

$$\delta_k = \frac{(\delta_u + \delta_l)}{2} \quad (3.11)$$

Here, maximum distance between F_x and F_y is $\delta_u = \delta_1 + \delta_2$, whereas $\delta_1 = |F_x - F_z|$ and $\delta_2 = |F_y - F_z|$. The parameter δ_l stands for the minimum distance between F_x and F_y

$$\delta_l = \sqrt{\delta_1^2 + \delta_2^2} \quad (3.12)$$

The relevance of the sharing range for the optimization process is illustrated in Figure 3.7, whereas the notation used in description of dynamic sharing is explained in Figure 3.8.

Finally, the shared fitness f'_i of the i th individual is given by [199]

$$f'_i = \frac{f_i}{\sum_{j=1}^{P_s} SF^{(i,j)}} \quad (3.13)$$

3.3.1.3 Selection

Selection allows controlling convergence properties of the optimization algorithm. This is realized by adjusting the probability of the best individuals to survive (i.e., changing selection pressure). If it is too low, the convergence rate decreases (in extreme cases the search process may become random). If it is too high, the best individuals quickly take over the population which may result in premature convergence.

In this work, Pareto-dominance tournament selection scheme is utilized [199]. The mechanism works as follows. Two candidate individuals (here denoted as $\mathbf{x}^{(1)}$ and $\mathbf{x}^{(2)}$) and a comparison set composed of c_s test designs are randomly selected from the population. The selection process is as follows [202]

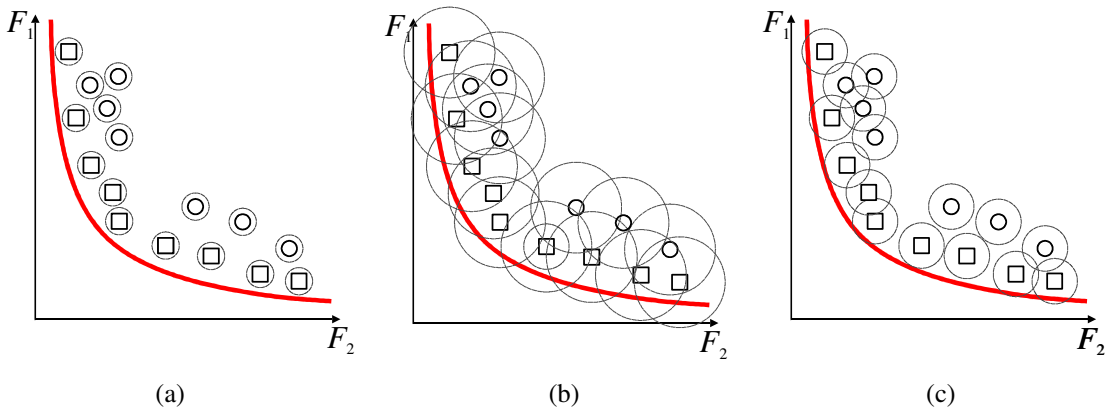


Figure 3.7: A conceptual illustration of the influence of the sharing radius on the optimization process: (a) for too small σ_r the fitness is not penalized even for the clustered individuals; (b) too large σ_r – even distant individuals are penalized; and (c) appropriate σ_r – only clustered designs are penalized. Dominated and non-dominated designs are marked by (\circ) and (\square) , respectively.

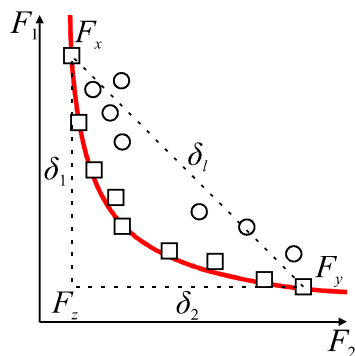


Figure 3.8: Explanation of symbol utilized in the definition of the dynamic sharing. Parameter δ_k is estimated by the average distance between the largest and smallest front sizes δ_u and δ_l , respectively [199].

1. Check domination (cf. Section 3.1) of the test designs over the candidates $\mathbf{x}^{(1)}$ and $\mathbf{x}^{(2)}$;
2. If neither or both candidates are dominated go to Step 3; otherwise go to Step 4;
3. Select the candidate with higher value of shared fitness (cf. Section 3.3.1.2);
4. Select $\mathbf{x}^{(1)}$ if it is non-dominated; otherwise select $\mathbf{x}^{(2)}$.

The size of comparison set is typically 10 percent of the population size. Change of the comparison set size modifies the preference given to non-dominated solutions. Consequently, it allows controlling the amount of selection pressure [202].

3.3.1.4 Recombination

Recombination is a stochastic operator that generates new individuals by combining information from the selected parents. Here, arithmetic recombination of the following form is utilized [187]

$$\mathbf{x}' = r \mathbf{x}^{(i)} + (1 - r) \mathbf{x}^{(j)} \quad (3.14)$$

where $\mathbf{x}^{(i)}$ and $\mathbf{x}^{(j)}$ are two parents, $r \in [0, 1]$ is a random number, and \mathbf{x}' is the offspring. The operation is performed with a probability p_c ; otherwise the offspring is created as unchanged copy of the first parent. In order to increase the chance of producing improved offspring solutions, recombination of parents is allowed only if they are sufficiently close and, consequently, similar to each other. This is controlled by a mating restriction mechanism described in Section 3.3.1.7. It is worth mentioning that recombination does not generate new information and thus it cannot be used as the only operator in MOEA. For conceptual illustration of recombination, see Figure 3.9(a).

3.3.1.5 Mutation

Mutation is another stochastic operator utilized in MOEA. It introduces small changes to the individuals so as to maintain diversity in the population. Let vector $\mathbf{x} = [x_1, \dots, x_d, \dots, x_D]^T$ denote individual. The mutation operator applied to its d th parameter is given by [188]

$$x_d' = \begin{cases} x_d - \sigma_m r_1^3 (x_d - l_d) & \text{if } r_2 < 0.5 \\ x_d + \sigma_m r_1^3 (u_d - x_d) & \text{if } r_2 \geq 0.5 \end{cases} \quad (3.15)$$

where σ_m is the mutation radius and $r_1, r_2 \in [0, 1]$. Parameters l_d and u_d denote lower and upper bounds for d th design variable (cf. Section 2.2.2.1). The modified individual is represented by vector $\mathbf{x}' = [x_1, \dots, x_d', \dots, x_D]^T$. Mutation is applied with the probability p_m , separately for each design vector component. Conceptual illustration of the operator is shown in Figure 3.9(b).

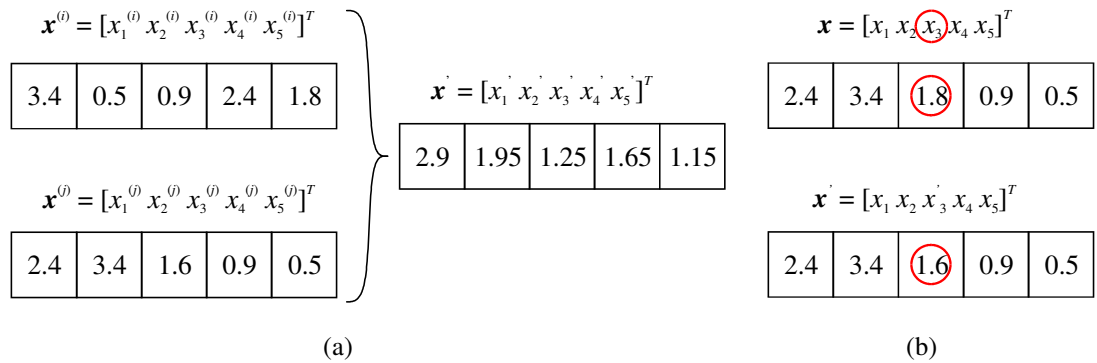


Figure 3.9: Evolutionary operators: (a) arithmetic recombination for $r = 0.5$; (b) mutation operator applied to third variable of the individual for $r_2 < 0.5$.

3.3.1.6 Elitism

The elitism mechanism (or a so-called archiving) preserves the best non-dominated individuals obtained during the optimization process. Elitism can be utilized during generation of the offspring population to ensure faster algorithm convergence [105]. However, larger number of Pareto-optimal solutions increases sensitivity of MOEA to the genetic drift and thus it should be carefully adjusted [105, 199].

A particular realization of the elitism mechanism may be to find a new Pareto-optimal set X_p' being a subset of X_p that is composed of contemporary non-dominated solutions and the offspring population. The mechanism can be realized in a batch mode where (3.13) is used to calculate the shared fitness of all individuals in X_p . Then, X_p' is generated by selecting the best ones. Elitism can be also realized in a recurrence mode which works as follows [199]:

1. Evaluate shared fitness of all individuals of X_p ;
2. Compose X_p' of the best individuals from X_p ;
3. Terminate the algorithm if the size of X_p' is equal to the size of population; otherwise set $X_p = X_p'$ and go to Step 1.

Although the recurrence mode is more CPU-intensive, it increases the probability of preserving local individuals and thus helps reducing discontinuities in Pareto-optimal set [199].

3.3.1.7 Mating Restrictions

Due to topological relationships between the Pareto front and the feature space, recombination of the two Pareto-optimal individuals which are not sufficiently close to each other will usually result in an offspring that is away from the Pareto front. In order to avoid such situations, a mating restriction mechanism can be introduced that forbids recombination of the parent individuals in case they are too far away from each other. The procedure is very simple and works as follows [203]:

1. Specify a parameter σ_p that defines the maximum distance between individuals for allowing them to mate;
2. After the selection step, select a random individual and search for its mate within a ball of radius σ_p ;
3. Perform mating if Step 2 leads to finding an appropriate individual; otherwise mate with a random individual.

In this work, maximum allowed distance between individuals is $\sigma_p = 3\sigma_r$.

3.3.1.8 Stopping Criteria

The optimization process continues until the termination condition is satisfied. A common approach is to terminate the algorithm after a user-defined maximum number of iterations. More efficient measure of the algorithm convergence is based on the rate of creating non-dominated individuals [199]

$$S_C^{(i)} = \frac{\bar{N}_{XP}^{(i)}}{N_{XP}^{(i)}} \quad (3.16)$$

where $N_{XP}^{(i)}$ stands for the number of Pareto-optimal designs in i th MOEA iteration and $\bar{N}_{XP}^{(i)}$ denotes the number of non-dominated individuals in the i th iteration that dominate Pareto-optimal solutions of the $i - 1$ iteration. Clearly, the lower $S_C^{(i)}$ the less shift towards the Pareto front is observed [199]. It should be noted that fluctuations of $S_C^{(i)}$ may occur across the algorithm iterations, thus a moving average of (3.17) can be utilized for the sake of regularization of the convergence measure [199]

$$\bar{S}_C^{(i)} = \sum_{j=i+1-l}^i \frac{S_C^{(j)}}{l} \quad (3.17)$$

where $l > 1$. The algorithm implementation utilized in this work is terminated when either the maximum number of iterations is reached or $\bar{S}_C^{(i)}$ computed in (3.17) is below the specified threshold.

4 MULTI-OBJECTIVE ANTENNA DESIGN

In this chapter, the methods and algorithms for fast multi-objective optimization of antenna structures are discussed. As mentioned before, antenna design is inherently a multi-objective task involving simultaneous improvement of several, usually conflicting requirements related to either the structure performance or its geometry. Although multi-objective optimization techniques have been developed since late 1980s, initially their applications to solving engineering problems were limited due to insufficient computational resources available at the time. The situation started changing in early 2000s, when the first works on the topic of multi-objective optimization of real-world antenna models were published [59, 103, 121, 192].

Conventional methods for solving multi-objective optimization problems are population-based metaheuristics. The main challenges related to their utilization for multi-criteria antenna optimization include: (i) high computational cost, (ii) large design variable space hindering identification of the trade-off designs, and (iii) large population required to obtain dense representation of the Pareto front. In the literature, these problems are mitigated by replacing EM antenna model with its computationally cheaper substitute [59, 103, 130] which, however, cannot guarantee accurate responses and involves further EM-based tuning. Other popular techniques exploit modified optimization algorithms which require fewer evaluations of the EM antenna model [80, 102, 122]. In this work, the difficulties mentioned above are alleviated by means of alternative approaches that allow for expedited multi-objective optimization of antennas.

The chapter is organized as follows. Section 4.1 provides brief formulation of the multi-objective antenna optimization problem. A detailed discussion of the core algorithm is given in Section 4.2. The design space reduction concept and reduction algorithms are described in details Section 4.3. Section 4.4 provides a description of Pareto set refinement methods. Section 4.5 is focused on comparative numerical studies of the developed techniques. Section 4.6 concludes the chapter.

4.1 Problem Formulation

For the convenience of the reader, the notation used throughout the section has been recalled here. $\mathbf{R}_f(\mathbf{x})$ stands for the high-fidelity model of the antenna structure at hand (cf. Section 2.1) which is assumed to be evaluated by means of an accurate yet CPU-intensive EM simulation [50, 82]. The response vector $\mathbf{R}_f(\mathbf{x})$ may represent an antenna reflection coefficient [50, 51],

radiation pattern [44, 54], gain [57, 58], etc. A set of adjustable parameters (i.e., antenna dimensions) is represented by a vector \mathbf{x} .

Let $F_k(\mathbf{x})$, where $k = 1, \dots, K$, be a k th design objective (see Section 3.1 for detailed description of the multi-criteria problem). In case of antennas, the goals can be related either to performance or to geometry. Performance objectives include minimization of reflection within a certain frequency band (particularly, to ensure $|S_{11}| < -10$ dB for a frequency range of interest) [141], minimization of the side lobe level [147], reduction of the axial ratio [59], maximization of the gain [106], etc. Geometry-related objectives can be defined with respect to e.g., maximal lateral size [64], overall occupied area (usually defined as a rectangle comprising entire design) [82], maximal value of certain dimension [64], or the volume (defined as cuboid comprising the structure). Normally, multi-objective antenna design problems are characterized by infinite number of globally optimal solutions which form a Pareto front (cf. Section 3.1). They can be found by means of MOEA algorithm. The latter, however, is numerically prohibitive when applied for optimization of real-world antenna structures [106].

In this work, the design process is expedited using an auxiliary low-fidelity model \mathbf{R}_c of the antenna (coarsely-discretized counterpart of \mathbf{R}_p). Typically, the \mathbf{R}_c model is evaluated using the same EM solver. The design optimization methodology is described in the following sections.

4.2 Optimization Algorithm

Design techniques that permit rapid multi-objective optimization of antenna structures are rare in the literature. Available methods involve utilization of inaccurate empirical antenna models [59, 130], or lead to sparse representations of the Pareto front [102]. In 2013, Koziel and Ogurtsov proposed a computationally efficient technique for multi-objective antenna optimization [64]. The method exploits variable-fidelity electromagnetic simulations, response surface approximations and surrogate-based optimization. The core of the procedure is a simple algorithm involving acquisition of data samples, construction of the RSA model, MOEA optimization and refinement of the selected Pareto-optimal designs using SBO. Despite its advantages, the technique of [64] is only applicable for relatively low-dimensional cases. The dimensionality problem is partially mitigated in [64] by decomposing the antenna into a radiator and a feeding network so that optimization structures with increased number of design parameters is possible. Notwithstanding, majority of modern antennas cannot be decomposed.

In 2014, Bekasiewicz *et al.* extended the original algorithm of [64] to antenna structures with multiple independent design parameters [204]. The modification of the method is based on the fact that Pareto-optimal solutions reside in a very small region of the design space so that the parameter ranges can be restricted considerably to allow feasible construction of the RSA model even when the design space dimension is relatively high [146, 205]. One of the main features of the method presented in [146] is that it allows identifying high-fidelity representation of the Pareto front by refining the selected designs obtained from the optimized RSA model. Although this approach provides satisfactory results, the computational cost of SBO increases with a number of designs considered in the refinement process. In 2014, Koziel *et al.* proposed an alternative scheme based on co-kriging surrogates [183]. Co-kriging permits generation of much denser representations of the Pareto-optimal sets. Both approaches are discussed in detail in the following subsections.

4.2.1 Optimization Algorithm Overview

The algorithm for expedited design optimization of antennas exploits variable-fidelity EM simulations and the kriging interpolation model \mathbf{R}_s (here, $\mathbf{R}_s(\mathbf{x}) = \mathbf{R}_{KR}(\mathbf{x})$, see Section 2.2.2.2). It should be noted that the core algorithm and all of its components are implemented within a MATLAB-based optimization framework [206].

The first step of the process is design space reduction (cf. Section 4.3). For low-dimensional problems, it is optional yet recommended to expedite construction of an accurate RSA model. For higher-dimensional cases, however, space reduction is necessary to construct the RSA mod-

el at reasonable computational cost. The reduction step is usually performed at the low-fidelity model level; however high-fidelity simulations and SBO methods may also be exploited at this step for improved accuracy.

The next step is acquisition of the low-fidelity training data for construction of the RSA model. The data samples are allocated using an appropriate design of experiments technique (cf. Section 2.2.2.1). The allocation strategy depends on dimensionality of the design problem. In this work, acquisition step is normally realized at points generated using Latin Hypercube Sampling [164] which (optionally) can be combined with various factorial design techniques [153]. As mentioned before, model identification is carried out using a DACE toolbox [167].

Accuracy of the RSA model depends on the number and allocation of training data, design space dimensionality and size, as well as nonlinearity of the antenna responses. Here, adaptive sampling is used with infill samples iteratively added to the training pool until a given threshold concerning generalization error of the model is fulfilled. It is assumed that the average relative root mean square (RMS) error should be less than 5 percent [207]. The model error is determined using cross-validation (cf. Section 2.2.2.3). The infill strategy is allocation of random samples satisfying LHS condition with respect to the overall training data set. Although the assumed error value is usually sufficient for identification of the initial Pareto set by means of population-based metaheuristics, in case of complex antenna responses, the desired RMS threshold may be lower.

In case of considerable discrepancy between \mathbf{R}_f and \mathbf{R}_s responses, the kriging model can be enhanced by means of surrogate-assisted techniques at certain (usually small) number of designs (post-refinement). Alternatively, SBO correction can be performed before model identification (pre-refinement). Typically, output space mapping and frequency scaling are utilized (cf. Section 2.2.3.1).

In the next step, the RSA model is optimized using a multi-objective evolutionary algorithm. The results of MOEA operation are considered as the initial approximation of a relevant fraction of the Pareto front. The optimization engine utilized here is an in-house implementation of MOEA which exploits mechanisms such as elitism, fitness sharing, mating restrictions and Pareto-dominance tournament selection (cf. Section 3.3.1).

Finally, the refinement of the initial Pareto set obtained using MOEA is performed (see Section 4.4). This step is necessary because the Pareto front representation obtained through optimization of the RSA model is of limited accuracy. In particular, two levels of approximation are utilized as the kriging model \mathbf{R}_s is an approximation to the training data obtained from \mathbf{R}_c model simulations. The discrepancies between \mathbf{R}_s and \mathbf{R}_f can be accounted for by means of appropriate correction. It should be noted that in most cases (except certain design space reduction routines described in Section 4.3.5) the high-fidelity model is not evaluated until the refinement step. Typically, the computational cost of the procedure corresponds to a few dozens of \mathbf{R}_f simulations.

The discussed expedited multi-objective optimization algorithm can be summarized as follows (see Figure 4.1 for a detailed block diagram):

1. (Optional) Perform design space reduction;
2. Sample the design space and acquire the \mathbf{R}_c data;
3. (Optional) Correct \mathbf{R}_c data using SBO (pre-refinement);
4. Construct the response surface approximation model \mathbf{R}_s ;
5. (Optional) Perform post-refinement of the \mathbf{R}_s model;
6. Obtain the initial representation of the Pareto front by MOEA optimization of \mathbf{R}_s ;
7. Carry out refinement procedure to obtain high-fidelity Pareto-optimal design.

It should be reiterated that the mechanisms utilized in Steps 2-6 have been discussed in Chapters 2 and 3. Design space reduction techniques and methods for refinement of the Pareto-optimal set are considered in the following sections.

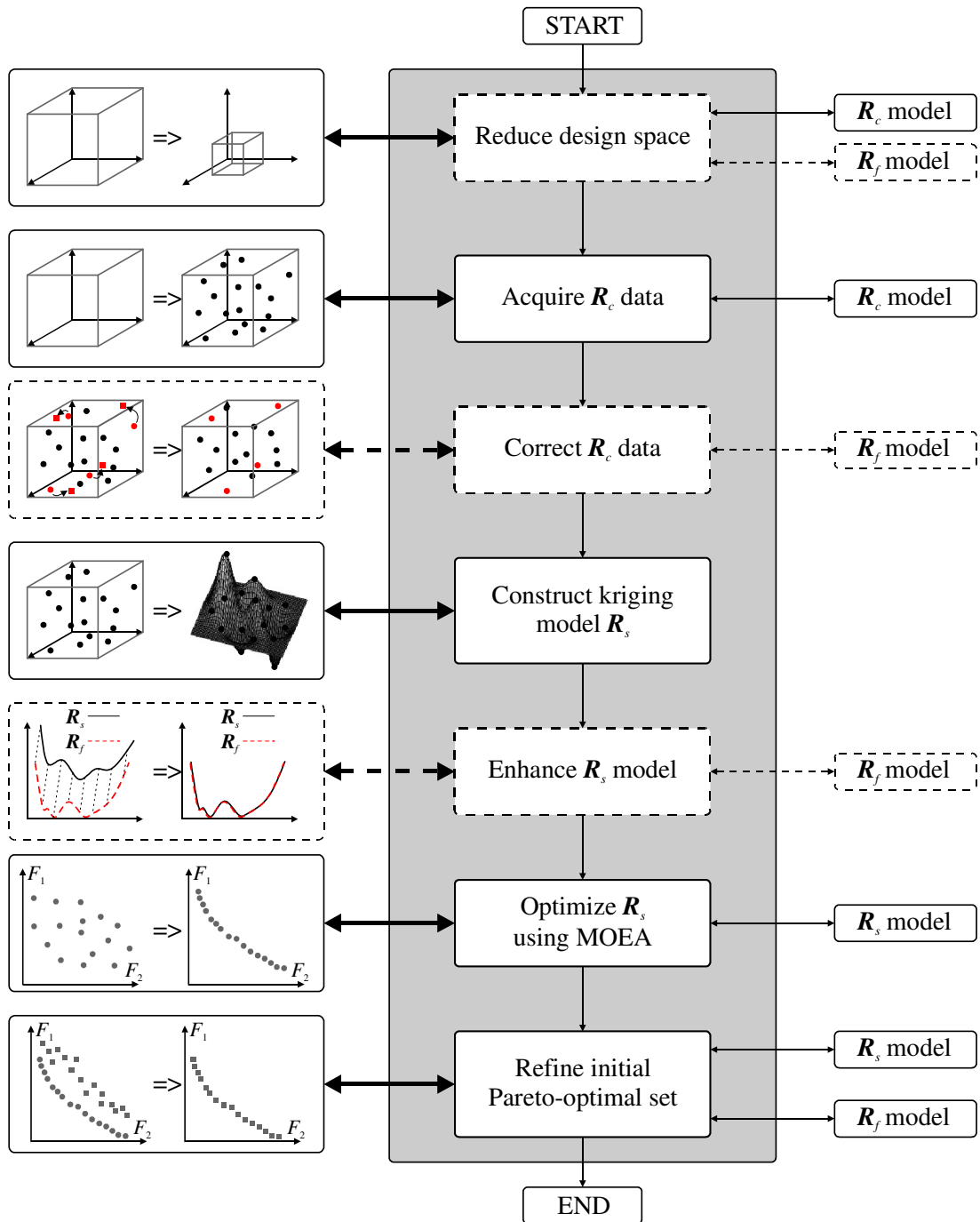


Figure 4.1: Expedited multi-objective optimization algorithm: design flow. Dashed lines denote optional steps. In the first (optional, yet highly recommended) stage, search space is refined to the region of interest. Subsequently, the R_c data (\bullet) is acquired. Next, the pre-refinement of the R_c data may be performed if needed. Then the RSA model R_s is identified. Optionally, RSA post-refinement may be performed. Afterwards, initial representation of the Pareto front is obtained using MOEA and R_s model. Finally, selected samples are refined using SBO. Note that usually the R_f model evaluations are not performed until the last algorithm step.

4.3 Design Space Reduction

In this work, Pareto-optimal set is obtained using MOEA optimization. Low cost of the process is ensured by execution of the algorithm on the RSA model. However, the number of training samples required to construct accurate model grows very quickly with the number of design parameters [64, 146, 208]. This is a serious problem for modern antenna structures which are

often parameterized using more than ten variables [50, 82, 146]. The cost of setting up the RSA for such structures may quickly surpass the computational savings of the surrogate-assisted MOEA optimization. Moreover, the ranges of design parameters are normally set rather wide to ensure that the Pareto set can be captured. Acquisition of sufficient amounts of training data within large spaces is prohibitive from the numerical point of view [205].

Pareto-optimal solutions, however, normally reside in a small region of the initially defined space [106]. Moreover, in antenna design problems, only a certain fraction of the Pareto front, i.e., the designs for which the in-band reflection coefficient $|S_{11}| \leq -10$ dB, is of interest [106]. In practice, the relevant region of the space may be orders of magnitude smaller (volume-wise) than the initially defined space (see Figure 4.2 for illustration). Its identification is desirable, because it allow for substantial reduction of the number of training samples required for a construction of a reliable RSA model [106, 146, 205].

It should be noted that the problem related to construction of RSA models within large design spaces has been previously undertaken in the field of structural and aerospace engineering [142, 209, 210]. Possible approaches include decomposition of the space to sub-regions represented by separate RSA models [209] or utilization of pattern-search-based surrogate management framework [210]. The infill points obtained during optimization can be also iteratively incorporated to the model to gradually increase its accuracy within the region of interest [142]. Although these techniques are useful for single-objective problems, they may be ineffective in multi-objective setups where the region of search space containing the solutions that are of interest is very small [146]. Instead, the problem can be addressed by means of design space reduction which is considered fundamental for successful multi-objective surrogate-assisted antenna optimization.

The aim of design space reduction is to limit ranges of the antenna parameters so that the resulting space is significantly smaller yet contains majority of the Pareto front that is of interest. Space reduction facilitates utilization of RSA models for multi-dimensional design problems due to increasing RSA accuracy. The latter can be expressed in terms of average minimum distance between the training points given by

$$\delta_p = \langle \delta_{ij} \rangle \quad (4.1)$$

where the distance δ_{ij} between two points \mathbf{x}_i and \mathbf{x}_j ($i = 1, 2, \dots, N$ and $j = 1, 2, \dots, N$) from the training set that are the closest with respect to each other is as follows

$$\delta_{ij} = \|\mathbf{x}_i - \mathbf{x}_j\|_2 \quad (4.2)$$

The RSA model error is proportional to

$$\delta_p \propto \left(\frac{1}{N} \right)^{\frac{1}{D}} \quad (4.3)$$

where N and D correspond to a total number of training samples and dimensionality of the search space, respectively.

As illustrated in Figure 4.3, construction of the model within reduced space results in faster decrease of δ_p than can be obtained by simply increasing the size of the training set. It should be noted that dimension ‘‘flattening’’ resulting from space reduction is non-uniform, i.e., certain dimensions can be flattened significantly more than others (cf. Figure 4.3). In other words, influence of space reduction on improvement of model accuracy for limited number of data samples is problem dependent and thus it cannot be rigorously estimated.

Important advantage of space reduction is possible reduction of the problem dimensionality: as the ranges of variability of certain parameters may be narrowed down to almost zero, they can

be excluded from the optimization process [205]. Figure 4.4 conceptually illustrates the influence of design space reduction on “flattening” of certain dimensions or reduction of the problem dimensionality.

In this section, several design space reduction methods that facilitate utilization of RSA models for optimization of many-dimensional antenna structures are discussed. The considered techniques allow for confinement of the design space to the region containing Pareto designs. Consequently, construction of an accurate RSA model can be performed using reasonable amount of training data.

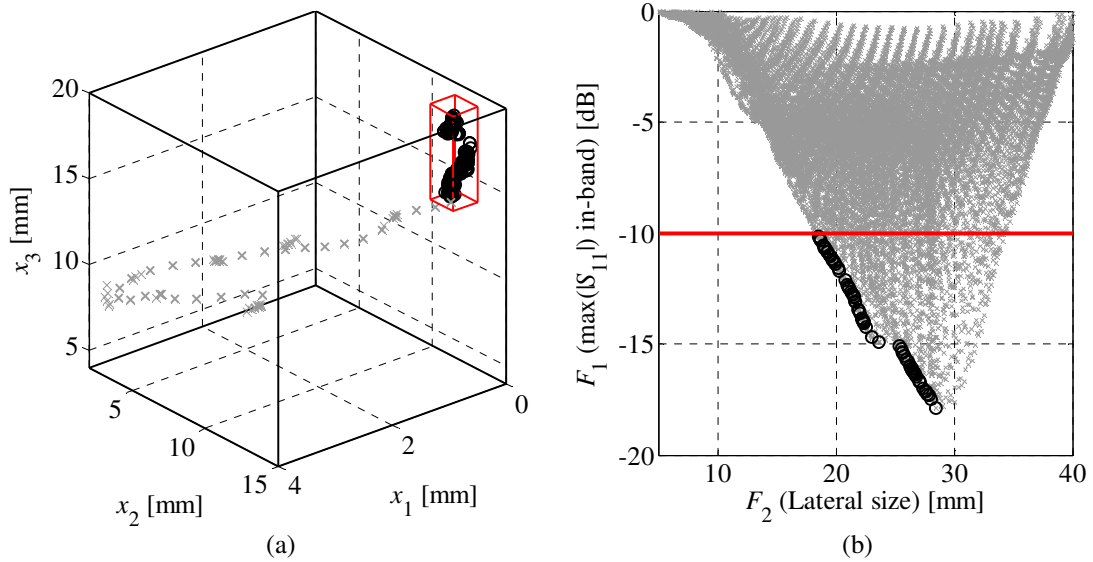


Figure 4.2: Multi-objective optimization of three-dimensional ($D = 3$) problem: (a) Pareto set inside design variable space; and (b) entire search space mapped to the feature space (\times). Note that only the Pareto designs for which $F_2 \leq -10$ dB (\circ) are of interest. All of them are confined within the red cuboid of (a) that is orders of magnitude smaller (volume-wise) than initial space (black cuboid) [106].

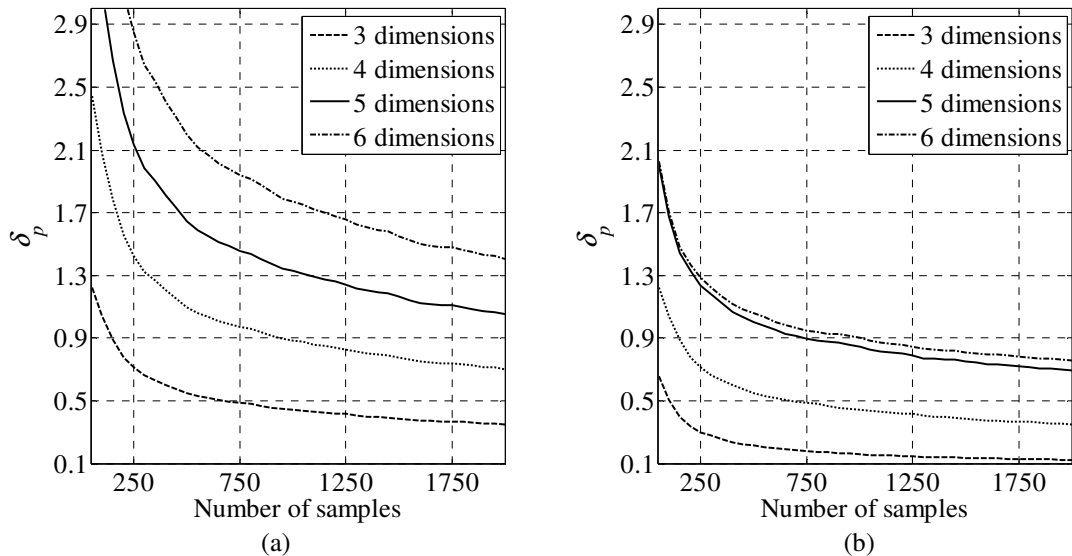


Figure 4.3: The average minimum distance between the training points, δ_p , as a function of the number of training samples and design variables of the problem at hand: (a) before; and (b) after design space reduction. Due to narrowing down variable ranges along certain dimensions, δ_p in (b) obtained for six dimensional problem is comparable to δ_p in (a) for three dimensional one. Note that dimension “flattening” is non-uniform: sixth dimension has been narrowed down the most, whereas fifth dimension has not been reduced at all.

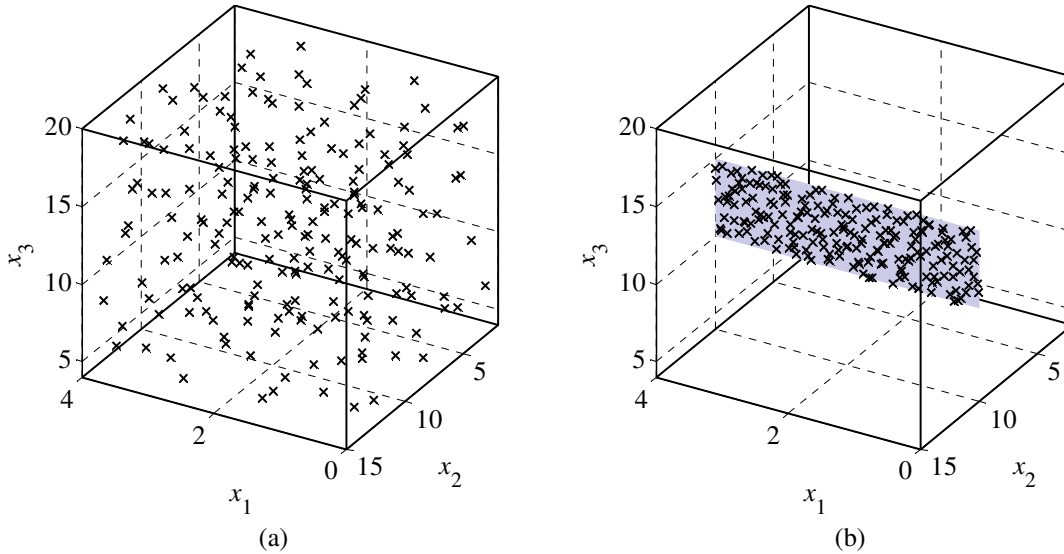


Figure 4.4: Conceptual illustration of the impact of design space reduction on the density of training samples (x): (a) initial design space; (b) reduced design space. Note that the problem has been reduced to two dimensions (parameter $x_2 = 10$ became fixed). Moreover the design has been flattened along x_3 from 4-20 in (a) to 10-15 in (b).

4.3.1 Pareto-Dominance Design Space Reduction

The first technique discussed here allows for identification of a relevant region of the design space based on the Pareto-dominance relation (cf. Section 3.1) [106, 204]. The procedure involves two stages. First, allocation of the Pareto front is estimated based on test samples evaluated along the initial space. Then, the region of interest is refined using the optimization algorithm. A more detailed formulation of the method is below.

Let X_I be the initial design space defined by the lower and upper bounds \mathbf{l} and \mathbf{u} (cf. Section 2.2.2.1) and X_D , defined by the refined bounds \mathbf{l}_D and \mathbf{u}_D , be the reduced design space that contains part of the Pareto front being of interest ($X_D \subset X_I$). In the first stage, the region X_D may be estimated using the following mechanisms: (i) reduction of the initial search space by rejecting regions that coincide with most dominated test samples, and (ii) approximating X_D using a set X_A of designs stored during the algorithm run. In each iteration, a star-distribution-based (cf. Section 2.2.2.1) testing set is generated on the faces of X_I and evaluated using the low-fidelity antenna model R_c . The designs that are the worst in the Pareto sense (i.e., the most dominated ones) are rejected together with sub-regions of X_I corresponding with them, whereas accepted solutions are accumulated in X_A . Subsequently, all the designs from X_A are ranked and the best of them (i.e., ones with $q_i \leq 2$; cf. Section 3.3.1.2) are utilized to define the bounds of the current approximation to X_D . The algorithm is terminated if the temporary region of interest X_D^* remains unchanged for three consecutive iterations.

The discussed algorithm can produce X_D^* that captures only a small fraction of the Pareto front. Therefore, in the second stage X_D^* is expanded by additional designs obtained from separate single-objective optimizations with respect to each objective (cf. Section 4.3.2). The starting points for the optimization are selected as follows [204]

$$\mathbf{x}_c^{(k)} = \max_{\mathbf{l}_r < \mathbf{x}_c < \mathbf{u}_r} F_k(R_c(\mathbf{x}_c)) \quad (4.4)$$

where $\mathbf{x}_c^{(k)}$ denote the designs from X_A that contribute to X_D^* and $k = 1, \dots, K$ is the number of design objectives (cf. Section 3.1). The method allows for reducing X_D by a few orders of magnitude (volume-wise) in comparison to X_I . A block diagram of the algorithm is shown in Figure 4.5, whereas its operation is illustrated in Figure 4.6.

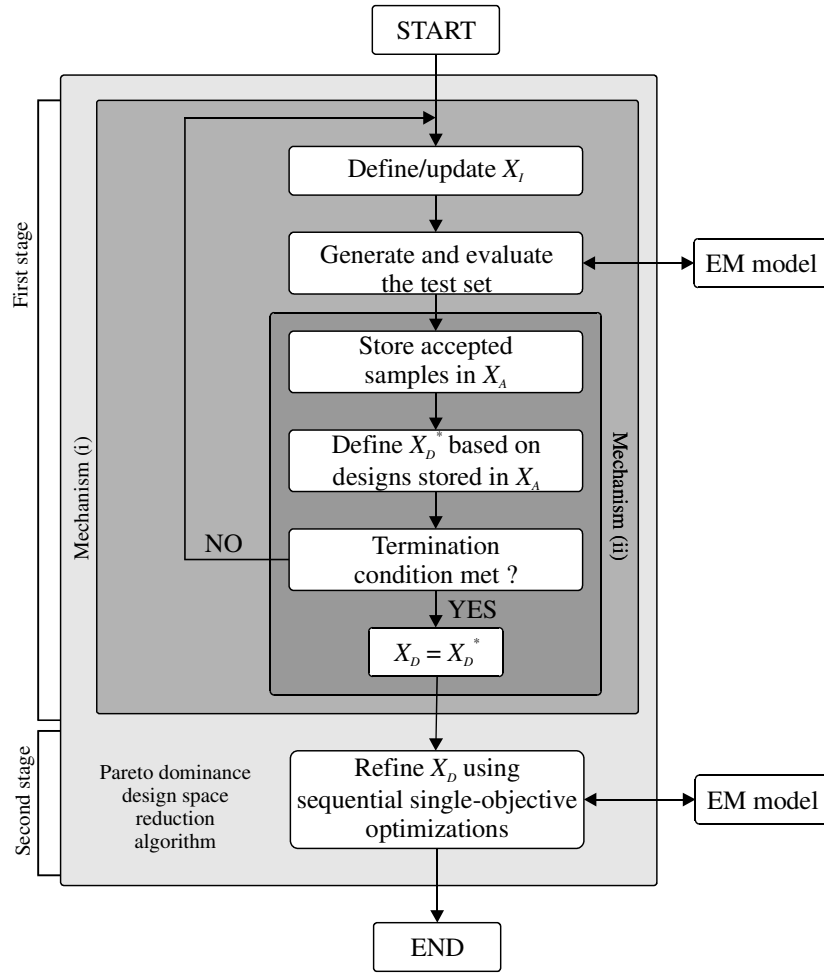


Figure 4.5: A block diagram of the Pareto-dominance-based design space reduction algorithm.

4.3.2 Sequential Single-Objective Optimizations

The sequential approach described here is the most versatile design space reduction algorithm considered in this dissertation. The method limits the search space to the region determined by the extreme Pareto-optimal designs obtained by means of single-objective optimizations, one objective at a time.

The algorithm operates as follows. The extreme Pareto-optimal designs may be determined as [106]

$$\mathbf{x}_c^{(k)} = \arg \min_{l \leq \mathbf{x} \leq u} F_k(\mathbf{R}_c(\mathbf{x}_c)) \quad (4.5)$$

where $\mathbf{x}_c^{(k)}$, $k = 1, 2, \dots, K$, denote the optimal low-fidelity model design obtained with respect to the k th objective (cf. Section 3.1), whereas l and u are lower and upper bounds of the initial design space X_l (cf. Section 2.2.2.1). It should be noted that selection of a starting point for the first optimization run is not straightforward (in this work it was usually performed based on engineering experience). However, subsequent optimizations can start from the previously optimized designs.

Finally, the lower and upper bounds l_s and u_s of the reduced space (see Figure 4.7) are defined as

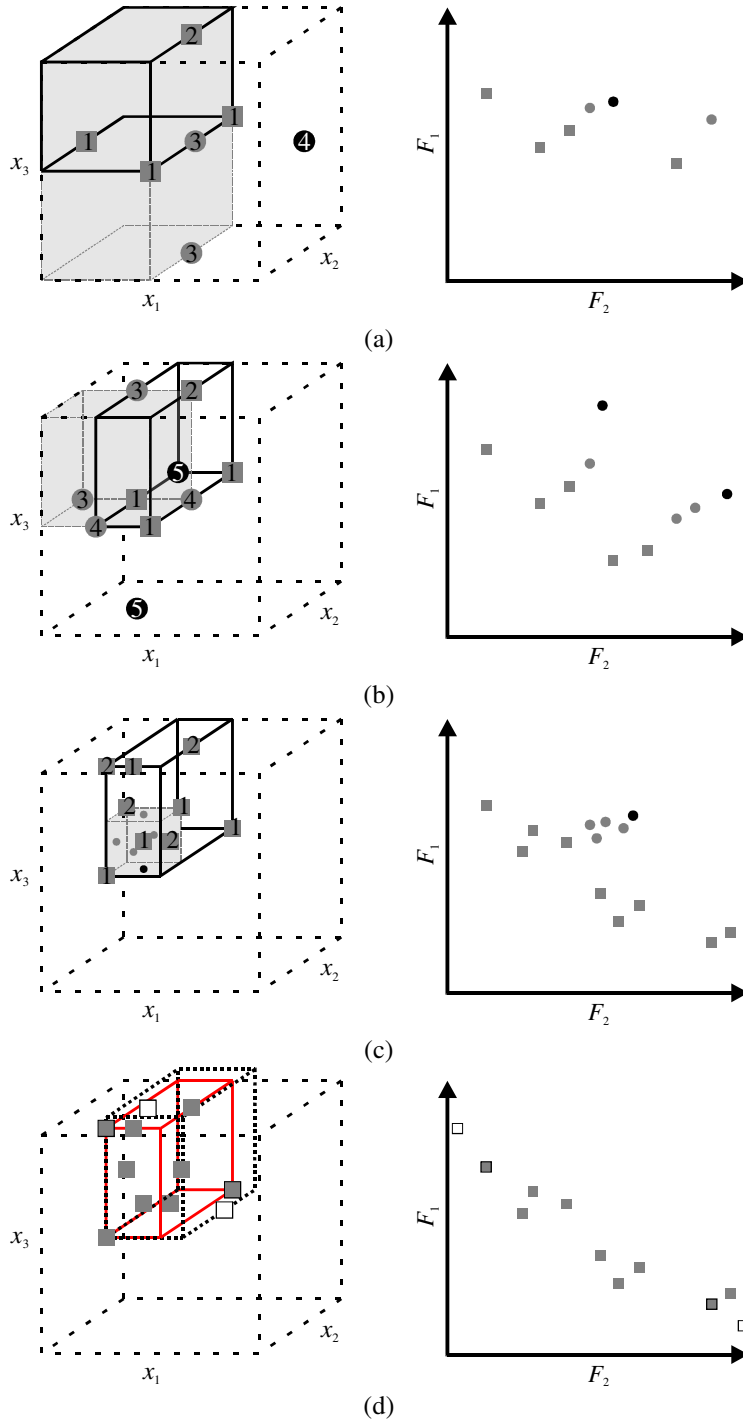


Figure 4.6: Pareto-dominance design space reduction workflow for $D = 3$: (a)-(c) the first stage of the algorithm; (d) X_D obtained after the second stage (\cdots). A light-gray area represents a fraction of X_I ($- -$) that coincides with the accepted test samples, whereas the temporary region of interest X_D^* is denoted as the solid cuboid. The black and gray circles represent the rejected and over-dominated samples, respectively, whereas the gray squares denote designs spanning X_D^* . The white squares represent the Pareto designs obtained by means of single-objective optimization runs.

$$l_s = \min \{ \mathbf{x}_c^{(1)}, \mathbf{x}_c^{(2)}, \dots, \mathbf{x}_c^{(k)} \} \quad (4.6)$$

$$\mathbf{u}_S = \max \{ \mathbf{x}_c^{(1)}, \mathbf{x}_c^{(2)}, \dots, \mathbf{x}_c^{(K)} \} \quad (4.7)$$

In practice, the refined space X_S is only a small sub-region of X_I . Consequently, the reliable RSA model can be identified within X_S using a limited number of training samples [106]. The block diagram of the method is shown in Figure 4.8.

Note that the reduced space may or may not contain the entire Pareto front. This depends on the geometry of the latter. Given the typical shapes of Pareto fronts for antenna structures it is however expected that majority of the front will be accounted for within X_S . The problem becomes more serious if the discrepancies between the high- and low-fidelity model responses are significant.

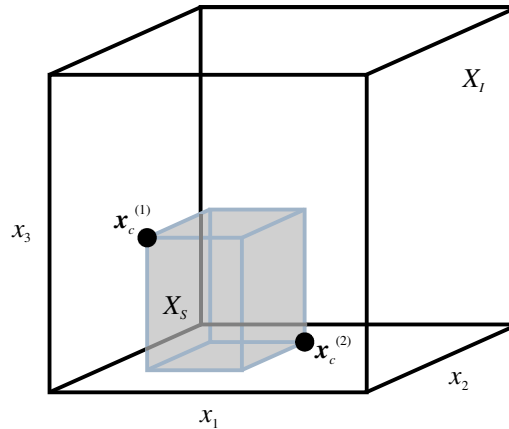


Figure 4.7: A conceptual illustration of the space reduction procedure for a two-objective problem in three-dimensional design space X_I . The refined search space X_S is constructed using the extreme designs $\mathbf{x}_c^{(1)}$ and $\mathbf{x}_c^{(2)}$ obtained by respective single-objective optimization runs.

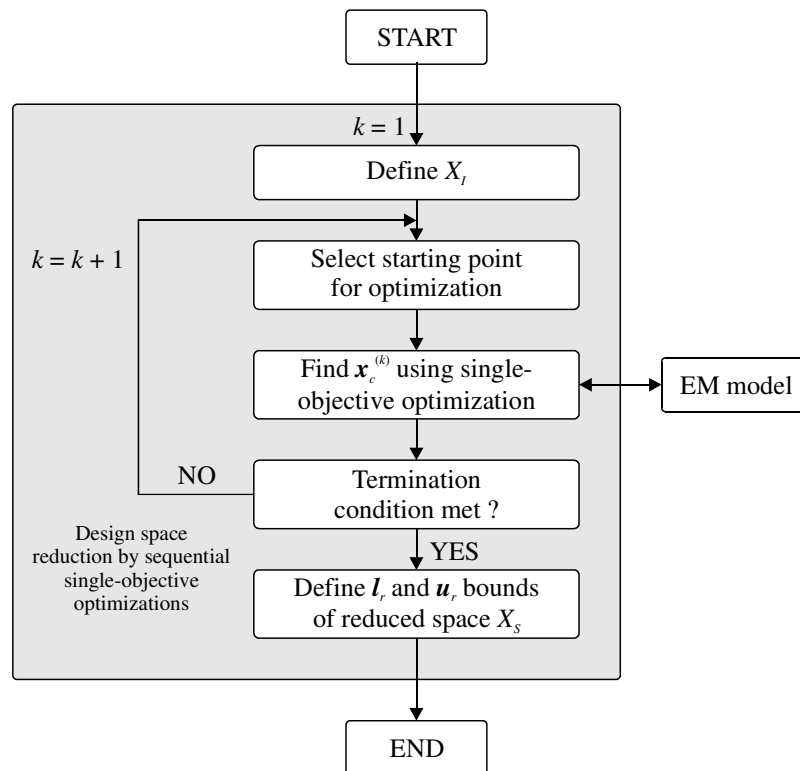


Figure 4.8: Design space reduction by means of sequential single-objective optimizations.

4.3.3 Rotational Design Space Reduction

In many situations, the RSA model construction may be expensive even if sequential reduction of the design space is performed [205]. For antenna structures described by over a dozen variables, more than a thousand of training samples may be required to set up an RSA model of acceptable accuracy (i.e., with relative RMS error below 5%; cf. Section 4.2.1) [146, 183, 211]. The reduction strategy described here is an extension of the sequential approach which allows for further refinement of the initially reduced space X_S (here, referred to as the hypercube or the box). The routine is based on an observation that for antenna design problems with two objectives the majority of the Pareto designs is—in practical cases—allocated close to the diagonal of the X_S . Consequently, space reduction can be achieved by rotating the box with respect to diagonal and its further reduction in all dimensions but diagonal one.

The method works as follows (see Figure 4.9 for conceptual illustration):

1. Perform initial design space reduction (cf. Section 4.3.2);
2. Rotate the obtained hypercube along its diagonal;
3. Perform reduction of the rotated box.

The rotation step—considered as the key element of the described routine—is performed as follows. Let \mathbf{e}_1 be a unit vector of the standard basis $\{\mathbf{e}_d\}_{d=1,2,\dots,D}$ associated with the longest dimension of the hypercube X_S . The aim of the procedure is to find the rotated base vectors \mathbf{e}_d . Let \mathbf{x}_0 and \mathbf{v} be the center of X_S and its associated unit vector, respectively. Both can be defined as [205]

$$\mathbf{x}_0 = \frac{\mathbf{x}_c^{(1)} + \mathbf{x}_c^{(2)}}{2} \quad (4.8)$$

$$\mathbf{v} = \frac{\mathbf{x}_c^{(1)} - \mathbf{x}_c^{(2)}}{\|\mathbf{x}_c^{(1)} - \mathbf{x}_c^{(2)}\|} \quad (4.9)$$

where $\mathbf{x}_c^{(1)}$ and $\mathbf{x}_c^{(2)}$ are given by (4.5). The space X_S is rotated around \mathbf{x}_0 with respect to a two-dimensional subspace M spanned by the vectors \mathbf{v} and \mathbf{e}_1 , so that the extreme designs $\mathbf{x}_c^{(1)}$ and $\mathbf{x}_c^{(2)}$ become the centers of its two faces. The subspace M is also spanned by \mathbf{e}_1 and its orthogonal vector \mathbf{v}_1 given by

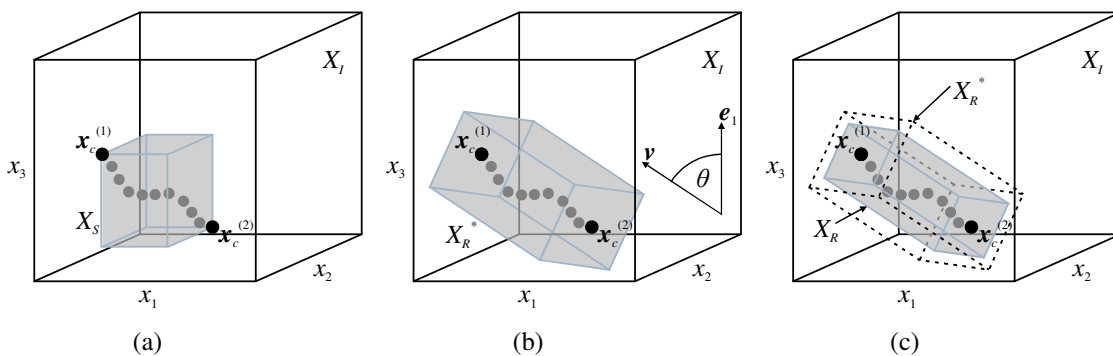


Figure 4.9: A conceptual illustration of the rotational design space reduction technique. The method can be summarized in three steps: (a) initial design space reduction; (b) rotation of the X_S along its diagonal; and (c) linear reduction of all the dimensions except the diagonal one. Black and gray circles represent the extreme Pareto designs obtained using the sequential method and the shape of the Pareto front (see Figure 4.2), respectively. The rotated box before its reduction is shown as a dashed cuboid. Parameters \mathbf{e}_1 , \mathbf{v} and θ are defined in the text.

$$\mathbf{v}_1 = \frac{\mathbf{v} - \mathbf{e}_1 \mathbf{e}_1^T \mathbf{v}}{\|\mathbf{v} - \mathbf{e}_1 \mathbf{e}_1^T \mathbf{v}\|} \quad (4.10)$$

The rotation angle θ of M is defined as

$$\cos \theta = \mathbf{v}^T \mathbf{e}_1 \quad (4.11)$$

Then the projection \mathbf{e}_d^p of \mathbf{e}_d onto the subspace M and its corresponding normal vector \mathbf{e}_d^v can be defined as follows

$$\mathbf{e}_d^p = \mathbf{e}_1 \mathbf{e}_1^T \mathbf{e}_d + \mathbf{v}_1 \mathbf{v}_1^T \mathbf{e}_d \quad (4.12)$$

$$\mathbf{e}_d^v = \mathbf{e}_d - \mathbf{e}_d^p \quad (4.13)$$

It should be noted that $\mathbf{e}_1 \mathbf{e}_d = 0$ if the number of dimensions is greater than one ($D > 1$). The rotation is applied only to \mathbf{e}_d^p , whereas \mathbf{e}_d^v remains intact. The projection \mathbf{e}_d^p is represented in the subspace M as

$$\mathbf{e}_d^p = \begin{bmatrix} \mathbf{e}_1^T \mathbf{e}_d & \mathbf{v}_1^T \mathbf{e}_d \end{bmatrix}^T \quad (4.14)$$

The vector \mathbf{e}_d^v is orthogonal to \mathbf{e}_1 , which means that it is parallel to the unit vector \mathbf{v}_1 . Therefore, for multidimensional search space (4.14) may be rewritten to

$$\mathbf{e}_d^p = \begin{bmatrix} 0 & \mathbf{v}_1^T \mathbf{e}_d \end{bmatrix}^T \quad (4.15)$$

The rotation matrix in M is given by

$$\mathbf{R} = \begin{bmatrix} \cos \theta & -\sin \theta \\ \sin \theta & \cos \theta \end{bmatrix} \quad (4.16)$$

Therefore, the rotated \mathbf{e}_d^p vector in the representation of M subspace is defined as

$$\mathbf{R} \cdot \mathbf{e}_d^p = \begin{bmatrix} \cos \theta & -\sin \theta \\ \sin \theta & \cos \theta \end{bmatrix} \cdot \begin{bmatrix} \mathbf{e}_1^T \mathbf{e}_d \\ \mathbf{v}_1^T \mathbf{e}_d \end{bmatrix} = \begin{bmatrix} \mathbf{e}_1^T \mathbf{e}_d \cos \theta - \mathbf{v}_1^T \mathbf{e}_d \sin \theta \\ \mathbf{e}_1^T \mathbf{e}_d \sin \theta + \mathbf{v}_1^T \mathbf{e}_d \cos \theta \end{bmatrix} \quad (4.17)$$

The entire vector \mathbf{e}_d upon rotation is

$$\begin{aligned} \mathbf{e}_d^{rot} &= \mathbf{e}_d^v + \mathbf{e}_d^{rot.p} = \mathbf{e}_d - \mathbf{e}_1 \mathbf{e}_1^T \mathbf{e}_d - \mathbf{v}_1 \mathbf{v}_1^T \mathbf{e}_d + \\ &+ \mathbf{e}_1 \left(\mathbf{e}_1^T \mathbf{e}_d \cos \theta - \mathbf{v}_1^T \mathbf{e}_d \sin \theta \right) + \mathbf{v}_1 \left(\mathbf{e}_1^T \mathbf{e}_d \sin \theta + \mathbf{v}_1^T \mathbf{e}_d \cos \theta \right) \mathbf{e}_1 = \\ &= \left[\mathbf{I} + \mathbf{e}_1 \left[\mathbf{e}_1^T (\cos \theta - 1) - \mathbf{v}_1^T \sin \theta \right] + \mathbf{v}_1 \left[\mathbf{e}_1^T \sin \theta + \mathbf{v}_1^T (\cos \theta - 1) \right] \right] \mathbf{e}_d \end{aligned} \quad (4.18)$$

where, \mathbf{I} denotes the identity matrix. The vector \mathbf{e}_d^{rot} is calculated for $d = 2, \dots, D$ [205]. It should be noted that $\mathbf{e}_1^{rot} = \mathbf{v}/\|\mathbf{v}\|$. Finally, the overall rotation matrix $\bar{\mathbf{R}}$ is given by

$$\bar{\mathbf{R}} = \mathbf{I} + \mathbf{e}_1 \left[\mathbf{e}_1^T (\cos \theta - 1) - \mathbf{v}_1^T \sin \theta \right] + \mathbf{v}_1 \left[\mathbf{e}_1^T \sin \theta + \mathbf{v}_1^T (\cos \theta - 1) \right] \quad (4.19)$$

The size s of the hypercube is

$$\mathbf{s} = [s_1 \cdots s_D]^T = \frac{(\mathbf{u}_S - \mathbf{l}_S)}{2} \quad (4.20)$$

where \mathbf{l}_S and \mathbf{u}_S are obtained from (4.6) and (4.7), respectively. After the rotation step, the new size s' of the box remains the same for all dimensions except s_1 which is equal to $\|\mathbf{v}\|/2$, that is

$$\mathbf{s}' = [s'_1 \cdots s'_D]^T = \left[\frac{\|\mathbf{v}\|}{2} \cdots s'_D \right]^T \quad (4.21)$$

In other words, the rotated box X_R^* is a convex hull of the vectors $s_d \mathbf{e}_d^{rot}$ shifted by \mathbf{x}_0 . The rotation of the initially reduced search space X_S is conceptually shown in Figure 4.9(b).

At the last step of the process, the rotated search space X_R is obtained by reduction of X_R^* in all dimensions except s_1 (see Figure 4.9(c)). The appropriate scaling rate can be found iteratively by comparing the Pareto sets obtained within the box with gradually reduced size until their contraction is noticeable. This approach, however, limits the potential benefits of the rotation step because it involves sampling of the regions that should be excluded. Instead, the rotated space can be scaled by *a priori* defined factor. Unfortunately, its determination is not straightforward, as for too large reduction a part of the Pareto front may not be captured within X_R . Too small coefficients, however, will result in sampling of the space regions that are away from X_p . Thus, the appropriate scaling is a trade-off between the cost of RSA construction and possible discrepancy between the Pareto set estimated in X_R and the actual Pareto front.

Here, a series of numerical experiments has been performed to estimate a reasonable space reduction factor. The tests involved multi-objective optimizations of three antennas with three, six, and sixteen geometrical variables [64, 205]. Various scaling ratios have been tested and Pareto sets corresponding to them have been compared with the ones obtained in the initially reduced hypercube X_S . It has been assumed that the scaling ratio is acceptable if the discrepancies between the Pareto sets (expressed in terms of the reflection coefficient) from X_S and X_R , respectively, are below 0.5 dB. The results shown in Figure 4.10 indicate that the Pareto sets are sufficiently close to each other for the reduction factor of 3. Assuming a relatively small rotation angle, this coefficient allows for reducing the volume of X_R by a factor 3^{D-1} compared to X_S [205]. Consequently, the number of samples required for the RSA model preparation may be considerably limited which reduces the overall computational cost of the multi-objective optimization. It should be emphasized that rotational space reduction does not involve any numerical overhead compared to the method of Section 4.3.2. The operation of the technique for a problem with three design variables is illustrated in Figure 4.11.

4.3.4 Design Space Confinement

Space reduction techniques described in the previous sections are well suited for problems with two objectives. Furthermore, sequential technique of Section 4.3.2 is also suitable for problems with larger number of objectives. Obviously, for the antenna at hand, the cost of the method is proportional to the number of considered objectives. Also, for problems with three and more objectives, the size of the reduced box obtained using the approach is typically larger than for two objective design tasks. This increases the cost of data acquisition. At the same time, the Pareto front is allocated in a certain region of the reduced space X_S (see Figure 4.12). In such a case, large amount of training data utilized for construction of RSA model in X_S will be away from X_p .

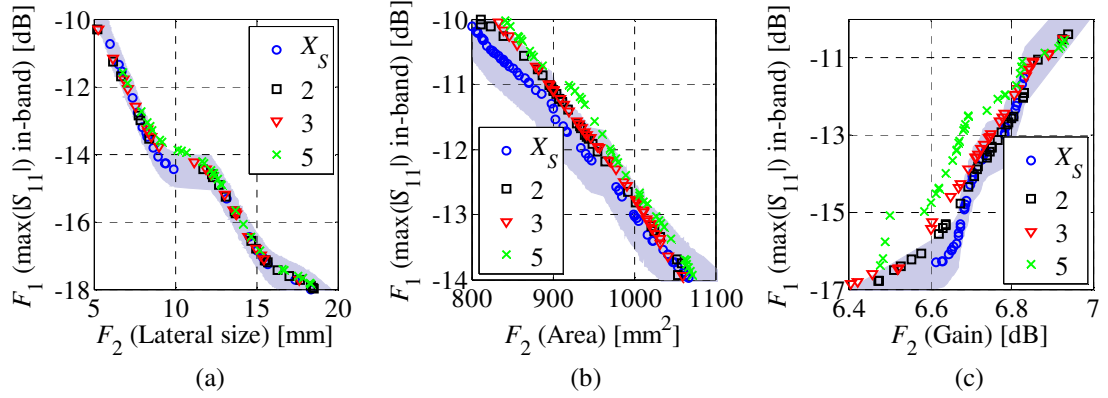


Figure 4.10: A comparison of Pareto fronts generated within X_S and X_R for problems with: (a) three; (b) six; and (c) sixteen variables. The violet area represents acceptable deviation of reduced Pareto fronts around X_S . The rotated space is scaled down by factors of 2, 3 and 5. The Pareto set obtained for ratio of 5 violates the 0.5 dB margin. In (c), the front obtained for factor of 3 slightly violates the assumed 0.5 dB margin. Note that in (c), the Pareto set obtained in X_S is shorter than the ones within the rotated spaces, which indicates that a number of optimal solutions are outside X_S .

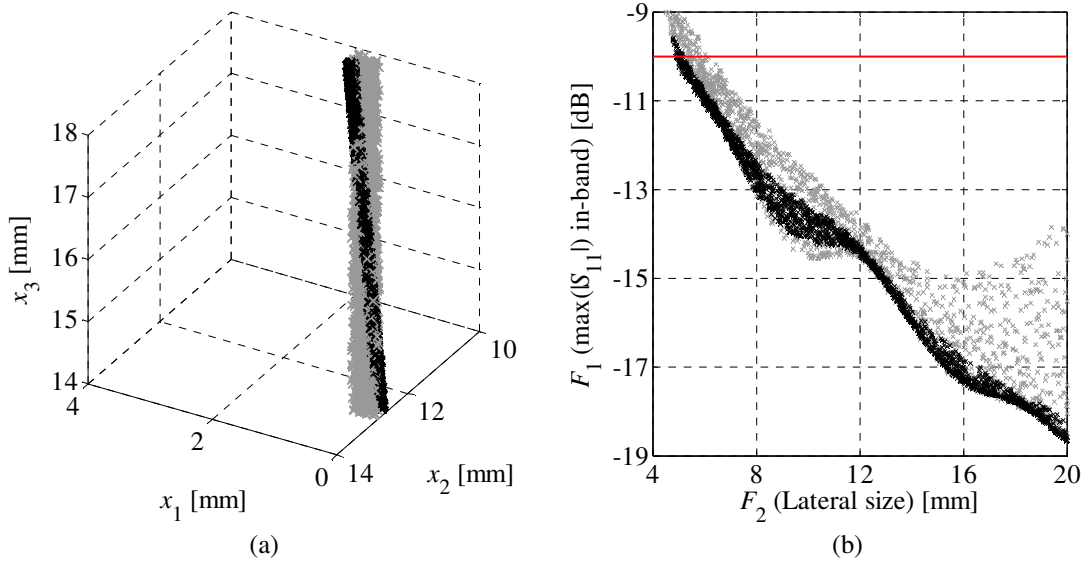


Figure 4.11: A visualization of solutions within the initially reduced design space (gray \times) and the rotated space scaled down by a factor of 3 (black \times): (a) three-dimensional design space; and (b) two-dimensional feature space. Note that the rotation allows for considerable reduction of the design space while the feature space responses are shifted towards the Pareto front.

The problem related to precise identification of the Pareto front for problems with more than two objectives can be addressed by means of a space confinement technique [177]. The idea behind the method is that the RSA model constructed within X_S can be utilized for rough identification of the design space region containing a part of the Pareto front which is of interest.

The algorithm works as follows. Let X_F be the feasible subset of the Pareto-optimal set obtained within the initially reduced search space X_S (see Section 4.3.2) [177]

$$X_F = \left\{ \mathbf{x}_c^{(n)} \right\}_{n=1, \dots, N_f} \quad (4.22)$$

The confinement procedure aims at identifying a set of unit vectors \mathbf{v}_d , $d = 1, \dots, D$ (cf. Section 4.3.3), as well as positive $\mathbf{d}_{p1,d}$ and negative $\mathbf{d}_{p2,d}$ ($d = 1, \dots, D$) dimensions defining the confined space X_C . The dimensions are defined with respect to the center point

$$\mathbf{x}_h = \frac{1}{N_f} \sum_n^{N_f} \mathbf{x}_c^{(n)} \quad (4.23)$$

Assume that the vectors $\mathbf{v}_1, \dots, \mathbf{v}_{d-1}$ are known. Then, let [177]

$$M_d = \mathbf{R}^D \setminus \text{span}(\{\mathbf{v}_1, \dots, \mathbf{v}_{d-1}\}) \quad (4.24)$$

be the orthogonal complement of the D -dimensional Euclidean space \mathbf{R}^D and the subspace spanned by \mathbf{v}_1 through \mathbf{v}_{d-1} . Note that $M^d = \mathbf{R}^D$ for $d = 1$. The unit vector \mathbf{v}_d is found as the direction at which the diameter of the orthogonal projection of $X_F - \{\mathbf{x}_h\}$ onto M_d , $P_d(X_F - \{\mathbf{x}_c\})$ reaches its minimum, i.e.,

$$\mathbf{v}_d = \arg \min_{\mathbf{v} \in M_d} G(P_d(X_F - \{\mathbf{x}_h\}), \mathbf{v}) \quad (4.25)$$

where the diameter G of a set Y in the direction of \mathbf{v} , $G(Y, \mathbf{v})$, is given by

$$G(Y, \mathbf{v}) = \max_{\mathbf{y} \in Y} \{\mathbf{v}^T \mathbf{y}\} - \min_{\mathbf{y} \in Y} \{\mathbf{v}^T \mathbf{y}\} \quad (4.26)$$

Having the vectors \mathbf{v}_d , one can determine the sizes $s_{p1,d}$ and $s_{p2,d}$ of the confined search space X_C

$$s_{p1,d} = \max_{\mathbf{x} \in X_F} \{\mathbf{v}_d^T \mathbf{x}\} \quad (4.27)$$

$$s_{p2,d} = -\min_{\mathbf{x} \in X_F} \{\mathbf{v}_d^T \mathbf{x}\} \quad (4.28)$$

The positive and negative dimensions obtained from (4.27) and (4.28), respectively, determine the maximum distance between the center point \mathbf{x}_h and the points from X_F along the directions of the vectors \mathbf{v}_d . It should be noted that the point \mathbf{x}_h may not be the center of the confined space X_C and thus both, positive and negative sizes have to be determined. A conceptual illustration of the technique is shown in Figure 4.12.

The space confinement algorithm can be summarized as follows (see also Figure 4.13):

1. Perform the initial design space reduction;
2. Construct the RSA model within X_S using sparsely sampled EM data;
3. Find the Pareto-optimal set within X_S using MOEA;
4. Confine the design to the region containing Pareto-optimal designs;
5. Identify the new RSA model \mathbf{R}_{sC} inside the confined space X_C .

Typically, the confined space X_C is significantly smaller than X_S . Moreover, the reduction rate is expected to increase with dimensionality of the design problem. The method, however, involves sampling of the initially reduced space which contributes to the overall cost of the space reduction process. On the other hand, the confinement technique allows for obtaining the RSA model with cost/accuracy ratio that is unattainable in the initially reduced space.

4.3.5 Space Reduction Using High-Fidelity Model Data

Interpolation models are utilized in this work not only to facilitate generation of the initial Pareto front through MOEA-based optimization but also to speed up the refinement stage. In some cases, the discrepancies between the low- and high-fidelity models may be significant. Large

misalignment between models limit the usefulness of the RSA for refinement because the high-fidelity Pareto-optimal designs may be allocated outside the reduced box. This problem is inherent to each space reduction method considered in this work. It can be mitigated by utilization of high-fidelity model designs for space reduction (see Figure 4.14 for illustration).

The procedure is as follows. Let $\mathbf{x}_f^{(k)}$, $k = 1, 2, \dots, K$, be the optimal high-fidelity model design obtained with respect to the k th objective. The $\mathbf{x}_f^{(k)}$ designs can be used together with the low-fidelity ones (see Section 4.3.2) to define the lower \mathbf{l}_S^* and upper \mathbf{u}_S^* bounds of the corrected reduced search space X_{Sr} [106, 146]

$$\mathbf{l}_{Sr} = \min \left\{ \mathbf{x}_c^{(1)}, \dots, \mathbf{x}_c^{(K)}, \mathbf{x}_f^{(1)}, \dots, \mathbf{x}_f^{(K)} \right\} \quad (4.29)$$

$$\mathbf{u}_{Sr} = \max \left\{ \mathbf{x}_c^{(1)}, \dots, \mathbf{x}_c^{(K)}, \mathbf{x}_f^{(1)}, \dots, \mathbf{x}_f^{(K)} \right\} \quad (4.30)$$

It should be noted that identification of the extreme high-fidelity designs increases the cost of design space reduction process. On the other hand, it allows obtaining more accurate representation of the high-fidelity Pareto front. Conceptual illustration of the method is shown in Figure 4.15.

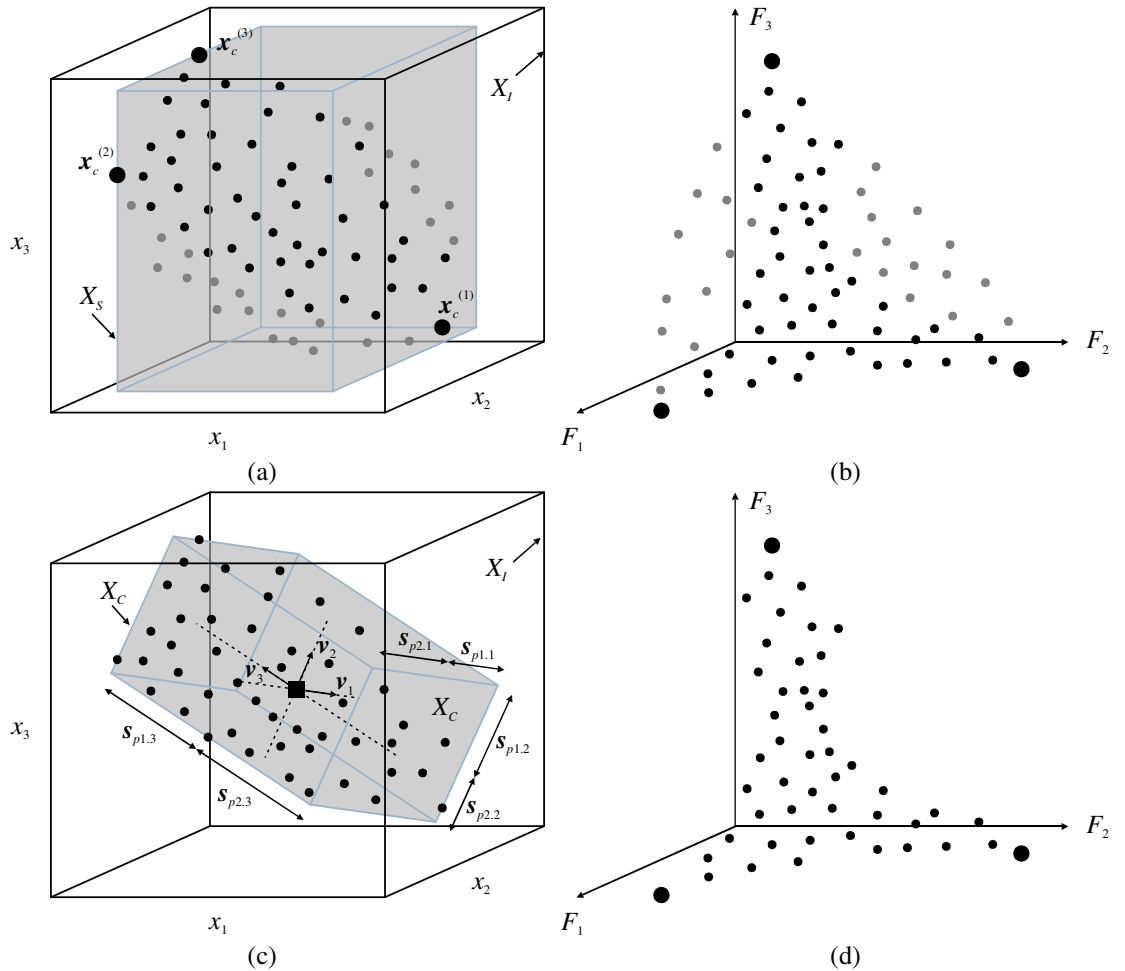


Figure 4.12: Conceptual illustration of the space confinement technique: (a) the initial Pareto set obtained within X_S and (b) its feature space representation. Black and gray dots represent the feasible (i.e., those with in-band reflection below -10 dB) and the infeasible designs, respectively. The confined space X_C : (c) a design space hypercube of minimal possible volume that contains all feasible Pareto designs; and (d) representation of the optimal set in the feature space. The dimensions $s_{p1,d}$ and $s_{p2,d}$ (here, $d = 1, 2, 3$) of the X_C are obtained with respect to the hub point (■). Unit vectors are \mathbf{v}_1 , \mathbf{v}_2 , and \mathbf{v}_3 .

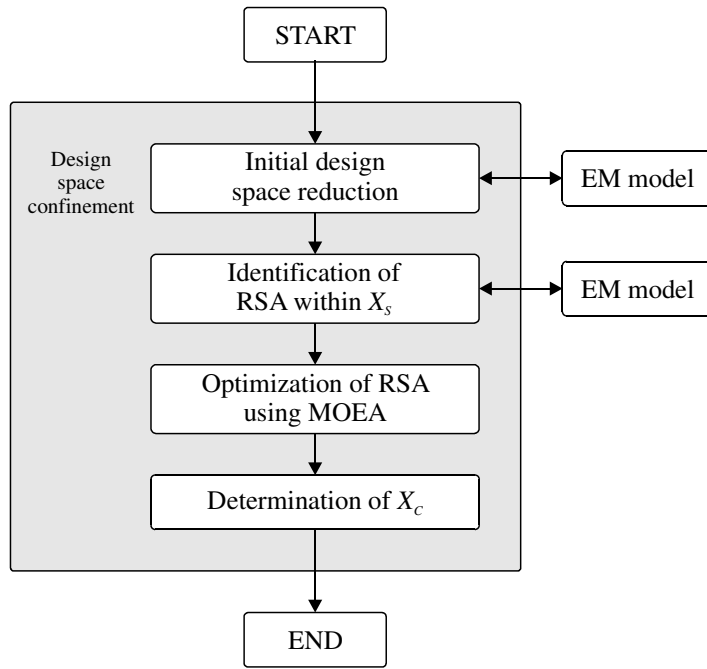


Figure 4.13: A block diagram of the design space confinement technique.

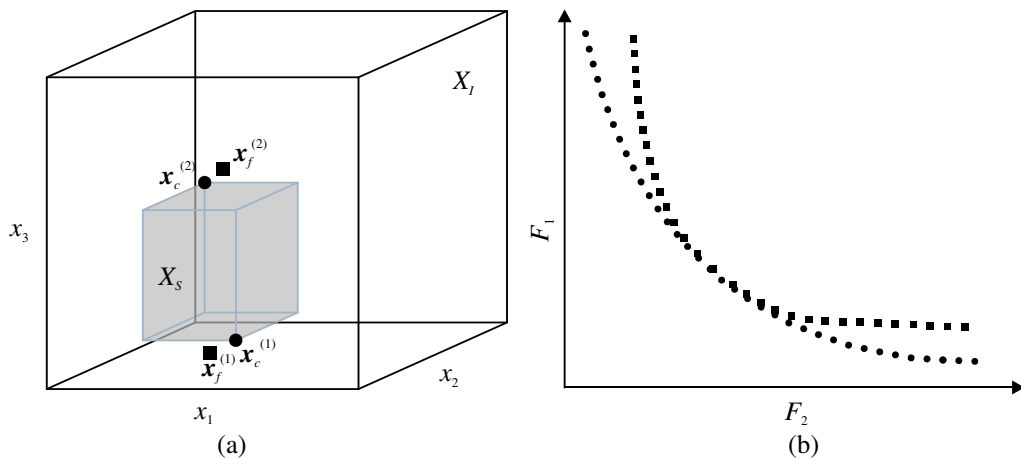


Figure 4.14: A design problem with two objectives: (a) the high- (■) and low-fidelity (●) extreme Pareto designs; and (b) the Pareto sets obtained by optimization of R_f (■) and R_c (●) models, respectively. Due to discrepancies between responses of both models, R_f extreme designs are located outside X_S . Consequently, portion of R_f Pareto set is away from the true Pareto front (see Section 5.1).

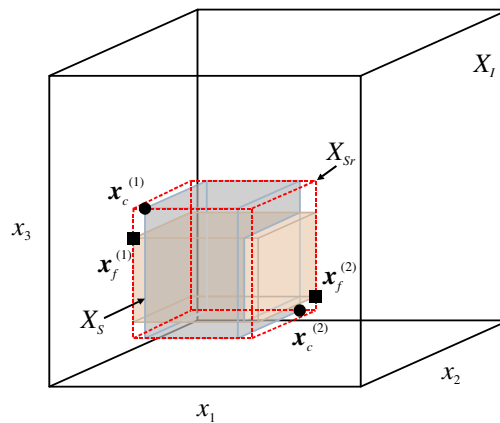


Figure 4.15: Corrected refined search space X_{Sr} constructed for a two-objective design problem – illustration.

4.4 Pareto Set Refinement

The algorithm presented in Figure 4.1 allows for obtaining Pareto-optimal designs through MOEA-based optimization of the RSA model. On the other hand, the resulting Pareto set is merely an approximation of the true Pareto front [64]. Its high-fidelity model-based representation can be obtained by means of refinement procedures. Here, two methods for correction of the initial Pareto set to the high-fidelity model level are considered: (i) response correction-based refinement and (ii) co-kriging-based refinement. More detailed description of both techniques is given below.

4.4.1 Pareto Set Refinement Using Response Correction

The first refinement approach described here allows for step-by-step construction of the high-fidelity Pareto set [64, 106]. In each iteration, the process begins from the designs selected along the initial Pareto set. Let $\mathbf{x}_s^{(j)}$, where $j = 1, \dots, J$, denote the selected designs found by MOEA. The chosen $\mathbf{x}_s^{(j)}$ solutions are refined using the output space mapping algorithm [178]. The OSM correction term is defined as follows (for a general description of the algorithm see Section 2.2.3.1) [185]

$$\mathbf{x}_f^{(j,i+1)} = \arg \min_{\mathbf{x}} F_1 \left(\mathbf{R}_s(\mathbf{x}) + \left[\mathbf{R}_f(\mathbf{x}_s^{(j,i)}) - \mathbf{R}_s(\mathbf{x}_s^{(j,i)}) \right] \right) \quad (4.31)$$

subject to

$$F_k(\mathbf{x}) \leq F_k(\mathbf{x}_s^{(j,i)}) \quad (4.32)$$

where $k = 2, \dots, K$. The block diagram of the algorithm is illustrated in Figure 4.16. The correction process (4.31) aims at minimizing the objective F_1 for each design $\mathbf{x}_f^{(j)}$ without degrading the remaining objectives as compared to $\mathbf{x}_s^{(j)}$. In practice, the constraint in (4.32) is often controlled using a penalty function. The surrogate model \mathbf{R}_s is corrected using the OSM term $\mathbf{R}_f(\mathbf{x}_s^{(j,i)}) - \mathbf{R}_s(\mathbf{x}_s^{(j,i)})$, so that it coincides with \mathbf{R}_f at the beginning of each iteration (here, the starting point $\mathbf{x}_f^{(j,0)} = \mathbf{x}_s^{(j)}$) [180]. Usually two to three iterations of (4.31) are required to find the refined high-fidelity model design $\mathbf{x}_f^{(j)}$. The procedure is repeated for all selected samples, so that the high-fidelity representation of the Pareto front is obtained. This set is the final outcome of the multi-objective optimization process [64, 106, 146].

Note that because of discrepancies between \mathbf{R}_f and \mathbf{R}_s it is rather unlikely to produce high-fidelity responses of all selected Pareto-optimal designs in close vicinity to the initial Pareto set. This is due to limited generalization of the RSA model. Nonetheless, at least shapes of the low- and high-fidelity Pareto fronts should resemble each other [64, 106]. The refinement of selected initial Pareto-optimal design is conceptually illustrated in Figure 4.17.

4.4.2 Pareto Set Refinement Using Co-Kriging

An alternative approach to the initial Pareto-optimal set refinement exploits co-kriging interpolation (cf. Section 2.2.3.2). The method is based on iterative enhancement of the surrogate model \mathbf{R}_s (here, $\mathbf{R}_s(\mathbf{x}) = \mathbf{R}_{Co}(\mathbf{x})$) using the high-fidelity samples and its further re-optimization using MOEA so that the resulting Pareto set becomes more and more accurate representation of \mathbf{R}_f [183, 208].

The correction algorithm considered here can be summarized as follows (see also Figure 4.18):

1. Construct/update the co-kriging surrogate \mathbf{R}_s ;
2. Optimize \mathbf{R}_s using MOEA to obtain Pareto-optimal set;
3. Evaluate \mathbf{R}_f at J locations selected along the current Pareto front representation;
4. Stop if termination condition is satisfied; otherwise go to Step 1.

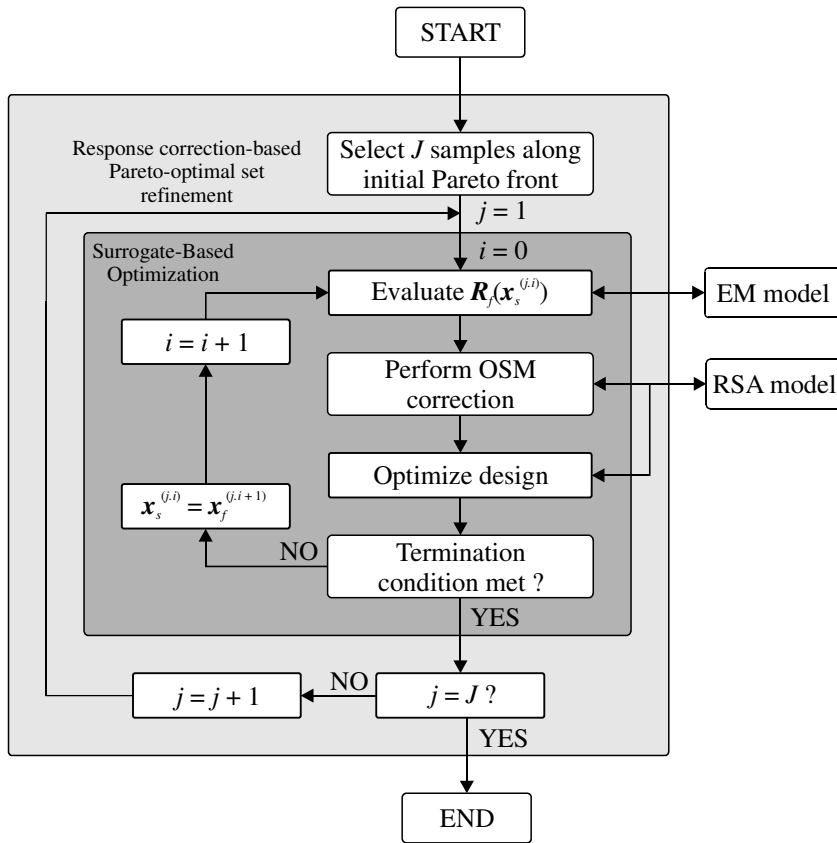


Figure 4.16: Block diagram of the response-correction-based Pareto-optimal set refinement technique. At the first step, J designs are selected along the initial Pareto front representation. Subsequently, each design is refined using the SBO routine. The process is repeated for all selected designs.

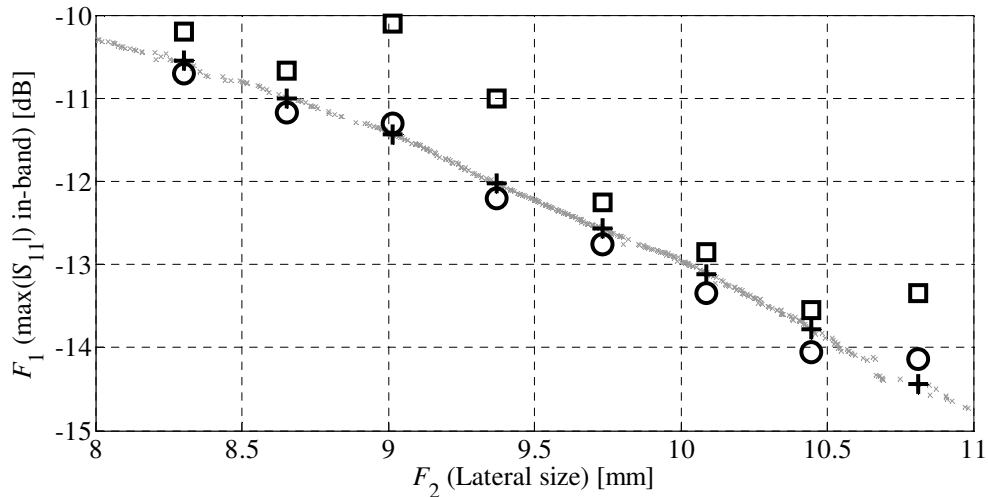


Figure 4.17: Pareto set refinement using response correction ($K = 2$). Initial representation of the Pareto front (\times) is refined at J (here, $J = 8$) designs ($+$). The R_f model representation of ($+$) before correction is denoted as (\square), whereas corrected designs are marked with (\circ).

In the first iteration of the algorithm the surrogate is a kriging model constructed using the R_c training data (cf. Section 2.2.3.2). In the next iterations, the R_f samples selected along the Pareto set are incorporated into co-kriging surrogate so that its accuracy along the Pareto front increases. Considering the two-dimensional feature space, evaluation of $J = 10$ high-fidelity designs

per iteration is usually sufficient for the refinement of the co-kriging model [183]. Normally, two to three iterations of the above procedure are sufficient to obtain an accurate representation of the high-fidelity Pareto-optimal set [183, 208]. The convergence criterion for the algorithm is defined as reflection-wise discrepancy between \mathbf{R}_f and \mathbf{R}_s at selected designs (see Figure 4.19). In this work the threshold value is set to 0.5 dB.

The co-kriging-based refinement is computationally efficient because it aims at improving the predicting capabilities of the \mathbf{R}_s model only in the vicinity of the Pareto front rather than in the entire search space. It should be noted that, for the same number of \mathbf{R}_f samples evaluated in each iteration, the numerical costs of co-kriging and response correction technique are comparable. On one hand, the latter is simpler to implement. On the other hand, co-kriging generates an accurate representation of the entire high-fidelity Pareto front, whereas the response correction produces a sparse discrete representation of the front. As mentioned before, the co-kriging model construction is realized using the SUMO (SURrogate MOdeling) Toolbox [168].

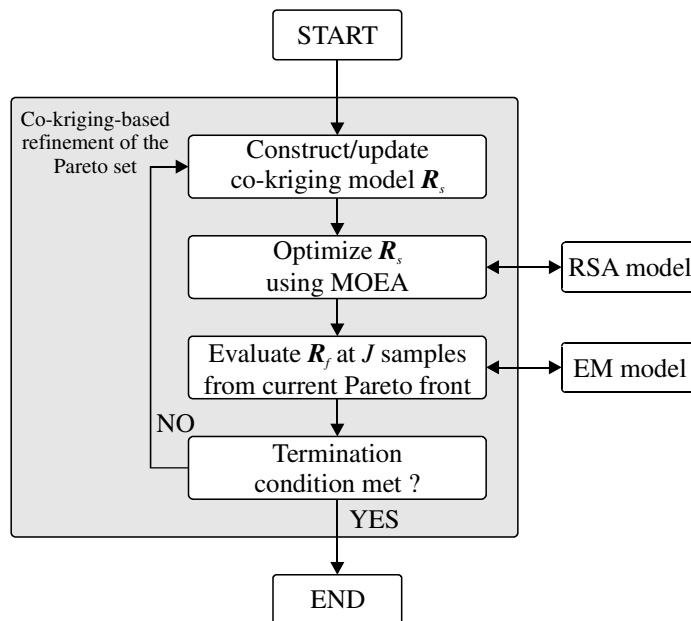


Figure 4.18: Co-kriging-based refinement of the Pareto-optimal set – block diagram.

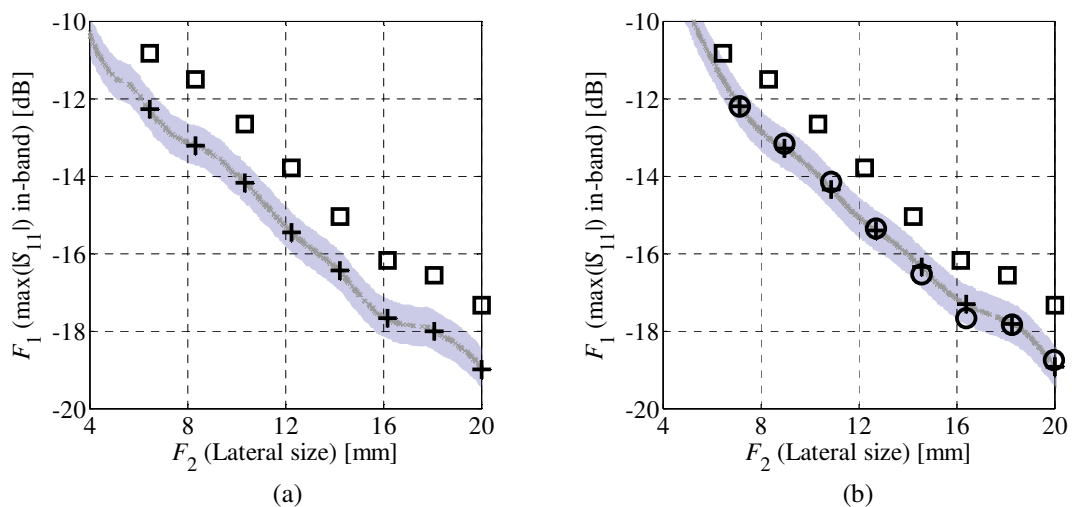


Figure 4.19: Pareto set refinement using co-kriging: (a) at first iteration of the algorithm, the high-fidelity representation (\square) of the Pareto front ($J = 8$) obtained for the selected \mathbf{R}_s designs (+) violates convergence criterion (i.e., maximal allowed discrepancy between \mathbf{R}_f and \mathbf{R}_s responses, here, marked as violet area); (b) the (\square) samples are incorporated into co-kriging model and the new Pareto front is obtained. Note that high-fidelity representation of the refined front (\circ) fulfills the convergence criterion.

4.5 Comparison of the Methods

The multi-objective optimization methodology of Section 4.2.1 is validated here based on numerical experiments. The emphasis is put on the investigating the effect of design space reduction on the algorithm operation. The comparisons concern the influence of the selected reduction algorithm on the size of the refined search space, the number of data samples required for RSA construction, the MOEA performance, the quality of the refined Pareto sets, and the overall design optimization cost. Finally, scalability of the multi-objective optimization algorithm for different space reduction techniques is discussed.

The comparison is carried out using three ultra-wideband antennas optimized with respect to two design objectives. Specifically, we consider a three-parameter monocone antenna [64], a planar six-variable dipole [212] and a planar nine-parameter monopole [157]. The numerical experiments are carried out under the following assumptions:

1. The RSA model is constructed using solely low-fidelity model data;
2. Data acquisition step is terminated if either the RMS error is below 3% or the number of training samples exceeds 2000;
3. The RMS error is calculated using cross-validation (cf. Section 2.2.2.3);
4. Pre-/Post-refinement of the RSA model is not performed;
5. The optimized high-fidelity Pareto front is represented using $N = 10$ samples;

Note that the RMS error of 3% or less is considered sufficient for the RSA model to be practically useful for design optimization purposes. On the other hand, handling too large amounts of training data may lead to numerical problems in model identification [205].

Comparative study is performed with respect to two objectives: $F_1(\mathbf{x})$ – minimization of the antenna reflection $|S_{11}|$ within the frequency band of interest, and $F_2(\mathbf{x})$ – reduction of the antenna size defined as a rectangle (or cuboid) $V(\mathbf{x})$ containing the structure at hand. The lower and upper frequencies of the considered bandwidth are $f_L = 3.1$ GHz and $f_H = 10.6$ GHz (UWB range), respectively. The objectives are defined as

$$F_1(\mathbf{x}) = \max \left\{ |S_{11}(\mathbf{x}, f)| : f_L \leq f \leq f_H \right\} \quad (4.33)$$

$$F_2(\mathbf{x}) = V(\mathbf{x}) \quad (4.34)$$

Normally, one is only interested in this part of the Pareto front for which the maximum in-band reflection of the antenna structure at hand does not exceed $S_t = -10$ dB. Therefore, design space reduction takes this into account by constraining the single-objective optimization problems (4.5) (with respect to objectives other than antenna reflection) only to designs that satisfy the aforementioned condition. An appropriate constraint can be rigorously formulated as $c(\mathbf{x}) \leq 0$ with c defined as

$$c(\mathbf{x}) = \max \left\{ |S_{11}(\mathbf{x}, f)| : f_L \leq f \leq f_H \right\} - S_t \quad (4.35)$$

The reduction rate (volume-wise) of the refined search space with respect to the initial one can be calculated as follows

$$\chi = \prod_{k=1}^d \delta^k \quad (4.36)$$

where δ^k , $k = 1, 2, \dots, d$, is given by

$$\delta^k = \begin{cases} p^k - p_r^k & \text{if } p^k - p_r^k > 0 \\ 1 & \text{otherwise} \end{cases} \quad (4.37)$$

Here, p^k and p_r^k denote range of the initial and reduced design spaces along the dimension k . It should be noted that (4.37) allows for calculating the space reduction factor χ even if certain dimensions are narrowed down to zero (see also Section 4.3).

The following space reduction routines are compared: (i) the Pareto ranking method (cf. Section 4.3.1); (ii) the sequential optimization approach (cf. Section 4.3.2); (iii) the corrected sequential method (cf. Section 4.3.5); and (iv) the rotational space reduction technique (cf. Section 4.3.3). The algorithm of Section 4.2.1 is also executed within the initial space X_I , to obtain the reference results. It should be noted that the extreme Pareto-optimal designs are obtained using the pattern search algorithm. Formulation of the latter can be found in [213]. The design space confinement technique of Section 4.3.4 is not considered here. The reason is that it is designed for problems with more than two objectives. Also, the method involves two data acquisition steps and thus it is of limited efficiency if two-objective tasks are considered. However, in Section 5.5, the performance comparison of confinement and sequential methods for three objective design problem is provided.

All computations have been performed on a microserver unit with two Intel Xeon E5540 processors (8 threads per CPU) and 6 GB of RAM. The electromagnetic models of the considered antenna structures are implemented in CST Microwave Studio and simulated using its transient solver [149]. Moreover, the algorithms for design space reduction, data acquisition, construction and evaluation of RSA models, as well as their further refinement are implemented in MATLAB [206].

4.5.1 Simulation Model Setup

Appropriate setup of the low- and high-fidelity models is the key for successful surrogate-assisted optimization [141]. Computational cost and accuracy of the EM model primarily depends on the mesh discretization density. In this work, both the low- and high-fidelity EM models are selected manually based on analysis of antenna responses at two different designs. A more detailed discussion on simulation setup for physics-based models can be found in Section 2.2.1.

4.5.2 UWB Monocone – Design and Optimization Setup

The first benchmark design is a UWB monocone antenna shown in Figure 4.20. The structure is composed of a cone-shaped driven element situated on a conductive plate. The radiator is terminated by a hemisphere [64]. The antenna is fed from the bottom through a 50 ohm coaxial line. The design variables considered for optimization are $\mathbf{x} = [z_1 \ z_2 \ r_1]^T$. The relative parameter is $r_2 = (r_1^2 - (z_1 + z_2)^2)^{0.5}$, whereas $r_0 = 0.635$ remains fixed in order to provide 50 ohm input impedance. The unit of all dimensions is mm. The initial design space X_I is defined using the arbitrarily selected bounds: $\mathbf{l} = [0 \ 8 \ 10]^T$ and $\mathbf{u} = [1.5 \ 20 \ 23]^T$, as well as the constraint $z_1 + z_2 \leq r_1 - 0.25$, imposed to ensure physical consistency of the structure.

The appropriate discretization levels of the low-fidelity antenna model \mathbf{R}_c and its high-fidelity counterpart \mathbf{R}_f are selected manually based on responses obtained for the two test designs $\mathbf{x}_{r1} = [1 \ 15 \ 19]^T$ and $\mathbf{x}_{r2} = [0.5 \ 14 \ 16]^T$ (cf. Section 4.5.1). The reflection characteristics obtained for various mesh densities are shown in Figure 4.21. The high-fidelity model \mathbf{R}_f contains ~1,400,000 hexahedral mesh cells with a typical simulation time of 23 min. The low-fidelity model \mathbf{R}_c consists of ~33,000 cells. Another simplification of the model includes representation of metal as a perfect electrical conductor (cf. Section 2.2.1). Its average evaluation time is 33 s, so that it is 42 times faster than \mathbf{R}_f . The cross-section visualization antenna models with selected mesh densities are provided in Figure 4.22.

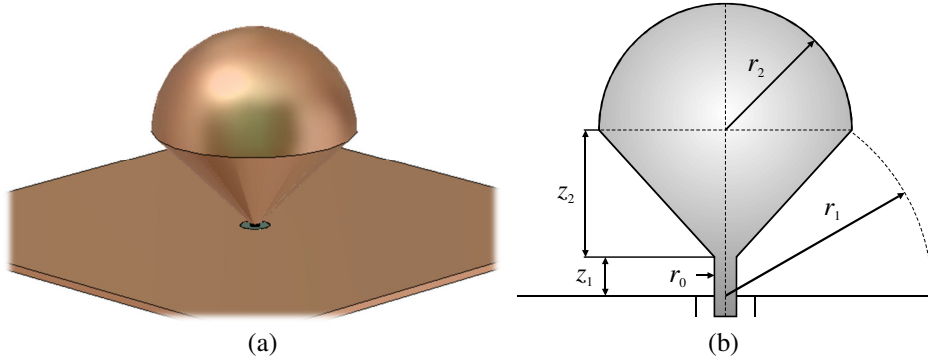


Figure 4.20: A UWB monocone antenna [64]: (a) 3D visualization; (b) cross-section view with highlighted geometrical details.

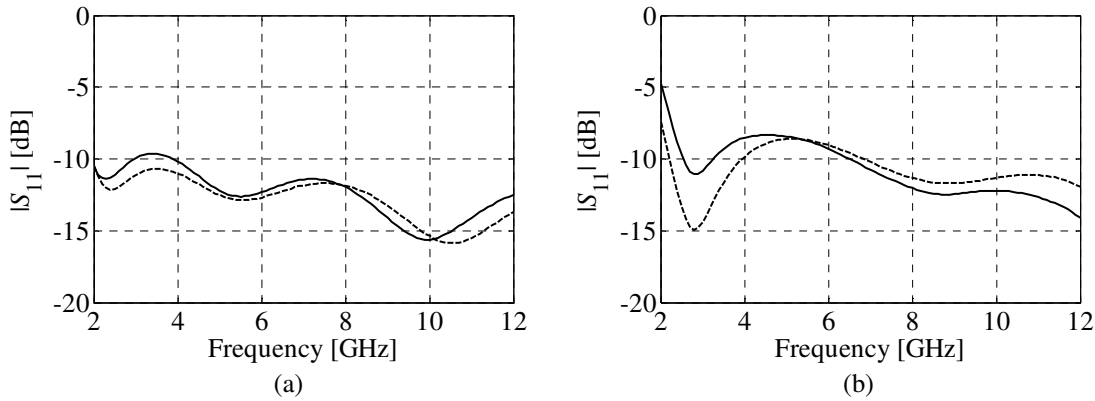


Figure 4.21: Reflection responses of the low- (---) and the high-fidelity (—) antenna models at the designs: (a) \mathbf{x}_{11} ; and (b) \mathbf{x}_{12} .

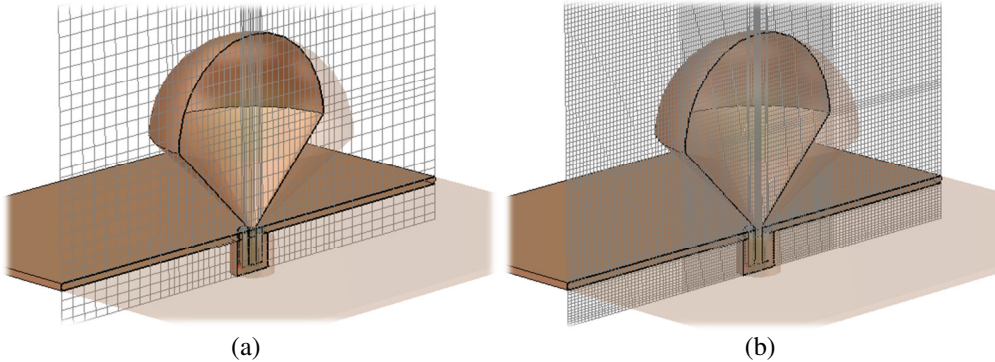


Figure 4.22: Cross-section mesh visualization for selected discretization levels of UWB monocone: (a) the low-; and (b) the high-fidelity model.

The design objectives are (4.33) and (4.34). The volume $V(\mathbf{x})$ is defined as a cuboid $A \times B \times C$, where $A = B = 2r_2$ and $C = z_1 + z_2 + r_2$, respectively.

4.5.2.1 Design Space Reduction

The setup of the space reduction algorithms under comparison is as follows. For the algorithm (i), the maximum number of pattern search-driven simulations is set to 200 per objective, whereas the acceptable domination rank of the selected samples is two. For algorithm (ii), the maximum number of model evaluations is 500 per objective. The scaling factor in method (iv) is set to 3, whereas the maximum number of the low-fidelity model simulations during refinement of the extreme Pareto samples in technique (iii) is 300. The starting point for the design space reduction algorithms is defined as the center of the initial search space. The design bounds of the reduced space regions X_D , X_S and X_{S_r} obtained using algorithms (i), (ii) and (iii) are: $\mathbf{l}^{(i)} = [0.3 \ 11.38 \ 9.8]^T$ and $\mathbf{u}^{(i)} = [0.81 \ 14.72 \ 23]^T$; $\mathbf{l}^{(ii)} = [0.01 \ 12.75 \ 14.09]^T$ and $\mathbf{u}^{(ii)} = [0.35 \ 12.99$

$19.79]^T$; $\mathbf{l}^{(iii)} = [0.01 \ 12.25 \ 14]^T$ and $\mathbf{u}^{(iii)} = [0.35 \ 12.99 \ 19.79]^T$, respectively. The reduced search space X_D is 10 times smaller (volume-wise) than the initial space X_I (cf. Section 4.5.2). It has been obtained after 28 \mathbf{R}_c evaluations of the first stage and 120 \mathbf{R}_c simulations of the second stage of (i). The volume-wise reduction factor χ of X_S is almost 500. It should be noted that incorporation of both the high- and low-fidelity Pareto designs results in enlargement of X_{S_r} with respect to X_S . Nonetheless, its reduction factor χ is still almost 160. Finally, algorithm (iv) allows for obtaining X_R characterized by the most significant reduction factor χ (almost 4500) as compared to X_I . It should be noted that X_R is rotated, thus it cannot be described using lower/upper bounds. The parameters of extreme Pareto designs and detailed data on space reduction rates of the algorithms are provided in Table 4.1. The frequency responses of the obtained designs are shown in Figure 4.23. It should be emphasized that for algorithms (ii)-(iv), the low-fidelity extreme designs are obtained by means of the sequential approach and thus they are the same.

The methods have also been compared in terms of the numerical cost (see Table 4.2). The results indicate that the algorithm (i) required a total of 148 \mathbf{R}_c model evaluations (about 1.4 hour of CPU-time). The number of low-fidelity model simulations required by the algorithm (iii) is 465, whereas (ii) and (iv) involved 256 \mathbf{R}_c simulations. Moreover, additional 4 \mathbf{R}_f simulations are necessary to refine the responses in (iii). The total CPU-time of (ii) and (iii) is about 2.4 hours (over 1.7 times the cost of (i)) and 5.8 hours (almost 4.3 times more than (i)), respectively. Note that the cost of (ii) and (iv) is the same since rotation of the search space does not involve any additional \mathbf{R}_c evaluations.

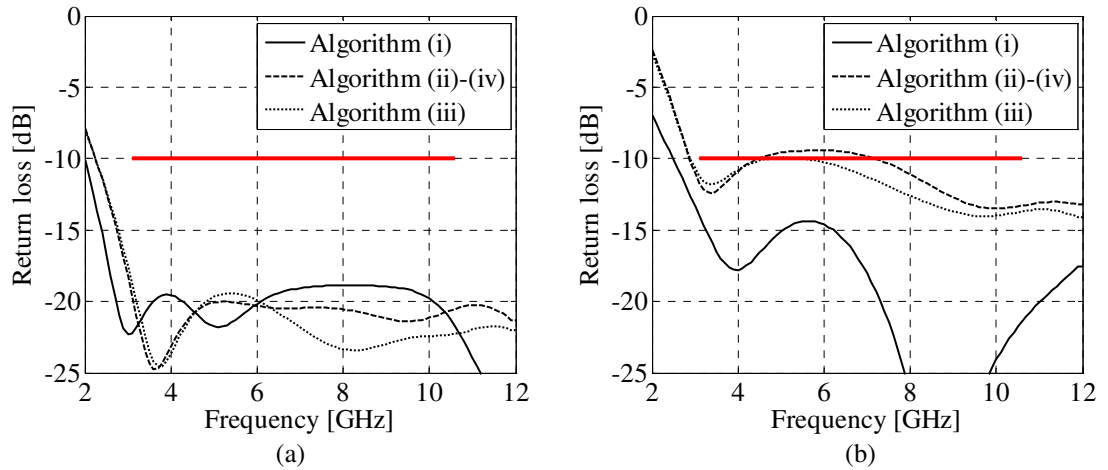


Figure 4.23: Antenna responses at the extreme Pareto-optimal designs obtained using the selected space reduction routines: (a) $\mathbf{x}_c^{(1)}$ – optimum w.r.t. objective F_1 ; and (b) $\mathbf{x}_c^{(2)}$ – optimum w.r.t. objective F_2 . The high-fidelity model response is denoted by (····).

TABLE 4.1: COMPARISON OF ALGORITHMS – SPACE REDUCTION RATE

Reduction Method	Low-Fidelity Corner Designs				High-Fidelity Corner Designs				Size of the Search space reduction [mm ³]	Space χ
	Design	z_1	z_2	r_1	Design	z_1	z_2	r_1		
	Initial space X_I	—	—	—	—	—	—	—		
Algorithm (i)	$\mathbf{x}_c^{(1)}$	0.30	14.72	23.00	—	—	—	—	22.29	10.323
	$\mathbf{x}_c^{(2)}$	0.81	11.38	9.80	—	—	—	—	—	—
Algorithm (ii)	$\mathbf{x}_c^{(1)}$	0.35	12.99	19.79	—	—	—	—	0.463	497.25
	$\mathbf{x}_c^{(2)}$	0.01	12.75	14.09	—	—	—	—	—	—
Algorithm (iii)	$\mathbf{x}_c^{(1)}$	0.35	12.99	19.79	$\mathbf{x}_f^{(1)}$	0.35	12.99	19.79	1.458	157.88
	$\mathbf{x}_c^{(2)}$	0.01	12.75	14.09	$\mathbf{x}_f^{(2)}$	0.17	12.25	14.00		
Algorithm (iv)	$\mathbf{x}_c^{(1)}$	0.35	12.99	19.79	—	—	—	—	0.052	4463.5
	$\mathbf{x}_c^{(2)}$	0.01	12.75	14.09	—	—	—	—		

TABLE 4.2: COMPUTATIONAL COST OF THE ALGORITHMS

Reduction method	Number of Algorithm Evaluations		Total Number of Evaluations		CPU-time			
					Absolute [min]	Relative to \mathbf{R}_f	$\Sigma [\mathbf{R}_f]$	Σ [h]
Algorithm (i)	Stage 1	$F_1(\mathbf{x})$: 28 \mathbf{R}_c			15.4	0.67		
	Stage 2	$F_1(\mathbf{x})$: 77 \mathbf{R}_c	148	\mathbf{R}_c	42.4	1.84	3.54	1.36
		$F_2(\mathbf{x})$: 43 \mathbf{R}_c			23.7	1.03		
Algorithm (ii)		$F_1(\mathbf{x})$: 83 \mathbf{R}_c	256	\mathbf{R}_c	45.7	1.98	6.12	2.35
		$F_2(\mathbf{x})$: 173 \mathbf{R}_c			95.2	4.14		
Algorithm (iii)	Step 1 [†]	$F_1(\mathbf{x})$: 83 \mathbf{R}_c			45.7	1.98		
		$F_2(\mathbf{x})$: 173 \mathbf{R}_c			95.2	4.14		
	Step 2 [#]	$F_1(\mathbf{x})$: 34 \mathbf{R}_c	465	\mathbf{R}_c	18.7	0.81	15.11	5.79
		1 \mathbf{R}_f	4	\mathbf{R}_f	23.0	1.00		
		$F_2(\mathbf{x})$: 175 \mathbf{R}_c			96.3	4.18		
		3 \mathbf{R}_f			69.0	3.00		
Algorithm (iv)		$F_1(\mathbf{x})$: 83 \mathbf{R}_c	256	\mathbf{R}_c	45.7	1.98	6.12	2.35
		$F_2(\mathbf{x})$: 173 \mathbf{R}_c			95.2	4.14		

[†] Initial design space reduction (cf. Section 4.3.2)

[#] Refinement of \mathbf{R}_c extreme points using SBO

4.5.2.2 Data Acquisition

Data acquisition is arranged here as an iterative procedure that involves the following mechanisms. Initially the search space is sampled using the selected design of experiment technique (cf. Section 2.2.2.1). Then, the low-fidelity EM antenna model is evaluated at the selected points. Finally, the cross-validation of the surrogate model constructed using the acquired training data is performed. The process is repeated until desired accuracy of the RSA model is obtained or the maximum allowed number of samples is reached. Since the antenna contains only three variables, enlargement of the training set by 10 samples per iteration is considered sufficient. Data points are generated using LHS algorithm. Here, the infill data points are allocated to ensure uniform distribution of the entire data set [164]. As mentioned before, the target relative RMS model error is 3 percent.

The key data concerning the number of samples required for construction of an accurate RSA model are gathered in Table 4.3. It should be noted that the refinement of the search space dramatically reduces the number of samples needed for RSA identification. A total of 600 \mathbf{R}_c simulations have been performed within X_I to obtain the model with the RMS error of 2.9%, whereas the RSA model of similar accuracy has been identified within X_D (algorithm (i)) using only 160 samples. A tremendous reduction of the computational cost has been observed for design spaces generated using the algorithms (ii), (iii) and (iv). The RSA models have been identified within these space regions using only 30, 40 and 20 evaluations of the low-fidelity model \mathbf{R}_c , respectively. Moreover, their RMS errors are below 1.5% which is over 50% less than the assumed threshold. At the same time, the average minimum distance between the samples δ_p is similar for all considered design spaces. It should be emphasized that construction of the RSA models in the refined regions of the space allows for reduction of the data acquisition cost by up to 30 times compared to X_I .

The convergence plots (i.e., model accuracy versus number of training samples) for the considered RSA models are shown in Figure 4.24. The local non-monotonicity of the curves is due to a relatively high variance of the cross-validation scheme.

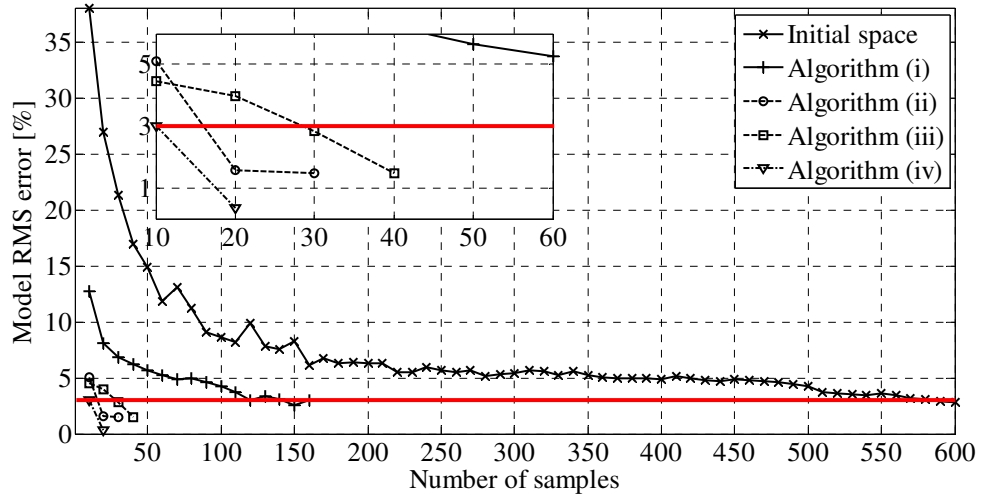


Figure 4.24: Convergence plots of response surface approximation models constructed within initial and refined search spaces.

TABLE 4.3: KEY INFORMATION ON THE DATA ACQUISITION STEP

Selected Solution Space	Number of Training Samples	RMS Error of the RSA Model [%]	Average Minimal Distance Between Samples	Training Set Size Reduction Ratio
Initial space X_I	600	2.86	0.43	—
Algorithm (i)	160	2.97	0.32	3.75
Algorithm (ii)	30	1.49	0.19	20
Algorithm (iii)	40	1.48	0.17	15
Algorithm (iv)	20	0.33	0.16	30

4.5.2.3 MOEA Optimization

The multi-objective evolutionary algorithm exploits mechanisms such as fitness sharing, elitism, mating restrictions and Pareto-dominance tournament selection (see Section 3.3.1 for a detailed description). The algorithm setup is mostly based on the rules of thumb derived from the literature [105, 114, 188, 193, 199]. It is as follows (see also Section 3.3.1)

- probability of mutation: 20%;
- probability of recombination: 70%;
- linear sharing function ($\gamma = 1$);
- dynamically determined sharing range σ_r ;
- proximity of individuals allowed for mating: $\sigma_p = 3\sigma_r$.

It should be emphasized that MOEA optimization is performed using a fast RSA and thus the cost of algorithm operation is low, even for large number of model simulations. Here, the number of iterations I and the population size N are set to 50 and 500 (a total of 25000 evaluations of the \mathbf{R}_s), respectively. For such a setup, the optimization cost is up to 90 s of the CPU-time which is very low comparing to other steps of the discussed multi-objective procedure, e.g., the CPU-time of space reduction is the order of hours. Thus, the cost of MOEA optimization is neglected.

The initial Pareto sets obtained for each search space region are shown in Figure 4.25, whereas their key parameters are gathered in Table 4.4. The results indicate that X_I and X_D (algorithm (i)) are redundant because their corresponding Pareto sets ranges are up to -6 dB with respect to F_1 . The comparison has been performed with respect to relevant fractions of the Pareto sets (i.e., with reflection below -10 dB). Note that shape of the Pareto front obtained using algorithm (i) is slightly different than the others. The reason is that the search space bounds of (i) only par-

tially overlap with the design spaces obtained using the remaining algorithms. The Pareto sets from X_I and search space regions determined using algorithms (ii)-(iv) resemble each other which means that they accurately captured the region of interest within X_I . The largest changes of antenna responses with respect to F_1 and F_2 (denoted as ΔF_1 and ΔF_2 , respectively; cf. Table 4.4) of 9.6 dB and 18500 mm³ (almost 81% of the volume change), respectively, can be observed for the initial space. The smallest variability (9.3 dB along F_1 and 16800 mm³ along F_2) is obtained within (iii). At the same time, the Pareto fronts from X_I and X_{S_r} (algorithm (iii)) exhibit the smallest discrepancy expressed as the average distance with respect to the selected design objective $dIS(F_k)$. In other words, misalignment between Pareto sets from X_I and X_{S_r} is the smallest among the obtained ones.

It should be noted that the stochastic nature of MOEA affects the optimization process. On one hand, the quality of the initial Pareto set is not critical when SBO-based correction is considered because the selected Pareto designs are merely starting points during refinement to the R_f model level. On the other hand, MOEA optimization is one of the steps in co-kriging-based model correction loop and poor algorithm setup may affect the quality of the high-fidelity Pareto set. Therefore, statistical analysis of the algorithm has been performed to evaluate influence of the model setup on the optimization results (cf. Appendix A1). Obtained results indicate that for $I = 50$ and $N = 500$ the variability of the Pareto sets is minor.

TABLE 4.4: KEY PROPERTIES OF THE OBTAINED PARETO SETS

Design Space	Objective F_1				Objective F_2				
	$\min(F_1)$	$\max(F_1)$	$\Delta(F_1)$	$dIS(F_1)$	$\min(F_2)$	$\max(F_2)$	$\Delta(F_2)$	$\Delta(F_2)$	$dIS(F_2)$
	[dB]	[dB]	[dB]	[dB]	[mm ³]	[mm ³]	[mm ³]	[%]	[mm ³]
Initial Space X_I	-19.6	-10.0	9.6	—	4400	22900	18500	80.8	—
Algorithm (i)	-19.6	-10.1	9.5	0.5	4700	23000	18300	79.6	1372
Algorithm (ii)	-19.5	-10.1	9.4	0.3	5200	22800	17600	77.2	557
Algorithm (iii)	-19.4	-10.1	9.3	0.1	5100	21900	16800	76.7	282
Algorithm (iv)	-19.5	-10.3	9.3	0.3	5200	22200	17000	76.6	603

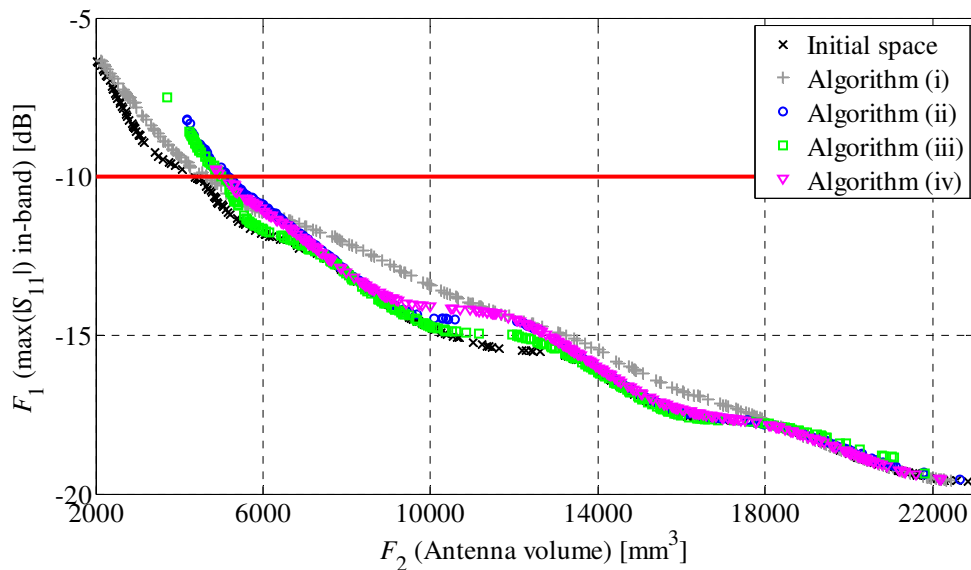


Figure 4.25: A comparison of the Pareto sets obtained within initial and refined search spaces.

4.5.2.4 Pareto Set Refinement

Here, response correction (cf. Section 4.4.1) and co-kriging (cf. Section 4.4.2) refinement of the initial Pareto-optimal sets are described. The first method has been applied to $N = 10$ design samples evenly selected along the obtained Pareto designs. Only the samples for which $F_1(\mathbf{x}) \leq -10$ have been considered. The correction procedure has been terminated after three iterations. The responses of the \mathbf{R}_s and \mathbf{R}_f designs are compared in Figure 4.26. The geometrical details of the refined samples are gathered in Table 4.5. It should be noted that the high-fidelity designs obtained in X_D (algorithm (i)) are different than the remaining ones (see Figure 4.26(b)). The reason is that they are found in another region of the search space (cf. Section 4.5.2.1). Nonetheless, F_1 and F_2 discrepancies between the Pareto fronts obtained in X_D and the remaining regions of the design space are below 1 dB, and 1500 mm^3 , respectively.

For the co-kriging, similarly as for response correction, the design samples have been selected evenly along Pareto sets and the procedure has been terminated after three iterations. A comparison of the corrected representations of the Pareto sets and the high-fidelity designs evaluated along them is shown in Figure 4.27. The results indicate very good agreement with the Pareto front obtained using the response correction technique. The geometrical details of the selected high-fidelity designs are collected in Table 4.6. It should be noted that the shapes of all high-fidelity Pareto sets are similar. Moreover, maximum discrepancy between the samples selected from the co-kriging-based sets and their \mathbf{R}_f counterparts is below 0.5 dB.

The computational costs of both refinement techniques are comparable. The most notable difference between both approaches is that response correction refines only the selected set of samples whereas co-kriging allows for correction of the entire Pareto front. Thus, co-kriging provides more comprehensive information about the considered antenna structure.

TABLE 4.5: RESPONSE CORRECTION REFINEMENT – SELECTED ANTENNA DESIGNS

		Selected Pareto-optimal designs									
		$\mathbf{x}_f^{(1)}$	$\mathbf{x}_f^{(2)}$	$\mathbf{x}_f^{(3)}$	$\mathbf{x}_f^{(4)}$	$\mathbf{x}_f^{(5)}$	$\mathbf{x}_f^{(6)}$	$\mathbf{x}_f^{(7)}$	$\mathbf{x}_f^{(8)}$	$\mathbf{x}_f^{(9)}$	$\mathbf{x}_f^{(10)}$
Initial Space X_f	F_1 [dB]	-9.89	-11.22	-13.10	-14.16	-15.41	-16.59	-17.84	-17.62	-18.47	-19.37
	F_2 [mm^3]	4491	5950	8636	10639	12748	14801	16925	18967	21018	22876
	z_1	0.49	0.00	0.06	0.10	0.14	0.19	0.23	0.30	0.34	0.35
	z_2	10.81	11.50	12.07	11.68	11.74	12.07	12.58	12.96	12.96	12.99
	r_1	13.07	13.86	15.26	15.85	16.59	17.36	18.15	18.83	19.34	19.79
Algorithm (i)	F_1 [dB]	-10.58	-11.49	-12.36	-13.58	-14.74	-15.98	-17.16	-17.67	-18.48	-19.39
	F_2 [mm^3]	4882	6946	8905	10998	13001	15036	16930	19104	21054	22922
	z_1	0.32	0.30	0.31	0.30	0.30	0.30	0.30	0.31	0.34	0.35
	z_2	11.47	11.84	11.74	11.48	11.63	11.92	12.38	12.97	12.96	12.99
	r_1	13.54	14.61	15.33	15.97	16.69	17.41	18.10	18.87	19.35	19.80
Algorithm (ii)	F_1 [dB]	-10.12	-12.51	-13.63	-14.47	-15.67	-16.97	-17.95	-17.67	-18.49	-19.35
	F_2 [mm^3]	5393	7377	9337	10461	13246	15226	17209	19125	21062	22839
	z_1	0.01	0.01	0.02	0.01	0.16	0.19	0.24	0.31	0.34	0.35
	z_2	12.76	12.77	12.75	12.76	12.76	12.76	12.76	12.97	12.97	12.99
	r_1	14.35	15.12	15.82	16.20	17.14	17.73	18.29	18.88	19.36	19.77
Algorithm (iii)	F_1 [dB]	-10.19	-12.43	-13.63	-14.91	-15.77	-16.89	-17.91	-17.66	-18.58	-19.37
	F_2 [mm^3]	5243	7244	9211	11184	13154	15142	17084	19107	21249	22883
	z_1	0.02	0.01	0.02	0.07	0.16	0.20	0.23	0.31	0.35	0.35
	z_2	12.62	12.37	12.43	12.25	12.25	12.25	12.64	12.97	12.96	12.99
	r_1	14.21	14.86	15.62	16.25	16.91	17.52	18.21	18.87	19.40	19.79
Algorithm (iv)	F_1 [dB]	-10.06	-12.26	-13.34	-14.38	-15.52	-16.72	-17.91	-17.66	-18.47	-19.36
	F_2 [mm^3]	5163	7089	9186	11133	13051	14993	17164	19063	21040	22394
	z_1	-0.04	0.01	0.06	0.10	0.16	0.19	0.23	0.31	0.34	0.35
	z_2	12.72	12.75	12.79	12.82	12.84	12.87	12.89	12.95	12.95	12.97
	r_1	14.21	15.00	15.80	16.48	17.12	17.70	18.32	18.85	19.35	19.67

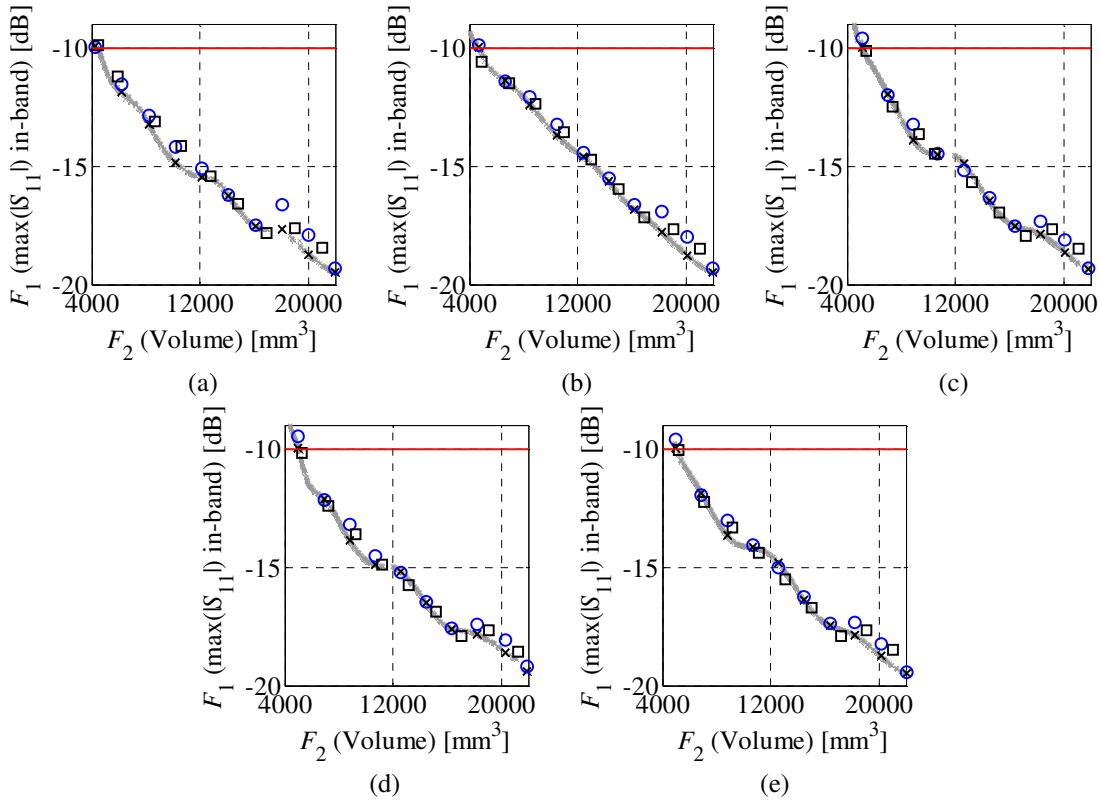


Figure 4.26: Response-correction-based refinement of the selected Pareto designs obtained within: (a) X_I ; and the following reduced regions of the search space: (b) X_D (algorithm (i)); (c) X_S (algorithm (ii)); (d) X_{SR} (algorithm (iii)); and (e) X_R (algorithm (iv)). Gray and black crosses denote the initial Pareto set and the selected Pareto designs, respectively. The blue circles and black squares are the \mathbf{R}_f model responses before and after the refinement, respectively. Note that even before the refinement step, the low- and high-fidelity model responses are similar which indicates their good correlation.

TABLE 4.6: CO-KRIGING-BASED REFINEMENT – SELECTED ANTENNA DESIGNS

		Selected Pareto-optimal designs									
		$x_f^{(1)}$	$x_f^{(2)}$	$x_f^{(3)}$	$x_f^{(4)}$	$x_f^{(5)}$	$x_f^{(6)}$	$x_f^{(7)}$	$x_f^{(8)}$	$x_f^{(9)}$	$x_f^{(10)}$
Initial Space X_I	F_1 [dB]	-10.09	-11.57	-12.81	-14.14	-15.04	-16.51	-17.67	-17.83	-18.59	-19.47
	F_2 [mm^3]	4053	6048	8034	10021	12044	14016	16000	18028	20037	21672
	z_1	0.11	0.03	0.02	0.02	0.15	0.14	0.18	0.22	0.25	0.29
	z_2	11.53	11.93	12.17	11.90	12.12	12.62	12.60	12.93	13.39	13.27
	r_1	13.07	14.14	15.06	15.68	16.51	17.31	17.88	18.55	19.23	19.58
Algorithm (i)	F_1 [dB]	-9.98	-11.32	-12.01	-13.16	-14.30	-15.54	-16.67	-17.07	-17.84	-18.99
	F_2 [mm^3]	4487	6440	8310	10324	12252	14242	16160	18093	20037	22002
	z_1	0.34	0.32	0.31	0.31	0.31	0.31	0.31	0.31	0.33	0.35
	z_2	11.55	11.96	11.55	11.55	12.25	12.39	12.48	12.75	13.39	13.27
	r_1	13.42	14.48	15.02	15.77	16.69	17.35	17.93	18.54	19.25	19.68
Algorithm (ii)	F_1 [dB]	-9.89	-12.17	-13.31	-14.59	-15.77	-16.59	-17.59	-18.21	-18.79	-19.25
	F_2 [mm^3]	5351	7219	9025	10894	12759	14613	16361	18362	20145	21956
	z_1	0.05	0.06	0.04	0.05	0.06	0.10	0.16	0.20	0.26	0.25
	z_2	12.81	12.77	12.79	12.79	12.78	12.78	12.78	12.78	12.97	12.97
	r_1	14.39	15.08	15.74	16.37	16.96	17.53	18.04	18.58	19.11	19.54
Algorithm (iii)	F_1 [dB]	-9.94	-12.16	-13.30	-14.64	-15.88	-16.05	-17.69	-18.19	-18.91	-19.47
	F_2 [mm^3]	5382	7219	9040	10900	12785	14612	16381	18395	20159	21923
	z_1	0.03	0.04	0.05	0.04	0.07	0.24	0.20	0.20	0.23	0.29
	z_2	12.82	12.82	12.79	12.80	12.80	12.85	12.77	12.96	12.96	12.95
	r_1	14.40	15.10	15.75	16.37	16.98	17.61	18.06	18.65	19.10	19.53
Algorithm (iv)	F_1 [dB]	-10.00	-12.22	-13.17	-14.17	-15.37	-16.55	-17.68	-17.85	-18.75	-19.44
	F_2 [mm^3]	5280	7148	8973	10866	12689	14571	16415	18271	20129	21863
	z_1	0.01	0.03	0.06	0.10	0.14	0.17	0.20	0.23	0.26	0.29
	z_2	12.77	12.77	12.80	12.83	12.84	12.88	12.90	12.92	12.99	12.99
	r_1	14.31	15.04	15.73	16.40	17.00	17.58	18.11	18.62	19.11	19.53

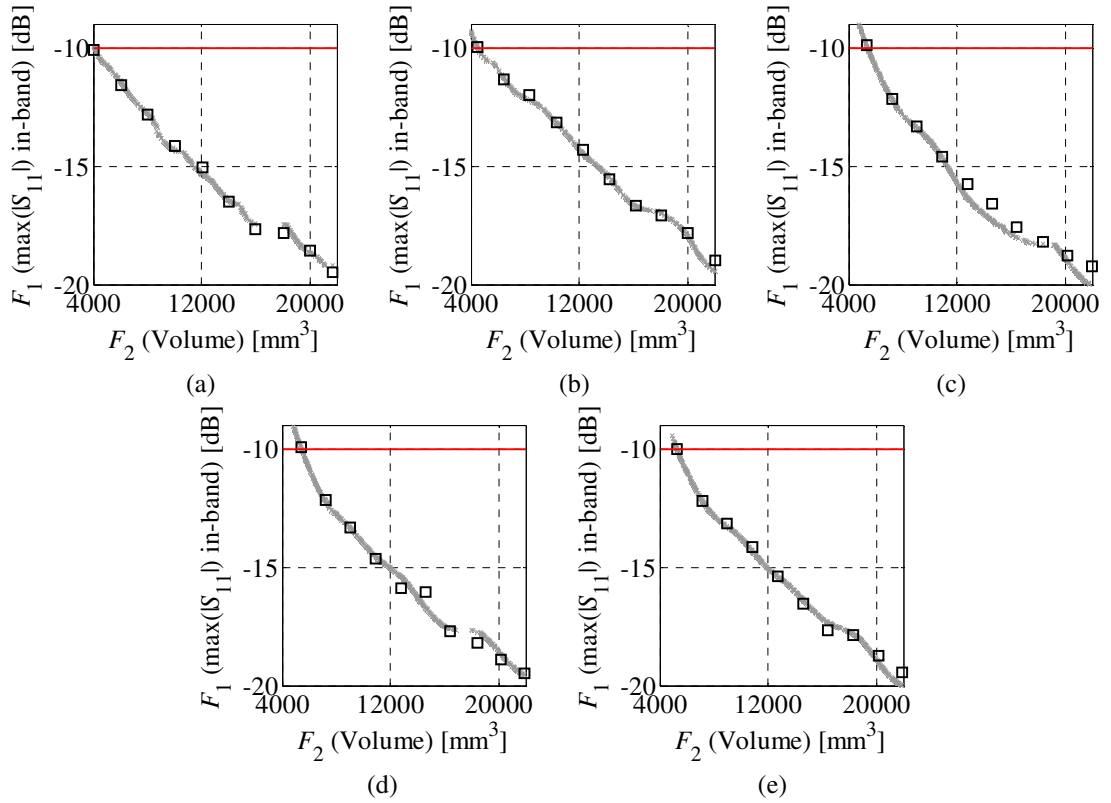


Figure 4.27: Co-kriging-based refinement of the initial Pareto sets in: (a) X_I ; and the reduced regions of the search space obtained using the following algorithms: (b) (i); (c) (ii); (d) (iii); and (e) (iv). Gray and black crosses represent the initial Pareto sets and the high-fidelity designs evaluated for verification.

4.5.2.5 Optimization Algorithm – Computational Cost

A detailed cost breakdown of the optimization process is provided in Table 4.7. The obtained results indicate that the compared reduction algorithms exhibit different performance in terms of the required number of R_c simulations. The total aggregated cost of antenna optimization within the initial space X_I corresponds to ~ 44.3 evaluations of the R_f model which is approximately 17 hours of CPU-time. Depending on the selected reduction algorithm, the CPU-time of optimization varies from 13.9 hours (about 36.2 R_f simulations) for the algorithm (iv) to 17.7 hours (approximately 46.1 R_f simulations) for the algorithm (iii). For the considered antenna, the computational savings resulting from optimization in reduced space are up to 20% with respect to X_I .

Based on the statistical analysis of MOEA (cf. Appendix A1), multi-objective optimization of the considered antenna require at least few thousands of model evaluations (which is an optimistic estimate). Assuming that the maximum number of MOEA simulations is limited to 5000 (the lowest number considered in Appendix A1), the estimated cost of direct R_c model optimization within X_I corresponds to 46 hours of CPU-time. At the same time, direct MOEA optimization of the high-fidelity model would require almost 80 days of the CPU-time.

It should be noted that the use of algorithm (iii) increased the overall optimization cost. The reason is that the method involves evaluations of the high-fidelity model. However, the geometry of considered antenna is described using only three parameters. It has been shown in the following sections that application of (iii) for space reduction of higher dimensional problems reduces the cost of multi-objective optimization as compared to direct optimization in X_I .

4.5.3 UWB Dipole – Design and Optimization Setup

The second benchmark structure is a uniplanar UWB dipole antenna shown in Figure 4.28. The structure consists of the tapered driven element and two rectangular parasitic strips [212]. The design is fed through a 50 ohm discrete port. The structure is implemented on a 1.58 mm thick

Rogers RT5880 dielectric substrate ($\epsilon_r = 2.2$, $\tan\delta = 0.0009$). The design variables are $\mathbf{x} = [l_0 \ w_0 \ a_0 \ l_p \ w_p \ s_0]^T$. Parameters $a_1 = 0.5$ and $w_1 = 0.5$ remain fixed (all dimensions are in mm). The initial design space X_I is defined using $\mathbf{l} = [10 \ 5 \ 0.5 \ 10 \ 1 \ 0.1]^T$ and $\mathbf{u} = [20 \ 15 \ 1 \ 15 \ 10 \ 1]^T$.

Mesh densities of the low- and high-fidelity antenna models are selected based on engineering experience (cf. Section 4.5.1). Designs utilized for discretization tests are: $\mathbf{x}_{r1} = [11.4 \ 23.3 \ 21 \ 4.5 \ 4.8 \ 10.2 \ 13.3 \ 39.5 \ 0.6]^T$ and $\mathbf{x}_{r2} = [9.1 \ 23.9 \ 21.7 \ 6.8 \ 3.1 \ 9.1 \ 8.4 \ 20.6 \ 1.3]^T$. The model \mathbf{R}_f is contains $\sim 12,500,000$ hexahedral cells and its average simulation time is 20 min. \mathbf{R}_c consists of $\sim 200,000$ cells. The low-fidelity model is also simplified by reducing its computational domain, representing metallization as perfect electrical conductor and neglecting dielectric losses. A typical simulation time of \mathbf{R}_c is 38 s (32 times faster than \mathbf{R}_f). The cross-section visualization of both antenna models with selected discretization levels are illustrated in Figure 4.29, whereas the antenna responses for the test designs at both levels of fidelity are shown in Figure 4.30.

The design objectives are the same as in Section 4.5.2. The antenna footprint (objective F_2) is defined as $V(\mathbf{x}) = w_s \times l_s$ where $w_s = 2w_p + 2s_0 + w_0$ and $l_s = 2l_0 + a_1$ (see Figure 4.28).

4.5.3.1 Design Space Reduction

Description of the space reduction algorithms setup can be found in Section 4.5.2.1. The bounds of the reduced regions X_D , X_S and X_{S_r} obtained using algorithms (i), (ii) and (iii) are: $\mathbf{l}^{(i)} = [14 \ 7.5 \ 0.65 \ 10.01 \ 1.75 \ 1.05]^T$ and $\mathbf{u}^{(i)} = [19.5 \ 14.8 \ 1 \ 12.9 \ 7.9 \ 1.45]^T$; $\mathbf{l}^{(ii)} = [17.09 \ 9.1 \ 0.53 \ 11.78 \ 4.3 \ 1.02]^T$ and $\mathbf{u}^{(ii)} = [17.73 \ 13.9 \ 0.73 \ 11.95 \ 6.4 \ 1.42]^T$; and $\mathbf{l}^{(iii)} = [16.97 \ 9.08 \ 0.53 \ 11.71 \ 4.3 \ 1.02]^T$ and $\mathbf{u}^{(iii)} = [17.77 \ 13.9 \ 0.73 \ 12.01 \ 6.4 \ 1.42]^T$, respectively. The volume-wise space reduction ratios χ of X_D , X_S and X_{S_r} with respect to X_I are 43, $5 \cdot 10^4$ and $2.2 \cdot 10^4$, respectively. Note that the search space obtained using (iii) is larger than X_S . The reduction rate of the rotated space X_R space determined using (iv) is $\chi = 1.1 \cdot 10^7$. The key parameters of the reduced regions of the space, including detailed dimensions of the extreme Pareto designs, are gathered in Table 4.8. The frequency characteristics of the extreme solutions are shown in Figure 4.31.

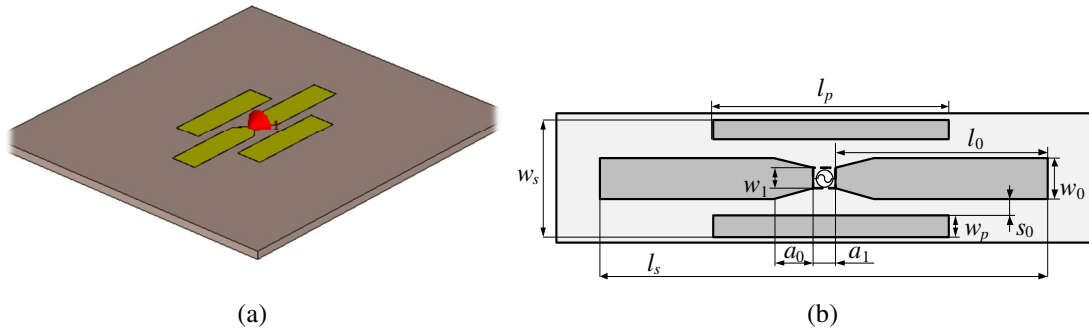


Figure 4.28: A uniplanar UWB dipole antenna [212]: (a) 3D visualization; (b) geometry with highlighted geometrical parameters.

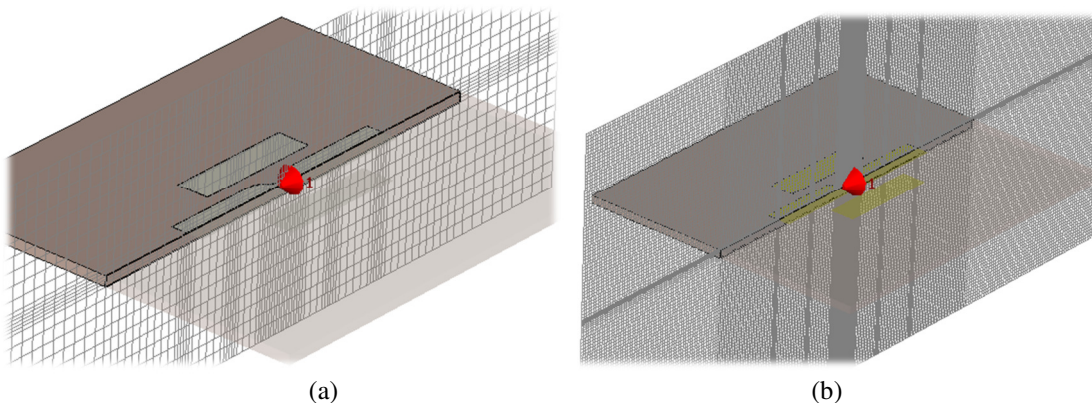


Figure 4.29: Cross-section view of the uniplanar UWB dipole antenna: (a) the low-fidelity model; (b) the high-fidelity model.

TABLE 4.7: COST BREAKDOWN OF MULTI-OBJECTIVE ANTENNA OPTIMIZATION

Algorithm Step	Selected Design Space Reduction Algorithm									
	Initial Space X_I		Algorithm (i)		Algorithm (ii)		Algorithm (iii)		Algorithm (iv)	
	Sim. Cost	Total [h]	Sim. Cost	Total [h]	Sim. Cost	Total [h]	Sim. Cost	Total [h]	Sim. Cost	Total [h]
Design Space Reduction	—	—	R_c 148	1.36	R_c 256	2.35	R_c 465	4.26	R_c 256	2.21
Data Acquisition and RSA construction	R_c 600	5.50	R_c 160	1.47	R_c 30	0.28	R_c 40	0.37	R_c 20	0.18
MOEA Optimization	R_s 25000	N/A	R_s 25000	N/A	R_s 25000	N/A	R_s 25000	N/A	R_s 25000	N/A
Refinement Using Response Correction [#]	R_s 1700	N/A	R_s 1930	N/A	R_s 1640	N/A	R_s 1870	N/A	R_s 1960	N/A
Refinement Using Co-Kriging [#]	R_s 50000	N/A	R_s 50000	N/A	R_s 50000	N/A	R_s 50000	N/A	R_s 50000	N/A
Total cost [†]	R_f ~44.3	17.0	R_f ~37.3	14.3	R_f ~38.9	14.1	R_f ~46.1	17.7	R_f ~36.2	13.9

[#]The refinement procedure is carried out using either response correction or co-kriging

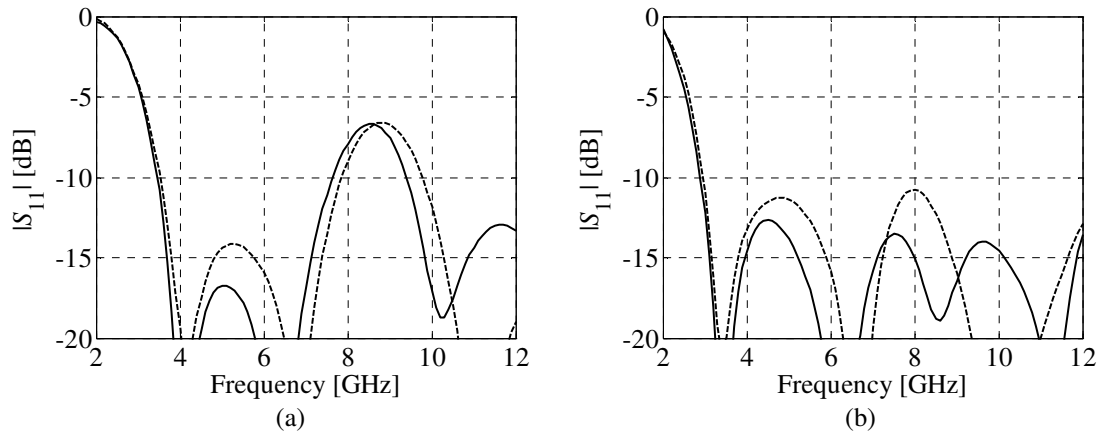
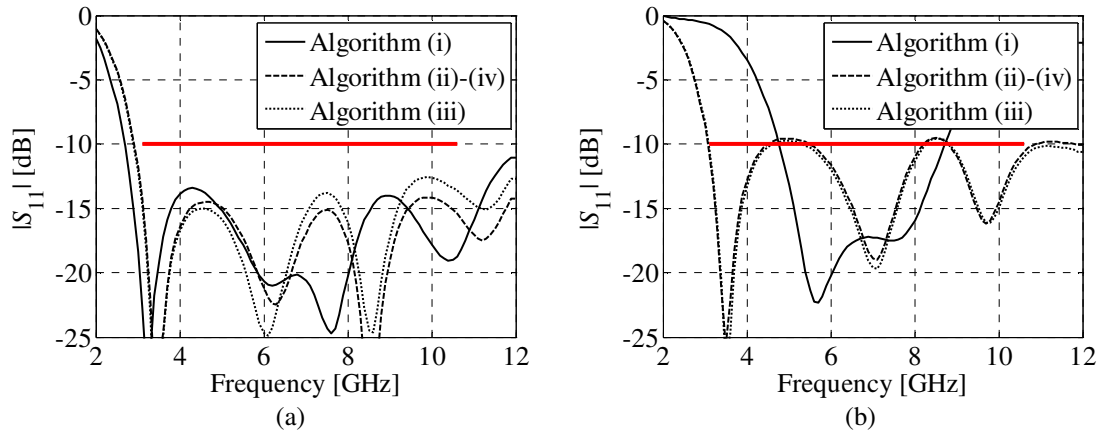
[†]Total cost of multi-objective design optimization includes only one refinement procedure

Figure 4.30: The high- (—) and the low-fidelity (---) model responses of UWB dipole for selected sets of parameters: (a) design x_{11} ; and (b) design x_{12} .

Figure 4.31: Reflection characteristics of the extreme Pareto designs obtained using routines (i)-(iv): (a) $x_c^{(1)}$ – optimal w.r.t. objective F_1 ; and (b) $x_c^{(2)}$ – optimal w.r.t. objective F_2 . The high-fidelity model response of (iii) is denoted by (····). Note large variability of shapes of structure responses.

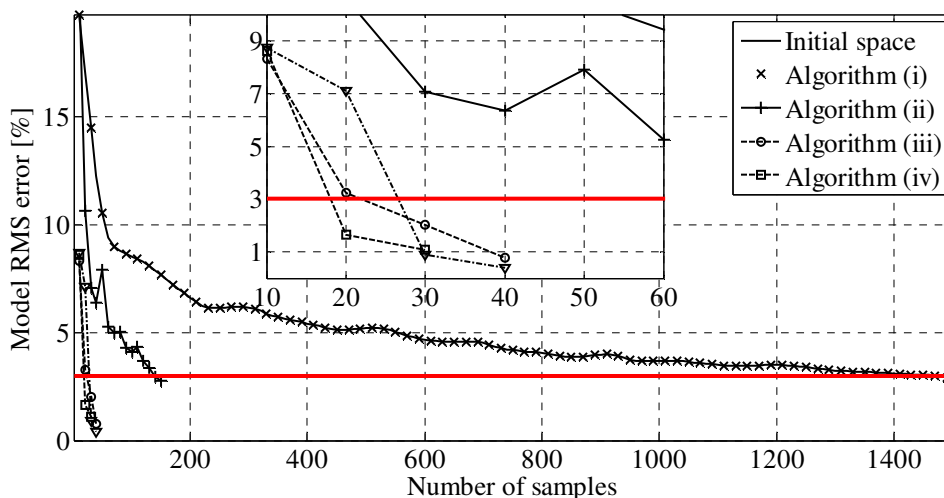
TABLE 4.8: COMPARISON OF THE ALGORITHMS – DESIGN SPACE REDUCTION

Reduction Method	Dimensions of Corner Designs							Size of the Search Space [mm ⁶]	Space Reduction Ratio χ
	Design	l_0	w_0	a_0	l_p	w_p	s_0		
Initial space X_I	—	—	—	—	—	—	—	4275	—
Algorithm (i)	$\mathbf{x}_c^{(1)}$	19.50	14.8	0.65	12.90	7.90	1.45	99.2	43.1
	$\mathbf{x}_c^{(2)}$	14.00	7.50	1.00	10.01	1.75	1.05		
Algorithm (ii)	$\mathbf{x}_c^{(1)}$	17.73	13.9	0.73	11.95	6.40	1.42	$8.66 \cdot 10^{-2}$	$4.94 \cdot 10^4$
	$\mathbf{x}_c^{(2)}$	17.09	9.10	0.53	11.78	4.30	1.02		
Algorithm (iii)	$\mathbf{x}_c^{(1)}$	17.73	13.9	0.73	11.95	6.40	1.42	$1.97 \cdot 10^{-1}$	$2.18 \cdot 10^4$
	$\mathbf{x}_c^{(2)}$	17.09	9.10	0.53	11.78	4.30	1.02		
	$\mathbf{x}_f^{(1)}$	17.77	13.9	0.73	12.01	6.40	1.41		
Algorithm (iv)	$\mathbf{x}_c^{(1)}$	17.73	13.9	0.73	11.95	6.40	1.42	$3.94 \cdot 10^{-4}$	$1.09 \cdot 10^7$
	$\mathbf{x}_c^{(2)}$	17.09	9.10	0.53	11.78	4.30	1.02		

Detailed data on design space reduction cost of the considered dipole antenna is gathered in Table 4.9. The results indicate that the CPU-time of algorithm (i) is about 3.5 hours (a total of 335 \mathbf{R}_c model simulations). At the same time, the space reduction performed using algorithms (ii) and (iv) involved 386 \mathbf{R}_c simulations (about 4 hours). The computational cost of (iii) is the highest among compared algorithms (almost 7.5 hours), since it required 583 \mathbf{R}_c model and 4 \mathbf{R}_f simulations, respectively.

4.5.3.2 Data Acquisition

Setup of the data acquisition step is the same as in Section 4.5.2.2. Table 4.10 gathers key information about the process. The obtained results indicate that the number of samples required for identification of the accurate RSA model can be quite limited when carried out in the reduced space. Identification of the surrogate within X_I involved 1500 simulations of the \mathbf{R}_c model to achieve required RMS error. Identification of the RSA in X_D (algorithm (i)) required 150 samples (10 times less as compared to X_I). At the same time, only 30 \mathbf{R}_c samples have been used for a construction of accurate RSA within X_{Rr} (algorithm (iii)). Finally, a total of 40 training samples have been exploited for a construction of surrogates within X_S (algorithm (ii)) and X_R (algorithm (iv)). It should be noted that RMS errors of the models generated in the space regions obtained by (ii)-(iv) are notably lower than the required 3%. Moreover, the average minimum distances between the samples from (ii)-(iv) are over 3 times lower than those obtained in X_I and X_D . The convergence plots for obtained RSA models are shown in Figure 4.32.


Figure 4.32: Cross-validation-based convergence plots of RSA models obtained in initial and reduced regions of the search space.

4.5.3.3 MOEA Optimization

The results of MOEA optimization for $I = 50$ and $N = 500$ (see Appendix A1) performed within each selected region of the design space are provided in Figure 4.33. The key data on the obtained Pareto sets is gathered in Table 4.11. The results indicate that a large part of the Pareto sets from X_I and X_D violate requirement concerning acceptable in-band reflection (maximum value of $F_1(\mathbf{x})$ in X_I and X_D is -2 dB and -5.3 dB, respectively). The obtained Pareto front representations are similar for $F_2(\mathbf{x}) > 750$ mm². For smaller footprints, the slope of the sets obtained within space regions determined by algorithms (ii)-(iv) increases, so that their minimal sizes for $F_1(\mathbf{x})$ below -10 dB are around 720 mm². Slight discrepancy between the Pareto sets for $F_2(\mathbf{x}) \leq 720$ mm² suggests that the single-objective optimization algorithm utilized to minimize $F_2(\mathbf{x})$ has reached the local minimum (cf. Section 4.3.2). The largest changes of responses with respect to $F_1(\mathbf{x})$ and $F_2(\mathbf{x})$ along the compared Pareto fronts are obtained in X_R (algorithm (iv)) and X_I , respectively. The discrepancies between the obtained Pareto sets (expressed as the average distance with respect to selected design objective $dIS(F_k)$) are acceptable. The computational cost of MOEA is negligible compared to overall cost of design optimization (cf. Section 4.5.2.3).

TABLE 4.9: COMPUTATIONAL COST OF CONSIDERED SPACE REDUCTION ALGORITHMS

Reduction method	Number of Algorithm Evaluations		Total Number of Evaluations		CPU-time					
					Absolute [min]	Relative to R_f	$\Sigma [R_f]$	$\Sigma [h]$		
Algorithm (i)	Stage 1	$F_1(\mathbf{x})$: 130 R_c	335	R_c	82.3	4.12	10.6	3.54		
	Stage 2	$F_1(\mathbf{x})$: 103 R_c			65.2	3.26				
		$F_2(\mathbf{x})$: 102 R_c			64.6	3.23				
Algorithm (ii)		$F_1(\mathbf{x})$: 181 R_c	386	R_c	114.6	5.73	12.2	4.07		
		$F_2(\mathbf{x})$: 205 R_c			129.8	6.49				
Algorithm (iii)	Step 1 [†]	$F_1(\mathbf{x})$: 181 R_c	583	R_c	114.6	5.73	22.5	7.48		
		$F_2(\mathbf{x})$: 205 R_c			129.8	6.49				
	Step 2 [#]	$F_1(\mathbf{x})$: 87 R_c			4	R_f			55.1	2.75
		2 R_f							40	2
		$F_2(\mathbf{x})$: 110 R_c							69.7	3.48
	2 R_f			40	2					
Algorithm (iv)		$F_1(\mathbf{x})$: 181 R_c	386	R_c	244.5	5.73	12.2	4.07		
		$F_2(\mathbf{x})$: 205 R_c			6.49					

[†] Initial design space reduction (cf. Section 4.3.2)

[#] Refinement of R_c extreme points using SBO

TABLE 4.10: DATA ACQUISITION – KEY INFORMATION

Selected Solution Space	Number of Training Samples	RMS Error of the RSA Model [%]	Average Minimal Distance Between Samples	Training Set Size Reduction Ratio
Initial space X_I	1500	2.83	1.08	—
Algorithm (i)	150	2.74	0.97	10
Algorithm (ii)	40	0.77	0.25	37.5
Algorithm (iii)	30	1.10	0.29	50
Algorithm (iv)	40	0.38	0.12	37.5

TABLE 4.11: KEY DATA ON OBTAINED PARETO SETS

Selected Reduction Method	Objective F_1				Objective F_2				
	$\min(F_1)$	$\max(F_1)$	$\Delta(F_1)$	$dIS(F_1)$	$\min(F_2)$	$\max(F_2)$	$\Delta(F_2)$	$\Delta(F_2)$	$dIS(F_2)$
	[dB]	[dB]	[dB]	[dB]	[mm ²]	[mm ²]	[mm ²]	[%]	[mm ²]
Initial Space X_I	-14.0	-10.1	3.9	—	644	1036	392	37.8	—
Algorithm (i)	-13.8	-10.0	3.8	0.24	672	1039	367	35.3	31
Algorithm (ii)	-13.9	-10.0	3.9	0.25	724	1004	280	27.9	44
Algorithm (iii)	-13.7	-10.0	3.7	0.19	718	999	281	28.1	26
Algorithm (iv)	-14.1	-10.0	4.1	0.26	715	1042	327	31.4	62

4.5.3.4 Pareto Set Refinement

The first considered technique is response correction. The samples have been evenly selected along the regions of interest of the obtained initial Pareto sets. For each design, the algorithm has been terminated after three iterations. A comparison of the low- and high-fidelity Pareto-optimal designs is shown in Figure 4.34, whereas detailed data on their dimensions is gathered in Table 4.12. The results of the refinement process are similar in all cases. It should be noted that small discrepancies between the \mathbf{R}_f and \mathbf{R}_s model samples indicate that the RSA model is a good representation of the high-fidelity one.

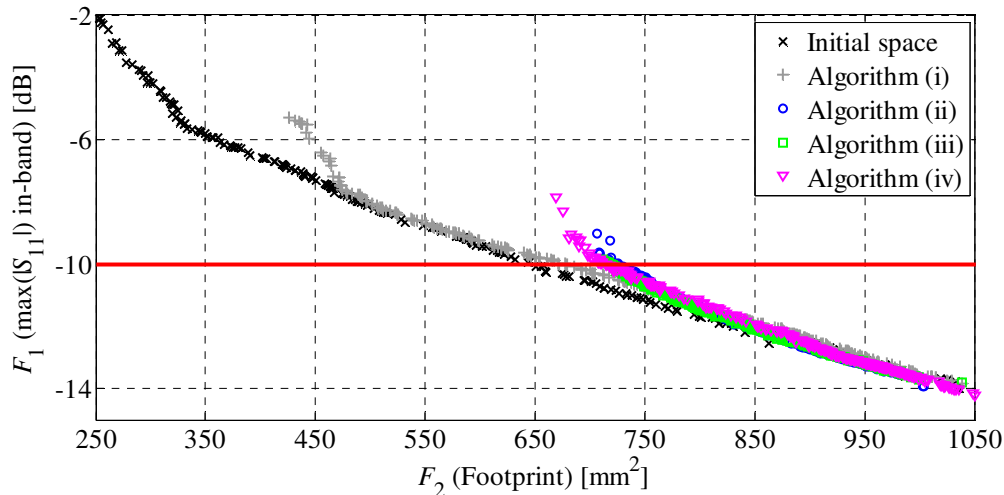


Figure 4.33: Comparison of the Pareto sets obtained within initial and refined search spaces.

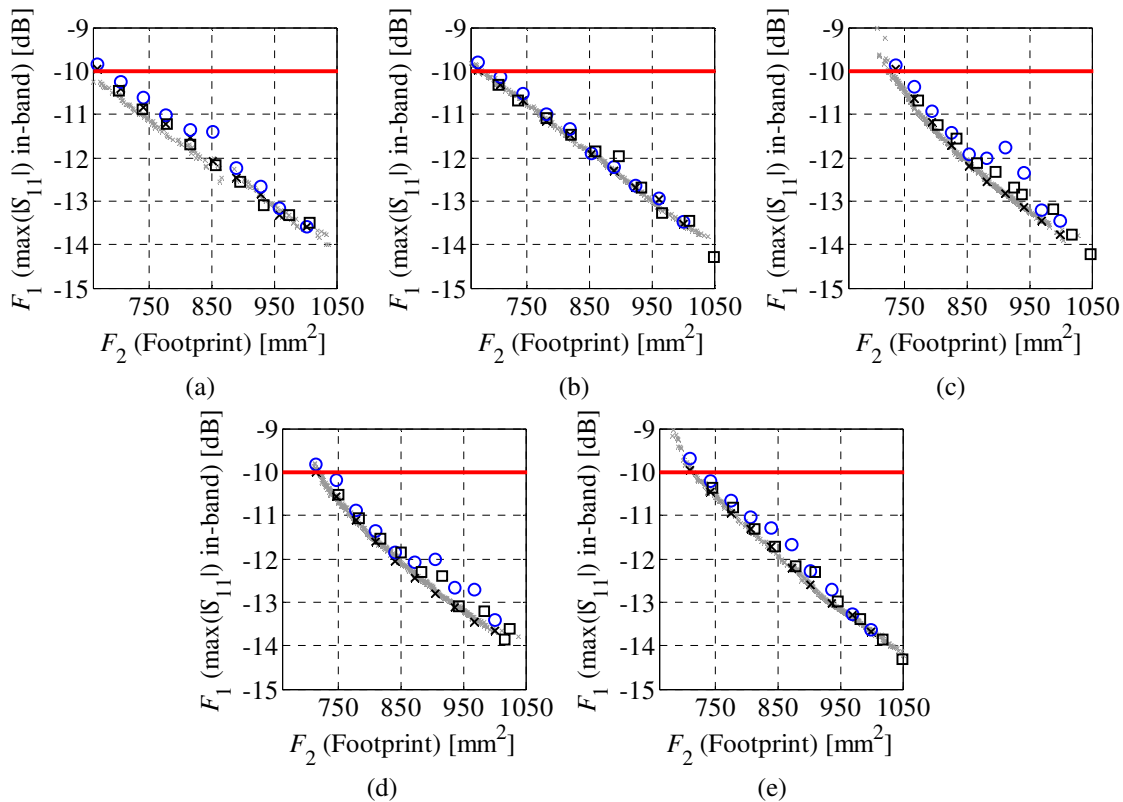


Figure 4.34: Response-correction-based refinement of the selected Pareto designs obtained in: (a) X_l , and the following reduced regions of the search space: (b) X_D – algorithm (i); (c) X_S – algorithm (ii); (d) X_{S_r} – algorithm (iii) and (e) X_R – algorithm (iv). Gray and black crosses denote the initial Pareto set and surrogate model designs selected for refinement. Blue circles and black squares represent the high-fidelity model responses before and after refinement, respectively.

The co-kriging refinement also exploits ten designs per iteration. Each time they are evenly selected along the Pareto sets. Figure 4.35 shows a comparison of the refined Pareto fronts with high-fidelity designs evaluated for verification purposes. The results are in a very good agreement. The geometrical details of the selected high-fidelity model designs are gathered in Table 4.13. It should be noted that despite utilization of different refinement schemes, the antenna parameters from Table 4.12 and Table 4.13 are similar. Also, the response correction and co-kriging techniques are comparable in terms of the computational cost.

4.5.3.5 Optimization Algorithm – Computational Cost

A detailed cost breakdown of the multi-objective design optimization procedure is provided in Table 4.14. An aggregated cost of the algorithm operation within X_I corresponds to about 77.5 R_f model evaluations (almost 26 hours of the CPU-time). At the same time, the cost of design optimization in the reduced regions of the search space varies from 14.5 hours (about 43.5 R_f simulations) to 17.8 hours (~53.4 R_f evaluations). It should be noted that, for the considered antenna structure, utilization of algorithms (ii) and (iv) allow for reducing the optimization cost by almost 44% compared to X_I . The estimated cost of direct MOEA optimization using EM antenna models and assuming 5000 evaluations (cf. Appendix A1) is 53 hours or 70 days for low- and high-fidelity model, respectively.

4.5.4 UWB Monopole – Design and Optimization Setup

The last benchmark design is a nine-variable UWB monopole antenna shown in Figure 4.36. The structure is composed of two trapezoids and a rectangle, stacked together into a radiator [157]. The antenna is fed through a 50 ohm microstrip line and it is implemented on a 0.762 thick Taconic RF-35 substrate ($\epsilon_r = 3.5$, $\tan\delta = 0.0018$). The vector of design parameters is $\mathbf{x} = [a_1 \ a_2 \ a_3 \ b_1 \ b_2 \ b_3 \ l \ w \ d]^T$, whereas variables $w_0 = 1.7$ and $o = 5$ remain fixed (all dimensions are in mm). The initial design X_I is defined using the following bounds: $\mathbf{l} = [7.5 \ 20 \ 21 \ 4 \ 3 \ 8 \ 8 \ 18.5 \ 0.5]^T$ and $\mathbf{u} = [11.5 \ 26 \ 25 \ 8 \ 7 \ 12 \ 16 \ 40.5 \ 1.5]^T$.

TABLE 4.12: DIPOLE ANTENNA – RESPONSE CORRECTION

		Selected Pareto-optimal designs							
		F_1 [dB]	F_2 [mm ²]	l_0	w_0	a_0	l_p	w_p	s_0
Initial Space X_I	$\mathbf{x}_f^{(2)}$	-10.88	739	16.66	10.97	0.77	11.04	4.03	1.42
	$\mathbf{x}_f^{(4)}$	-11.70	816	16.87	11.95	0.82	11.23	4.46	1.48
	$\mathbf{x}_f^{(6)}$	-12.55	895	17.20	12.75	0.70	11.64	4.87	1.58
	$\mathbf{x}_f^{(8)}$	-13.31	974	17.56	13.44	0.64	12.00	5.51	1.45
	$\mathbf{x}_f^{(10)}$	-14.05	1052	17.84	13.45	0.72	12.25	6.55	1.28
Algorithm (i)	$\mathbf{x}_f^{(2)}$	-10.67	736	16.56	10.81	0.83	10.71	4.19	1.35
	$\mathbf{x}_f^{(4)}$	-11.46	821	16.73	11.81	0.94	10.89	4.74	1.43
	$\mathbf{x}_f^{(6)}$	-11.96	897	17.20	12.66	0.75	11.16	5.21	1.31
	$\mathbf{x}_f^{(8)}$	-13.28	967	17.26	13.19	0.85	11.23	5.77	1.44
	$\mathbf{x}_f^{(10)}$	-14.30	1050	17.72	14.09	0.72	11.79	6.12	1.45
Algorithm (ii)	$\mathbf{x}_f^{(2)}$	-11.23	803	17.18	10.63	0.54	11.95	5.06	1.15
	$\mathbf{x}_f^{(4)}$	-12.12	866	17.28	11.44	0.58	11.78	5.44	1.19
	$\mathbf{x}_f^{(6)}$	-12.69	926	17.43	12.27	0.59	11.76	5.70	1.26
	$\mathbf{x}_f^{(8)}$	-13.19	988	17.60	12.92	0.74	11.90	6.10	1.28
	$\mathbf{x}_f^{(10)}$	-14.21	1048	17.73	13.90	0.71	11.81	6.25	1.37
Algorithm (iii)	$\mathbf{x}_f^{(2)}$	-11.07	783	17.05	10.44	0.57	11.80	4.90	1.20
	$\mathbf{x}_f^{(4)}$	-11.86	851	17.21	11.22	0.57	11.90	5.31	1.27
	$\mathbf{x}_f^{(6)}$	-12.40	916	17.31	12.50	0.65	11.43	5.50	1.30
	$\mathbf{x}_f^{(8)}$	-13.21	983	17.57	13.32	0.72	11.79	5.77	1.36
	$\mathbf{x}_f^{(10)}$	-13.61	1024	17.70	13.74	0.70	11.89	6.08	1.32
Algorithm (iv)	$\mathbf{x}_f^{(2)}$	-10.82	778	17.16	10.28	0.58	11.83	4.86	1.18
	$\mathbf{x}_f^{(4)}$	-11.71	845	17.28	11.13	0.60	11.87	5.24	1.26
	$\mathbf{x}_f^{(6)}$	-12.30	909	17.45	11.81	0.65	11.91	5.68	1.26
	$\mathbf{x}_f^{(8)}$	-13.38	982	17.63	13.06	0.66	11.90	5.96	1.25
	$\mathbf{x}_f^{(10)}$	-14.31	1049	17.72	13.80	0.75	11.91	6.29	1.41

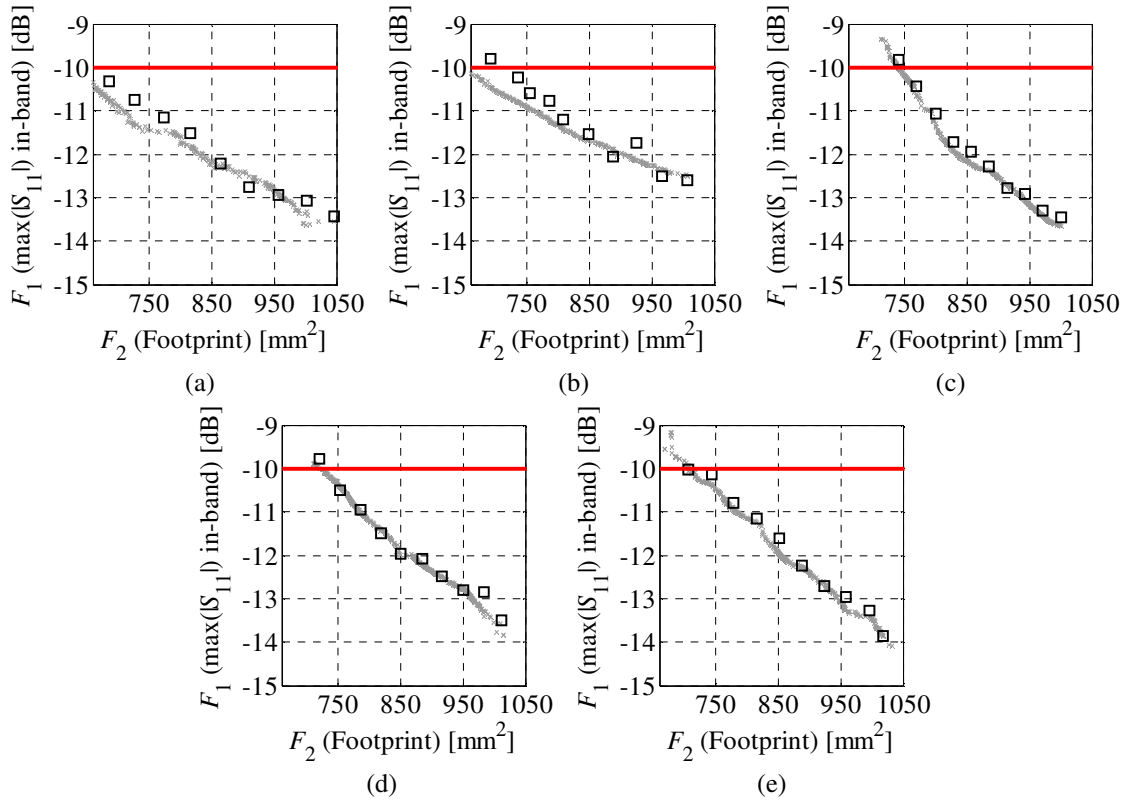


Figure 4.35: Refinement of the Pareto sets using co-kriging in: (a) X_i ; and the following regions of the search space (b) X_D ; (c) X_S ; (d) X_{S_r} and (e) X_R . Gray crosses and black squares represent \mathbf{R}_f Pareto set and \mathbf{R}_f designs evaluated for verification.

TABLE 4.13: DIPOLE ANTENNA – CO-KRIGING REFINEMENT

		Selected Pareto-optimal designs							
		F_1 [dB]	F_2 [mm ²]	l_0	w_0	a_0	l_p	w_p	s_0
Initial Space X_f	$\mathbf{x}_f^{(2)}$	-10.32	686	16.55	11.04	0.66	10.84	3.13	1.56
	$\mathbf{x}_f^{(4)}$	-11.15	774	16.82	11.87	0.70	11.19	3.82	1.57
	$\mathbf{x}_f^{(6)}$	-12.21	864	17.25	12.51	0.63	11.59	4.49	1.60
	$\mathbf{x}_f^{(8)}$	-12.95	956	17.41	12.95	0.65	11.47	5.54	1.52
	$\mathbf{x}_f^{(10)}$	-13.42	1046	17.91	13.32	0.63	12.51	6.28	1.47
Algorithm (i)	$\mathbf{x}_f^{(2)}$	-10.23	737	16.77	10.93	0.80	10.98	3.97	1.38
	$\mathbf{x}_f^{(4)}$	-10.78	786	16.81	11.23	0.76	11.03	4.64	1.26
	$\mathbf{x}_f^{(6)}$	-11.54	848	17.39	10.85	0.77	11.61	5.32	1.28
	$\mathbf{x}_f^{(8)}$	-11.74	926	17.44	11.48	0.79	11.63	5.84	1.28
	$\mathbf{x}_f^{(10)}$	-12.60	1006	17.59	12.00	0.79	11.65	6.34	1.29
Algorithm (ii)	$\mathbf{x}_f^{(2)}$	-10.43	769	17.23	9.90	0.57	11.85	4.87	1.17
	$\mathbf{x}_f^{(4)}$	-11.71	828	17.22	11.03	0.55	11.85	5.10	1.23
	$\mathbf{x}_f^{(6)}$	-12.28	884	17.37	11.69	0.55	11.87	5.50	1.20
	$\mathbf{x}_f^{(8)}$	-12.91	943	17.53	12.19	0.63	11.89	5.91	1.26
	$\mathbf{x}_f^{(10)}$	-13.45	1001	17.59	13.37	0.64	11.88	5.99	1.36
Algorithm (iii)	$\mathbf{x}_f^{(2)}$	-10.49	753	17.18	9.94	0.58	11.81	4.71	1.13
	$\mathbf{x}_f^{(4)}$	-11.50	819	17.27	11.04	0.56	11.84	4.91	1.26
	$\mathbf{x}_f^{(6)}$	-12.08	884	17.37	11.29	0.62	11.87	5.77	1.13
	$\mathbf{x}_f^{(8)}$	-12.81	950	17.44	12.28	0.70	11.86	6.07	1.22
	$\mathbf{x}_f^{(10)}$	-13.51	1012	17.65	13.39	0.64	11.88	6.05	1.40
Algorithm (iv)	$\mathbf{x}_f^{(2)}$	-10.14	743	17.11	9.91	0.55	11.81	4.68	1.07
	$\mathbf{x}_f^{(4)}$	-11.15	816	17.33	10.62	0.61	11.87	5.07	1.21
	$\mathbf{x}_f^{(6)}$	-12.25	887	17.36	11.76	0.63	11.89	5.48	1.24
	$\mathbf{x}_f^{(8)}$	-12.96	958	17.65	12.46	0.68	11.90	5.84	1.31
	$\mathbf{x}_f^{(10)}$	-13.87	1017	17.62	13.42	0.73	11.94	6.15	1.38

TABLE 4.14: COST BREAKDOWN OF MULTI-OBJECTIVE ANTENNA OPTIMIZATION

Algorithm Step	Selected Design Space Reduction Algorithm									
	Initial Space X_I		Algorithm (i)		Algorithm (ii)		Algorithm (iii)		Algorithm (iv)	
	Sim. Cost	Total [h]	Sim. Cost	Total [h]	Sim. Cost	Total [h]	Sim. Cost	Total [h]	Sim. Cost	Total [h]
Design Space Reduction	—	—	R_c 335	3.54	R_c 386	4.07	R_c 583	6.14	R_c 386	4.07
							R_f 4	1.33		
Data Acquisition and RSA construction	R_c 1500	15.83	R_c 150	1.58	R_c 40	0.42	R_c 30	0.32	R_c 40	0.42
MOEA Optimization	R_s 25000	N/A	R_s 25000	N/A	R_s 25000	N/A	R_s 25000	N/A	R_s 25000	N/A
Refinement Using Response Correction [#]	R_s 2882	N/A	R_s 2811	N/A	R_s 1916	N/A	R_s 2472	N/A	R_s 3367	N/A
	R_f 30	10	R_f 30	10	R_f 30	10	R_f 30	10	R_f 30	10
Refinement Using Co-Kriging [#]	R_s 50000	N/A	R_s 50000	N/A	R_s 50000	N/A	R_s 50000	N/A	R_s 50000	N/A
	R_f 30	10	R_f 30	10	R_f 30	10	R_f 30	10	R_f 30	10
Total cost [†]	R_f ~77.5	25.83	R_f ~45.4	15.12	R_f ~43.5	14.49	R_f ~53.4	17.79	R_f ~43.5	14.49

[#]The refinement procedure is carried out using either response correction or co-kriging

[†]Total cost of multi-objective design optimization includes only one refinement procedure

Discretization levels of the low- and high-fidelity models are determined based on visual inspection of the antenna responses for two test designs $\mathbf{x}_{t1} = [11.38 \ 23.28 \ 20.96 \ 4.49 \ 4.79 \ 10.22 \ 13.31 \ 39.49 \ 0.6]^T$ and $\mathbf{x}_{t2} = [9.07 \ 23.93 \ 21.68 \ 6.82 \ 3.12 \ 9.11 \ 8.37 \ 20.64 \ 1.3]^T$. The high-fidelity model R_f contains about 2,500,000 mesh cells and its typical simulation time is 15 min. The low-fidelity model R_c contains ~110,000 cells (47 s of the simulation time), so that it is 19 times faster than R_f . Other simplifications of R_c include representation of metal as perfect electric conductor (PEC) and utilization of lossless substrate. The reflection characteristics of the high- and low-fidelity model at the test designs are shown in Figure 4.37, whereas the cross-section view of mesh discretization densities are provided in Figure 4.38.

The antenna footprint (objective F_2) is defined as $V(\mathbf{x}) = A \times B$ ($A = \max\{a_1, a_2, a_3, w + o\}$ and $B = b_1 + b_2 + b_3 + l + d + o$).

4.5.4.1 Design Space Reduction

The setup of the compared space reduction algorithms is the same as in Section 4.5.2.1. The design space regions X_D , X_S and X_{S_r} determined using algorithms (i), (ii) and (iii) are described by the following bounds: $\mathbf{l}^{(i)} = [9.5 \ 21.1 \ 23 \ 5 \ 5 \ 8.4 \ 12 \ 18.5 \ 0.53]^T$ and $\mathbf{u}^{(i)} = [11.1 \ 23.4 \ 24.8 \ 5 \ 5 \ 9 \ 16 \ 37.5 \ 0.65]^T$; $\mathbf{l}^{(ii)} = [8.96 \ 21.05 \ 22.63 \ 4.54 \ 4.74 \ 8.74 \ 8.58 \ 20.02 \ 0.58]^T$ and $\mathbf{u}^{(ii)} = [10.92 \ 23.34 \ 24.1 \ 7.13 \ 5.64 \ 10.18 \ 13.31 \ 39.49 \ 0.6]^T$; and $\mathbf{l}^{(iii)} = [8.96 \ 21.05 \ 22.63 \ 4.54 \ 4.74 \ 8.14 \ 8.08 \ 19.02 \ 0.58]^T$ and $\mathbf{u}^{(iii)} = [10.92 \ 23.34 \ 24.1 \ 7.13 \ 5.64 \ 10.18 \ 14.31 \ 39.49 \ 0.85]^T$, respectively. The volume-wise space reduction with respect to X_I is four orders of magnitude for X_D and X_S , as well as three orders for X_{S_r} . At the same time, the search space region X_R determined using the algorithm (iv) is eight orders of magnitude smaller than X_I . It should be noted that dimensionality of the space X_D is reduced, i.e., variables $b_1 = 5$ and $b_2 = 5$ remain fixed along X_D . The key data concerning the reduced regions of the search space is gathered in Table 4.15. The frequency characteristics of the corner designs are shown in Figure 4.39.

A detailed cost breakdown of the space reduction step is provided in Table 4.16. The results indicate that the CPU-time of the algorithm (i) run is about 5.3 hours (a total of 402 R_c model simulations). At the same time, the space reduction using algorithms (ii) and (iv) involved 690 R_c simulations which is about 9 hours of CPU-time. As expected, the numerical cost of algorithm (iii) is the highest among the compared ones. It involves 1164 R_c and 4 R_f model simulations (~16 hours).

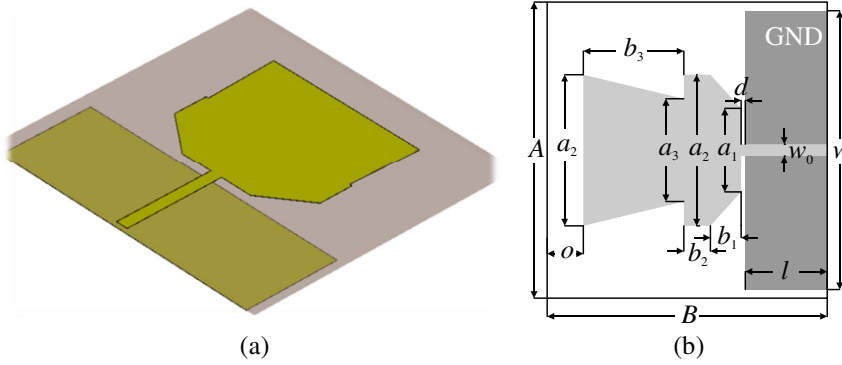


Figure 4.36: A planar UWB monopole [157]: (a) 3D view; (b) geometry with highlighted parameters.

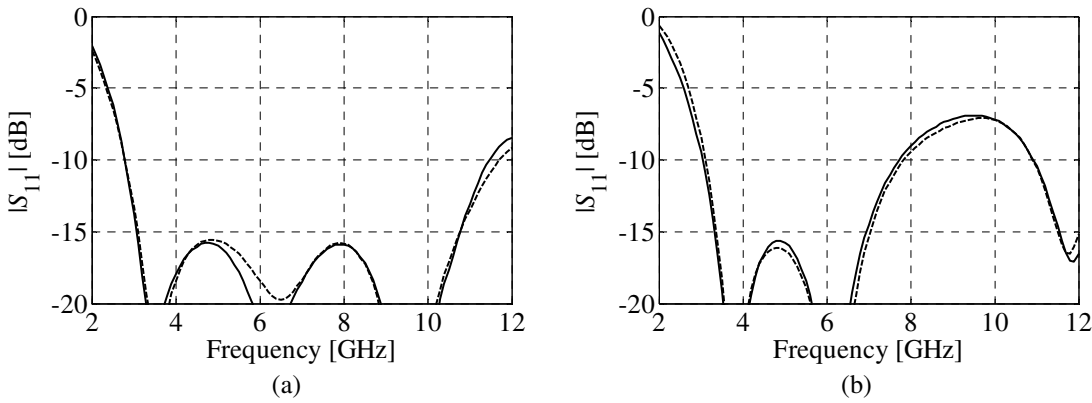


Figure 4.37: The high- (—) and low-fidelity (---) model responses at designs: (a) x_{1} ; and (b) x_{2} .

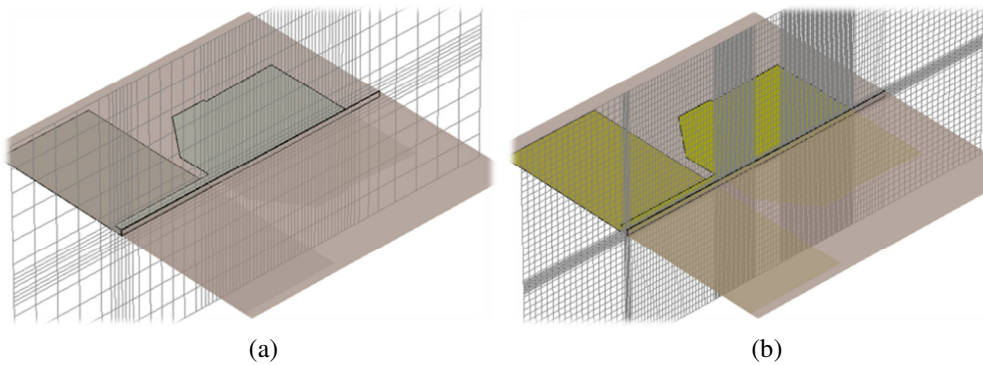


Figure 4.38: Cross-section view of UWB antenna discretization: (a) the low-fidelity model; and (b) the high-fidelity model.

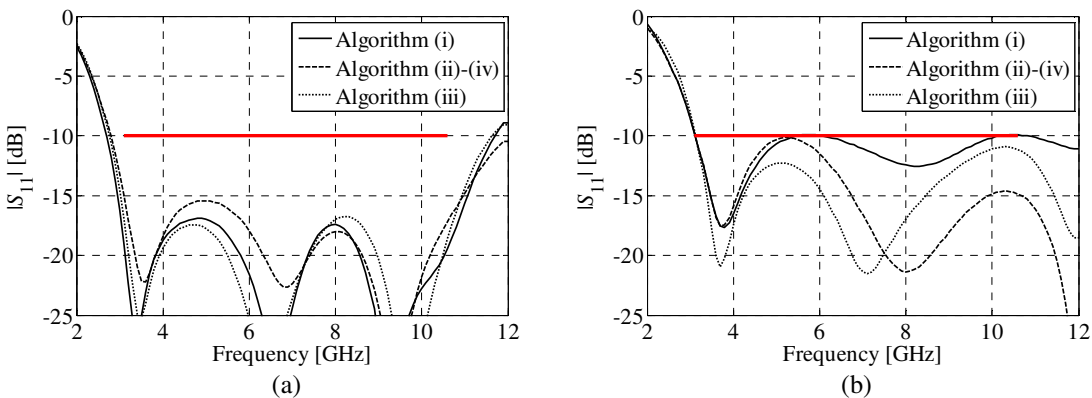


Figure 4.39: Reflection responses of the extreme Pareto-optimal designs obtained using algorithms (i)-(iv): (a) $x_c^{(1)}$ – optimal w.r.t. objective F_1 ; and (b) $x_c^{(2)}$ – optimal w.r.t. objective F_2 . The high-fidelity model response of (iii) is denoted by (— · —).

TABLE 4.15: COMPARISON OF THE ALGORITHMS – DESIGN SPACE REDUCTION

Reduction Method	Dimensions of Corner Designs										Size of the Search space [mm ⁹]	Space Reduction Ratio χ
	Design	a_1	a_2	a_3	b_1	b_2	b_3	l	w	d		
Initial space X_I	—	—	—	—	—	—	—	—	—	—	$1.1 \cdot 10^6$	—
Algorithm (i)	$\mathbf{x}_c^{(1)}$	11.10	23.40	23.00	5.00	5.00	9.00	16.00	37.50	0.65	37.8	$2.86 \cdot 10^4$
	$\mathbf{x}_c^{(2)}$	9.50	21.10	24.80	5.00	5.00	8.40	12.00	18.50	0.53		
Algorithm (ii)	$\mathbf{x}_c^{(1)}$	10.92	23.34	22.63	4.54	4.74	10.18	13.31	39.49	0.58	34.1	$3.16 \cdot 10^4$
	$\mathbf{x}_c^{(2)}$	8.96	21.05	24.10	7.13	5.64	8.74	8.58	20.02	0.60		
Algorithm (iii)	$\mathbf{x}_c^{(2)}$	8.96	21.05	24.10	7.13	5.64	8.74	8.58	20.02	0.60	10^3	10^3
	$\mathbf{x}_f^{(1)}$	10.92	23.34	22.78	4.54	4.74	10.18	14.31	37.49	0.58		
	$\mathbf{x}_f^{(2)}$	8.96	21.05	24.10	7.13	5.64	8.14	8.08	19.02	0.85		
Algorithm (iv)	$\mathbf{x}_c^{(1)}$	10.92	23.34	22.63	4.54	4.74	10.18	13.31	39.49	0.58	$5.5 \cdot 10^{-3}$	$1.97 \cdot 10^8$
	$\mathbf{x}_c^{(2)}$	8.96	21.05	24.10	7.13	5.64	8.74	8.58	20.02	0.60		

TABLE 4.16: COMPARISON OF THE ALGORITHMS – COMPUTATIONAL COST

Reduction method	Number of Algorithm Evaluations		Total Number of Evaluations		CPU-time						
					Absolute [min]	Relative to \mathbf{R}_f	$\Sigma [\mathbf{R}_f]$	Σ [h]			
Algorithm (i)	Stage 1	$F_1(\mathbf{x})$: 190	\mathbf{R}_c	402	\mathbf{R}_c	148.8	9.92	20.99	5.25		
	Stage 2	$F_1(\mathbf{x})$: 104	\mathbf{R}_c			81.47	5.43				
		$F_2(\mathbf{x})$: 108	\mathbf{R}_c			84.60	5.64				
Algorithm (ii)		$F_1(\mathbf{x})$: 220	\mathbf{R}_c	690	\mathbf{R}_c	172.33	11.49	36.03	9.01		
		$F_2(\mathbf{x})$: 470	\mathbf{R}_c			368.17	24.54				
Algorithm (iii)	Step 1 [†]	$F_1(\mathbf{x})$: 220	\mathbf{R}_c	1164	\mathbf{R}_c	172.33	11.49	64.78	16.20		
		$F_2(\mathbf{x})$: 470	\mathbf{R}_c			368.17	24.54				
	Step 2 [#]	$F_1(\mathbf{x})$: 220	\mathbf{R}_c			4	\mathbf{R}_f			30	2
		2	\mathbf{R}_f			30	2				
		$F_2(\mathbf{x})$: 254	\mathbf{R}_c			198.96	13.26				
Algorithm (iv)		$F_1(\mathbf{x})$: 220	\mathbf{R}_c	690	\mathbf{R}_c	172.33	11.49	36.03	9.01		
		$F_2(\mathbf{x})$: 470	\mathbf{R}_c			368.17	24.54				

[†] Initial design space reduction (cf. Section 4.3.2)

[#] Refinement of \mathbf{R}_c extreme points using SBO

4.5.4.2 Data Acquisition

The key data concerning the acquisition step is provided in Table 4.17 (see Section 4.5.2.2 for algorithm setup). The obtained results indicate that the design space reduction allows for considerable reduction of the number of samples required for construction of reliable RSA models. Almost two thousands of low-fidelity training samples were obtained in X_I in order to construct the RSA with RMS error below 3 percent. At the same time, only 80 samples were needed to setup the \mathbf{R}_s model within X_D (RMS error of only 1.9%). Identification of the RSA model in X_S (algorithm (ii)) and X_{S_r} (algorithm (iii)) required 140 and 180 \mathbf{R}_c samples (over 10 times less as compared to X_I), respectively. The RMS errors of both models are just below the acceptable threshold. Construction of the RSA within X_R (algorithm (iv)) involved only 40 training samples (48 times less than for X_I). Also, the RSA model set-up within X_R features the smallest RMS error and average minimum distance between samples (see Table 4.17). The convergence plots of considered RSA models are shown in Figure 4.40.

4.5.4.3 MOEA Optimization

The Pareto sets obtained within the considered regions of the design space for $I = 50$ and $N = 500$ (see Appendix A1) are shown in Figure 4.41, whereas more detailed data is provided in Table 4.18. The results indicate that for all compared design space regions, the range of $F_1(\mathbf{x})$ is below -7 dB. The discrepancies between the obtained Pareto sets are larger as compared to the previously considered antennas. Depending on selected search space region, discrepancies between the obtained Pareto sets are up to 2 dB (see Figure 4.41). The largest discrepancy (expressed as the average distance with respect to the selected objective $DIS(F_k)$) can be observed between the Pareto sets found in X_D (algorithm (i)) and X_I results from reduced dimensionality of the former (cf. Section 4.5.4.1). The average distance between X_R and X_I with respect to objectives $F_1(\mathbf{x})$ and $F_2(\mathbf{x})$ is 0.7 dB and 73 mm^2 , respectively. This is satisfactory considering that X_R is eight orders of magnitude smaller than X_I . Moreover, the Pareto sets found in X_I and X_{S_r} (algorithm (iii)) exhibit the smallest discrepancy (see Table 4.18).

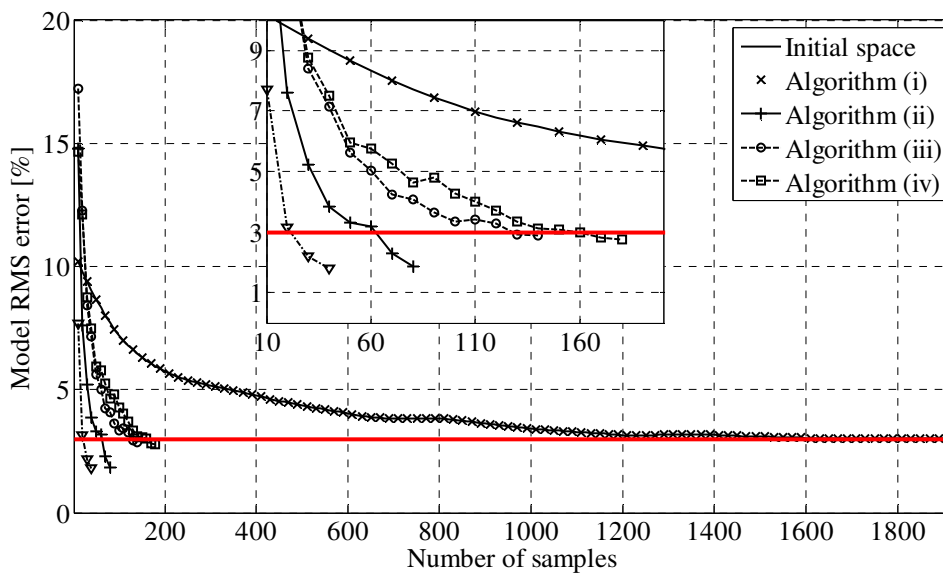


Figure 4.40: Convergence plots of RSA models obtained using cross-validation technique.

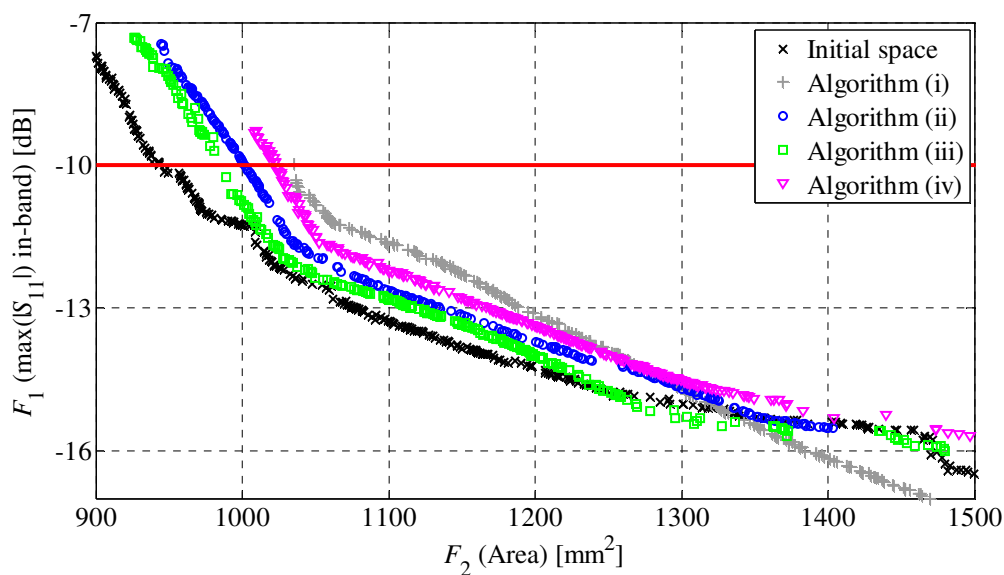


Figure 4.41: The Pareto sets obtained within initial and refined regions of the design space.

TABLE 4.17: KEY INFORMATION ON THE DATA ACQUISITION STEP

Selected Solution Space	Number of Training Samples	RMS Error of the RSA Model [%]	Average Minimal Distance Between Samples	Training Set Size Reduction Ratio
Initial space X_I	1920	2.77	2.11	—
Algorithm (i)	80	1.85	1.30	24
Algorithm (ii)	140	2.87	1.45	13.71
Algorithm (iii)	180	2.76	1.55	10.67
Algorithm (iv)	40	1.81	0.81	48

TABLE 4.18: KEY PROPERTIES OF THE OBTAINED PARETO SETS

Selected Reduction Method	Objective F_1				Objective F_2				
	$\min(F_1)$	$\max(F_1)$	$\Delta(F_1)$	$DIS(F_1)$	$\min(F_2)$	$\max(F_2)$	$\Delta(F_2)$	$\Delta(F_2)$	$DIS(F_2)$
	[dB]	[dB]	[dB]	[dB]	[mm ²]	[mm ²]	[mm ²]	[%]	[mm ²]
Initial Space X_I	-16.6	-10.0	6.6	—	943	1548	605	39.1	—
Algorithm (i)	-17.9	-10.3	7.6	1.01	1036	1576	540	34.3	83.86
Algorithm (ii)	-15.5	-10.1	5.4	0.50	1002	1404	402	28.6	47.59
Algorithm (iii)	-16.0	-10.0	6.0	0.28	984	1509	525	34.8	32.04
Algorithm (iv)	-15.7	-10.0	5.7	0.72	1023	1497	474	31.7	73.73

4.5.4.4 Pareto Set Refinement

The design samples utilized by the response correction technique (cf. Section 4.4.1) have been evenly selected along the parts of the Pareto sets for which $F_1(\mathbf{x}) \leq -10$ dB. For each design, the algorithm has been terminated after three iterations. Figure 4.42 shows a comparison of the initial and the refined Pareto sets, whereas detailed dimensions of selected Pareto designs are gathered in Table 4.19. The refined high-fidelity samples are close to the initial Pareto set which indicate good correlation between the low- and high-fidelity models.

The Pareto sets obtained using co-kriging, as well as the \mathbf{R}_f designs evaluated for verification are shown in Figure 4.43. The dimensions of the selected high-fidelity samples are provided in Table 4.20. The results are in very good agreement. The reflection-wise discrepancies between the Pareto sets and \mathbf{R}_f samples are below 0.5 dB.

4.5.4.5 Optimization Algorithm – Computational Cost

Table 4.21 presents a cost breakdown of the multi-objective optimization procedure. The results indicate that the design space reduction considerably influences the overall cost of the optimization process. The total cost of antenna optimization in X_I corresponds to about 130.3 \mathbf{R}_f simulations (~32.6 hours), whereas the CPU-time related to expedited design within search space regions obtained using algorithms (i)-(iv) vary from 13.8 hours (~55 \mathbf{R}_f simulations) to 26 hours (~104 \mathbf{R}_f evaluations). It should be noted that—for the considered antenna—utilization of space reduction allow for limiting the cost of multi-objective algorithm operation by up to 58% as compared to design within X_I . The estimated cost of direct MOEA optimization using \mathbf{R}_c or \mathbf{R}_f model for 5000 simulations (cf. Appendix A1) is 65 hours or 52 days, respectively.

4.5.5 Scalability of Multi-Objective Antenna Optimization Algorithm

The analysis of the algorithm scalability has been performed based on the relative design optimization cost (expressed in terms of the number of \mathbf{R}_f model evaluations for the respective antenna structure) and the selected space reduction method. Figure 4.44 shows a graphical representation of the dependence between the total cost of the algorithm operation and the dimensionality of the problem (see Table 4.7, Table 4.14 and Table 4.21).

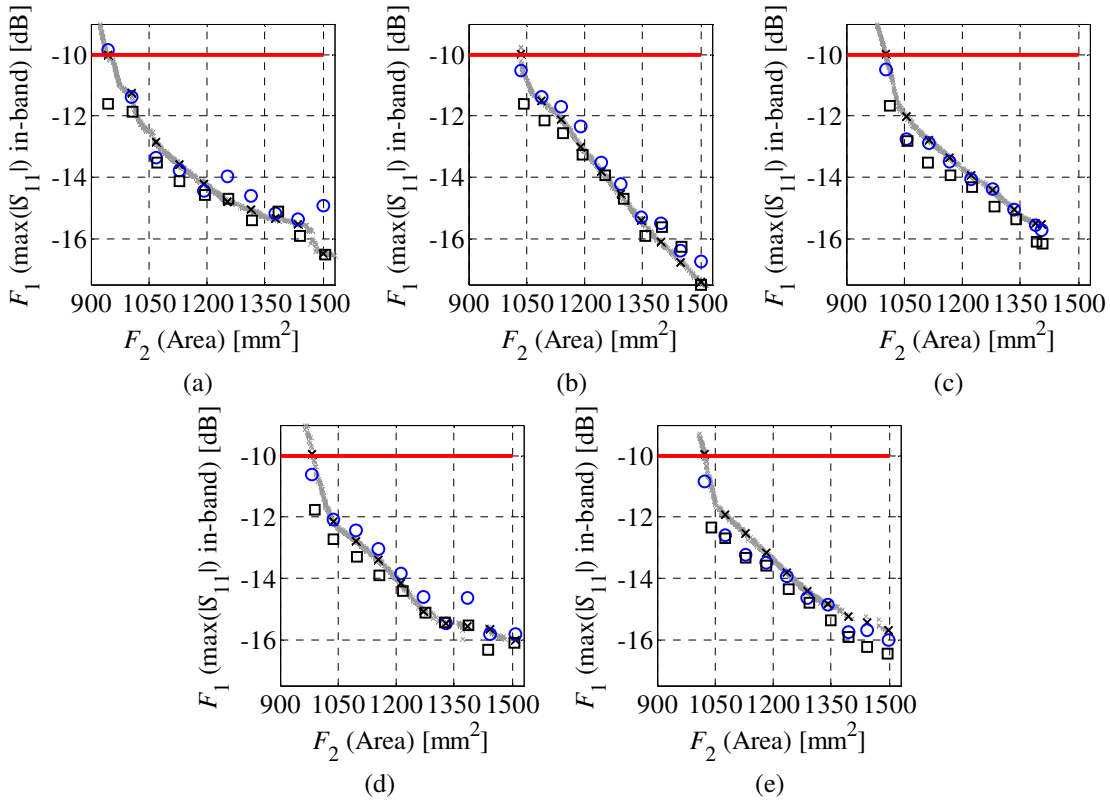


Figure 4.42: Response correction refinement of the selected low-fidelity designs obtained in: (a) X_f , and the following reduced regions of the search space: (b) X_D – algorithm (i); (c) X_S – algorithm (ii); (d) X_{S_r} – algorithm (iii) and (e) X_R – algorithm (iv). Gray and black crosses denote initial Pareto set and selected Pareto-optimal designs, respectively. Blue circles and black squares represent the high-fidelity model responses before and after correction step, respectively.

TABLE 4.19: RESPONSE CORRECTION-BASED REFINEMENT – SELECTED ANTENNA DESIGNS

		Selected Pareto-optimal designs										
		F_1 [dB]	F_2 [mm ²]	a_1	a_2	a_3	b_1	b_2	b_3	l	w	D
Initial Space X_f	$\mathbf{x}_f^{(2)}$	-11.85	1008	8.37	20.43	22.26	5.32	4.55	10.46	11.03	22.26	0.62
	$\mathbf{x}_f^{(4)}$	-14.11	1129	9.31	23.46	23.61	7.10	4.02	8.55	11.75	25.51	0.63
	$\mathbf{x}_f^{(6)}$	-14.69	1255	11.49	20.68	24.01	6.76	4.60	9.29	10.19	29.44	0.82
	$\mathbf{x}_f^{(8)}$	-15.12	1384	11.48	21.07	23.81	6.76	4.59	9.29	10.18	29.43	0.81
	$\mathbf{x}_f^{(10)}$	-16.54	1506	11.48	22.26	22.86	5.55	4.66	11.55	10.25	35.03	0.76
Algorithm (i)	$\mathbf{x}_f^{(2)}$	-12.16	1095	9.82	21.11	24.27	5.00	5.00	8.98	12.81	24.29	0.53
	$\mathbf{x}_f^{(4)}$	-13.27	1195	9.57	21.11	24.80	5.00	5.00	8.99	12.65	27.10	0.57
	$\mathbf{x}_f^{(6)}$	-14.71	1302	11.09	21.12	24.79	5.00	5.00	8.70	14.07	28.93	0.63
	$\mathbf{x}_f^{(8)}$	-15.63	1401	11.09	21.38	24.67	5.00	5.00	8.72	14.61	30.97	0.64
	$\mathbf{x}_f^{(10)}$	-17.51	1501	11.09	21.88	24.76	5.00	5.00	8.47	15.49	32.94	0.65
Algorithm (ii)	$\mathbf{x}_f^{(2)}$	-12.83	1058	9.31	22.22	23.34	6.03	4.98	9.28	11.44	23.29	0.59
	$\mathbf{x}_f^{(4)}$	-13.95	1170	9.44	21.89	23.57	6.09	4.97	9.12	11.47	26.42	0.59
	$\mathbf{x}_f^{(6)}$	-14.95	1284	9.72	21.73	23.86	5.45	5.41	9.59	11.73	28.99	0.60
	$\mathbf{x}_f^{(8)}$	-16.11	1391	10.36	22.91	24.08	5.76	5.01	10.01	11.68	31.55	0.59
	$\mathbf{x}_f^{(10)}$	-16.17	1406	10.50	22.78	24.09	5.75	4.95	10.08	11.77	31.88	0.60
Algorithm (iii)	$\mathbf{x}_f^{(2)}$	-12.72	1038	9.18	21.58	23.33	6.60	4.98	9.09	10.39	23.21	0.66
	$\mathbf{x}_f^{(4)}$	-13.92	1158	9.99	21.62	23.89	6.28	4.99	9.22	11.01	26.21	0.65
	$\mathbf{x}_f^{(6)}$	-15.12	1275	10.90	21.11	23.58	5.98	4.89	9.08	11.86	29.09	0.77
	$\mathbf{x}_f^{(8)}$	-15.52	1386	10.38	21.87	23.47	5.73	5.26	9.89	10.56	32.42	0.73
	$\mathbf{x}_f^{(10)}$	-16.09	1507	10.91	22.18	24.09	4.82	4.90	9.52	14.29	33.52	0.68
Algorithm (iv)	$\mathbf{x}_f^{(2)}$	-12.70	1075	8.97	21.75	24.10	6.82	5.44	8.88	9.74	24.47	0.60
	$\mathbf{x}_f^{(4)}$	-13.58	1182	9.45	21.61	23.83	6.27	5.30	9.10	10.59	27.07	0.60
	$\mathbf{x}_f^{(6)}$	-14.81	1293	9.57	21.91	23.63	5.91	5.19	9.41	11.23	29.62	0.59
	$\mathbf{x}_f^{(8)}$	-15.93	1394	10.09	22.78	23.35	5.74	5.16	9.67	11.73	31.79	0.59
	$\mathbf{x}_f^{(10)}$	-16.45	1497	10.88	22.79	23.13	5.41	5.01	10.12	12.20	34.04	0.59

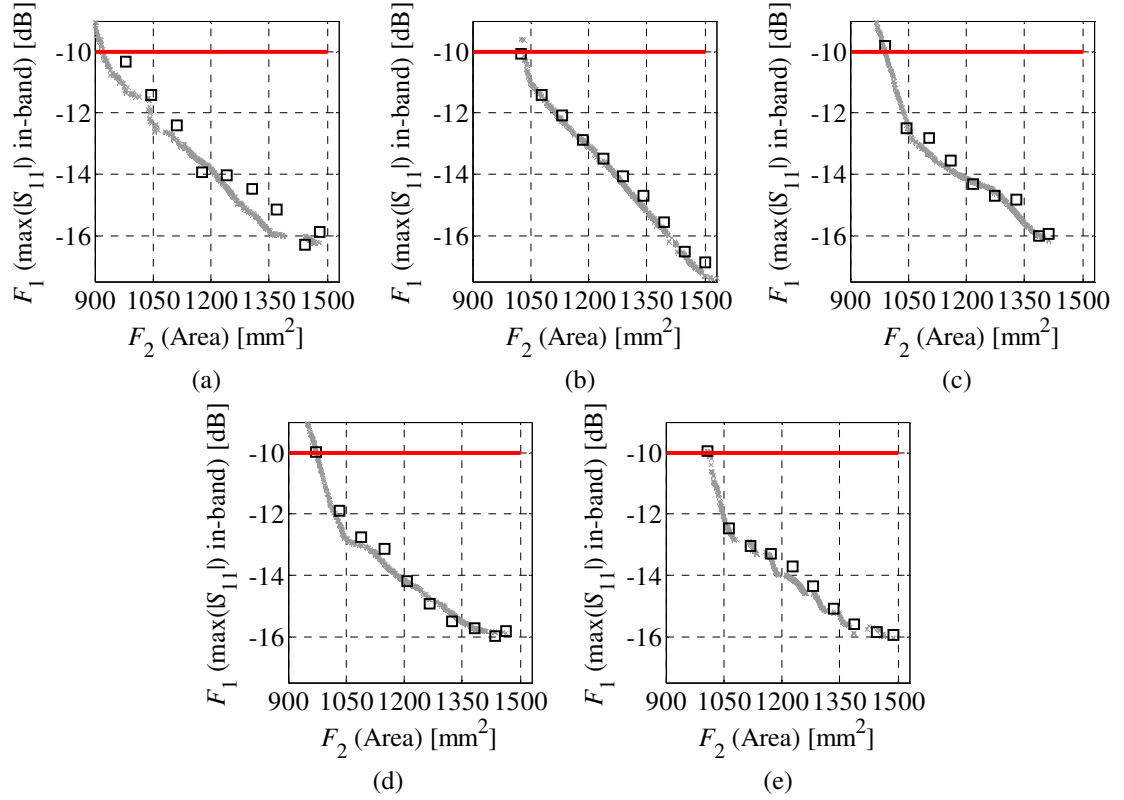


Figure 4.43: Refinement of the Pareto sets using co-kriging within: (a) X_j ; and the following regions of the search space (b) X_D ; (c) X_S ; (d) X_{S_r} and (e) X_R . Gray crosses and black squares represent \mathbf{R}_f Pareto set and \mathbf{R}_f designs evaluated for verification.

TABLE 4.20: CO-KRIGING-BASED REFINEMENT – SELECTED DESIGNS

		Selected Pareto-optimal designs										
		F_1 [dB]	F_2 [mm ²]	a_1	a_2	a_3	b_1	b_2	b_3	l	w	d
Initial Space X_j	$\mathbf{x}_f^{(2)}$	-10.32	979	9.38	22.06	21.19	5.84	4.18	9.71	10.55	22.28	0.62
	$\mathbf{x}_f^{(4)}$	-12.40	1111	10.45	23.68	23.53	6.61	4.30	8.49	11.51	25.44	0.67
	$\mathbf{x}_f^{(6)}$	-14.02	1240	10.18	20.66	23.15	6.11	5.12	9.09	10.31	29.23	0.78
	$\mathbf{x}_f^{(8)}$	-15.15	1368	10.46	22.37	22.81	6.70	4.73	9.22	11.06	31.66	0.76
	$\mathbf{x}_f^{(10)}$	-15.89	1481	10.46	23.42	24.75	6.18	4.16	10.56	11.98	33.48	0.74
Algorithm (i)	$\mathbf{x}_f^{(2)}$	-11.42	1079	10.07	21.35	24.09	5.00	5.00	8.72	12.74	24.10	0.57
	$\mathbf{x}_f^{(4)}$	-12.89	1184	10.04	21.24	24.47	5.00	5.00	8.80	13.09	26.57	0.56
	$\mathbf{x}_f^{(6)}$	-14.08	1289	10.66	21.37	24.46	5.00	5.00	8.66	13.88	28.81	0.59
	$\mathbf{x}_f^{(8)}$	-15.57	1395	10.95	21.84	24.35	5.00	5.00	8.61	14.70	30.84	0.60
	$\mathbf{x}_f^{(10)}$	-16.87	1500	10.94	22.38	24.22	5.00	5.00	8.63	15.29	32.97	0.59
Algorithm (ii)	$\mathbf{x}_f^{(2)}$	-12.49	1045	9.33	22.13	23.09	6.00	5.10	9.11	11.41	23.05	0.59
	$\mathbf{x}_f^{(4)}$	-13.54	1160	9.55	21.90	23.45	5.86	5.04	9.26	11.55	26.08	0.59
	$\mathbf{x}_f^{(6)}$	-14.70	1273	10.05	21.86	23.69	5.74	5.22	9.46	11.67	28.79	0.60
	$\mathbf{x}_f^{(8)}$	-16.00	1387	10.19	22.81	23.88	5.72	5.01	9.88	11.83	31.45	0.60
	$\mathbf{x}_f^{(10)}$	-15.94	1412	10.09	22.76	23.89	5.68	5.01	9.97	11.77	32.13	0.60
Algorithm (iii)	$\mathbf{x}_f^{(2)}$	-11.88	1032	9.48	21.57	23.12	6.15	5.29	9.14	10.51	22.97	0.66
	$\mathbf{x}_f^{(4)}$	-13.12	1149	10.10	21.57	23.50	6.34	5.20	8.54	11.15	26.19	0.72
	$\mathbf{x}_f^{(6)}$	-14.92	1265	9.95	21.69	23.78	5.91	4.94	9.26	11.74	28.79	0.67
	$\mathbf{x}_f^{(8)}$	-15.72	1382	10.58	22.20	23.43	5.93	5.07	8.70	12.79	31.29	0.72
	$\mathbf{x}_f^{(10)}$	-15.81	1462	10.66	22.05	22.88	5.40	5.17	8.83	13.78	32.71	0.69
Algorithm (iv)	$\mathbf{x}_f^{(2)}$	-12.47	1063	9.07	21.24	23.97	6.60	5.53	9.02	9.66	24.20	0.60
	$\mathbf{x}_f^{(4)}$	-13.28	1173	9.54	21.76	23.62	6.34	5.31	9.30	10.41	26.72	0.60
	$\mathbf{x}_f^{(6)}$	-14.34	1281	9.62	21.97	23.73	6.09	5.40	9.18	10.68	29.68	0.60
	$\mathbf{x}_f^{(8)}$	-15.60	1386	10.13	22.65	23.36	5.87	5.18	9.69	11.53	31.58	0.59
	$\mathbf{x}_f^{(10)}$	-15.94	1489	10.22	22.68	22.87	5.41	5.06	10.02	12.13	33.97	0.59

TABLE 4.21: COST BREAKDOWN OF THE MULTI-OBJECTIVE ANTENNA OPTIMIZATION

Algorithm Step	Selected Design Space Reduction Algorithm									
	Initial Space		Algorithm (i)		Algorithm (ii)		Algorithm (iii)		Algorithm (iv)	
	Sim. Cost	Total [h]	Sim. Cost	Total [h]	Sim. Cost	Total [h]	Sim. Cost	Total [h]	Sim. Cost	Total [h]
Design Space Reduction	—	—	R_c 402	5.25	R_c 690	9.01	R_c 1164	15.20	R_c 690	9.01
Data Acquisition and RSA construction	R_c 1920	25.07	R_c 80	1.04	R_c 140	1.82	R_c 180	2.35	R_c 40	0.52
MOEA Optimization	R_s 25000	N/A	R_s 25000	N/A	R_s 25000	N/A	R_s 25000	N/A	R_s 16000	N/A
Refinement Using Response Correction [#]	R_s 4109	N/A	R_s 3375	N/A	R_s 2754	N/A	R_s 3524	N/A	R_s 4008	N/A
	R_f 30	7.5	R_f 30	7.5	R_f 30	7.5	R_f 30	7.5	R_f 30	7.5
Refinement Using Co-Kriging [#]	R_s 50000	N/A	R_s 50000	N/A	R_s 50000	N/A	R_s 50000	N/A	R_s 32000	N/A
	R_f 30	7.5	R_f 30	7.5	R_f 30	7.5	R_f 30	7.5	R_f 30	7.5
Total cost [!]	R_f ~130.3	32.57	R_f ~55.2	13.79	R_f ~73.3	18.33	R_f ~104.0	26.05	R_f ~68.1	17.03

[#]The refinement procedure is carried out using either response correction or co-kriging

[!]Total cost of multi-objective design optimization includes only one refinement procedure

The results indicate that the most expensive steps are design space reduction and correction of the initial Pareto set. As described in Section 4.3.2, the space reduction involves a sequence of single-objective optimizations (also using surrogate-assisted methods; cf. Section 4.3.5). This stage is realized using pattern search algorithm [213]. Its computational complexity is more or less $O(D^2)$ where D is the number of antenna geometrical parameters. Since the cost of the Pareto set refinement is constant, it is expected that the contribution of data acquisition step to the overall cost of multi-objective optimization will noticeably grow with the problem dimensionality (this has been confirmed in [214]).

It should be noted that the cost of the Pareto set refinement, expressed in the number of high-fidelity simulations, does not depend on the number of antenna adjustable parameters regardless the selected model correction technique. The reason is that the refinement always involves the same number of 30 R_f simulations. At the same time, optimization of the corrected RSA does not contribute to the computational cost (cf. Section 4.5.2.3).

The rate in which the computational cost increases with dimensionality of the problem depends on the selected space reduction method (see Figure 4.44). The latter, however, reduces the ranges of the design variables—which is critical for feasible construction of the surrogate—but not the problem dimensionality in general. Nonetheless, the number of design variables for the benchmark problem of Section 4.5.4 has been limited (from 9 to 7) by the algorithm of Section 4.3.1 because the extreme Pareto designs it identified have been found to have virtually the same values for two of the parameters. It should be noted that the growth of the space reduction and RSA construction cost mostly apply to low-fidelity model evaluations and thus the increase of the multi-objective optimization cost for the selected space reduction routines is more or less quadratic (see Figure 4.44). Therefore, scalability of the method for the discussed space reduction algorithms and the considered ranges of benchmark antenna dimensionalities can be considered as very good from the practical point of view. Note that observed nonlinearity of the cost increase between different antennas is due to different speed-up ratios between their low- and high-fidelity models (i.e., for monocone antenna R_s is 42 times faster than R_f , but for monopole the speed-up ratio is only 19). More detailed discussion on the scalability of the optimization algorithm with increasing dimensionality of the problem can be found in [214].

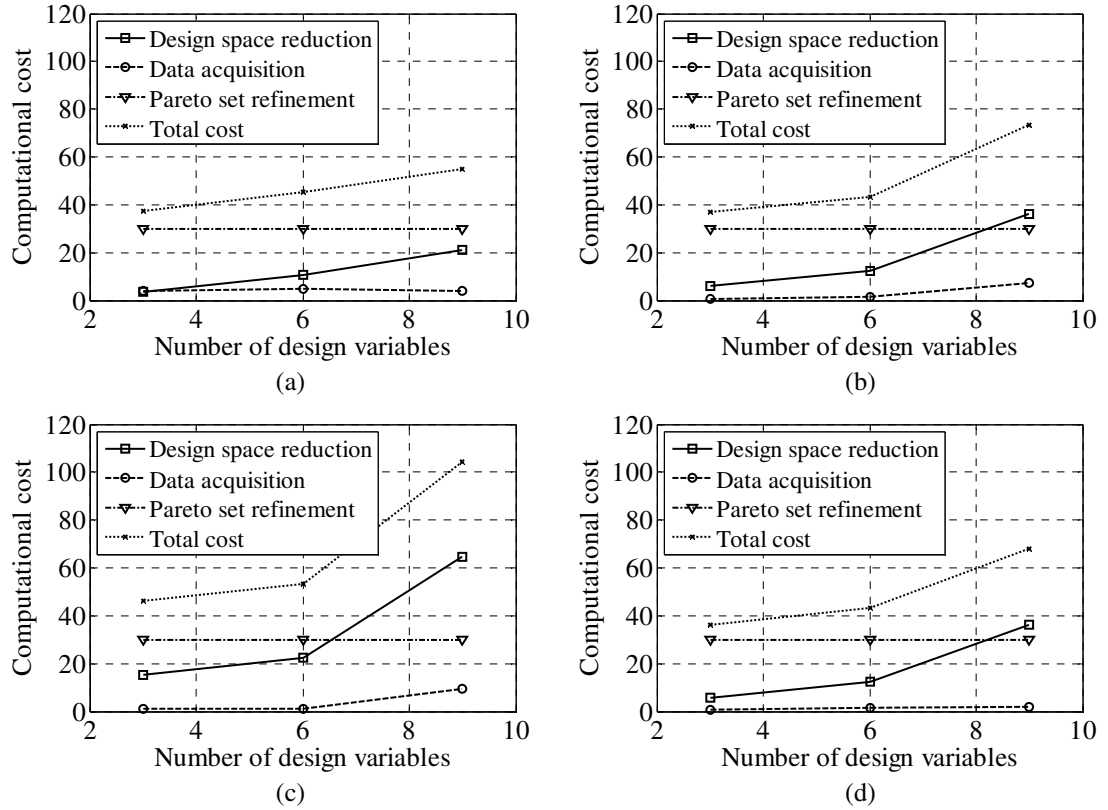


Figure 4.44: Dependency of computational cost (relative to R_f) of multi-objective antenna optimization on the problem dimensionality. The plots indicate the overall cost as well as the costs of various stages of the design process within search spaces obtained using: (a) algorithm (i); (b) algorithm (ii); (c) algorithm (iii); and (d) algorithm (iv).

4.6 Summary and Algorithm Limitations

In this chapter, a technique for expedited multi-objective optimization of numerically demanding antennas has been discussed. One of the most important components of the considered algorithm is design space reduction which allows for MOEA-based optimization of antenna structures with many geometrical parameters (see Chapter 5). Four of the described reduction methods have been comprehensively validated and compared based on three benchmark structures. The obtained results indicate large potential of the algorithm and reduction techniques for limiting the computational cost of multi-objective antenna optimization.

It should be noted that application of certain space reduction techniques may not be beneficial for low-dimensional design problems (see Table 4.7). Also, the cost of design space reduction increases with the dimensionality of the problem and thus, for multi-parameter antennas, it significantly contributes to the overall cost of the optimization process. Nonetheless, it can be reduced by identification of extreme Pareto designs using more efficient methods than pattern search. For instance, optimization could be performed using local approximation models or methods exploiting response features of the antenna at hand [215, 216].

The considered multi-objective algorithm provides promising results (both, in terms of computational cost and the quality of the high-fidelity Pareto sets). However, certain limitations can be identified:

- Computational cost and performance of the optimization process (including design space reduction, surrogate model construction, etc.) depend on the speed and accuracy of the low-fidelity model. Current implementation of the optimization framework leaves low-fidelity model setup up to the user. Automation of this process is highly desirable.

- The reduction techniques considered here do not guarantee that all Pareto-optimal designs are contained in the reduced space. The amount of the “lost” designs depend on both the low-fidelity model accuracy and geometry of the Pareto front. Appropriate strategies for extending the reduced portion of the space should be developed and implemented.
- The computational cost of surrogate model construction grows very quickly with the problem dimensionality (even though it is established in the reduced space). Therefore, alternative approaches that do not rely of approximation model should be developed to alleviate this problem.

5 DESIGN EXAMPLES

In this chapter, numerical verification of the discussed expedited multi-objective optimization methodology is performed. The flexibility of the algorithm for solving different types of design problems is demonstrated by individual adjustment of the design flow (cf. Section 4.2.1) for each design problem, where the adjustment is understood as selection of the specific algorithm mechanisms that allow for increasing its efficiency both in terms of reliability and computational cost. The discussed methods are applied for solving design tasks with two and three design requirements. The optimization technique is validated based on six real-world design problems including four planar antennas, a narrow-band dielectric resonator antenna (DRA), and a UWB impedance transformer. The considered design objectives include: minimization of maximum in-band reflection, reduction of the structure footprint/volume, maximization of the gain, as well as minimization of the difference between minimal and maximal E-field strength at the selected frequency.

The EM models of each structure considered in this chapter are designed in CST Microwave Studio and simulated using its time-domain solver [149]. The numerical cost of multi-objective design using discussed methods and algorithms is compared with the estimated cost of direct MOEA-based optimization.

Applications of the discussed multi-objective optimization approach exceed the class of planar UWB antennas. The method can be also utilized to other microwave and antenna structures (e.g., narrow-band, non-planar, multi-port, etc.). This has been demonstrated using the DRA and the impedance transformer. Both structures exceeds the main scope of this dissertation.

The chapter is organized as follows. In Sections 5.1 to 5.4, multi-objective design optimization of a 13-variable UWB monopole antenna, a 14-variable multiple-input-multiple-output (MIMO) antenna, a 24-variable quasi-Yagi-Uda antenna and an 8-parameter planar Yagi-Uda antenna are discussed. In Section 5.5, design of a 6-variable DRA with respect to three objectives is considered. Finally, in Section 5.6, optimization of a 15-variable microstrip 50-to-130 ohm impedance transformer is carried out.

5.1 UWB Monopole Antenna

The first design example is a planar UWB monopole shown in Figure 5.1 [122, 146]. The structure consists of a driven element in the form of three stacked trapezoids fed through a microstrip line. The input impedance is 50 ohm. The antenna is implemented on a Taconic RF-35 dielectric substrate ($\epsilon_r = 3.5$, $\tan\delta = 0.0018$, $h = 0.762$ mm). The design variables are $\mathbf{x} = [a_1 a_2 a_3 a_4 a_5 a_6 b_1 b_2 b_3 w_2 l d o]^T$, whereas $w_1 = 1.7$ remain fixed to ensure 50 ohm input impedance. The unit for all parameters is mm.

The high-fidelity model \mathbf{R}_f of the structure contains 2,500,000 hexahedral mesh cells and its average simulation time is 10 minutes. The low-fidelity model \mathbf{R}_c contains $\sim 33,600$ cells and its typical simulation time is 22 seconds. Other simplifications of the latter include utilization of lossless dielectric with zero thickness and representation of metallization as PEC. The lower and upper bounds of the initial space X_I are $\mathbf{l} = [5 \ 5 \ 5 \ 5 \ 5 \ 1 \ 1 \ 0.2 \ 8 \ 20 \ 5]^T$ and $\mathbf{u} = [25 \ 25 \ 25 \ 25 \ 25 \ 25 \ 15 \ 15 \ 15 \ 2 \ 15 \ 40 \ 10]^T$. The following design objectives are considered: F_1 – minimization of antenna maximum in-band reflection given by (4.33) within 3.1 GHz to 10.6 GHz frequency range and F_2 – reduction of the footprint defined as $V(\mathbf{x}) = w_a \times l_a$ rectangle (4.34), where $w_a = l + d + b_1 + b_2 + b_3 + o$ and $l_a = w_2 + o$.

The design space reduction has been performed using the method of Section 4.3.5 [146]. The refined search space X_{S_r} is defined by the following lower and upper bounds: $\mathbf{l}_{S_r} = [10.07 \ 21.63 \ 22.2 \ 21 \ 20.8 \ 22.7 \ 3.2 \ 3.8 \ 12.32 \ 0.57 \ 8.3 \ 22.07 \ 5.0]^T$ and $\mathbf{u}_{S_r} = [11.3 \ 21.96 \ 24.3 \ 24.15 \ 21.27 \ 24.6 \ 3.9 \ 4 \ 13.08 \ 0.74 \ 11.2 \ 39.35 \ 5.75]^T$. The volume-wise reduction of the X_{S_r} with respect to X_I is 10^{14} . The number of \mathbf{R}_c model samples evaluated in single iteration of the data acquisition/RSA construction loop (cf. Section 4.2.1) is set to 500. Training data is allocated using LHS [164]. The final RSA model \mathbf{R}_s has been set-up using 1500 \mathbf{R}_c samples (three iterations) and its corresponding RMS error is 3.5 percent. It should be noted that the average minimum distance between the training samples (4.1) after the first and the last iteration is $\delta_p = 0.62$ mm and $\delta_p = 0.57$ mm, respectively. At the same time, the accuracy improvement of the \mathbf{R}_s , expressed as a relation between RMS errors of the initial (6%) and final RSAs, of 1.72 is much better than $3^{1/13} = 1.08$. This is due to the flattening effect (cf. Section 4.3). For the sake of comparison, the same set of 1500 \mathbf{R}_c samples has been rescaled to the initial space X_I and evaluated. The resulting RSA model is characterized by the RMS error of over 22% and thus it is too inaccurate to be used in the optimization process.

The RSA model constructed in X_{S_r} has been optimized using MOEA (setup: 100 generations, 500 individuals). In the next step, the selected Pareto-optimal designs have been refined to the high-fidelity model level using the response correction technique of Section 4.4.1. A comparison of \mathbf{R}_f - and \mathbf{R}_s -based representations of the Pareto front is shown in Figure 5.2(a). The footprint of the smallest antenna design that fulfills requirements for the in-band reflection is 1134 mm^2 , whereas the solution with the largest area of 1475 mm^2 features $|S_{11}|$ of only -15.2 dB. Variability of the objectives F_1 and F_2 along the Pareto front is 5.2 dB and 341 mm^2 (over 23%), respectively. The detailed dimensions of the high-fidelity Pareto-optimal solutions are gathered in Table 5.3, whereas the reflection characteristics of the selected designs are shown in Figure 5.3.

The obtained results indicate conflicting nature of the selected design objectives. The Pareto designs have been acquired for the model lacking an SMA (SubMiniature version A) connector. At the same time, utilization of the SMA connector (for the sake of measurements) affects the antenna reflection. Because of the effect of the SMA connector on the antenna electrical characteristics it may be preferable for the designer to choose the design for experimental verification purposes that is within certain margin with respect to -10 dB threshold (say 2 dB). Moreover, field characteristics of the considered antenna have been excluded from design specifications. Experimental validation of the antenna—including field properties—is provided in Section 6.1.

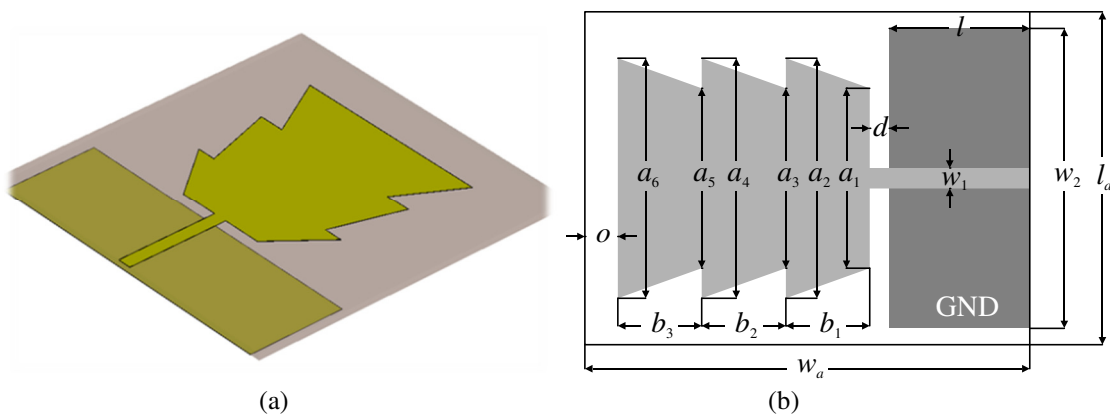


Figure 5.1: A UWB monopole antenna [122]: (a) 3D visualization; and (b) geometrical details.

For the sake of comparison, the high-fidelity Pareto front obtained in X_{S_f} has been compared to its corresponding representation obtained in the space region determined using the method of Section 4.3.2 (Figure 5.2). The results indicate that—for the algorithm of Section 4.3.2—the discrepancies between the \mathbf{R}_s and \mathbf{R}_f responses vary noticeably along the Pareto front. The reason is that a portion of the optimal \mathbf{R}_f model solutions is outside the region of the design space determined by the technique of Section 4.3.2. As a consequence, the response correction algorithm is unable to account for the misalignments between \mathbf{R}_s and \mathbf{R}_f .

The computational cost of the design optimization procedure corresponds to about 118 \mathbf{R}_f simulations (almost 20 hours of CPU-time) and it includes: 800 \mathbf{R}_c and 4 \mathbf{R}_f simulations for the design space reduction step, 1500 \mathbf{R}_c evaluations for the data acquisition/RSA construction step, as well as 30 \mathbf{R}_f simulations for the refinement of ten Pareto designs (three iterations per sample). At the same time, the estimated cost of direct MOEA optimization of \mathbf{R}_f and \mathbf{R}_c models is about 347 days and 306 hours, respectively (the estimation is based on the number of \mathbf{R}_s simulations required by MOEA). A detailed cost breakdown of the design optimization process is provided in Table 5.2.

5.2 UWB MIMO Antenna

Consider a compact UWB MIMO antenna shown in Figure 5.4 [31, 208]. The structure is implemented on a 0.762-mm-thick Taconic RF-35 substrate. The antenna consists of two rectangular monopole radiators fed through separate 50 ohm microstrip lines. The slots within the ground plane allow for obtaining wideband impedance matching. Moreover, the compact geometry of the structure is ensured by means the I-shaped and L-shaped ground plane stubs both of which increase the current path. The driven elements are located perpendicularly to each other in order to achieve high isolation between them. The antenna is described by a 14-variable vector: $\mathbf{x} = [a_1 \ a_2 \ c_1 \ d_1 \ d_2 \ d_3 \ g_1 \ g_2 \ g_3 \ s_1 \ s_2 \ s_3 \ s_4 \ s_5]^T$. Parameter $w_1 = 1.7$ is fixed to ensure 50 ohm input impedance. All dimensions are in mm.

The high-fidelity model \mathbf{R}_f consists of $\sim 1,600,000$ mesh cells and its average evaluation time is 20 minutes. The low-fidelity model \mathbf{R}_c contains $\sim 140,000$ mesh cells and its typical simulation time is 71 seconds. The initial search space X_I is defined by the following bounds: $\mathbf{l} = [5 \ 5 \ 0.2 \ 2 \ 2 \ 2 \ 1 \ 20 \ 0 \ 1 \ 0.2 \ 0.2 \ 0.2]^T$, and $\mathbf{u} = [15 \ 15 \ 2 \ 10 \ 10 \ 10 \ 15 \ 10 \ 30 \ 2 \ 8 \ 2 \ 6 \ 5]^T$.

The design objective F_1 is to minimize of the maximum reflection coefficients $|S_{11}|$ and $|S_{22}|$ of both radiators within the UWB band (3.1 GHz to 10.6 GHz). In other words, only the designs satisfying $\max\{|S_{11}|_{3.1 \text{ GHz to } 10.6 \text{ GHz}}\} \leq -10$ dB and $\max\{|S_{22}|_{3.1 \text{ GHz to } 10.6 \text{ GHz}}\} \leq -10$ dB are of interest. The objective F_2 is to minimize the antenna footprint $V(\mathbf{x}) = A_1 \times A_2$, where $A_1 = g_1 + d_2 + w_1 + d_3 + s_5$ and $A_2 = g_3 + s_4 + g_1$. Moreover, in-band isolation (denoted as $|S_{21}|$ and $|S_{12}|$) between radiators in the MIMO structure should be possibly large. However, isolation mainly depends on the distance between antennas and thus is not explicitly controlled.

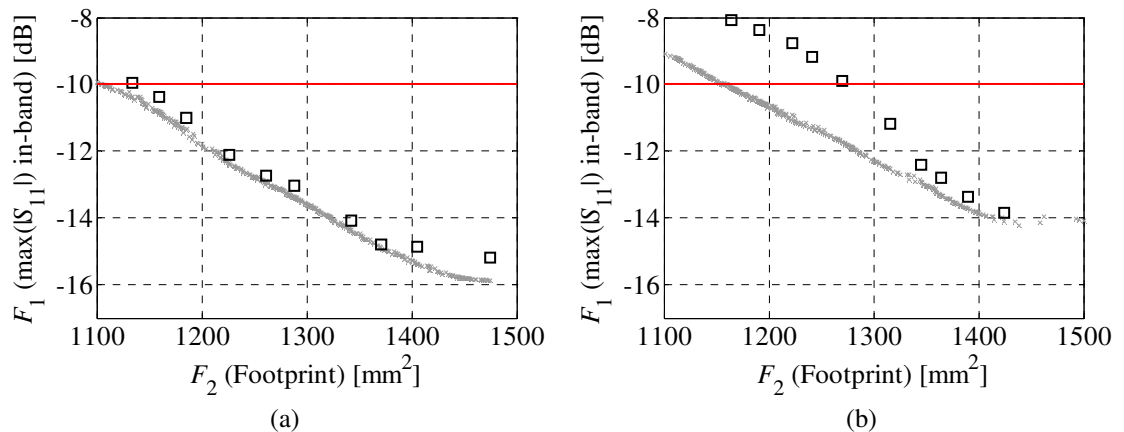


Figure 5.2: The \mathbf{R}_f (\square) and \mathbf{R}_s (\times) Pareto sets of the UWB monopole antenna obtained within design space regions determined using: (a) method of Section 4.3.5 [146]; and (b) method of Section 4.3.2.

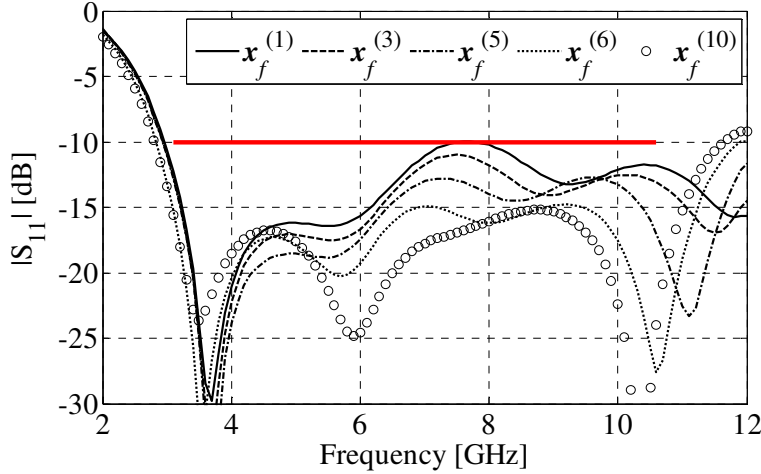

Figure 5.3: Reflection characteristics of the Pareto-optimal antenna designs selected from Table 5.1 [146].

TABLE 5.1: UWB MONOPOLE ANTENNA: DETAILED DIMENSIONS OF SELECTED DESIGNS

		Antenna designs									
		$x_f^{(1)}$	$x_f^{(2)}$	$x_f^{(3)}$	$x_f^{(4)}$	$x_f^{(5)}$	$x_f^{(6)}$	$x_f^{(7)}$	$x_f^{(8)}$	$x_f^{(9)}$	$x_f^{(10)}$
Antenna Parameters	F_1 [dB]	-10.0	-10.4	-11.0	-12.1	-12.7	-13.5	-14.1	-14.8	-14.9	-15.2
	F_2 [mm ²]	1134	1159	1185	1226	1261	1315	1342	1371	1405	1475
	a_1	10.07	10.09	10.38	11.06	11.11	11.14	11.11	10.95	10.97	10.90
	a_2	21.63	21.68	21.69	21.69	21.70	21.94	21.91	21.82	21.76	21.77
	a_3	22.20	22.20	22.20	22.20	22.20	22.20	22.20	22.23	22.20	22.38
	a_4	21.00	21.00	21.00	21.00	21.32	21.36	21.64	22.00	22.79	22.44
	a_5	20.80	20.87	20.98	21.02	21.04	20.93	20.94	20.92	21.01	20.88
	a_6	22.70	22.70	23.12	24.25	24.07	24.15	23.80	24.28	23.70	24.07
	b_1	3.90	3.90	3.87	3.54	3.64	3.83	3.86	3.88	3.90	3.89
	b_2	3.80	3.80	3.80	3.80	3.89	3.95	3.93	3.99	3.92	3.99
	b_3	12.32	12.32	12.32	12.32	12.38	12.62	12.72	13.01	13.02	13.08
	w_2	0.60	0.60	0.61	0.61	0.62	0.64	0.65	0.63	0.67	0.65
	L	11.15	11.15	11.12	11.04	11.05	10.82	10.74	10.62	10.60	10.59
	D	28.34	29.03	29.77	31.28	31.99	33.18	33.87	34.40	35.35	37.00
	O	5.00	5.00	5.00	5.00	5.00	5.00	5.00	5.02	5.00	5.09

TABLE 5.2: MULTI-OBJECTIVE OPTIMIZATION OF UWB MONOPOLE: COST BREAKDOWN

Algorithm step	Number of model evaluations	CPU-time	
		Absolute [h]	Relative to R_f
Design space reduction	R_c	800	4.89
	R_f	4	0.67
Data acquisition and RSA construction	R_c	1500	9.17
MOEA optimization	R_s	50000	N/A
Pareto set refinement	R_f	30	5
Total cost	N/A	N/A	19.73
Direct search (low-fidelity model) [#]	R_c	50000	305.6
Direct search (high-fidelity model) [#]	R_f	50000	8333.3

[#] Estimated based on the number of R_s evaluations during MOEA optimization

The reduced region of the search space X_{Sr} has been obtained using the method of Section 4.3.5. Its corresponding bounds are: $\mathbf{l}_{Sr} = [9.8 \ 9.5 \ 1 \ 6.14 \ 6.7 \ 5.83 \ 6.33 \ 5 \ 27 \ 0.72 \ 3.94 \ 1 \ 3.24 \ 0.44]^T$, $\mathbf{u}_{Sr} = [10 \ 10 \ 1.3 \ 6.82 \ 7.21 \ 6.1 \ 10.89 \ 5 \ 29.17 \ 1 \ 4.2 \ 1.3 \ 3.64 \ 0.98]^T$. It should be noted that the dimen-

sionality of the problem has been reduced to 13 parameters because $g_2 = 5$ for all (\mathbf{R}_c and \mathbf{R}_f) extreme designs. The reduced space X_{Sr} is 10^{12} times smaller (volume-wise) as compared to X_7 . The kriging interpolation model \mathbf{R}_s has been constructed using 1000 LHS-allocated \mathbf{R}_c training samples (100 samples per iteration; cf. Section 4.2.1) and 4 \mathbf{R}_c extreme designs obtained by space reduction. The cross-validation-based RMS error of the RSA is below 2 percent.

In the next step, the initial Pareto set has been obtained by MOEA optimization (setup: 500 individuals, 50 iterations) of the \mathbf{R}_s model. Subsequently, the Pareto front has been refined using the co-kriging methodology (cf. Section 4.4.2). The number of MOEA iterations has been reduced to 25 because the initial population for co-kriging-based correction is already a good representation of the Pareto front (cf. Section 4.4). The convergence of the process has been obtained after three iterations, i.e., a total of 30 \mathbf{R}_f model evaluations.

For the sake of numerical validation, a set of ten high-fidelity designs has been selected along the obtained Pareto front and evaluated (see Figure 5.5(a) for comparison). The alignment between the optimized co-kriging surrogate and the \mathbf{R}_f test samples is very good. The largest design with footprint of 1050 mm^2 exhibits the lowest in-band reflection of -12.5 dB . The area of the antenna that fulfills design specifications is 875 mm^2 . The variability of objectives F_1 and F_2 along the Pareto front is 2.5 dB and 175 mm^2 (almost 17%), respectively. The details concerning the selected high-fidelity Pareto set are gathered in Table 5.3, whereas the frequency responses of the selected optimal designs are shown in Figure 5.6. It should be noted that the high-fidelity Pareto front obtained using response correction indicate that inaccuracy of the \mathbf{R}_c increases along X_{Rr} (see Figure 5.5(b)) which justifies the utilization of co-kriging refinement.

From practical point of view, the antenna is “flexible” with respect to reflection and size requirements. At the same time, the influence of MIMO miniaturization on isolation between the radiators is limited (see Figure 5.6). This is because the changes of the parameter g_3 that affects the distance between along the Pareto designs are limited.

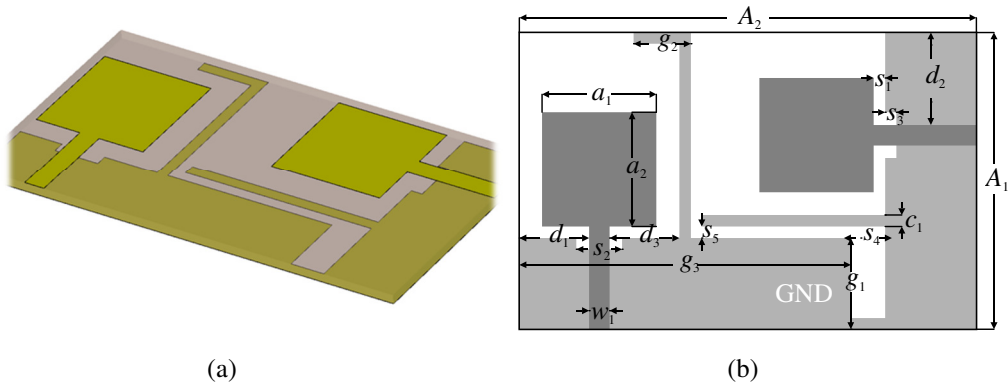


Figure 5.4: A compact UWB MIMO antenna: (a) 3D visualization; and (b) geometrical details [208].

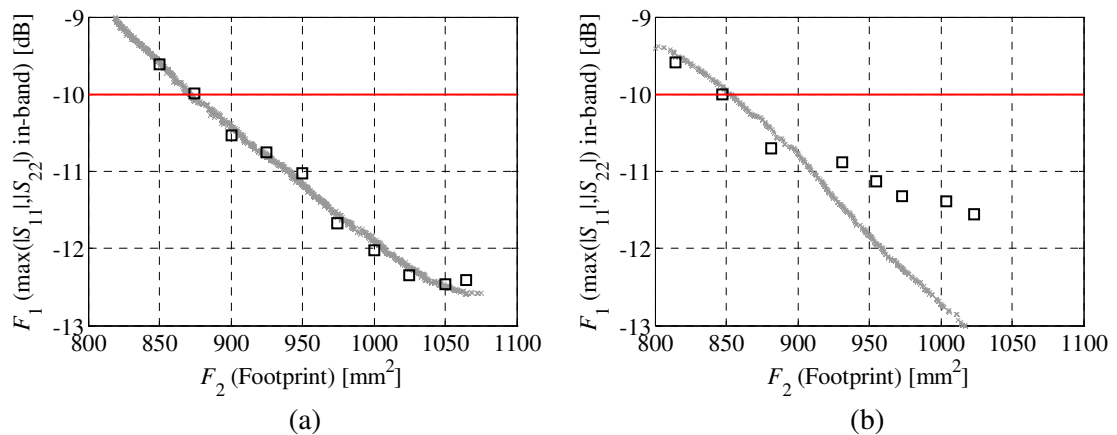


Figure 5.5: The \mathbf{R}_s (\times) and \mathbf{R}_f (\square) Pareto sets obtained using: (a) co-kriging; and (b) response correction techniques [208]. Note that inaccuracy of \mathbf{R}_s Pareto set in (b) increases for lower reflection levels.

TABLE 5.3: SELECTED DESIGNS OF THE COMPACT UWB MIMO ANTENNA

		Antenna designs									
		$\mathbf{x}_f^{(1)}$	$\mathbf{x}_f^{(2)}$	$\mathbf{x}_f^{(3)}$	$\mathbf{x}_f^{(4)}$	$\mathbf{x}_f^{(5)}$	$\mathbf{x}_f^{(6)}$	$\mathbf{x}_f^{(7)}$	$\mathbf{x}_f^{(8)}$	$\mathbf{x}_f^{(9)}$	$\mathbf{x}_f^{(10)}$
F_1 [dB]		-9.6	-10.0	-10.5	-10.8	-11.0	-11.7	-12.0	-12.3	-12.5	-12.4
F_2 [mm ²]		850	874	900	925	950	975	1000	1025	1050	1064
Antenna Parameters [#]	a_1	9.90	9.91	9.89	9.89	9.85	9.86	9.87	9.88	9.87	9.89
	a_2	9.64	9.66	9.63	9.67	9.63	9.61	9.61	9.62	9.61	9.67
	c_1	1.21	1.21	1.22	1.24	1.24	1.24	1.24	1.24	1.24	1.25
	d_1	6.50	6.50	6.47	6.46	6.44	6.43	6.40	6.42	6.42	6.42
	d_2	6.97	6.97	6.95	6.90	6.86	6.86	6.83	6.83	6.86	6.86
	d_3	5.93	5.93	5.95	5.94	5.98	5.94	5.91	5.91	5.91	5.90
	g_1	7.25	7.62	7.98	8.38	8.72	9.12	9.44	9.78	10.09	10.30
	g_3	27.22	27.23	27.25	27.39	27.50	27.47	27.75	27.79	27.86	27.92
	s_1	0.79	0.76	0.80	0.78	0.80	0.79	0.84	0.79	0.81	0.81
	s_2	4.05	4.04	4.05	4.04	4.04	4.05	4.03	4.01	4.05	4.01
s_3	1.10	1.07	1.06	1.05	1.07	1.05	1.06	1.08	1.08	1.09	
s_4	3.38	3.40	3.42	3.40	3.41	3.44	3.41	3.42	3.40	3.42	
s_5	0.61	0.64	0.71	0.70	0.71	0.71	0.75	0.79	0.83	0.80	

[#] Parameter $g_2 = 5$ obtained in the course of design space reduction is excluded from table

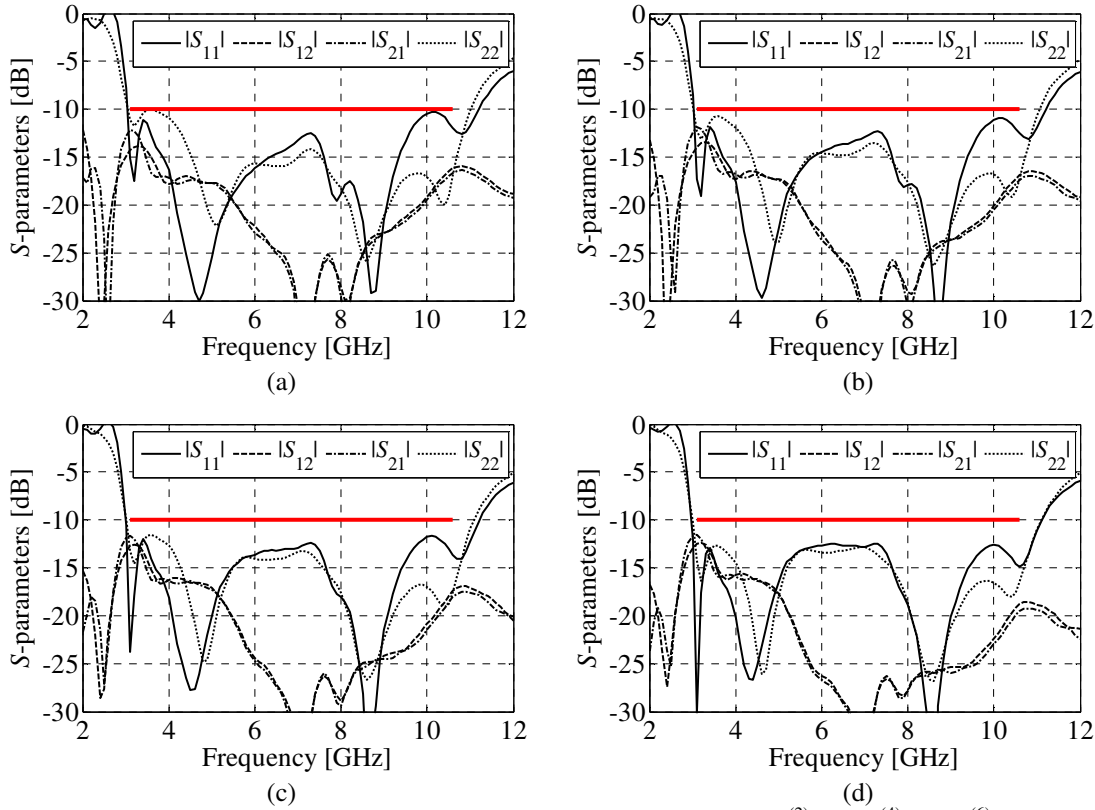


Figure 5.6: Frequency characteristics of the UWB MIMO antenna: (a) $\mathbf{x}_f^{(2)}$; (b) $\mathbf{x}_f^{(4)}$; (c) $\mathbf{x}_f^{(6)}$; and (d) $\mathbf{x}_f^{(9)}$. Note that reduction of antenna footprint has limited influence on the isolation (denoted as $|S_{21}|$ and $|S_{12}|$) between radiators [208].

The cost of the optimization process corresponds to about 204 evaluations of the \mathbf{R}_f model (~493 h of CPU-time) and it includes: a total of 1869 \mathbf{R}_c (1025 and 844 \mathbf{R}_c for optimization with respect to F_1 and F_2 , respectively) and 4 \mathbf{R}_f simulations to identify the reduced space X_{Sr} , 1000 \mathbf{R}_c evaluations for construction of the \mathbf{R}_s model, and a total of 30 \mathbf{R}_f simulations for co-kriging-based refinement of the initial Pareto set. At the same time, the estimated cost of direct MOEA optimization (25000 evaluations) within X_I is 493 hours or 347 for \mathbf{R}_c or \mathbf{R}_f , respectively. A detailed cost breakdown of the design optimization procedure is provided in Table 5.4.

TABLE 5.4: COMPACT MIMO ANTENNA: COST BREAKDOWN OF MULTI-OBJECTIVE DESIGN

Algorithm step	Number of model evaluations	CPU-time		
		Absolute [h]	Relative to R_f	
Design space reduction	R_c	1869	36.86	110.58
	R_f	4	1.33	4
Data acquisition and RSA construction	R_c	1000	19.72	59.17
MOEA optimization	R_s	25000	N/A	N/A
Pareto set	R_f	30	10	30
refinement	R_s	37500	N/A	N/A
Total cost	N/A	N/A	67.91	203.75
Direct search (low-fidelity model) [#]	R_c	25000	493.1	1479.3
Direct search (high-fidelity model) [#]	R_f	25000	8333.3	25000

[#] Estimated based on the number of R_s evaluations during MOEA optimization

5.3 Planar Quasi-Yagi-Uda Antenna

The third design example is a compact planar quasi-Yagi-Uda antenna shown in Figure 5.7 [86, 205]. As before, the structure is implemented on the Taconic RF-35 substrate. The antenna consists of a dipole-driven element excited by a coplanar stripline (CPS) and two directors. The dipole is fed through a microstrip-to-CPS transition. An impedance transformer allows for obtaining wideband operation of the antenna. Moreover, the compact geometry is ensured by two symmetrical ground plane stubs which increase the current path. The design is represented by a 24-variable vector: $\mathbf{x} = [w_0 d_1 d_2 g_1 l_1 l_2 l_3 l_4 l_6 l_7 l_8 l_f o_1 o_2 s_1 s_2 s_3 w_1 w_2 w_3 w_4 w_5 w_7 w_8]^T$. The relative parameter is $l_5 = 3l_3$, whereas $d_3 = 3$, $d_4 = 6.5$, $w_f = 1.7$ and $w_6 = 1$ (all dimensions are in mm). The bounds of the initial search space X_I are: $\mathbf{l} = [20 \ 0 \ 1 \ 1 \ 0.1 \ 1 \ 0.2 \ 0.2 \ 1 \ 5 \ 5 \ 0 \ 0 \ 1 \ 1 \ 1 \ 0.2 \ 1.2 \ 2 \ 2.9 \ 0.5 \ 0.5 \ 0.5]^T$ and $\mathbf{u} = [40 \ 1 \ 5 \ 5 \ 4 \ 4 \ 1.2 \ 1.2 \ 5 \ 13 \ 13 \ 13 \ 2 \ 2 \ 4 \ 4 \ 4 \ 1.2 \ 2.2 \ 3 \ 3.9 \ 2.5 \ 2.5 \ 2.5]^T$.

Two antenna models are utilized: the high- (~2,100,000 mesh cells; average simulation time: 13 min) and the low-fidelity (~80,000 cells; simulation: 40 s) one. Two design objectives are considered, i.e., F_1 – minimization of maximal in-band reflection (4.33) and F_2 – maximization of antenna average gain G . The second objective is given by

$$F_2(\mathbf{x}) = -\left\{ \langle G(\mathbf{x}, f) \rangle : f_L \leq f \leq f_H \right\} \quad (5.1)$$

where $f_L = 4$ GHz and $f_H = 10$ GHz define the frequency band of interest.

The search X_I has been reduced using the method of Section 4.3.3 [205]. It should be noted that, in the course of design space reduction, objective in (5.1) has been constrained by (4.35). After the first step of the process (cf. Section 4.3.2), dimensionality of the problem has been reduced to 16 parameters because $l_f = 7.5$, $w_1 = 0.7$, $w_0 = 28.86$, $l_4 = 0.58$, $o_2 = 0.13$, $d_2 = 3$, $l_7 = 9.47$ and $l_8 = 6.21$ remain fixed for both extreme Pareto designs. Therefore, the initially reduced space X_S is represented by the vector $\mathbf{x} = [d_1 g_1 l_1 l_2 l_3 l_6 o_1 s_1 s_2 s_3 w_2 w_3 w_4 w_5 w_7 w_8]^T$. The lower and upper bounds of X_S are $\mathbf{l}_S = [0.65 \ 1.63 \ 1.9 \ 2.02 \ 0.72 \ 2.6 \ 0.09 \ 2 \ 2 \ 2 \ 1.7 \ 2.3 \ 2.9 \ 1.6 \ 1.68 \ 2.24]^T$ and $\mathbf{u}_S = [0.68 \ 3.09 \ 2 \ 2.07 \ 0.96 \ 2.83 \ 1.09 \ 2.2 \ 2.13 \ 3.73 \ 2.04 \ 2.92 \ 3.4 \ 2.08 \ 2.43 \ 2.45]^T$. The space region X_S is 10^{18} times (volume-wise) smaller as compared to X_I . In the next step, X_S has been rotated and reduced by a factor of 3 with respect to all dimensions except the one corresponding to the main diagonal of the original box. The rotated design space X_R is 7 orders of magnitude smaller than X_S , thus the total reduction factor is 10^{25} .

In the next step, the kriging interpolation model R_s has been identified within X_R . The acceptable accuracy of the RSA has been obtained using only 502 LHS-allocated training samples. The RMS error of R_s is 2 percent. For the sake of comparison, the RSA has been also constructed within X_S .

The data acquisition process has been terminated after 2000 R_c simulations (RSA model error 3%). Both models have been utilized for MOEA optimization (algorithm setup: 50 iterations, 500 individuals) and the obtained initial Pareto sets have been refined using response correction technique of Section 4.4.1. A comparison between R_f and R_s representations of the Pareto fronts from X_S and X_R is shown in Figure 5.8. The results indicate that the slope of the front from X_S is noticeably larger than for the one from X_R , which is due to the limited exploration capabilities of the MOEA near to corners of the 16-dimensional search space. This problem is mitigated in X_R because the extreme designs are located on its faces. It should be noted that despite the worse accuracy, the cost of RSA construction within X_S is four times higher than in X_R .

The high-fidelity model design from the rotated search space with the highest average gain of 6.84 dB simultaneously exhibits the worst in-band reflection of -11 dB. The design with the lowest reflection of -16.7 dB features the smallest average gain of 6.43 dB. The variability of objectives F_1 and F_2 along the Pareto front is 5.7 dB and 0.41 dB, respectively. The detailed dimensions of the selected Pareto-optimal designs are gathered in Table 5.5 whereas their corresponding frequency characteristics are shown in Figure 5.9. It should be noted that, for considered antenna topology, modification of dimensions has limited impact on the gain. One can consider design of the structure with respect to other performance requirements (e.g., minimization of reflection, maximization of front-to-back ratio, or size reduction). The experimental validation of the considered antenna is described in Section 6.2.

The detailed cost breakdown of the design optimization procedure is provided in Table 5.6. The numerical cost of the multi-objective antenna design corresponds to about 205 R_f simulations (~ 45 hours of CPU-time). The design space reduction process involved 2917 R_c simulations (1076 R_c for minimization of the maximal reflection and 1841 R_c for maximization of average gain), 502 R_c evaluations for the acquisition of training samples and 30 R_f simulations for refinement of selected Pareto-optimal designs (three iterations). It should be noted that the estimated cost of direct MOEA-based optimization (25000 model evaluations) of the R_f model of discussed antenna is over 260 days of the CPU-time. The estimated cost of direct R_c model optimization corresponds to over 1280 R_f evaluations (~ 278 hours). Moreover, the cost of MOEA optimization in X_S is over 61 hours of CPU-time.

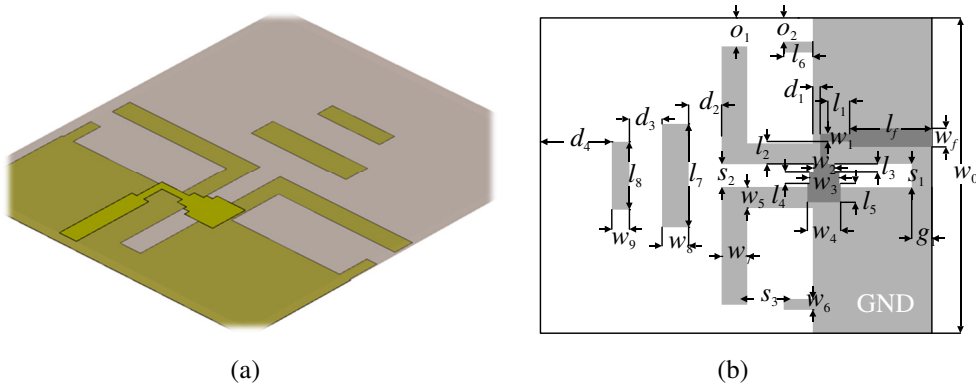


Figure 5.7: Planar quasi-Yagi-Uda antenna: (a) 3D visualization; and (b) geometrical details [205].

TABLE 5.5: QUASI YAGI-UDA ANTENNA: SELECTED DESIGNS

	Objectives		Antenna parameters																
	F_1 [dB]	F_2 [dB]	d_1	g_1	l_1	l_2	l_3	l_6	o_1	s_1	s_2	s_3	w_2	w_3	w_4	w_5	w_7	w_8	
Antenna designs	$\mathbf{x}_f^{(1)}$	-9.4	6.88	0.68	1.48	1.99	2.08	0.75	2.65	0.90	2.19	2.14	3.59	1.97	2.88	3.04	2.13	2.49	2.44
	$\mathbf{x}_f^{(2)}$	-11.0	6.83	0.67	1.84	1.99	2.07	0.73	2.66	1.01	2.14	2.09	3.35	1.95	2.76	3.05	1.92	2.33	2.43
	$\mathbf{x}_f^{(3)}$	-12.6	6.78	0.67	2.15	1.96	2.05	0.80	2.66	0.72	2.12	2.09	3.15	1.95	2.68	3.14	1.87	2.25	2.38
	$\mathbf{x}_f^{(4)}$	-13.5	6.73	0.67	2.31	1.96	2.06	0.81	2.69	0.64	2.10	2.07	3.05	1.90	2.64	3.13	1.82	2.16	2.37
	$\mathbf{x}_f^{(5)}$	-14.0	6.69	0.67	2.32	1.95	2.05	0.82	2.70	0.58	2.09	2.06	2.90	1.86	2.61	3.15	1.78	2.07	2.36
	$\mathbf{x}_f^{(6)}$	-15.0	6.60	0.66	2.62	1.93	2.03	0.88	2.78	0.31	2.05	2.03	2.60	1.83	2.49	3.21	1.74	1.99	2.33
	$\mathbf{x}_f^{(7)}$	-16.0	6.54	0.66	2.75	1.93	2.04	0.92	2.79	0.19	2.08	2.04	2.46	1.77	2.55	3.31	1.70	1.91	2.28
	$\mathbf{x}_f^{(8)}$	-16.4	6.51	0.66	2.76	1.91	2.04	0.91	2.79	0.21	2.03	2.02	2.32	1.79	2.50	3.28	1.71	1.87	2.30
	$\mathbf{x}_f^{(9)}$	-16.5	6.47	0.65	2.91	1.92	2.03	0.93	2.84	0.16	2.04	2.03	2.24	1.80	2.50	3.36	1.65	1.83	2.30
	$\mathbf{x}_f^{(10)}$	-16.7	6.43	0.65	2.95	1.91	2.03	0.93	2.85	0.29	2.02	2.02	2.08	1.76	2.43	3.42	1.59	1.84	2.28

[#] Parameters l_f , w_1 , w_0 , l_4 , o_2 , d_2 , l_7 and l_8 are excluded from the table

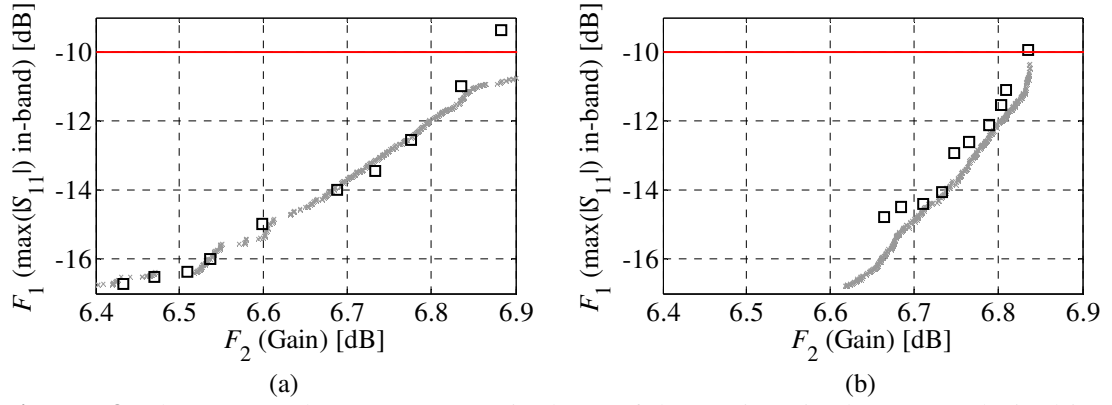


Figure 5.8: The R_f (\square) and R_s (\times) Pareto-optimal sets of the quasi-Yagi-Uda antenna obtained in: (a) rotated; and (b) initially reduced search spaces [205].

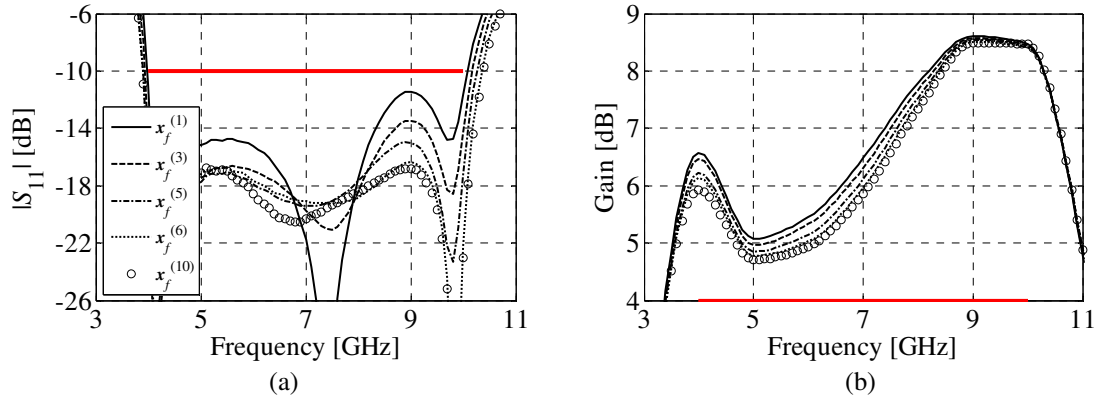


Figure 5.9: Frequency responses of quasi-Yagi-Uda antenna [205]: (a) reflection; and (b) gain. For corresponding dimensions of the designs see Table 5.5.

TABLE 5.6: QUASI YAGI-UDA ANTENNA: DESIGN COST BREAKDOWN

Algorithm step	Number of model evaluations	CPU-time		
		Absolute [h]	Relative to R_f	
Design space reduction	R_c	2917	32.41	149.59
Data acquisition and RSA construction	R_c	502	5.58	25.74
MOEA optimization	R_s	25000	N/A	N/A
Pareto set refinement	R_f	30	6.5	30
Total cost	N/A	N/A	44.49	205.33
Optimization within X_S (total cost) [†]	N/A	N/A	61.15	282.26
Direct search (low-fidelity model) [#]	R_c	25000	277.78	1282.1
Direct search (high-fidelity model) [#]	R_f	25000	5416.7	25000

[#] Estimated based on the number of R_s evaluations during MOEA optimization

[†] Data acquisition terminated after 2002 R_c simulations

5.4 Planar Yagi-Uda antenna

Consider a planar Yagi-Uda antenna shown in Figure 5.10 [106, 148]. The antenna is implemented on a Rogers RO6010 dielectric substrate ($\epsilon_r = 10.2$, $\tan\delta = 0.0023$, $h = 0.635$ mm). It consists of a driven element fed by a microstrip-to-coplanar strip transition, a director and an asymmetrical microstrip balun. The input impedance is 50 ohm. The design variables are: $x =$

$[s_1 \ s_2 \ v_1 \ v_2 \ u_1 \ u_2 \ u_3 \ u_4]^T$, whereas parameters $w_1 = w_3 = w_4 = 0.6$, $w_2 = 1.2$, $u_5 = 1.5$, $s_3 = 3$ and $v_3 = 17.5$ are fixed (all dimensions in mm).

The high-fidelity model \mathbf{R}_f of the structure consists of $\sim 1,500,000$ hexahedral mesh cells and its average evaluation time is 18 min. The low-fidelity model \mathbf{R}_c contains $\sim 85,680$ mesh cells. Its typical simulation time is 110 s. The bounds of the initial search space X_I are: $\mathbf{l} = [3.8 \ 2.8 \ 8.0 \ 4.0 \ 3.0 \ 4.5 \ 1.8 \ 1.3]^T$, and $\mathbf{u} = [4.4 \ 4.5 \ 9.8 \ 5.2 \ 4.2 \ 5.2 \ 2.6 \ 1.8]^T$. Two design objectives are considered: F_1 – minimization of the antenna maximal reflection (4.33) and F_2 maximization of average gain (5.1), respectively.

The design space reduction has been performed using the algorithm of Section 4.3.1 [204]. Note that during space reduction (5.1) has been constrained by (4.35). The first stage of the process has been terminated after 153 \mathbf{R}_c simulations. The second stage has been completed after 137 evaluations of the \mathbf{R}_c model. The bounds of the refined space X_D are $\mathbf{l}_D = [4.1 \ 3.63 \ 8.11 \ 4.27 \ 3.6 \ 4.67 \ 1.8 \ 1.3]^T$ and $\mathbf{u}_D = [4.4 \ 4.5 \ 8.9 \ 5.4 \ 3.8 \ 4.85 \ 2.2 \ 1.55]^T$. The volume-wise reduction of X_D with respect to X_I is 10^3 .

In contrary to the previously described design cases, the iterative construction of the RSA model \mathbf{R}_s has not been performed here. The kriging model has been constructed within X_D using a total of 1344 \mathbf{R}_s model samples (1000 allocated using LHS, 256 obtained at the corners of X_D , as well as 88 obtained in the course of space reduction). The average relative RMS error of the \mathbf{R}_s , calculated using cross-validation scheme, is 3 percent. For the sake of comparison, the same set of 1344 samples has been rescaled to X_I and utilized for construction of the RSA. However, RMS error of 9% makes model unsuitable for optimization. It should be noted that the number of samples required for construction of a reliable RSA in X_I should be increased by at least 3 orders—estimated using (4.3)—which is infeasible from the point of view of numerical cost.

In the next step, the initial Pareto set has been obtained by MOEA optimization (setup: 500 individuals; 100 generations) of the \mathbf{R}_s model from X_D . Then a set of ten Pareto-optimal designs has been refined using the method of Section 4.4.1. The high- and low-fidelity Pareto front representations are compared in Figure 5.11(a). It should be noted that the slope of the initial Pareto set increases for the lower values of the average gain. At the same time, it remains more or less constant for the high-fidelity designs. The discrepancies result from increasing inaccuracy of the low-fidelity model \mathbf{R}_c along X_D . This problem could be mitigated by utilization of co-kriging-based-refinement instead of response correction technique (see Figure 5.11(b)).

The optimized antenna design with the lowest acceptable reflection of -10.5 dB features the average gain of almost 6.4 dB. At the same time, the solution with the lowest in-band reflection of -19.8 dB exhibits the average gain of about 5.5 dB. Therefore, variability of objectives F_1 and F_2 along the region of Pareto set of interest is 9.3 dB and 0.9 dB, respectively. Although change of the antenna in-band gain is limited, it is over twice as large as for the structure of Section 5.3. From this perspective, identification of Pareto designs may be justified. The key data on the optimized antenna designs is gathered in Table 5.7. The frequency responses of the selected samples are shown in Figure 5.12. It should be noted that, similarly to the results of Section 5.3, the variability of reflection along the Pareto front is about ten times larger than the change of average gain.

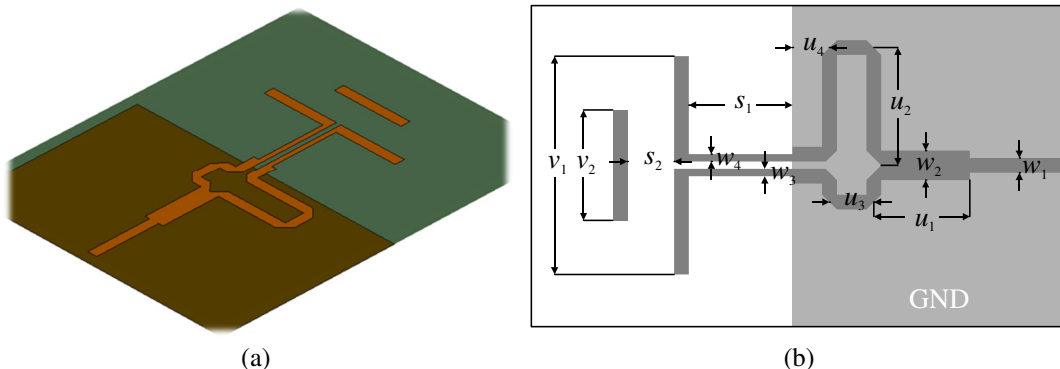


Figure 5.10: An eight-variable planar Yagi-Uda antenna: (a) 3D visualization; and (b) top-view with geometrical details [106].

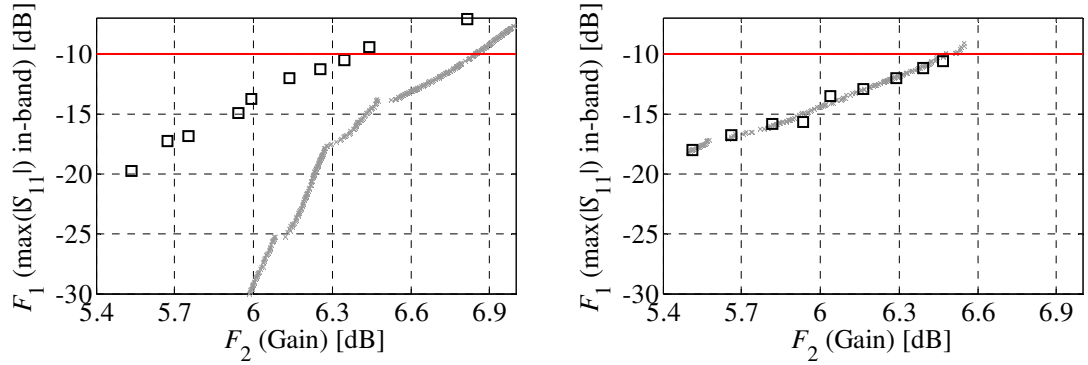


Figure 5.11: Planar Yagi-Uda antenna: comparison of the low- (\times) and high-fidelity (\square) Pareto front representations obtained using: (a) response correction [106]; and (b) co-kriging [217].

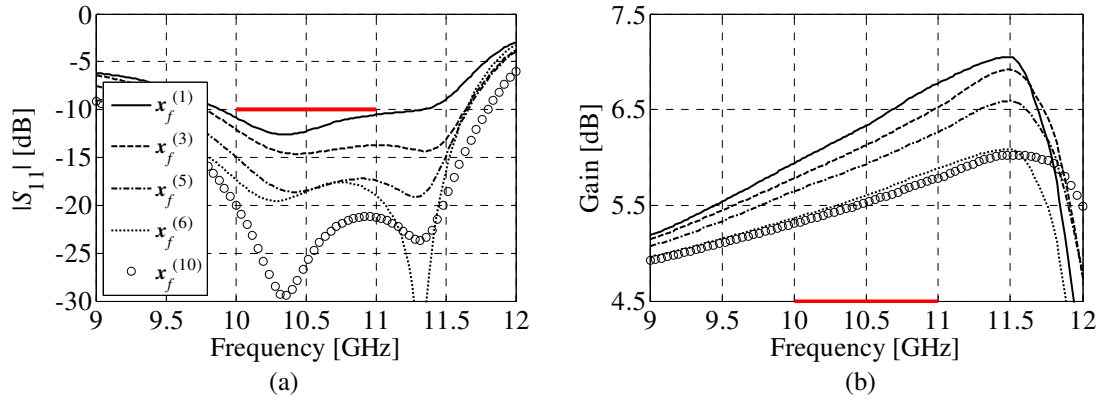


Figure 5.12: Frequency responses of Yagi-Uda antenna: (a) reflection; and (b) gain. For corresponding dimensions of the designs see Table 5.7.

TABLE 5.7: SELECTED DESIGNS OF PLANAR YAGI-UDA ANTENNA

	Objectives		Antenna parameters								
	F_1 [dB]	F_2 [dB]	d_1	g_1	l_1	l_2	l_3	l_6	o_1	s_1	
Antenna designs	$x_f^{(1)}$	-7.1	6.81	4.12	3.64	8.89	4.34	3.80	4.73	2.13	1.50
	$x_f^{(2)}$	-9.4	6.44	4.11	3.63	8.86	4.39	3.80	4.73	2.12	1.49
	$x_f^{(3)}$	-10.5	6.35	4.11	3.63	8.87	4.43	3.80	4.73	2.12	1.49
	$x_f^{(4)}$	-11.3	6.26	4.12	3.71	8.83	4.54	3.73	4.76	2.17	1.51
	$x_f^{(5)}$	-12.0	6.14	4.12	3.69	8.84	4.57	3.73	4.76	2.17	1.51
	$x_f^{(6)}$	-13.8	5.99	4.13	3.77	8.82	4.59	3.73	4.77	2.17	1.51
	$x_f^{(7)}$	-15.0	5.94	4.13	3.80	8.81	4.61	3.72	4.77	2.18	1.51
	$x_f^{(8)}$	-16.8	5.75	4.20	4.28	8.48	4.49	3.69	4.76	2.18	1.46
	$x_f^{(9)}$	-17.3	5.67	4.18	4.35	8.29	4.86	3.67	4.78	2.11	1.51
	$x_f^{(10)}$	-19.8	5.54	4.39	4.43	8.11	5.40	3.78	4.84	2.20	1.55

The total computational cost of multi-objective optimization process corresponds to about 188 R_f simulations (~ 56 hours of CPU-time) and it includes: 290 and 1256 R_c for design space reduction and data acquisition, as well as 30 R_f evaluations for the refinement of 10 selected antenna designs. The estimated cost of direct MOEA-based optimization (50,000 simulations) is almost 64 days for the R_c model and 625 days for the R_f model. The cost breakdown of the multi-objective antenna design is provided in Table 5.8.

5.5 Quasi-Isotropic Dielectric Resonator Antenna

In this section, multi-objective design optimization of a quasi-isotropic dielectric resonator antenna is considered [177, 218]. It should be noted that the DRA features narrow-band operation (the expected bandwidth is only 4%) and, from this perspective, it is beyond the main scope of this dissertation.

TABLE 5.8: OPTIMIZATION OF YAGI-UDA ANTENNA: COST BREAKDOWN

Algorithm step	Number of model evaluations	CPU-time		
		Absolute [h]	Relative to R_f	
Design space reduction	R_c	290	8.86	29.53
Data acquisition and RSA construction	R_c	1256	38.38	127.93
MOEA optimization	R_s	50000	N/A	N/A
Pareto set refinement	R_f	30	9	30
Total cost	N/A	N/A	56.24	187.46
Direct search (low-fidelity model) [#]	R_c	50000	1527.8	5092.6
Direct search (high-fidelity model) [#]	R_f	25000	15000	50000

[#] Estimated based on the number of R_s evaluations during MOEA optimization

The structure is shown in Figure 5.13. It consists of a cuboid shape Taconic CER-10 dielectric resonator ($\epsilon_r = 10$, $\tan\delta = 0.0035$) and a driven element in the form of a coaxial probe located within the material. The probe is fed from the bottom through a coaxial transmission line. The input impedance is 50 ohm. The antenna is modified with respect to the original design of [218] in order to introduce additional degrees of freedom for the probe location. Consequently, a better control of the structure response can be ensured in the course of the optimization process. The antenna design parameters are $\mathbf{x} = [a \ b \ c \ o_{1r} \ o_{2r} \ l_r]^T$. The relative variables are $o_1 = o_{1r} \cdot a$, $o_2 = o_{1r} \cdot b$ and $l = l_r \cdot c$, whereas dimensions $d = 1.26$ and $g = 0.82$ are fixed to ensure 50 ohm input impedance. Moreover, the conductor thickness is $t = 0.05$ (see Figure 5.13(b)). Note that utilization of the relative variables is necessary to ensure geometrical consistency of the design. The initial search space X_I is defined using the following bounds: $\mathbf{l} = [3 \ 3 \ 3 \ -0.45 \ -0.45 \ 0]^T$ and $\mathbf{u} = [30 \ 30 \ 30 \ 0.45 \ 0.45 \ 0.9]^T$. The unit for all non-relative dimensions is mm.

The design is conducted using high- (~1,000,000 mesh cells, average evaluation time: 21 min) and the low-fidelity (~55,000 cells; evaluation time: 35 s) antenna models. The following design objectives are considered: F_1 – minimization of the maximum reflection within 2.4 GHz to 2.5 GHz frequency band of interest, F_2 – minimization of antenna volume $V(\mathbf{x}) = a \times b \times c$ and F_3 – reduction of difference between minimal and maximal E-field strength in x-z plane (cf. Figure 5.13). The objectives F_1 and F_2 are given by (4.33) and (4.34). The objective F_3 is defined as

$$F_3(\mathbf{x}) = \max \{E(\mathbf{x}, \varphi)\} - \min \{E(\mathbf{x}, \varphi)\} \quad (5.2)$$

where $E(\mathbf{x}, \varphi)$ represents E-field strength for the given angle φ ($0^\circ \leq \varphi \leq 360^\circ$) in x-z plane. The objective is calculated at the center frequency of 2.45 GHz.

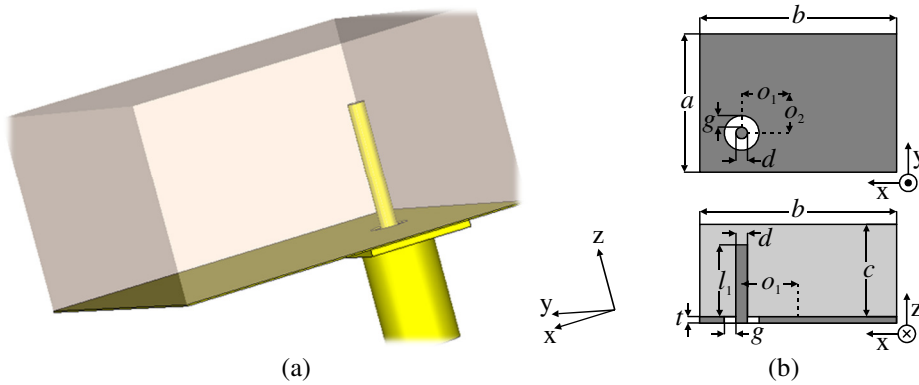


Figure 5.13: Compact quasi-isotropic DRA antenna: (a) 3D visualization; (b) bottom and cross section views with geometrical details. Dark- and light-shade gray represent metal parts of the antenna and the dielectric resonator, respectively [185].

It should be noted that, in general, the objectives F_2 and F_3 are not conflicted. The reason is that the radiation pattern in x-z plane is the Fourier transform of the field in the aperture determined by the antenna dimension corresponding to this plane (in this case, the dimension b) [89]. As a consequence, the omnidirectional properties of the DRA in the x-z plane will deteriorate with increasing b . Nonetheless, other parameters may also contribute to the radiation pattern, to some extent. From this perspective, multi-objective optimization with respect to F_2 and F_3 is still considered relevant.

The search space X_I has been reduced using the algorithm of Section 4.3.4 [177, 185]. Note that, in the course of space reduction, objectives F_2 and F_3 have been constrained by (4.35). The initially reduced space X_S , obtained after the first step of the algorithm, is defined by the following bounds: $\mathbf{l}_S = [3.3 \ 24.5 \ 14.5 \ -0.03 \ 0.37 \ 0.63]^T$ and $\mathbf{u}_S = [29.8 \ 30 \ 15.8 \ 0.16 \ 0.45 \ 0.98]^T$. Note that X_S is four orders of magnitude smaller (volume-wise) than X_I . In the next step, the \mathbf{R}_f model has been evaluated at the extreme Pareto samples utilized to define X_S . Obtained responses have been used to perform pre-refinement of the \mathbf{R}_c model responses by means of the space mapping technique (cf. Section 2.2.3.1). Subsequently, five iterations of the data acquisition/RSA construction loop have been performed within X_S . The kriging interpolation model \mathbf{R}_s has been constructed using 576 samples of the corrected \mathbf{R}_c model. The training set consists of 500 LHS-allocated samples (100 samples per iteration) supplemented with 64 corners of the X_S and additional 12 samples obtained during the pre-refinement step. The cross-validation-based RMS error of the \mathbf{R}_s model is 3 percent.

The initial Pareto front has been obtained using MOEA (setup: 2000 individuals, 50 iterations). Subsequently, its feasible fraction (i.e., designs with maximum in-band reflection below -10 dB) has been utilized for the confinement of the design space. It should be noted that the confined space X_C is over 10 times smaller (volume-wise) than X_S . The overall reduction rate of X_C in comparison to X_I is 10^5 . The \mathbf{R}_{sC} model has been constructed within X_C using only 170 LHS-allocated \mathbf{R}_c samples (RMS error 1.5%). Finally, MOEA optimization of the \mathbf{R}_{sC} model has been performed to obtain the final Pareto-optimal set. It should be noted that due to the pre-refinement of the low-fidelity training data, the RSA model constructed within X_C is sufficiently accurate. Consequently, no further refinement is required and the Pareto set obtained in X_C is considered the final outcome of the design optimization procedure. For the sake of verification, a set of Pareto samples has been evaluated using the \mathbf{R}_f model (see Figure 5.14(a)). Although the results are in good agreement, a slight misalignment of the reflection responses between \mathbf{R}_{sC} and \mathbf{R}_f can be observed. The reason is a residual inaccuracy of the corrected low-fidelity model (the discrepancies are below 0.5 dB). At the same time, the responses of F_2 and F_3 remain accurate.

Among the evaluated high-fidelity designs, the antenna with the smallest volume features the largest E-field discrepancy of 7.9 dB and reflection of -10.6 dB. The design with the lowest E-field variations of 4.81 dB simultaneously exhibits the largest volume (over $11,000 \text{ mm}^3$) and barely acceptable reflection (-10 dB). Finally, the lowest in-band reflection of -11.4 dB has been obtained for the design with volume of almost 5700 mm^3 and E-field discrepancy of 6.84 dB. The ranges of variability of objectives F_1 , F_2 , and F_3 along the Pareto front are 2.3 dB, 7823 mm^3 and 3.1 dB, respectively. The reflection responses and the radiation pattern characteristics of the antenna designs from Table 5.9 are shown in Figure 5.15(a) and Figure 5.16(a), respectively. The results gathered in Table 5.9 indicate that the omnidirectional properties of the antenna (objective F_3) change inversely proportional to b . However, for designs $\mathbf{x}_f^{(1)}$ and $\mathbf{x}_f^{(2)}$, a slight deterioration of the radiation pattern with the increase of b can be observed which suggests that other parameters also contribute to F_3 .

The results indicate that multi-objective optimization of DRA allows for obtaining diverse design solutions for problems with more than two objectives. Selected Pareto-optimal structures could be utilized for volume-limited applications or for tasks where highly omnidirectional properties are desired. Also, some of the Pareto designs provide reflection margin that is sufficient to mitigate the risk of violating specification (e.g., due to fabrication tolerances).

The numerical cost of antenna optimization corresponds to about 42 \mathbf{R}_f simulations (~ 14.5 hours of CPU-time). The cost includes: 610 \mathbf{R}_c evaluations required to determine X_I , 4 \mathbf{R}_f simulations for pre-refinement of the \mathbf{R}_c model, 567 \mathbf{R}_c simulations for construction of the initial RSA, and

170 \mathbf{R}_c to establish the kriging model \mathbf{R}_{sC} in the confined space X_C . The estimated cost of direct MOEA optimization (100,000 simulations) of \mathbf{R}_f and \mathbf{R}_c model is about 4 years and over 40 days, respectively.

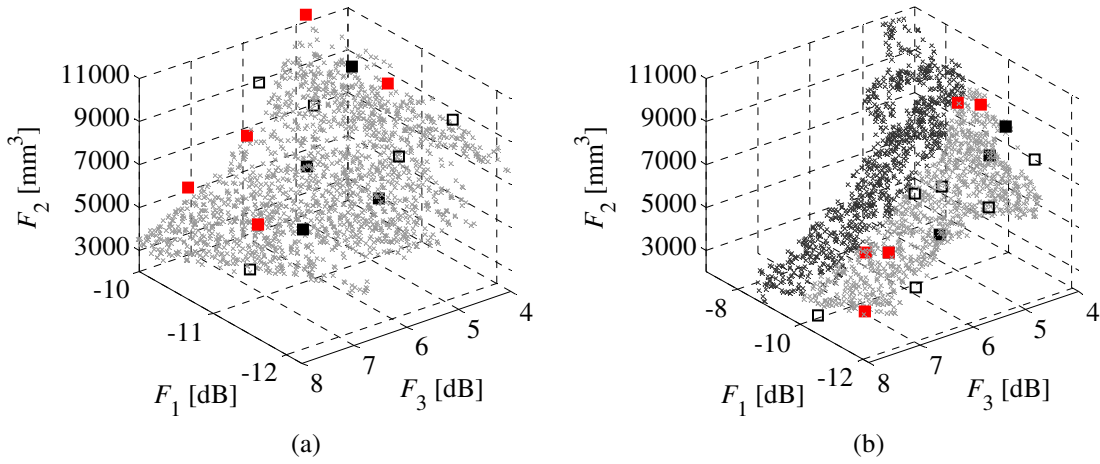


Figure 5.14: Pareto front representations of the DRA antenna from [177]: (a) confined space X_C ; (b) reduced space X_S . The \mathbf{R}_f and \mathbf{R}_s Pareto designs are denoted by squares and light-shade gray crosses, respectively. The dark-shade gray crosses represent designs that are outside the region of interest ($|S_{11}| > -10$ dB). Detailed dimensions of the designs represented by non-empty squares are collected in Table 5.9 and Table 5.10. Responses of designs represented by red squares are shown in Figure 5.15 and Figure 5.16.

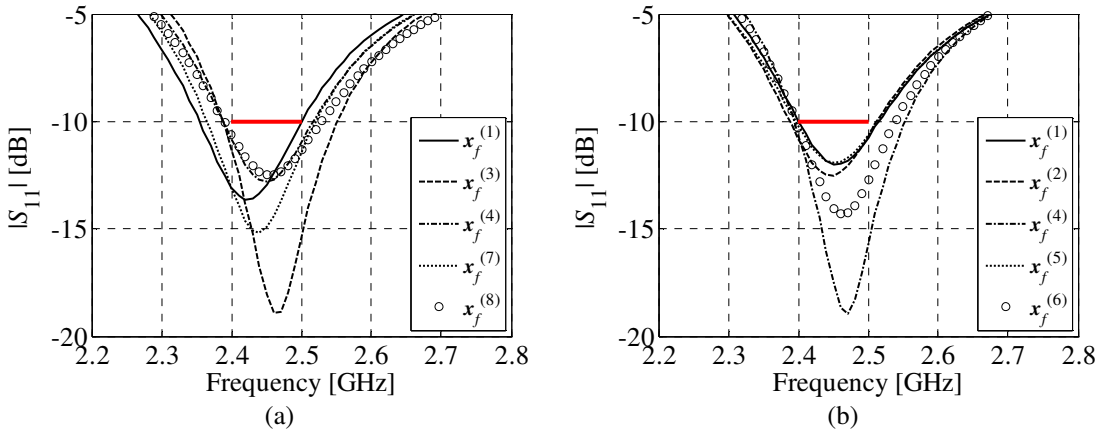


Figure 5.15: Reflection responses of selected Pareto-optimal designs obtained in: (a) confined space X_C ; and (b) initially reduced space X_S [177].

TABLE 5.9: DRA ANTENNA DESIGNS OBTAINED IN X_C

	Objectives			Antenna parameters					
	F_1 [dB]	F_2 [mm ³]	F_3 [dB]	a	b	c	o_{1r}	o_{2r}	l_r
$\mathbf{x}_f^{(1)}$	-10.0	11337	4.81	29.24	25.22	15.37	0.085	0.424	0.648
$\mathbf{x}_f^{(2)}$	-10.7	10337	4.92	27.04	25.30	15.11	0.089	0.413	0.655
$\mathbf{x}_f^{(3)}$	-11.3	10812	5.05	28.86	25.42	14.74	0.071	0.403	0.635
$\mathbf{x}_f^{(4)}$	-10.8	6760	5.93	16.47	27.17	15.11	0.052	0.423	0.641
$\mathbf{x}_f^{(5)}$	-9.9	4691	6.87	10.98	28.47	15.01	0.052	0.418	0.687
$\mathbf{x}_f^{(6)}$	-10.8	4898	6.91	11.38	28.59	15.06	0.079	0.406	0.665
$\mathbf{x}_f^{(7)}$	-11.4	5699	6.84	13.28	28.60	15.00	0.127	0.390	0.649
$\mathbf{x}_f^{(8)}$	-10.6	3514	7.90	8.00	29.62	14.83	0.094	0.398	0.715
$\mathbf{x}_f^{(9)}$	-11.2	4168	7.61	9.61	29.46	14.72	0.070	0.403	0.698
$\mathbf{x}_f^{(10)}$	-10.5	8522	5.37	21.41	26.24	15.17	0.058	0.417	0.643

For the sake of comparison, the multi-objective design has been also performed in X_S . The RSA model has been constructed using the same set of 576 R_c samples. However, pre-refinement of the training data has not been considered here. The initial Pareto set has been obtained using MOEA. The algorithm setup is the same as above. Subsequently, a set of 14 designs selected along the initial Pareto front has been refined using the response correction technique. Figure 5.14(b) shows a comparison of the low- and high-fidelity Pareto fronts.

The reflection characteristics and radiation patterns of the high-fidelity antenna designs selected from Table 5.10 are shown in Figure 5.15(b) and Figure 5.16(b). The results indicate that the design with the lowest E-field discrepancy of 4.97 dB features the volume of 9781 mm³ and reflection of -10 dB. The antenna design characterized by the smallest volume also features the highest E-field strength discrepancy (8.1 dB). The maximum in-band reflection of this design is -10.8 dB. Finally, the lowest in-band reflection of -13.2 dB has been obtained for the antenna structure with the volume of 10164 mm³ and E-field discrepancy of 5.43 dB. The ranges of variability of F_1 , F_2 , and F_3 along the Pareto front are 3.2 dB, 7308 mm³ and 3.1 dB, respectively.

The total design optimization cost in X_S corresponds to $\sim 75 R_f$ simulations (~ 26.2 hours of CPU-time). The cost includes: 610 R_c and 567 R_c simulations for determination of X_S and RSA construction, as well as 42 R_f evaluations required for the refinement of designs selected from the initial Pareto set. It should be noted that the lack of the pre-refinement step significantly increased the CPU-time of multi-objective optimization. The detailed cost breakdown of the design process can be found in Table 5.11.

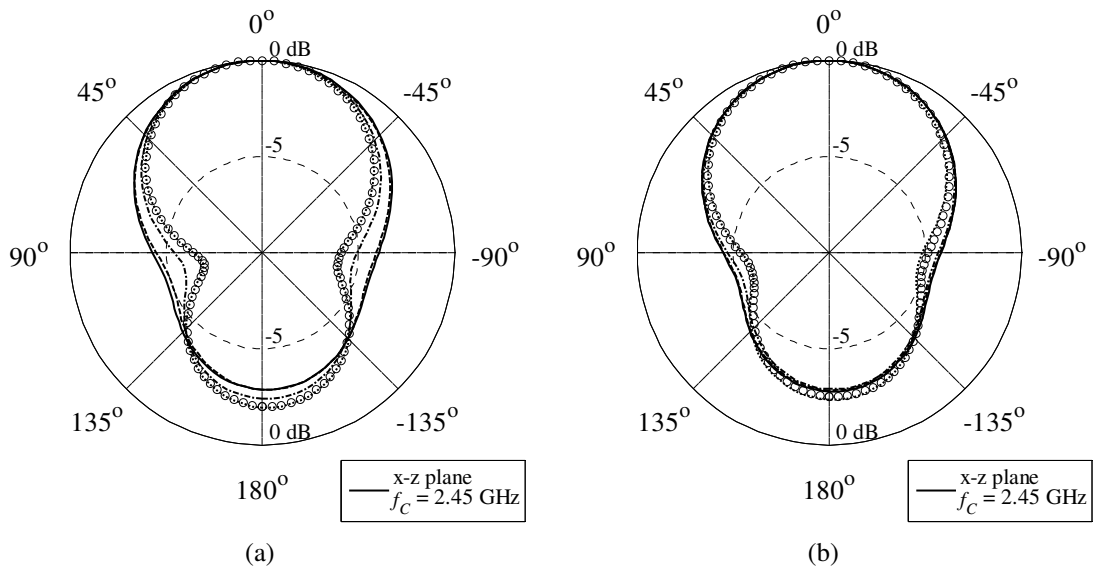


Figure 5.16: E-field radiation patterns of DRA antenna for selected Pareto-optimal designs obtained in: (a) confined space X_C ; and (b) initially reduced space X_S [177]. For explanation of markers see Figure 5.15.

TABLE 5.10: DRA ANTENNA DESIGNS OBTAINED IN X_S

	Objectives			Antenna parameters						
	F_1 [dB]	F_2 [mm ³]	F_3 [dB]	a	b	c	o_{1r}	o_{2r}	l_r	
Antenna designs	$x_f^{(1)}$	-10.0	9781	4.97	25.49	25.47	15.07	0.039	0.432	0.659
	$x_f^{(2)}$	-10.8	10424	5.02	27.10	25.64	15.00	0.035	0.439	0.659
	$x_f^{(3)}$	-10.2	6564	5.94	16.09	27.17	15.01	0.061	0.435	0.657
	$x_f^{(4)}$	-10.4	4793	6.95	11.33	28.54	14.82	0.074	0.406	0.686
	$x_f^{(5)}$	-10.8	3116	8.11	6.74	29.91	15.45	0.117	0.430	0.671
	$x_f^{(6)}$	-11.8	3963	7.84	9.18	29.67	14.55	0.110	0.408	0.690
	$x_f^{(7)}$	-13.2	10164	5.43	26.62	26.28	14.53	0.048	0.422	0.633
	$x_f^{(8)}$	-10.9	7342	5.82	18.33	27.01	14.83	0.070	0.448	0.633
	$x_f^{(9)}$	-12.4	5057	7.22	11.82	29.05	14.73	0.003	0.402	0.633
	$x_f^{(10)}$	-12.6	7870	5.95	19.91	27.26	14.50	0.082	0.449	0.633

TABLE 5.11: DRA ANTENNA OPTIMIZATION: COST BREAKDOWN

Algorithm step	Number of model evaluations	CPU-time		
		Absolute [h]	Relative to R_f	
Initial space reduction	R_c	610	5.93	16.94
Pre-refinement of R_c	R_f	4	1.4	4
Data acquisition and RSA construction	R_c	567	5.51	15.75
MOEA optimization	R_s	100000	N/A	N/A
Space confinement and RSA reset	R_c	170	1.65	4.72
MOEA optimization	R_s	100000	N/A	N/A
Pareto set refinement	R_f	0	0	0
Total cost	N/A	N/A	14.5	41.41
Optimization within X_S (total cost)	N/A	N/A	26.14	74.69
Direct search (low-fidelity model) [#]	R_c	100000	972.2	2778.3
Direct search (high-fidelity model) [#]	R_f	100000	35000	100000

[#] Estimated based on the number of R_s evaluations during MOEA optimization

The results of comparison indicate that, for the considered antenna design, identification of X_C is more numerically demanding than determination of X_S [185]. It should be emphasized that one of the most important properties of space confinement technique is the ability to accurately narrow down the space to the region containing feasible solutions. As a consequence, the model $R_{s,c}$ can be constructed using a very limited number of R_c samples. Moreover, due to space confinement, a vast majority of the Pareto set obtained within X_C fulfills the requirement with respect to the minimum acceptable reflection which is not the case in X_S (see Figure 5.14). The results indicate that the space confinement method may be useful for solving design problems with multiple design objectives. At the same it, its computational cost is larger as compared to other space reduction methods discussed in this work. As shown in this section, this problem can be mitigated by means of appropriate correction techniques (pre- or post-refinement of the RSA model). They, however, are useful only if correlation between the high- and low-fidelity models is good. The cost may be also reduced by limiting number of samples utilized for a construction of RSA within X_S .

5.6 Compact UWB Impedance Transformer

The aim of the last design example is to demonstrate that expedited multi-objective optimization method described in this work can be also applied to microwave structures. The design example is a compact three section microstrip impedance transformer shown in Figure 5.17 [120, 219]. The circuit consists of T-shaped compact microstrip resonant cells (CMRCs) [220]. The CMRC is constructed as a combination of series high-impedance and shunt low-impedance microstrip sections and it is an electrical equivalent of conventional transmission line at a certain frequency. For the sake of brevity, details related to the design of CMRC structures are not discussed here. Interested reader is referred to, e.g., [219-221].

The transformer is supposed to match the 50 ohm input to 130 ohm load within 3.1 GHz to 10.6 GHz frequency range. The structure is implemented on a 0.762 mm thick Taconic RF-35 substrate. The design is represented by a 15-variable vector: $\mathbf{x} = [w_{11} w_{21} w_{31} l_{21} l_{31} w_{12} w_{22} w_{32} l_{22} l_{32} w_{13} w_{23} w_{33} l_{23} l_{33}]^T$. Parameters $w_{i1} = 1.7$ and $w_{i2} = 0.15$ remain fixed to ensure desired source and load impedances. All dimensions are in mm.

The high-fidelity model R_f of the transformer consists of about 1,200,000 mesh cells and its average simulation time is 12 min. The low-fidelity model R_c contains ~55,000 cells (simulation time 49 s). Two design objectives are considered: F_1 – minimization of maximal in-band reflec-

tion and F_2 – reduction of the structure footprint $V(\mathbf{x}) = A \times B$ where $A = 2 \cdot (l_{21} + l_{31}) + w_{21} + w_{12} + 2 \cdot (l_{22} + l_{32}) + w_{22} + w_{13} + 2 \cdot (l_{23} + l_{33}) + w_{23}$ and $B = w_{11} + w_{31} + l_{31}$. The objectives are given by (4.33) and (4.34). The bounds of the initial search space X_I are $\mathbf{l} = [0.15 \ 0.15 \ 0.15 \ 0.5 \ 0.15 \ 0.15 \ 0.15 \ 0.15 \ 0.15 \ 0.15 \ 0.15 \ 0.15 \ 0.5 \ 0.15]^T$ and $\mathbf{u} = [1 \ 1 \ 1 \ 5 \ 0.5 \ 1 \ 1 \ 1 \ 5 \ 0.5 \ 1 \ 1 \ 1 \ 5 \ 0.5]^T$. Note that \mathbf{l} and \mathbf{u} are defined so that the technology limitations of the circuit (i.e., minimal width of narrow strips and slots) are accounted for [220].

The design space reduction has been performed using the algorithm of Section 4.3.2 [120]. Space reduction has been performed with constraint (4.35) imposed on objective (4.34). The dimensionality of X_S is reduced to 12 variables because $w_{21} = 0.15$, $l_{31} = 0.15$ and $w_{33} = 0.15$ are fixed for both extreme Pareto designs. The new vector of parameters is $\mathbf{x} = [w_{11} \ w_{31} \ l_{21} \ w_{12} \ w_{22} \ w_{32} \ l_{22} \ l_{32} \ w_{13} \ w_{23} \ l_{23} \ l_{33}]^T$. The reduced space X_S is defined by the following bounds: $\mathbf{l}_S = [0.24 \ 0.49 \ 0.86 \ 0.36 \ 0.15 \ 0.21 \ 1.73 \ 0.15 \ 0.16 \ 0.15 \ 1.8 \ 0.14]^T$ and $\mathbf{u}_S = [0.39 \ 0.89 \ 1.66 \ 0.44 \ 0.16 \ 0.25 \ 2.33 \ 0.15 \ 0.17 \ 0.20 \ 2.32 \ 0.15]^T$. It should be noted that X_S is 16 orders smaller (volume-wise) than X_I .

The kriging interpolation model (RMS error 2%) has been constructed in X_S using 1002 samples (1000 LHS-based obtained in 10 iterations of the data acquisition/RSA construction loop and 2 low-fidelity extreme Pareto designs). In the next step, the model has been optimized using MOEA (algorithm setup: 500 individuals; 50 iterations). Finally, a set of 10 designs selected along the initial Pareto front has been refined by means of response correction technique (cf. Section 4.4.1). A comparison of the low- and high-fidelity Pareto sets is shown in Figure 5.18. The obtained results are in good agreement.

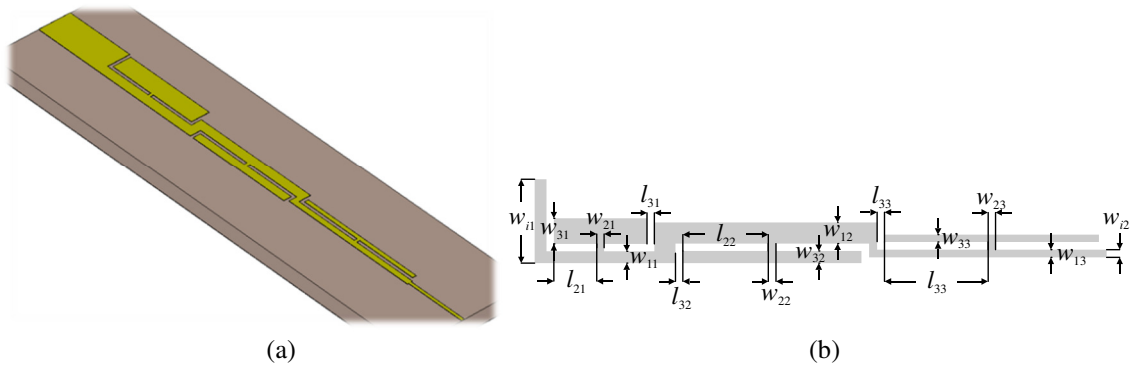


Figure 5.17: A 3-section CMRC-based UWB impedance transformer [120]: (a) 3D visualization; and (b) geometrical details.

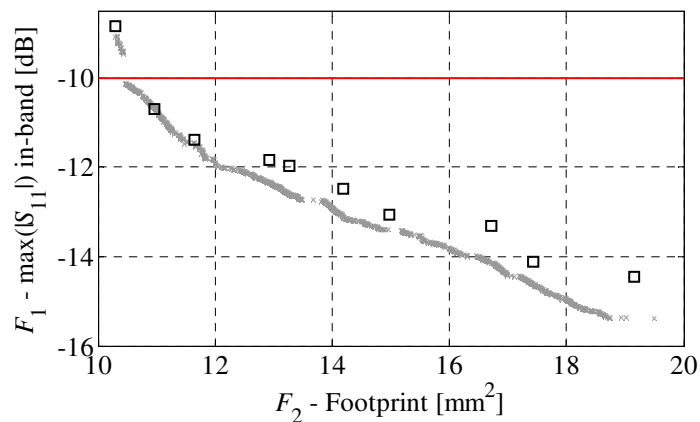


Figure 5.18: The low- (×) and the high-fidelity (□) Pareto front representations of 3-section impedance transformer [120].

The high-fidelity model design with the lowest in-band reflection of -14.4 dB features the largest area of 19.5 mm². The footprint of the smallest structure with acceptable reflection (-10.7 dB) is 11 mm². Therefore, the variability of F_1 and F_2 along the Pareto set is 3.7 dB and 8.5 mm² (43%), respectively. Frequency responses of the selected high-fidelity designs from Table 5.12 are shown in Figure 5.19. It should be noted that the footprint of conventional 50-to-130 ohm impedance transformer operating within defined frequency range is 26.1 mm² [219]. Therefore, the CMRC-based designs obtained using the discussed multi-objective optimization algorithm offer miniaturization rates of up to 55 percent. From this perspective, reduction of transformer size may be considered important. On the other hand, structure miniaturization results in worsening of its electrical performance (similarly as for other considered design problems) and thus selection appropriate trade-off between requirements depends on application of the transformer.

The numerical cost of transformer optimization corresponds to 133 evaluations of the high-fidelity model (~ 27 hours) and it includes: $520 R_c$, $1000 R_c$, and $30 R_f$ evaluations for design space reduction, data acquisition and refinement of the samples selected along the initial Pareto set, respectively. At the same time, the estimated cost (25000 evaluations) of direct MOEA optimization of R_f and R_s model is 208 days and 333 hours, respectively. The detailed cost breakdown of expedited multi-objective design procedure is provided in Table 5.13.

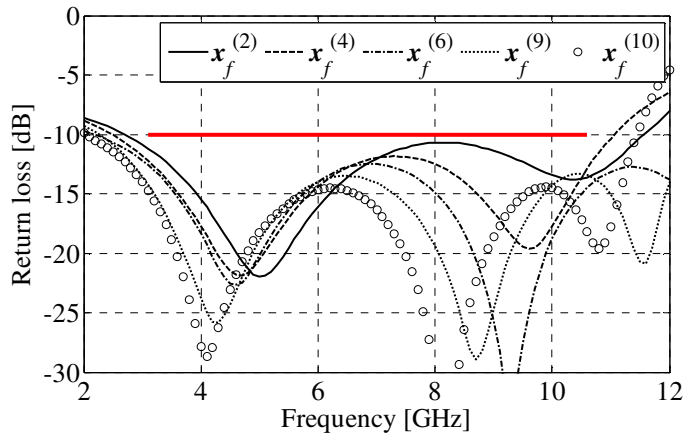


Figure 5.19: Reflection characteristics of UWB impedance matching transformer for selected Pareto-optimal designs [120].

TABLE 5.12: UWB IMPEDANCE TRANSFORMER: SELECTED PARETO-OPTIMAL DESIGNS

	Objectives		Antenna parameters											
	F_1 [dB]	F_2 [dB]	w_{11}	w_{31}	l_{21}	w_{12}	w_{22}	w_{32}	l_{22}	l_{32}	w_{13}	w_{23}	l_{23}	l_{33}
$x_f^{(1)}$	-8.9	10.3	0.244	0.496	1.069	0.424	0.153	0.208	1.844	0.152	0.161	0.165	1.894	0.151
$x_f^{(2)}$	-10.7	11.0	0.376	0.496	0.865	0.417	0.151	0.246	1.735	0.150	0.160	0.150	1.798	0.150
$x_f^{(3)}$	-11.4	11.7	0.394	0.496	0.869	0.411	0.155	0.246	1.735	0.153	0.160	0.151	2.032	0.151
$x_f^{(4)}$	-11.8	12.9	0.378	0.566	1.168	0.411	0.154	0.220	1.741	0.153	0.161	0.152	2.031	0.150
$x_f^{(5)}$	-12.0	13.3	0.378	0.559	1.368	0.407	0.153	0.220	1.741	0.153	0.163	0.197	2.009	0.151
$x_f^{(6)}$	-12.5	14.2	0.331	0.706	1.496	0.356	0.153	0.223	1.734	0.153	0.169	0.157	1.799	0.151
$x_f^{(7)}$	-13.1	15.0	0.335	0.740	1.540	0.359	0.154	0.230	1.798	0.153	0.168	0.175	1.817	0.151
$x_f^{(8)}$	-13.3	16.7	0.382	0.739	1.547	0.412	0.153	0.210	2.017	0.152	0.160	0.180	2.034	0.150
$x_f^{(9)}$	-14.1	17.4	0.389	0.772	1.609	0.399	0.153	0.229	2.020	0.151	0.161	0.174	2.047	0.151
$x_f^{(10)}$	-14.4	19.2	0.392	0.842	1.561	0.421	0.153	0.207	2.198	0.152	0.160	0.165	2.182	0.151

Parameters $w_{21} = 0.15$, $l_{31} = 0.15$ and $w_{33} = 0.15$ are excluded from the table

TABLE 5.13: UWB IMPEDANCE TRANSFORMER: COST BREAKDOWN

Algorithm step	Number of model evaluations	CPU-time		
		Absolute [h]	Relative to R_f	
Design space reduction	R_c	520	7.08	35.39
Data acquisition and RSA construction	R_c	1000	13.61	68.06
MOEA optimization	R_s	25000	N/A	N/A
Pareto set refinement	R_f	30	6	30
Total cost	N/A	N/A	26.69	133.45
Direct search (low-fidelity model) [#]	R_c	25000	333.33	1666.7
Direct search (high-fidelity model) [#]	R_f	25000	5000	25000

[#] Estimated based on the number of R_s evaluations during MOEA optimization

6 EXPERIMENT

In this chapter, experimental verification of the antenna structures designed by means of expedited multi-objective optimization techniques considered in this work has been discussed. Comparison of the simulated and measured characteristics has been performed using two examples: the UWB monopole antenna of Section 5.1 and the quasi-Yagi-Uda structure of Section 5.3. Three designs—selected along the obtained Pareto fronts—have been manufactured. Simulations and measurements have been compared with respect to reflection, E-field radiation pattern (at three frequencies and two planes) and realized gain (in case of the quasi-Yagi structure). The measurements have been conducted at Reykjavik University, Iceland and Gdansk University of Technology, Poland.

6.1 UWB Monopole Antenna

The Pareto-optimal designs $\mathbf{x}_f^{(2)}$, $\mathbf{x}_f^{(6)}$ and $\mathbf{x}_f^{(10)}$ (see Table 5.1 for detailed dimensions) of the UWB monopole antenna of Section 5.1 have been manufactured. The photographs of the fabricated structures can be found in Figure 6.1. It should be noted that the sizes of the structures vary considerably.

A comparison of simulations and measurements in terms of reflection responses is shown in Figure 6.2. All designs fulfill the requirement concerning the maximum acceptable $|S_{11}|$ (assumed to be below -10 dB). The maximum measured in-band reflection is -13.5 dB, -11.8 and -10.5 dB for design $\mathbf{x}_f^{(10)}$, $\mathbf{x}_f^{(6)}$ and $\mathbf{x}_f^{(2)}$, respectively. At the same time, the values obtained from simulations are -15.2 dB, -13.5 dB and -10.4 dB. The peak difference between the measured and the simulated reflection characteristics is 1.7 dB for $\mathbf{x}_f^{(10)}$ and $\mathbf{x}_f^{(6)}$, and only 0.1 dB for $\mathbf{x}_f^{(2)}$. On the other hand, the shapes of the simulated and the measured characteristics are different. Noticeable discrepancies include frequency shift of the resonances as well as different number of resonances (see Figure 6.2(a)).

The E-field radiation patterns of the considered antenna realizations are shown in Figure 6.3. The comparison of the responses has been performed in the x-z (horizontal) and the y-z (elevation) planes for frequencies 4 GHz, 7 GHz and 10 GHz (see Figure 6.1 for visualization). In order to allow for numerical assessment of the discrepancies between the results, the radiation patterns have been expressed as the difference between maximal and minimal E-field strength along the selected plane. A comparison of the measured and simulated values is provided in Table 6.1. The obtained results indicate that measured E-field strength ratios are larger than simulated and increase with frequency. Moreover, in x-z plane the E-field characteristics are omnidirectional which is typical for planar monopole structures. Despite noticeable discrepancies between the simulations and measurement, shapes of obtained radiation patterns are similar.

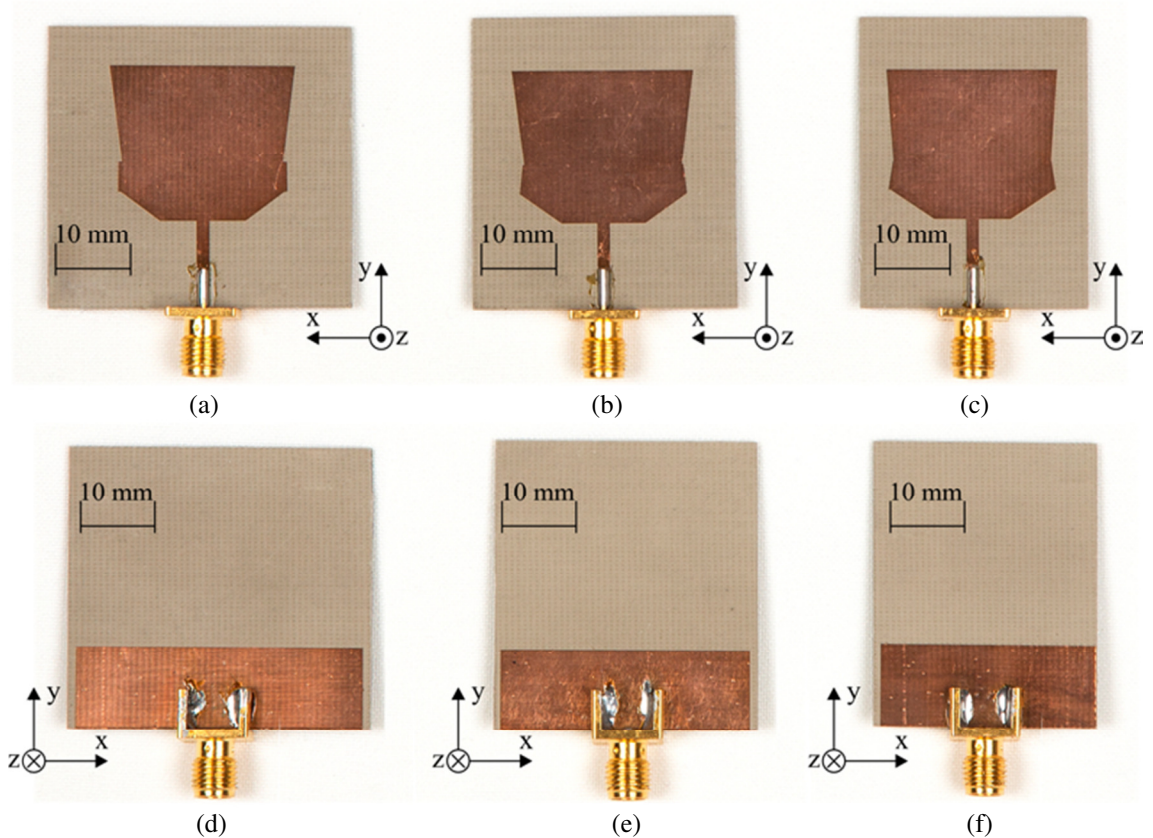


Figure 6.1: A photograph of fabricated UWB monopole antenna prototypes: (a)-(c) top-view; (d)-(f) bottom-view. The selected designs are: (a), (d) $\mathbf{x}_f^{(10)}$; (b), (e) $\mathbf{x}_f^{(6)}$; and (c), (f) $\mathbf{x}_f^{(2)}$. For detailed dimensions of selected antenna designs see Table 5.1.

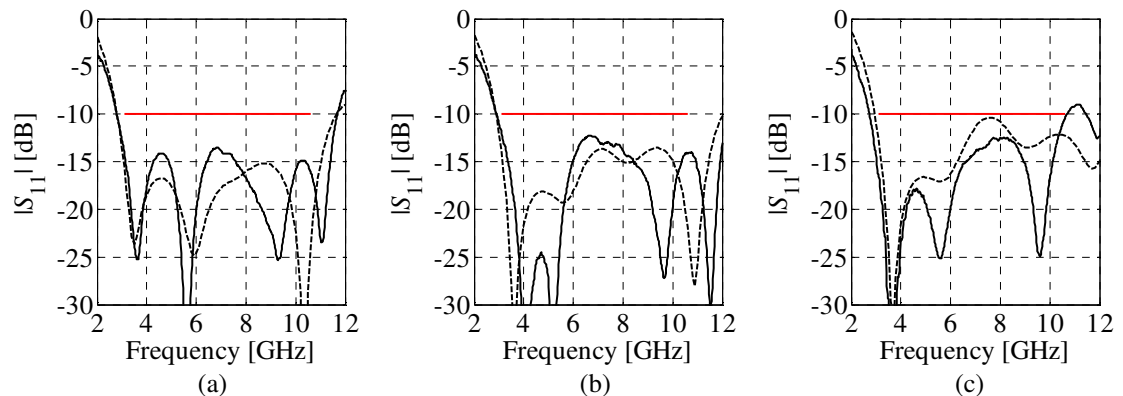


Figure 6.2: Comparison of simulated (---) and measured (—) reflection characteristics of UWB monopole antenna at: (a) design $\mathbf{x}_f^{(10)}$; (b) design $\mathbf{x}_f^{(6)}$; (c) design $\mathbf{x}_f^{(2)}$.

Discrepancies between the simulated and measured characteristics of the considered antenna designs are mostly due to utilization of simplified high-fidelity EM model that lacks the SMA connector. To some extent, differences between the results are also introduced by antenna fabrication and assembly tolerances, as well as electrically large setup utilized in the measurement process.

6.2 Quasi-Yagi-Uda Antenna

The Pareto-optimal designs $\mathbf{x}_f^{(2)}$, $\mathbf{x}_f^{(5)}$ and $\mathbf{x}_f^{(10)}$ of the quasi-Yagi-Uda antenna of Section 5.3 have been fabricated. Photographs of the manufactured structures are shown in Figure 6.4,

whereas their detailed dimensions are gathered in Table 5.5. Visible geometrical differences between the considered structures include slightly different sizes (design $\mathbf{x}_f^{(2)}$ is the smallest whereas $\mathbf{x}_f^{(10)}$ is the largest; note that miniaturization of antenna was not of concern). Moreover, the considered antennas exhibit different allocations of ground plane stubs, as well as different widths and lengths of the reflectors.

A comparison of antenna reflection characteristics is shown in Figure 6.5. The obtained results indicate that design $\mathbf{x}_f^{(2)}$ slightly violates the assumed design specification ($|S_{11}| > -10$ dB). The maximum measured in-band reflection is -11.3 dB, -12 dB and -9.6 dB for the design $\mathbf{x}_f^{(10)}$, $\mathbf{x}_f^{(5)}$ and $\mathbf{x}_f^{(2)}$, respectively. The corresponding simulated values are -16.7 dB -14 dB and -11 dB, so that the peak discrepancies between simulations and measurements are 5.4 dB, 2 dB and 1.4 dB. It should be noted that considerable difference of the maximum in-band $|S_{11}|$ for the design $\mathbf{x}_f^{(10)}$ is a consequence of misalignment between the simulated and measured characteristics. The measured bandwidth of the antenna at $\mathbf{x}_f^{(10)}$ is 350 MHz narrower than simulated one. At the same time, the reflection measured for the design $\mathbf{x}_f^{(2)}$ is 400 MHz broader than the one obtained from simulations. The discrepancies between responses of the EM model and fabricated prototypes also include different number of resonances.

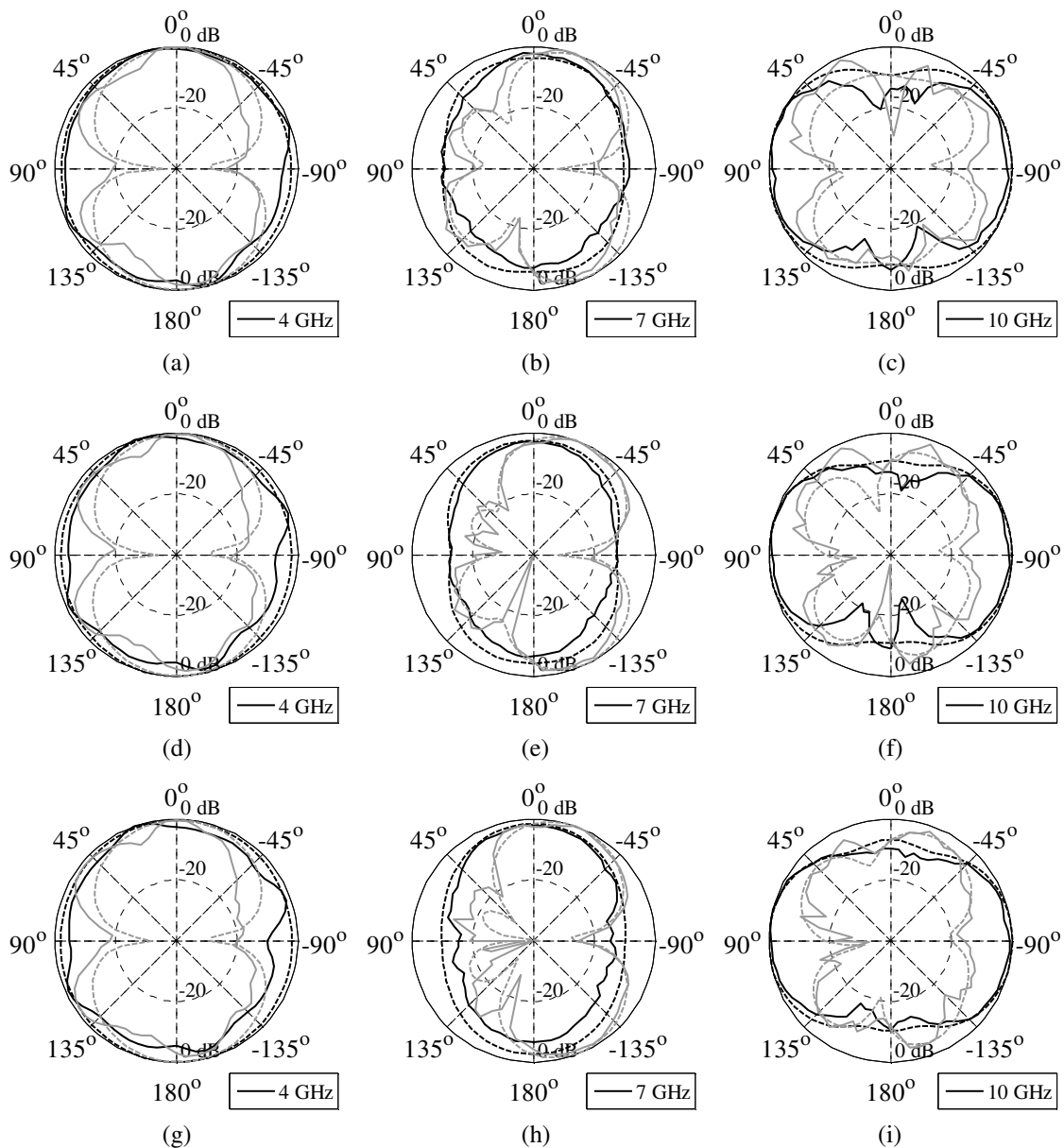


Figure 6.3: Comparison of simulated (---) and measured (—) E-field radiation pattern characteristics of UWB monopole antennas in x-z (black lines) and y-z (gray lines) planes: (a)-(c) design $\mathbf{x}_f^{(10)}$; (d)-(f) design $\mathbf{x}_f^{(6)}$; (g)-(i) design $\mathbf{x}_f^{(2)}$.

The gain characteristics of the considered antenna designs are compared in Figure 6.6. The shapes of the simulated and measured characteristics are similar. On the other hand, in the 4 GHz to 6 GHz range, the gain levels of the measured prototypes (measured using three antenna method [89]) are noticeably lower than for the simulated characteristics. The measured average in-band gain for designs $\mathbf{x}_f^{(2)}$, $\mathbf{x}_f^{(5)}$ and $\mathbf{x}_f^{(10)}$ is 6.05 dB, 6.16 dB and 6.23 dB, respectively. The corresponding simulated values are 6.83 dB, 6.68 dB and 6.43 dB, so that the differences between obtained results are 0.78 dB, 0.52 dB and 0.2 dB.

The simulated and measured E-field radiation patterns of the antenna designs are shown in Figure 6.7. The results are compared in y-z (elevation) and x-y (horizontal) planes (see Figure 6.4 for visualization) for 5 GHz, 7 GHz and 9 GHz frequencies. The measured and simulated front-to-back (F/B) ratios for selected antenna designs are gathered in Table 6.2. The obtained results are similar; however measured F/B rates are slightly larger.

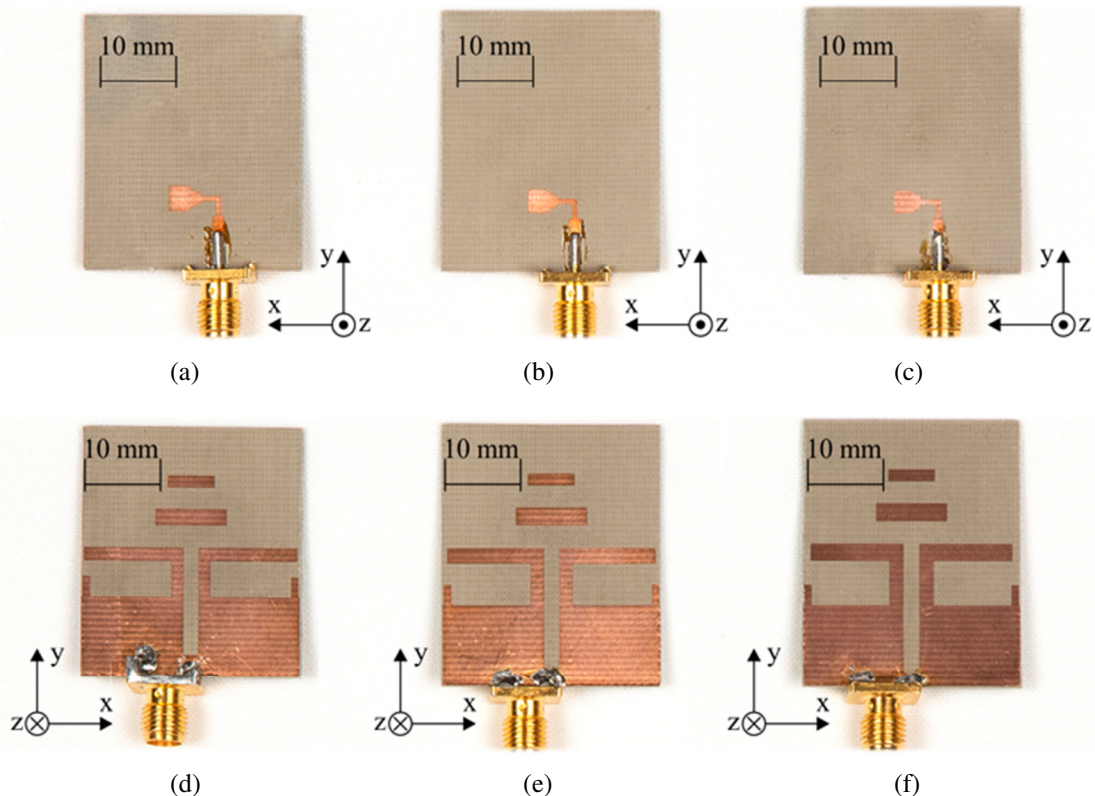


Figure 6.4: Planar quasi Yagi-Uda antenna – photograph of fabricated prototypes: (a)-(c) top-view; (d)-(f) bottom-view. The selected designs are: (a), (d) $\mathbf{x}_f^{(2)}$; (b), (e) $\mathbf{x}_f^{(5)}$; and (c), (f) $\mathbf{x}_f^{(10)}$. For detailed dimensions of manufactured structures see Table 5.5.

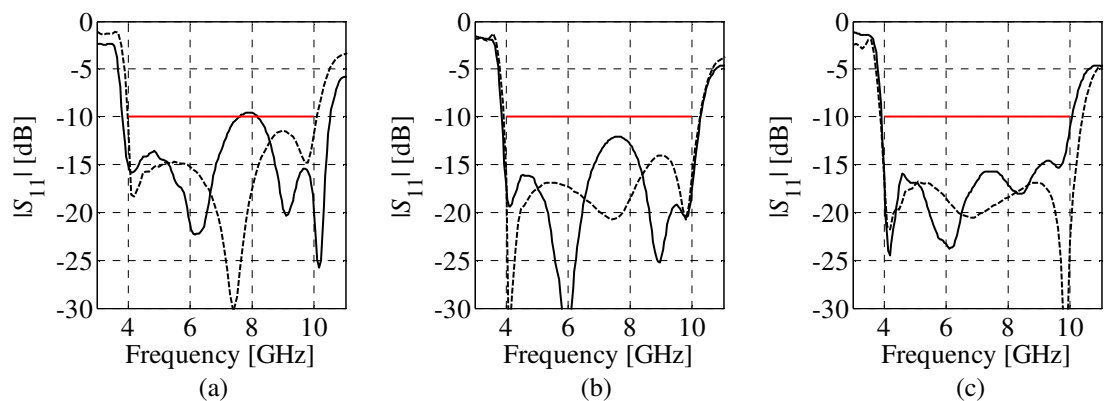


Figure 6.5: Comparison of simulated (---) and measured (—) reflection characteristics of quasi Yagi-Uda antenna: (a) design $\mathbf{x}_f^{(2)}$; (b) design $\mathbf{x}_f^{(5)}$; (d) design $\mathbf{x}_f^{(10)}$.

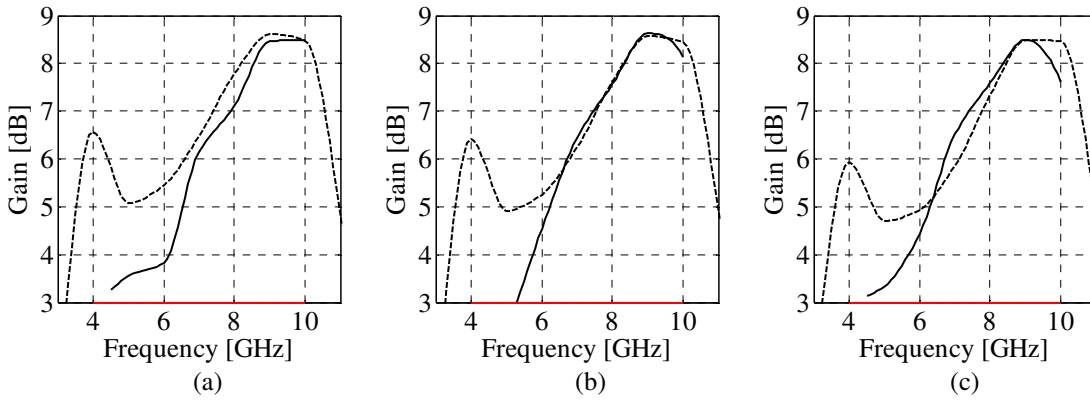


Figure 6.6: Planar quasi-Yagi-Uda antenna – comparison of simulated (– –) and measured (—) gain characteristics: (a) design $x_f^{(2)}$; (b) design $x_f^{(5)}$; (d) design $x_f^{(10)}$.

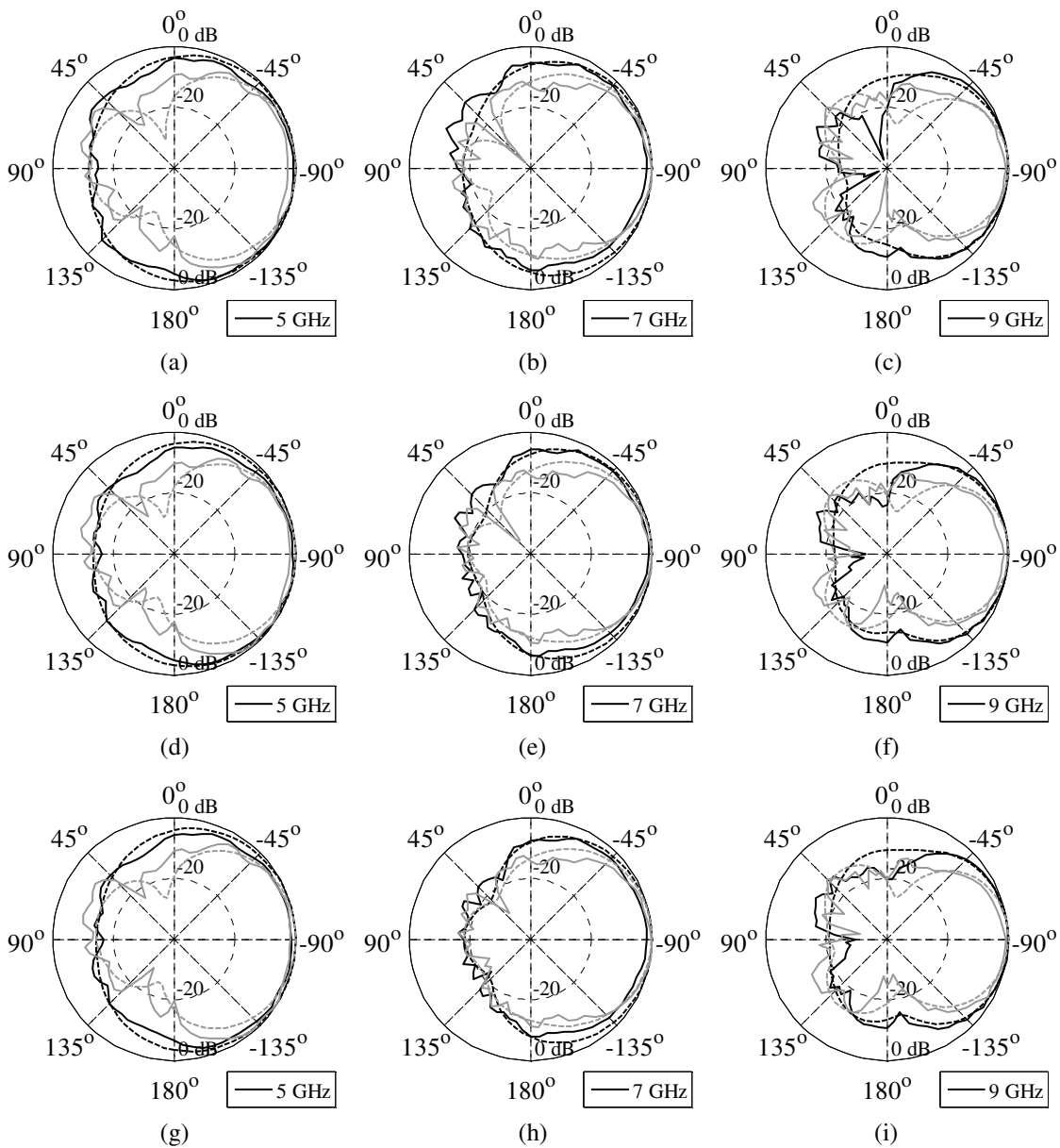


Figure 6.7: Comparison of simulated (– –) and measured (—) E-field radiation patterns of the quasi-Yagi-Uda antenna in y-z (black lines) and x-y (gray lines) planes: (a)-(c) design $x_f^{(10)}$; (d)-(f) design $x_f^{(6)}$; (g)-(i) design $x_f^{(2)}$.

The differences between simulations and measurements result from utilization of the EM antenna model that lacks the SMA connector. As shown in [82], the SMA connector should be included in the EM models of compact structures because it notably influences the behavior of the structure (e.g., for the considered antenna structure, the measured $|S_{11}|$ exhibits an additional in-band resonance which is most likely introduced by the SMA connector [82]). To some extent, discrepancies between the results also result from the fabrication tolerances, electrically large measurement equipment, as well as imperfections of the measurement setup (e.g., manual positioning of antennas for gain measurements based on the three antenna method). Moreover, the considered antenna is small and thus precision of the prototype assembly (board cutting, SMA positioning, etc.) is rather important.

TABLE 6.1: E-FIELD STRENGTH RATIOS OF UWB MONOPOLE ANTENNA

		Simulation			Measurement			
		Frequency	$x_f^{(2)}$	$x_f^{(5)}$	$x_f^{(10)}$	$x_f^{(2)}$	$x_f^{(5)}$	$x_f^{(10)}$
x-z plane [dB]	4 GHz	1.95	2.09	2.23	9.02	6.94	4.68	
	7 GHz	8.28	10.22	6.81	13.48	10.31	9.59	
	10 GHz	10.67	11.01	9.35	16.45	21.03	18.30	
y-z plane [dB]	4 GHz	31.77	33.87	35.75	19.08	19.93	20.86	
	7 GHz	42.23	31.64	32.22	29.47	23.53	19.49	
	10 GHz	28.04	20.50	20.83	24.35	22.76	21.72	

TABLE 6.2: QUASI YAGI-UDA ANTENNA: COMPARISON OF F/B RATIO

		Simulation			Measurement			
		Frequency	$x_f^{(2)}$	$x_f^{(5)}$	$x_f^{(10)}$	$x_f^{(2)}$	$x_f^{(5)}$	$x_f^{(10)}$
y-z plane [dB]	5 GHz	14.52	13.65	12.11	15.11	15.37	14.35	
	7 GHz	21.85	20.93	17.84	17.91	17.48	16.99	
	9 GHz	21.06	22.92	26.04	27.97	31.30	33.75	
x-y plane [dB]	5 GHz	26.44	27.54	30.40	24.58	22.47	19.25	
	7 GHz	23.07	25.50	30.71	24.94	29.63	27.82	
	9 GHz	25.85	25.83	25.14	26.12	27.03	28.76	

7 DISCUSSION AND RECOMMENDATIONS

The main focus of this work were strategies for computationally efficient multi-objective design optimization of antenna structures. By suitable combination of variable-fidelity electromagnetic simulations, design space reduction techniques, data-driven surrogate models, response correction methods, the algorithms presented in Chapters 2 through 4 permit feasible handling of multiple objectives and generating available trade-off designs for expensive EM antenna models, including the cases when the number of geometry parameters is large. In this chapter, a brief quantitative discussion of this algorithmic framework is provided, including analysis of its various components, and—more importantly—recommendations for algorithm setup when dealing with specific types of antenna structures.

7.1 Quantitative Discussion of Algorithm Components

The multi-objective optimization framework discussed in this work contains several important components, including design space reduction, data-driven surrogate modeling scheme, multi-objective evolutionary algorithm, and design refinement procedures. Most of the operations are performed at the level of low-fidelity antenna model (here, obtained from coarse-discretization EM simulations). Some of these components are critical from the point of view of feasible handling of multi-dimensional design spaces, others influence both the performance of the algorithm (in terms of the quality of the final Pareto set obtained) and its computational cost. Certain components are of minor importance. In the remaining part of this section, a brief characterization of all the framework components is provided taking into account the aforementioned factors.

Design space reduction is the first step of the optimization framework. It is critical for handling multi-dimensional design problems. Restricting search space to the region containing Pareto front allows for construction of an accurate RSA model using a limited number of training samples. The following methods have been described in this work:

- The sequential approach (cf. Section 4.3.2) is the most versatile method. It can be utilized to handle problems with two- or more design objectives. It is simple to use and easy to implement. However, it may be of limited accuracy in case of large misalignment between the low- and high-fidelity models (see Section 5.1).

- The Pareto-dominance-based technique (cf. Section 4.3.1) exploits a mechanism that rapidly narrows down the initial search space to a small region. The method may be useful for problems that lack reasonably good starting point for using sequential approach. However, usefulness of Pareto method decreases with the increasing dimensionality and size of the search space. The reason is that star-distribution DoE is often too sparse to allow for accurate identification of the region containing the Pareto front.
- The rotational approach (cf. Section 4.3.3) is very efficient, especially for design problems with multiple parameters. Its computational cost is the same as that of sequential method. The rotational technique can only be used (as it is formulated in this work) for two-objective problems. It assumes that the Pareto front is allocated close to the line segment spanned by the extreme Pareto-optimal design. This assumption is typically valid for most antenna structures, yet, in some cases, the method may fail to capture the entire front.
- The space confinement technique (cf. Section 4.3.4) is an alternative way of finding the region of the design space that contains Pareto-optimal design. It is particularly useful for constrained problems, where certain acceptability thresholds are imposed on one or more objectives. However, its numerical cost is higher compared to other reduction approaches.

Accuracy of all of the aforementioned methods can be improved by incorporating high-fidelity extreme Pareto-optimal designs (cf. Section 4.3.5) at the expense of some extra computational overhead.

The central components of the design framework are data-driven models (cf. Section 2.2.2). They are essential to enable fast multi-objective optimization using population-based algorithms. For the sake of computational efficiency, they are constructed from low-fidelity model data (cf. Section 2.2.1). The model accuracy threshold is set to 3% (in terms of the average RMS error estimated using cross-validation). In case of computational budget constraints, it is possible to relax this condition, however, it may lead to reduced accuracy of determining the Pareto front. In this work, the modeling technique of choice is kriging interpolation (mostly due to easy access through various third-party toolboxes [167], [168]), however, any other approximation technique (e.g., radial basis functions [171], support vector regression [172], or Gaussian process regression [173]) can be used as well. The particular modeling is not critical here.

The next step of the design process is MOEA-based optimization (cf. Section 3.3.1). Here, an in-house implementation based on [200] is utilized. However, any multi-objective version of any population-based metaheuristic can be used as well. Nor computational efficiency of the algorithm, nor its performance are critical for the overall results of the considered optimization framework. In this work, a default value of 25,000 objective function evaluations has been used as a termination criterion for MOEA. In terms of the CPU time, the cost is negligible compared to EM simulation. Potential inaccuracies that may occur during the process as a result of data-driven model optimization imperfections may still be corrected at the design refinement stage.

The design refinement is an important step of the design process that elevates the initial Pareto-optimal designs to the high-fidelity model level. In majority of algorithm configurations, this is the only step that exploits high-fidelity model evaluations. Two refinement methods (different in terms of the utilized mechanisms, optimization cost and complexity), have been considered in this work:

- Response correction (cf. Section 4.4.1) is the simpler one. It is easy to implement and allows for controlling the cost of the refinement process by selecting the desired number of high-fidelity Pareto designs to be obtained. The results presented in this work indicate that the accuracy of response correction depends on correlation between the high- and low-fidelity models (see Section 5.2).
- The co-kriging-based method (cf. Section 4.4.2) allows for refinement of the entire Pareto set at a time and thus provides more comprehensive information about the structure at hand. On the other hand, co-kriging method is more difficult to implement and more sensitive to MOEA setup than response correction (cf. Appendix A1).

Furthermore, misalignment between the low- and high-fidelity models can be reduced before executing design refinement. This stage can be realized using, e.g., space mapping techniques [152], [174], [175], [176]. Although incurring extra computational overhead, it usually leads to improved accuracy of the refinement stage.

Most operations of the design framework are performed at the low-fidelity model level. On one hand, the model should be possibly cheap to reduce the cost of algorithm operation. On the other hand, reasonable accuracy of the model is particularly important for design space reduction but also data-driven surrogate construction. Having this in mind, finding appropriate balance between accuracy and evaluation cost of the low-fidelity model is desired. Unfortunately, automated determination of the low-fidelity model setup is still an open problem. In practice (including all examples considered in this work), the low-fidelity model was selected based on visual inspection of the structure responses and using grid convergence studies.

7.2 Discussion and Recommendations

Here, a few remarks concerning recommendations of specific algorithm setup are given. The following factors should be considered while determining the algorithm setup: (i) user experience, (ii) quality of available low-fidelity model, and (iii) problem-specific knowledge (e.g., relative importance of particular geometry parameters).

For less experienced users, configuration of the algorithm with sequential design space reduction and response correction is recommended due to simplicity of implementation and versatility. Such configuration is also flexible in terms of the number of Pareto designs for refinement.

For more experienced users, tailoring the algorithm configuration to the design problem at hand is recommended. Depending on the number of design objectives and space dimensionality, rotational or confinement methods should be considered for space reduction. Also, co-kriging-based refinement is recommended as the method that allows for obtaining more comprehensive information about trade-offs between design objectives.

In most cases, LHS is recommended as design of experiments technique of choice. However, for lower dimensional problems (say, up to 7-8 variables—128-256 design space corners) a combination of LHS with factorial DoE methods should be considered to ensure better RSA accuracy in the vicinity of the search space corners.

As indicated earlier, the importance of the multi-objective optimization engine (here, MOEA) is minor (both in terms of computational cost and reliability of the process), virtually any multi-objective version of popular population-based metaheuristic can be used as available for the user. Similarly, other types of approximation models (e.g., support vector regression or Gaussian process regression) can be used as data-driven surrogate based on what is available.

For narrow-band structures, frequency scaling of training data before construction of the data-driven model is recommended to reduce the cost of further refinement of the initial Pareto set. At the same time, it may not be necessary for broadband structures because their coarsely-discretized models exhibit smaller frequency-shift-like discrepancies.

8 SUMMARY

In this dissertation, a design framework for fast multi-objective optimization antenna structures has been discussed. The method utilizes design space reduction, response surface approximations, population-based metaheuristics and surrogate-based techniques. In the design process, the RSA model constructed using low-fidelity model data is optimized using a multi-objective evolutionary algorithm. The initial Pareto set obtained this way is further corrected using surrogate-assisted methods.

Space reduction extends applicability of the method to multi-dimensional problems by narrowing down the design space to the region containing Pareto-optimal designs. Five reduction techniques, suitable for solving various design problems, have been described. They have been numerically validated in terms of accuracy, computational cost, the size of reduced space and quality of the high-fidelity Pareto front representations. The influence of space reduction on scalability of the algorithm cost with respect to the number of design variables has been also investigated.

The design framework has been numerically validated through two-objective design of seven wideband antennas with 3 to 24 design parameters, a three-objective design of a narrow-band DRA, and two-objective optimization of a compact three-section impedance matching transformer. The last two structures have been considered to indicate that the method can be also applied for design of other structures than UWB antennas. The cost of the algorithm operation is low compared to direct population-based multi-objective optimization of high-fidelity EM model. The numerical results have been confirmed by experimental validation of two antenna structures.

The most important original contributions of this dissertation include:

- enhancement of RSA models applicability to multi-dimensional problems and development of five space reduction techniques;
- a detailed comparison of the developed space reduction techniques;
- analysis of the scalability properties of the optimization algorithm with respect to the number of antenna design parameters;
- statistical analysis of the MOEA for design problems with three to nine adjustable parameters;
- comparison of the Pareto set refinement techniques;
- implementation of the discussed methods and algorithms in a MATLAB-based design optimization framework;
- expedited design optimization of eight antennas and impedance transformer with respect to two and three objectives, and experimental validation of two of them.

To the best knowledge of the author, this is the only approach reported so far in the literature that allows—using a single PC machine—for obtaining a reliable representation of the high-fidelity Pareto set at a practically acceptable computational cost. Depending on the problem complexity, the absolute CPU time of the optimization process is up to a few dozen hours, compared to a few months required by conventional methods.

8.1 Conclusions

The main focus of this work was computationally efficient multi-objective optimization of antenna structures. The obtained numerical and experimental results indicate that the goals of this dissertation have been achieved and theses have been positively verified (see also Section 1.2).

As demonstrated, appropriate combination of variable-fidelity EM simulations, approximation models, surrogate-assisted techniques and evolutionary algorithms allow for expedited optimization of high-fidelity EM models of real-world antenna structures. On the other hand, the cost of obtaining accurate RSA models (critical for the considered design framework) grows very quickly with dimensionality of the design space. Applicability of the technique to multi-dimensional antenna structures (demonstrated for up to 24-parameter cases) can be maintained by utilization of appropriate space reduction methods.

It should be emphasized that the algorithmic framework considered here offers dramatic reduction of the computational cost compared to conventional methods. For the considered design cases, the cost of antenna optimization using the presented approach corresponds to up to 200 evaluations of the high-fidelity EM model. At the same time, estimated cost of direct population-based optimization of high-fidelity EM models is two to three orders higher.

8.2 Future Work

The discussed design framework addresses difficulties pertinent to multi-objective optimization of EM models of antenna structures. On the other hand, successful application of the algorithm depends, to some extent, on engineering experience and it cannot guarantee that the entire Pareto front is captured. Also, certain components of the framework need further improvements.

The computational cost and reliability of the design space reduction step can be improved by using better single-objective algorithms. This could be realized using adjoint sensitivity-based methods embedded in trust region framework. Feature-based optimization or methods based on local approximation models may also be of interest.

Also, the framework requires mechanism that allows for expanding the data-driven model to ensure that true Pareto front is captured. This may be realized by expanding the region determined by the space reduction algorithm and allocating additional training samples therein.

Another (quantitatively significant) enhancement would be to completely change the strategy of generating the initial Pareto front representation by using deterministic procedures rather than metaheuristic. This could be realized by finding the path connecting the extreme Pareto-optimal designs using methods similar to pattern search and operating directly on low-fidelity EM models.

A separate problem is related to determination of the low-fidelity model with appropriate speed-to-accuracy ratio. Although manual selection of the low-fidelity model that is sufficiently accurate representation of the high-fidelity model is relatively simple, determination of the best possible trade-off between the model quality and its simulation cost is still an open problem. One of the difficulties is development of relevant measure of discrepancy between the low- and high-fidelity models. It should be emphasized that solution to this problem is of importance not only from the point of view of expedited multi-objective optimization but surrogate-based design methods in general.

Finally, handling expensive simulation models and their optimization with respect to multiple criteria is ubiquitous in many engineering disciplines. The multi-objective framework presented

Design of Wideband Antennas By Means of Fast Multi-Objective Optimization

here may be useful for efficient handling of other microwave structures including couplers, power dividers, beam-forming networks for antenna arrays, phase shifters and many others. Also it may be of practical importance in areas such as photonics, aerospace engineering, heat transfer or mechanical engineering, to name just a few.

REFERENCES

- [1] H. R. Hertz, "Ueber sehr schnelle elektrische schwingungen," *Annalen der Physik*, vol. 267, no. 7, pp. 421–448, 1887.
- [2] H. R. Hertz, *Untersuchungen Uber die Ausbreitung der elektrischen Kraft*, 2nd ed. Leipzig: Johann Ambrosius Barth, 1894.
- [3] J. C. Maxwell, *A Treatise on Electricity & Magnetism*, 3rd ed. New York: Dover Publications, 1954.
- [4] H. H. Beverage, C. W. Rice, and E. W. Kellog, "The wave antenna a new type of highly directive antenna," *J. American Institute Electrical Eng.*, vol. 42, no. 3, pp. 258–269, 1923.
- [5] H. Diamond and G. Davies, "Characteristics of airplane antennas for radio range beacon reception," *Proc. Institute Radio Eng.*, vol. 20, no. 2, pp. 346–358, 1932.
- [6] H. Kohler, "Antenna design for field-strength gain," *Proc. IRE*, vol. 32, no. 10, pp. 611–616, 1944.
- [7] H. Yagi and S. Uda, "Projector of the sharpest beam of electric waves," *Proc. Imperial Academy Japan*, vol. 2, no. 2, pp. 49–52, 1929.
- [8] H. Beggerow, "Luftleitergebilde fur luftschiffe," DE Patent 225204, Sep. 19, 1909.
- [9] A. B. Bailey, "Antenna system," US Patent 2184729, Apr. 15, 1937.
- [10] E. J. Sterba, "Directive antenna system," US Patent 1885151, Jul. 30, 1929.
- [11] P. S. Carter, "Short wave antenna," US Patent 2175253, Feb. 15, 1938.
- [12] H. Black, J. Beyer, T. Grieser, and F. Polkinghorn, "A multichannel microwave radio relay system," *Trans. American Institute Electrical Eng.*, vol. 65, no. 12, pp. 798–806, 1946.
- [13] H. Sobol, "Microwave communications - an historical perspective," *IEEE Trans. Microwave Theory Tech.*, vol. 32, no. 9, pp. 1170–1181, 1984.
- [14] R. Watson, *Radar Origins Worldwide: History of Its Evolution in 13 Nations Through World War II*. Victoria: Trafford, 2009.
- [15] A. O. Bauer, "Some aspects of German airborne radar technology, 1942 to 1945," in *DEHS Autumn Symp.*, pp. 1–32, Sheivenham, 2006.
- [16] H. Harmuth, *Transmission of Information by Orthogonal Functions*. New York: Springer, 1969.
- [17] L. Y. Astanin, "Analysis of electron current in a traveling wave field by beam velocity modulation," *Vopr. Radioelektroniki*, vol. 12, 1964.
- [18] G. F. Ross, "A time domain criterion for the design of wideband radiation elements," *IEEE Trans. Ant. Prop.*, vol. 16, no. 3, pp. 355–356, 1968.
- [19] T. W. Barrett, "History of ultrawideband (UWB) radar & communications: Pioneers and innovators," in *Prog. EM Symp.*, pp. 1–42, Cambridge, 2000.
- [20] G. F. Ross, "Transmission and reception system for generating and receiving base-band pulse duration pulse signals without distortion for short base-band communication system," US Patent 3728632, Apr. 17, 1973.

- [21] P. van Etten, "The present technology of impulse radars," in *Proc. Int. Radar Conf.*, pp. 535–539, London, 1977.
- [22] P. R. Moffatt, D.L., "A subsurface electromagnetic pulse radar," *Geophysics*, vol. 41, no. 3, pp. 506–518, 1976.
- [23] Federal Communications Commission (FCC), "Revision of part 15 of the commission rules regarding ultra-wideband transmission systems," Washington, Tech. Rep. FCC 02-48, 2002.
- [24] D. Yadav and V. Tiwari, "UWB antenna designing: challenges and solutions," *Int. J. Computing, Comm. Instrumentation Eng.*, vol. 1, no. 1, pp. 39–42, 2014.
- [25] H. Dunger and R. Bosch, "World-wide regulation and standardisation overview," EUWB, Tech. Rep. 215669, 2008.
- [26] Council of European Union, "Commission of European Communities Decision no 2007/131/EC," 2007, <http://eur-lex.europa.eu>.
- [27] Council of European Union, "Commission of European Communities Decision no 2009/343/EC," 2009, <http://eur-lex.europa.eu>.
- [28] Council of European Union, "Commission Implementing Decision no 2014/702/EU," 2014, <http://eur-lex.europa.eu>.
- [29] Z. N. Chen, "UWB antennas: design and application," in *Int. Conf. Inf. Comm. Signal Proces.*, pp. 1–5, Singapore, 2007.
- [30] H. Schantz, "Introduction to ultra-wideband antennas," in *IEEE Conf. UWB Syst. Technol.*, pp. 1–9, Reston, 2003.
- [31] L. Liu, S. Cheung, and T. Yuk, "Compact MIMO antenna for portable devices in UWB applications," *IEEE Trans. Ant. Prop.*, vol. 61, no. 8, pp. 4257–4264, 2013.
- [32] J.-F. Li, Q.-X. Chu, Z.-H. Li, and X.-X. Xia, "Compact dual band-notched UWB MIMO antenna with high isolation," *IEEE Trans. Ant. Prop.*, vol. 61, no. 9, pp. 4759–4766, 2013.
- [33] M. Bod, H. Hassani, and M. Taheri, "Compact UWB printed slot antenna with extra Bluetooth, GSM, and GPS bands," *IEEE Ant. Wireless Prop. Lett.*, vol. 11, pp. 531–534, 2012.
- [34] S. Koziel and A. Bekasiewicz, "Small antenna design using surrogate-based optimization," in *IEEE Ant. Prop. Society Int. Symp.*, pp. 585–586, Memphis, 2014.
- [35] T. Sakamoto and T. Sato, "Code-division multiple transmission for high-speed UWB radar imaging with an antenna array," *IEEE Trans. Geoscience Remote Sensing*, vol. 47, no. 4, pp. 1179–1186, 2009.
- [36] J. Shao, G. Fang, Y. Ji, K. Tan, and H. Yin, "A novel compact tapered-slot antenna for GPR applications," *IEEE Ant. Wireless Prop. Lett.*, vol. 12, pp. 972–975, 2013.
- [37] M. Elmansouri, S. Sanghai, and D. Filipovic, "High-power ultra-wideband spiral antenna arrays," in *USNC-URSI National Radio Sci. Meeting*, pp. 1–1, Boulder, 2014.
- [38] D. Valderas, J. I. Sancho, D. Puente, C. Ling, and X. Chen, *Ultrawideband Antennas: Design and Applications*. London: Imperial College Press, 2011.
- [39] X. Chen, J. Liang, S. Wang, Z. Wang, and C. Parini, "Small ultra wideband antennas for medical imaging," in *Loughborough Ant. Prop. Conf.*, pp. 28–31, Loughborough, 2008.
- [40] M. Fantuzzi, D. Masotti, and A. Costanzo, "A novel integrated UWB-UHF one-port antenna for localization and energy harvesting," *IEEE Trans. Ant. Prop.*, vol. 63, no. 9, pp. 3839–3848, 2015.
- [41] T. Peter, T. Rahman, S. Cheung, R. Nilavalan, H. Abutarboush, and A. Vilches, "A novel transparent UWB antenna for photovoltaic solar panel integration and RF energy harvesting," *IEEE Trans. Ant. Prop.*, vol. 62, no. 4, pp. 1844–1853, 2014.
- [42] Y.-J. Ren, C.-P. Lai, P.-H. Chen, and R. Narayanan, "Compact ultrawideband UHF array antenna for through-wall radar applications," *IEEE Ant. Wireless Prop. Lett.*, vol. 8, pp. 1302–1305, 2009.
- [43] A. Dumoulin, M. John, M. Ammann, and P. McEvoy, "Optimized monopole and dipole antennas for UWB asset tag location systems," *IEEE Trans. Ant. Prop.*, vol. 60, no. 6, pp. 2896–2904, 2012.
- [44] N. Chahat, M. Zhadobov, R. Sauleau, and K. Ito, "A compact UWB antenna for on-body applications," *IEEE Trans. Ant. Prop.*, vol. 59, no. 4, pp. 1123–1131, 2011.
- [45] M. Ur-Rehman, Q. Abbasi, M. Akram, and C. Parini, "Design of band-notched ultra wideband antenna for indoor and wearable wireless communications," *IET Microwaves, Ant. Prop.*, vol. 9, no. 3, pp. 243–251, 2015.
- [46] S.-W. Su, J.-H. Chou, and K.-L. Wong, "Internal ultrawideband monopole antenna for wireless USB dongle applications," *IEEE Trans. Ant. Prop.*, vol. 55, no. 4, pp. 1180–1183, 2007.

- [47] L. Guo, X. Chen, and C. Parini, "Miniature ultra-wideband antenna for wireless universal serial bus dongle applications," *IET Microwaves, Ant. Prop.*, vol. 6, no. 1, pp. 113–119, 2012.
- [48] H. Jafari, J. Deen, S. Hranilovic, and N. Nikolova, "Co-polarised and cross-polarised antenna arrays for breast cancer detection," *IET Microwaves, Ant. Prop.*, vol. 1, no. 5, pp. 1055–1058, 2007.
- [49] X. Li, E. J. Bond, B. Van Veen, and S. Hagness, "An overview of ultra-wideband microwave imaging via space-time beamforming for early-stage breast-cancer detection," *IEEE Ant. Prop. Magazine*, vol. 47, no. 1, pp. 19–34, 2005.
- [50] S. Koziel, S. Ogurtsov, W. Zieniutycz, and A. Bekasiewicz, "Design of a planar UWB dipole antenna with an integrated balun using surrogate-based optimization," *IEEE Ant. Wireless Prop. Lett.*, vol. 14, pp. 366–369, 2015.
- [51] A. Gautam, S. Yadav, and B. Kanaujia, "A CPW-fed compact UWB microstrip antenna," *IEEE Ant. Wireless Prop. Lett.*, vol. 12, pp. 151–154, 2013.
- [52] N. T. Tokan, A. Neto, F. Tokan, and D. Cavallo, "Comparative study on pulse distortion and phase aberration of directive ultra-wideband antennas," *IET Microwaves, Ant. Prop.*, vol. 7, no. 12, pp. 1021–1026, 2013.
- [53] Z. J. Tang, J. Zhan, and H. L. Liu, "Compact CPW-fed antenna with two asymmetric U-shaped strips for UWB communications," *Electronics Lett.*, vol. 48, no. 14, pp. 810–812, 2012.
- [54] G. Reddy, A. Kamma, S. Kharche, J. Mukherjee, and S. Mishra, "Cross-configured directional UWB antennas for multidirectional pattern diversity characteristics," *IEEE Trans. Ant. Prop.*, vol. 63, no. 2, pp. 853–858, 2015.
- [55] T. Roshna, U. Deepak, V. Sajitha, K. Vasudevan, and P. Mohanan, "A compact UWB MIMO antenna with reflector to enhance isolation," *IEEE Trans. Ant. Prop.*, vol. 63, no. 4, pp. 1873–1877, 2015.
- [56] Z. N. Chen, T. See, and X. Qing, "Small printed ultrawideband antenna with reduced ground plane effect," *IEEE Trans. Ant. Prop.*, vol. 55, no. 2, pp. 383–388, 2007.
- [57] M. Ding, R. Jin, J. Geng, Q. Wu, and G. Yang, "Auto-design of band-notched UWB antennas using mixed model of 2D GA and FDTD," *Electronics Lett.*, vol. 44, no. 4, pp. 257–258, 2008.
- [58] L. Guo, S. Wang, X. Chen, and C. Parini, "A small printed quasi-self-complementary antenna for ultrawideband systems," *IEEE Ant. Wireless Prop. Lett.*, vol. 8, pp. 554–557, 2009.
- [59] B. Aljibouri, E. Lim, H. Evans, and A. Sambell, "Multiobjective genetic algorithm approach for a dual-feed circular polarised patch antenna design," *Electronics Lett.*, vol. 36, no. 12, pp. 1005–1006, 2000.
- [60] F. Afshinmanesh, A. Marandi, and M. Shahabadi, "Design of a single-feed dual-band dual-polarized printed microstrip antenna using a boolean particle swarm optimization," *IEEE Trans. Ant. Prop.*, vol. 56, no. 7, pp. 1845–1852, 2008.
- [61] L. Guo, S. Wang, X. Chen, and C. Parini, "Study of compact antenna for UWB applications," *Electronics Lett.*, vol. 46, no. 2, pp. 115–116, 2010.
- [62] C. Sim, W.-T. Chung, and C.-H. Lee, "Compact slot antenna for UWB applications," *IEEE Ant. Wireless Prop. Lett.*, vol. 9, pp. 63–66, 2010.
- [63] S. Koziel and S. Ogurtsov, "Design of compact UWB monopoles using dielectric loading and numerical optimization," in *European Conf. Ant. Prop.*, pp. 2452–2455, Gothenburg, 2013.
- [64] S. Koziel and S. Ogurtsov, "Multi-objective design of antennas using variable-fidelity simulations and surrogate models," *IEEE Trans. Ant. Prop.*, vol. 61, no. 12, pp. 5931–5939, 2013.
- [65] Y. Zhao, Z. Shen, and W. Wu, "Conformal SIW H-plane horn antenna on a conducting cylinder," *IEEE Ant. Wireless Prop. Lett.*, vol. 14, pp. 1271–1274, 2015.
- [66] H. AbuTarboush, M. Farooqui, and A. Shamim, "Inkjet-printed wideband antenna on resin-coated paper substrate for curved wireless devices," *IEEE Ant. Wireless Prop. Lett.*, vol. 15, pp. 20–23, 2016.
- [67] A. Durgun, C. Balanis, C. Birtcher, and D. Allee, "Design, simulation, fabrication and testing of flexible bow-tie antennas," *IEEE Trans. Ant. Prop.*, vol. 59, no. 12, pp. 4425–4435, 2011.
- [68] H. Khaleel, H. Al-Rizzo, D. Rucker, and S. Mohan, "A compact polyimide-based UWB antenna for flexible electronics," *IEEE Ant. Wireless Prop. Lett.*, vol. 11, pp. 564–567, 2012.
- [69] A. Jafargholi, M. Kamyab, and M. Veysi, "Spiral array architecture, design, synthesis and application," *IET Microwaves, Ant. Prop.*, vol. 5, no. 5, pp. 503–511, 2011.
- [70] M. Elmansouri and D. Filipovic, "Pulse distortion and mitigation thereof in spiral antenna-based UWB communication systems," *IEEE Trans. Ant. Prop.*, vol. 59, no. 10, pp. 3863–3871, 2011.
- [71] A. Amert and K. Whites, "Miniaturization of the biconical antenna for ultrawideband applications," *IEEE Trans. Ant. Prop.*, vol. 57, no. 12, pp. 3728–3735, 2009.

- [72] C.-C. Lin, "Compact bow-tie quasi-self-complementary antenna for UWB applications," *IEEE Ant. Wireless Prop. Lett.*, vol. 11, pp. 987–989, 2012.
- [73] W. Yeoh and W. Rowe, "An UWB conical monopole antenna for multiservice wireless applications," *IEEE Ant. Wireless Prop. Lett.*, vol. 14, pp. 1085–1088, 2015.
- [74] G. Almpanis, C. Fumeaux, J. Frohlich, and R. Vahldieck, "A truncated conical dielectric resonator antenna for body-area network applications," *IEEE Ant. Wireless Prop. Lett.*, vol. 8, pp. 279–282, 2009.
- [75] S.-Y. Chen, P.-H. Wang, and P. Hsu, "Uniplanar log-periodic slot antenna fed by a CPW for UWB applications," *IEEE Ant. Wireless Prop. Lett.*, vol. 5, no. 1, pp. 256–259, 2006.
- [76] J. Yang, "Periodicity of the input impedance of log-periodic array antennas," *IET Microwaves, Ant. Prop.*, vol. 6, no. 10, pp. 1117–1122, 2012.
- [77] Y. Ranga, A. Verma, and K. Esselle, "Planar-monopole-fed, surface-mounted quasi-TEM horn antenna for UWB systems," *IEEE Trans. Ant. Prop.*, vol. 58, no. 7, pp. 2436–2439, 2010.
- [78] X. Li, S. Hagness, M. Choi, and D. Van Der Weide, "Numerical and experimental investigation of an ultrawideband ridged pyramidal horn antenna with curved launching plane for pulse radiation," *IEEE Ant. Wireless Prop. Lett.*, vol. 2, no. 1, pp. 259–262, 2003.
- [79] V. Rumsey, "Frequency independent antennas," in *IRE Int. Convention Record*, vol. 5, pp. 114–118, New York, 1957.
- [80] S. Chamaani, M. Abrishamian, and S. Mirtaheri, "Time-domain design of UWB Vivaldi antenna array using multiobjective particle swarm optimization," *IEEE Ant. Wireless Prop. Lett.*, vol. 9, pp. 666–669, 2010.
- [81] G. Pandey, H. Verma, and M. Meshram, "Compact antipodal Vivaldi antenna for UWB applications," *Electronics Lett.*, vol. 51, no. 4, pp. 308–310, 2015.
- [82] A. Bekasiewicz and S. Koziel, "Structure and computationally efficient simulation-driven design of compact UWB monopole antenna," *IEEE Ant. Wireless Prop. Lett.*, vol. 14, pp. 1282–1285, 2015.
- [83] M. Srifi, S. Podilchak, M. Essaaidi, and Y. Antar, "Compact disc monopole antennas for current and future ultrawideband (UWB) applications," *IEEE Trans. Ant. Prop.*, vol. 59, no. 12, pp. 4470–4480, 2011.
- [84] S. Nair, V. Shameena, R. Dinesh, and P. Mohanan, "Compact semicircular directive dipole antenna for UWB applications," *Electronics Lett.*, vol. 47, no. 23, pp. 1260–1262, 2011.
- [85] K. Kiminami, A. Hirata, and T. Shiozawa, "Double-sided printed bow-tie antenna for UWB communications," *IEEE Ant. Wireless Prop. Lett.*, vol. 3, no. 1, pp. 152–153, 2004.
- [86] J. Wu, Z. Zhao, Z. Nie, and Q.-H. Liu, "Bandwidth enhancement of a planar printed quasi-Yagi antenna with size reduction," *IEEE Trans. Ant. Prop.*, vol. 62, no. 1, pp. 463–467, 2014.
- [87] J. Yeo and J.-I. Lee, "Bandwidth enhancement of double dipole quasi-Yagi antenna using stepped slotline structure," *IEEE Ant. Wireless Prop. Lett.*, vol. 15, pp. 694–697, 2016.
- [88] R. C. Hansen, "Fundamental limitations in antennas," *Proc. IEEE*, vol. 69, no. 2, pp. 170–182, 1981.
- [89] C. A. Balanis, *Antenna Theory: Analysis and Design*, 3rd ed. Hoboken: Wiley-Interscience, 2005.
- [90] L. Wang, L. Xu, X. Chen, R. Yang, L. Han, and W. Zhang, "A compact ultrawideband diversity antenna with high isolation," *IEEE Ant. Wireless Prop. Lett.*, vol. 13, pp. 35–38, 2014.
- [91] D. T. Nguyen, D. H. Lee, and H. C. Park, "Very compact printed triple band-notched UWB antenna with quarter-wavelength slots," *IEEE Ant. Wireless Prop. Lett.*, vol. 11, pp. 411–414, 2012.
- [92] N. T. Nguyen, A. Boriskin, A. Rolland, L. Le Coq, and R. Sauleau, "Shaped lens-like dome for UWB antennas with a Gaussian-like radiation pattern," *IEEE Trans. Ant. Prop.*, vol. 61, no. 4, pp. 1658–1664, 2013.
- [93] S. Koziel and A. Bekasiewicz, "Variable-fidelity optimization of antennas using adjoint sensitivities," in *Loughborough Ant. Prop. Conf.*, pp. 412–415, Loughborough, 2014.
- [94] S.-W. Qu, C.-H. Chan, and Q. Xue, "Ultrawideband composite cavity-backed folded sectorial bowtie antenna with stable pattern and high gain," *IEEE Trans. Ant. Prop.*, vol. 57, no. 8, pp. 2478–2483, 2009.
- [95] J. Yang and A. Kishk, "A novel low-profile compact directional ultra-wideband antenna: The self-grounded bow-tie antenna," *IEEE Trans. Ant. Prop.*, vol. 60, no. 3, pp. 1214–1220, 2012.
- [96] M. Mirzapour, S. Razavi, and S. Armaki, "Ultra-wideband planar LPDA antenna with mode converter balun," *Electronics Lett.*, vol. 50, no. 12, pp. 848–850, 2014.
- [97] O. Ahmed, A. Sebak, and T. Denidni, "Compact UWB printed monopole loaded with dielectric resonator antenna," *Electronics Lett.*, vol. 47, no. 1, pp. 7–8, 2011.
- [98] T. Li, H. Zhai, G. Li, L. Li, and C. Liang, "Compact UWB band-notched antenna design using interdigital capacitance loading loop resonator," *IEEE Ant. Wireless Prop. Lett.*, vol. 11, pp. 724–727, 2012.

- [99] L. Lizzi, F. Viani, R. Azaro, and A. Massa, "Optimization of a spline-shaped UWB antenna by PSO," *IEEE Ant. Wireless Prop. Lett.*, vol. 6, pp. 182–185, 2007.
- [100] M. Ghassemi, M. Bakr, and N. Sangary, "Antenna design exploiting adjoint sensitivity-based geometry evolution," *IET Microwaves, Ant. Prop.*, vol. 7, no. 4, pp. 268–276, 2013.
- [101] S. Koulouridis, D. Psychoudakis, and J. Volakis, "Multiobjective optimal antenna design based on volumetric material optimization," *IEEE Trans. Ant. Prop.*, vol. 55, no. 3, pp. 594–603, 2007.
- [102] M. John and M. Ammann, "Antenna optimization with a computationally efficient multiobjective evolutionary algorithm," *IEEE Trans. Ant. Prop.*, vol. 57, no. 1, pp. 260–263, 2009.
- [103] Y. Kuwahara, "Multiobjective optimization design of Yagi-Uda antenna," *IEEE Trans. Ant. Prop.*, vol. 53, no. 6, pp. 1984–1992, 2005.
- [104] V. Pareto, *Manual of Political Economy*. New York: Augustus M. Kelley Publishers, 1971.
- [105] K. Deb, *Multi-Objective Optimization Using Evolutionary Algorithms*. New York: John Wiley & Sons, 2001.
- [106] A. Bekasiewicz, S. Koziel, and W. Zieniutycz, "Design space reduction for expedited multi-objective design optimization of antennas in highly-dimensional spaces," in *Solving Computationally Expensive Engineering Problems: Methods and Applications*, S. Koziel, L. Leifsson, and X.-S. Yang, Eds., pp. 113–147. New York: Springer, 2014.
- [107] E.-G. Talbi, *Metaheuristics: From Design to Implementation*. New York: John Wiley & Sons, 2009.
- [108] X.-S. Yang, "A new metaheuristic bat-inspired algorithm," in *Nature Inspired Cooperative Strategies for Optimization*, series Studies in Computational Intelligence, C. Cruz, J. Gonzalez, N. Krasnogor, D. Pelta, and G. Terrazas, Eds., vol. 284, pp. 65–74. Berlin Heidelberg: Springer-Verlag, 2010.
- [109] X.-S. Yang and S. Deb, "Engineering optimisation by cuckoo search," *Int. J. Mathematical Model. Num. Opt.*, vol. 1, no. 4, pp. 330–343, 2010.
- [110] X.-S. Yang, "Firefly algorithms for multimodal optimization," in *Stochastic Algorithms: Foundations and Applications*, series Theoretical Computer Science and General Issues, O. Wanatabe and T. Zeugmann, Eds., vol. 5792, pp. 169–178. Berlin Heidelberg: Springer-Verlag, 2009.
- [111] M. Dorigo, "Optimization, learning and natural algorithms," PhD thesis, Politecnico di Milano, Italy, 1992.
- [112] X. Xiao-Feng, W.-J. Zhang, and Z.-L. Yang, "Social cognitive optimization for nonlinear programming problems," in *Int. Conf. Machine Learning Cybernetics*, pp. 779–783, Beijing, 2002.
- [113] J. Kennedy, "The particle swarm: social adaptation of knowledge," in *IEEE Int. Conf. Evolutionary Comp.*, pp. 303–308, Indianapolis, 1997.
- [114] C. Coello Coello, G. Lamont, and D. Van Veldhuizen, *Evolutionary algorithms for solving multi-objective problems*. New York: Springer, 2007.
- [115] K. Deb, M. Mohan, and S. Mishra, "Evaluating the ϵ -domination based multi-objective evolutionary algorithm for a quick computation of Pareto-optimal solutions," *Evolutionary Comp.*, vol. 13, no. 4, pp. 501–525, 2005.
- [116] J. D. Knowles and D. W. Corne, "Approximating the nondominated front using the pareto archived evolution strategy," *Evolutionary Comp.*, vol. 8, no. 2, pp. 149–172, 2000.
- [117] L. Rosa, K. Saitoh, K. Kakihara, and M. Koshiba, "Genetic-algorithm assisted design of C-band CROW-miniaturized PCW interleaver," *J. Lightwave Technol.*, vol. 27, no. 14, pp. 2678–2687, 2009.
- [118] S. Hussain and H. A. Gabbar, "Gearbox fault detection using real coded genetic algorithm and novel shock response spectrum features extraction," *J. Nondestructive Evaluation*, vol. 33, no. 1, pp. 111–123, 2014.
- [119] A. Viccini and D. Quagliarella, "Inverse and direct airfoil design using a multiobjective genetic algorithm," *AIAA J.*, vol. 25, no. 9, pp. 1499–1505, 1997.
- [120] S. Koziel and A. Bekasiewicz, "Strategies for computationally feasible multi-objective simulation-driven design of compact RF/microwave components," *Eng. Comp.*, vol. 33, no. 1, pp. 184–201, 2016.
- [121] R. Ramos, R. Saldanha, R. Takahashi, and F. Moreira, "The real-biased multiobjective genetic algorithm and its application to the design of wire antennas," *IEEE Trans. Magnetics*, vol. 39, no. 3, pp. 1329–1332, 2003.
- [122] X.-S. Yang, K. T. Ng, S. H. Yeung, and K. F. Man, "Jumping genes multiobjective optimization scheme for planar monopole ultrawideband antenna," *IEEE Trans. Ant. Prop.*, vol. 56, no. 12, pp. 3659–3666, 2008.

- [123] N. Jin and Y. Rahmat-Samii, "Advances in particle swarm optimization for antenna designs: real-number, binary, single-objective and multiobjective implementations," *IEEE Trans. Ant. Prop.*, vol. 55, no. 3, pp. 556–567, 2007.
- [124] J. Robinson and Y. Rahmat-Samii, "Particle swarm optimization in electromagnetics," *IEEE Trans. Ant. Prop.*, vol. 52, no. 2, pp. 397–407, 2004.
- [125] N. Jin and Y. Rahmat-Samii, "Hybrid real-binary particle swarm optimization (HPSO) in engineering electromagnetics," *IEEE Trans. Ant. Prop.*, vol. 58, no. 12, pp. 3786–3794, 2010.
- [126] S. Goudos, Z. Zaharis, D. Kampitaki, I. Rekanos, and C. Hilar, "Pareto optimal design of dual-band base station antenna arrays using multi-objective particle swarm optimization with fitness sharing," *IEEE Trans. Magnetics*, vol. 45, no. 3, pp. 1522–1525, 2009.
- [127] I. Hanninen, "Optimization of a reflector antenna system," CST AG, Darmstadt, CST whitepaper, 2012.
- [128] J. Johnson and V. Rahmat-Samii, "Genetic algorithms in engineering electromagnetics," *IEEE Ant. Prop. Magazine*, vol. 39, no. 4, pp. 7–21, 1997.
- [129] M. Donelli and A. Massa, "Computational approach based on a particle swarm optimizer for microwave imaging of two-dimensional dielectric scatterers," *IEEE Trans. Microwave Theory Tech.*, vol. 53, no. 5, pp. 1761–1776, 2005.
- [130] B. Aljibouri, A. Sambell, and B. Sharif, "Application of genetic algorithm to design of sequentially rotated circularly polarised dual-feed microstrip patch antenna array," *Electronics Lett.*, vol. 44, no. 12, pp. 708–709, 2008.
- [131] S. Zhang and Y. Zhang, "Analysis and synthesis of millimeter-wave microstrip grid-array antennas," *IEEE Ant. Prop. Magazine*, vol. 53, no. 6, pp. 42–55, 2011.
- [132] M. Yelten, T. Zhu, S. Koziel, P. Franzone, and M. Steer, "Demystifying surrogate modeling for circuits and systems," *IEEE Circuits Syst. Magazine*, vol. 12, no. 1, pp. 45–63, 2012.
- [133] N. Queipo, R. Haftka, W. Shyy, T. Goel, R. Vaidynathan, and P. Tucker, "Surrogate based analysis and optimization," *Prog. Aerospace Sci.*, vol. 41, no. 1, pp. 1–28, 2005.
- [134] T. Simpson, J. Pelplinski, P. Koch, and J. Allen, "Metamodels for computer-based engineering design: survey and recommendations," *Eng. with Computers*, vol. 17, pp. 129–150, 2001.
- [135] J. Bandler, Q. Cheng, S. Dakrouy, A. Mohamed, M. Bakr, K. Madsen, and J. Sondergaard, "Space mapping: the state of the art," *IEEE Trans. Microwave Theory Tech.*, vol. 52, no. 1, pp. 337–361, 2004.
- [136] S. Koziel, Q. S. Cheng, and J. Bandler, "Space mapping," *IEEE Microwave Magazine*, vol. 9, no. 6, pp. 105–122, 2008.
- [137] D. Echeverria, D. Lahaye, L. Encica, E. Lomonova, P. Hemker, and A. Vandenput, "Manifold-mapping optimization applied to linear actuator design," *IEEE Trans. Magnetics*, vol. 42, no. 4, pp. 1183–1186, 2006.
- [138] S. Koziel, L. Leifsson, and S. Ogurtsov, "Reliable EM-driven microwave design optimization using manifold mapping and adjoint sensitivity," *Microwave Opt. Technol. Lett.*, vol. 55, no. 4, pp. 809–813, 2013.
- [139] S. Koziel and L. Leifsson, "Generalised shape-preserving response prediction for accurate modelling of microwave structures," *IET Microwaves, Ant. Prop.*, vol. 6, no. 12, pp. 1332–1339, 2012.
- [140] S. Koziel, "Derivative-free microwave design optimisation using shape-preserving response prediction and space mapping," *IET Sci. Measurement Technol.*, vol. 6, no. 1, pp. 13–20, 2012.
- [141] S. Koziel and S. Ogurtsov, *Antenna design by simulation-driven optimization*, series Springer Briefs in Optimization. New York: Springer, 2014.
- [142] A. I. Forrester and A. J. Keane, "Recent advances in surrogate-based optimization," *Prog. Aerospace Sci.*, vol. 45, no. 1-3, pp. 50–79, 2009.
- [143] I. Couckuyt, S. Koziel, and T. Dhaene, "Surrogate modeling of microwave structures using kriging, co-kriging and space mapping," *Int. J. Numer. Model.*, vol. 26, no. 1, pp. 64–73, 2013.
- [144] S. Koziel and J. Bandler, "Accurate modeling of microwave devices using kriging-corrected space mapping surrogates," *Int. J. Num. Model.*, vol. 25, no. 1, pp. 1–14, 2012.
- [145] W. Yamazaki and D. J. Mavriplis, "Derivative-enhanced variable fidelity surrogate modeling for aerodynamic functions," *AIAA J.*, vol. 51, no. 1, pp. 126–137, 2013.
- [146] S. Koziel, A. Bekasiewicz, and W. Zieniutycz, "Expedited EM-driven multiobjective antenna design in highly dimensional parameter spaces," *IEEE Ant. Wireless Prop. Lett.*, vol. 13, pp. 631–634, 2014.
- [147] S. Koziel, S. Ogurtsov, W. Zieniutycz, and L. Sorokosz, "Simulation-driven design of microstrip antenna subarrays," *IEEE Trans. Ant. Prop.*, vol. 62, no. 7, pp. 3584–3591, 2014.

- [148] Y. Qian, W. Deal, N. Kaneda, and T. Itoh, "Microstrip-fed quasi-Yagi antenna with broadband characteristics," *Electronics Lett.*, vol. 34, no. 23, pp. 2194–2196, 1998.
- [149] CST Microwave Studio, v. 2013, CST AG, Bad Nauheimer Str. 19, D-64289 Darmstadt, Germany, 2013.
- [150] Ansys HFSS, v. 14.0, ANSYS, Inc., Southpointe 275 Technology Drive, Canonsburg, PA 15317, 2012.
- [151] A. I. Forrester, A. Sobester, and A. J. Keane, *Engineering Design via Surrogate Modelling: A Practical Guide*. Chichester: John Wiley & Sons, 2008.
- [152] S. Koziel, J. Bandler, and K. Madsen, "Towards a rigorous formulation of the space mapping technique for engineering design," in *IEEE Int. Symp. Circuits Syst.*, vol. 6, pp. 5605–5608, Kobe, 2005.
- [153] S. Koziel, D. Echeverria Ciaurri, and L. Leifsson, "Surrogate-based methods," in *Computational Optimization, Methods and Algorithms*, series Studies in Computational Intelligence, S. Koziel and X.-S. Yang, Eds., vol. 356, pp. 33–59. Berlin Heidelberg: Springer-Verlag, 2011.
- [154] J. Nocedal and S. Wright, *Numerical Optimization*, 2nd ed. New York: Springer, 2006.
- [155] A. Conn, K. Scheinberg, and L. Vicente, *Introduction to Derivative-Free Optimization*. Philadelphia: MPS-SIAM Series on Optimization, 2009.
- [156] D. M. Pozar, *Microwave Engineering*. Hoboken: John Wiley & Sons, 2012.
- [157] S. Koziel and A. Bekasiewicz, "Fast EM-driven size reduction of antenna structures by means of adjoint sensitivities and trust regions," *IEEE Ant. Wireless Prop. Lett.*, vol. 14, pp. 1681–1684, 2015.
- [158] A. Duffy, G. Zhang, S. Koziel, and L. Wang, "Objective selection of minimum acceptable mesh refinement for EMC simulations," *IEEE Trans. EM Compatibility*, vol. 57, no. 5, pp. 1266–1269, 2015.
- [159] S. Koziel and A. Bekasiewicz, "Variable-fidelity design optimization of antennas with automated model selection," in *European Conf. Ant. Prop.*, Davos, to appear, 2016.
- [160] S. Haykin, *Neural Networks: A Comprehensive Foundation*. Upper Saddle River: Prentice-Hall, 1998.
- [161] A. Giunta, S. Wojtkiewicz, and M. Eldred, "Overview of modern design of experiments methods for computational simulations," *AIAA J.*, pp. 1–17, 2003.
- [162] S. Leary, A. Bhaskar, and A. Keane, "Optimal orthogonal-array-based latin hypercubes," *J. Applied Statistics*, vol. 30, pp. 585–598, 2003.
- [163] K. Q. Ye, "Orthogonal column latin hypercubes and their application in computer experiments," *J. American Statistical Assoc.*, vol. 93, pp. 1430–1439, 1998.
- [164] B. Beachkofski and R. Grandhi, "Improved distributed hypercube sampling," in *AIAA/ASME/ASCE/AHS/ASC Structures, Structural Dynamics, and Materials Conf.*, pp. 1–7, Denver, 2002.
- [165] D. G. Krige, "A statistical approach to some basic mine valuation problems on the Witwatersrand," *J. Chemical, Metallurgical Mining Eng. Society South Africa*, vol. 52, no. 6, pp. 119–139, 1951.
- [166] G. Matheron, "Principles of geostatistics," *Economic Geology*, vol. 58, no. 8, pp. 1246–1266, 1963.
- [167] S. Lophaven, H. Nielsen, and J. Sondergaard, "DACE: a Matlab kriging toolbox," Technical University of Denmark, Tech. Rep., 2002.
- [168] D. Gorissen, K. Crombecq, I. Couckuyt, T. Dhaene, and P. Demeester, "A surrogate modeling and adaptive sampling toolbox for computer based design," *J. Machine Learning Res.*, vol. 11, pp. 2051–2055, 2010.
- [169] S. Koziel, S. Ogurtsov, I. Couckuyt, and T. Dhaene, "Variable-fidelity electromagnetic simulations and co-kriging for accurate modeling of antennas," *IEEE Trans. Ant. Prop.*, vol. 61, no. 3, pp. 1301–1308, 2013.
- [170] D. R. Jones, "A taxonomy of global optimization methods based on response surfaces," *J. Global Opt.*, vol. 21, pp. 345–383, 2001.
- [171] S. M. Wild, R. G. Regis, and C. A. Shoemaker, "Orbit: optimization by radial basis function interpolation in trust-regions," *SIAM J. Scientific Computing*, vol. 30, no. 6, pp. 3197–3219, 2008.
- [172] A. Christmann and I. Steinwart, *Support Vector Machines*. New York: Springer, 2008.
- [173] C. Rasmussen and C. Williams, *Gaussian Processes for Machine Learning*. Cambridge: The MIT Press, 2006.
- [174] J. Bandler, R. Biernacki, S. H. Chen, P. Grobelny, and R. Hemmers, "Space mapping technique for electromagnetic optimization," *IEEE Trans. Microwave Theory Tech.*, vol. 42, no. 12, pp. 2536–2544, 1994.
- [175] J. Bandler, Q. Cheng, N. Nikolova, and M. Ismail, "Implicit space mapping optimization exploiting pre-assigned parameters," *IEEE Trans. Microwave Theory Tech.*, vol. 52, no. 1, pp. 378–385, 2004.

- [176] J. Bandler, R. Biernacki, S. H. Chen, R. Hemmers, and K. Madsen, "Electromagnetic optimization exploiting aggressive space mapping," *IEEE Trans. Microwave Theory Tech.*, vol. 43, no. 12, pp. 2874–2882, 1995.
- [177] S. Koziel and A. Bekasiewicz, "Fast multiobjective optimization of narrowband antennas using RSA models and design space reduction," *IEEE Ant. Wireless Prop. Lett.*, vol. 14, pp. 450–453, 2015.
- [178] J. Bandler, Q. Cheng, D. Gebre-Mariam, K. Madsen, F. Pedersen, and J. Sondergaard, "EM-based surrogate modeling and design exploiting implicit, frequency and output space mappings," in *IEEE MTT-S Int. Microwave Symp. Digest*, vol. 2, pp. 1003–1006, Philadelphia, 2003.
- [179] S. Koziel and L. Leifsson, "EM-simulation-driven antenna design using multi-point response correction," in *IEEE Int. Symp. Ant. Prop.*, pp. 414–415, 2013.
- [180] N. M. Alexandrov and R. M. Lewis, "An overview of first-order model management for engineering optimization," *Opt. Eng.*, vol. 2, no. 4, pp. 413–430, 2001.
- [181] M. C. Kennedy and A. O'Hagan, "Predicting the output from complex computer code when fast approximations are available," *Biometrika*, vol. 87, no. 1, pp. 1–13, 2000.
- [182] M. D. Morris, T. J. Mitchell, and D. Ylvisaker, "Design and analysis of computer experiments: use of derivatives in surface prediction," *Technometrics*, vol. 35, no. 3, pp. 243–255, 1993.
- [183] S. Koziel, A. Bekasiewicz, I. Couckuyt, and T. Dhaene, "Efficient multi-objective simulation-driven antenna design using co-kriging," *IEEE Trans. Ant. Prop.*, vol. 62, no. 11, pp. 5900–5905, 2014.
- [184] D. Jones, M. Schonlau, and W. Welch, "Efficient global optimization of expensive black-box functions," *J. Global Opt.*, vol. 13, pp. 455–492, 1998.
- [185] A. Bekasiewicz, S. Koziel, W. Zieniutycz, and L. Leifsson, "Expedited simulation-driven multi-objective design optimization of quasi-isotropic dielectric resonator antenna," in *Simulation-driven modeling and optimization*, series Springer Proceedings in Mathematics & Statistics, S. Koziel, L. Leifsson, and X.-S. Yang, Eds. New York: Springer, 2016.
- [186] S. Voss, "Meta-heuristics: the state of the art," in *Local Search for Planning and Scheduling*, series Lecture Notes in Computer Science, A. Nareyek, Ed., vol. 2148, pp. 1–23. Berlin Heidelberg: Springer-Verlag, 2001.
- [187] A. E. Eiben and J. E. Smith, *Introduction to Evolutionary Computing*, series Natural Computing. Berlin Heidelberg: Springer-Verlag, 2003.
- [188] Z. Michalewicz, *Genetic Algorithms + Data Structures = Evolution Programs*, 3rd ed. Berlin Heidelberg: Springer-Verlag, 1996.
- [189] J. L. Cohon and D. H. Marks, "A review and evaluation of multiobjective programming techniques," *Water Resources Res.*, vol. 11, no. 2, pp. 208–220, 1975.
- [190] L. A. Zadeh, "Optimality and nonscalar-valued performance criteria," *IEEE Trans. Automatic Control*, vol. 8, no. 1, pp. 59–60, 1963.
- [191] J. T. Richardson, M. R. Palmer, G. E. Liepins, and M. Hilliard, "Some guidelines for genetic algorithms with penalty functions," in *Proc. Int. Conf. Genetic Algorithms*, pp. 191–197, San Francisco, 1989.
- [192] N. Venkatarayalu and T. Ray, "Optimum design of Yagi-Uda antennas using computational intelligence," *IEEE Trans. Ant. Prop.*, vol. 52, no. 7, pp. 1811–1818, 2004.
- [193] C. M. Fonseca and P. J. Fleming, "Multiobjective optimization," in *Handbook of Evolutionary Computation*, T. Back, D. Fogel, and Z. Michalewicz, Eds., vol. 1. Bristol: Institute of Physics Publishing and Oxford University Press, 1997.
- [194] C. M. Fonseca and P. J. Fleming, "Genetic algorithms for multiobjective optimization: Formulation, discussion and generalization," in *Proc. Int. Conf. Genetic Algorithms*, pp. 1–8, San Francisco, 1993.
- [195] F. Gembicki, "Vector optimization for control with performance and parameter sensitivity indices," PhD thesis, Case Western Reserve University, Cleveland, Ohio, USA, 1974.
- [196] R. S. Rosenberg, "Simulation of genetic populations with biochemical properties," PhD thesis, University of Michigan, Ann Arbor, Michigan, USA, 1967.
- [197] J. Schaffer, "Multiple objective optimization with vector evaluated genetic algorithms," PhD thesis, Vanderbilt University, Nashville, Tennessee, USA, 1984.
- [198] D. Wolpert and W. Macready, "No free lunch theorems for optimization," *IEEE Trans. Evolutionary Comp.*, vol. 1, no. 1, pp. 67–82, 1997.
- [199] K. Tan, E. Khor, and T. Lee, *Multiobjective Evolutionary Algorithms and Applications*, series Advanced Information and Knowledge Processing. London: Springer, 2005.

- [200] C. Fonseca, “Multiobjective genetic algorithms with application to control engineering problems,” PhD thesis, University of Sheffield, Sheffield, UK, 1995.
- [201] D. E. Goldberg and J. Richardson, “Genetic algorithms with sharing for multimodal function optimization,” in *Proc. Int. Conf. Genetic Algorithms App.*, pp. 41–49, Hillsdale, 1987.
- [202] J. Horn, N. Nafpliotis, and D. Goldberg, “A niched Pareto genetic algorithm for multiobjective optimization,” in *Proc. IEEE Conf. Evolutionary Comp.*, vol. 1, pp. 82–87, Orlando, 1994.
- [203] K. Deb and D. E. Goldberg, “An investigation of niche and species formation in genetic function optimization,” in *Proc. Int. Conf. Genetic Algorithms*, pp. 42–50, San Francisco, 1989.
- [204] A. Bekasiewicz, S. Koziel, and W. Zieniutycz, “Design space reduction and variable-fidelity EM simulations for feasible Pareto optimization of antennas,” in *Int. Review Prog. Applied Comp. EM*, Jacksonville, 2014.
- [205] S. Koziel and A. Bekasiewicz, “Fast multi-objective surrogate-assisted design of multi-parameter antenna structures through rotational design space reduction,” *IET Microwaves, Ant. Prop.*, vol. 10, no. 6, pp. 624–630, 2016.
- [206] MathWorks MATLAB, v. 2012a, MathWorks, Inc., 3 Apple Hill Drive, Natick, MA 01760, 2012.
- [207] D. Gorissen, I. Couckuyt, E. Laermans, and T. Dhaene, “Multiobjective global surrogate modeling, dealing with the 5-percent problem,” *Eng. with Computers*, vol. 26, no. 1, pp. 81–98, 2010.
- [208] S. Koziel and A. Bekasiewicz, “Low-cost multi-objective optimization and experimental validation of UWB MIMO antenna,” *Eng. Comp.*, to appear, 2016.
- [209] P. Lollini, A. Bondavalli, and F. D. Giandomenico, “A decomposition-based modeling framework for complex systems,” *IEEE Trans. Reliability*, vol. 58, no. 1, pp. 20–33, 2009.
- [210] A. Booker, J. Dennis, P. Frank, D. Serafini, V. Torczon, and M. Trosset, “A rigorous framework for optimization of expensive functions by surrogates,” *Structural Opt.*, vol. 17, no. 1, pp. 1–13, 1999.
- [211] A. Bekasiewicz, S. Koziel, and W. Zieniutycz, “Low-cost multi-objective optimization Yagi-Uda antenna in multi-dimensional parameter space,” in *Int. Conf. Microwave Radar Wireless Comm.*, vol. 2, pp. 653–656, Gdansk, 2014.
- [212] T. Spence and D. Werner, “A novel miniature broadband/multiband antenna based on an end-loaded planar open-sleeve dipole,” *IEEE Trans. Ant. Prop.*, vol. 54, no. 12, pp. 3614–3620, 2006.
- [213] T. Kolda, R. Lewis, and V. Torczon, “Optimization by direct search: new perspectives on some classical and modern methods,” *SIAM Review*, vol. 45, no. 3, pp. 385–482, 2003.
- [214] S. Koziel and A. Bekasiewicz, “On scalability of surrogate-assisted multi-objective optimization of antenna structures exploiting variable-fidelity EM-simulation models,” *Eng. Opt.*, to appear, 2016.
- [215] S. Koziel and A. Bekasiewicz, “Fast simulation-driven feature-based optimization of compact dual-band microstrip branch-line coupler,” *Int. J. RF and Microwave CAE*, vol. 26, no. 1, pp. 13–20, 2016.
- [216] S. Koziel, “Computationally efficient multi-fidelity multi-grid design optimization of microwave structures,” *Applied Comp. EM Society J.*, vol. 25, no. 7, pp. 578–586, 2010.
- [217] S. Koziel and A. Bekasiewicz, “Recent developments in simulation-driven multi-objective design of antennas,” *Bulletin Polish Academy Sci. Tech. Sci.*, vol. 63, no. 3, pp. 781–789, 2015.
- [218] Y.-M. Pan, K. W. Leung, and K. Lu, “Compact quasi-isotropic dielectric resonator antenna with small ground plane,” *IEEE Trans. Ant. Prop.*, vol. 62, no. 2, pp. 577–585, 2014.
- [219] P. Kurgan, A. Bekasiewicz, and M. Kitlinski, “On the low-cost design of abbreviated multi-section planar matching transformer,” *Microwave Opt. Technol. Lett.*, vol. 57, no. 3, pp. 521–525, 2015.
- [220] A. Bekasiewicz, P. Kurgan, and M. Kitlinski, “A new approach to a fast and accurate design of microwave circuits with complex topologies,” *IET Microwaves, Ant. Prop.*, vol. 6, no. 14, pp. 1616–1622, 2012.
- [221] A. Bekasiewicz, S. Koziel, and B. Pankiewicz, “Accelerated simulation-driven design optimisation of compact couplers by means of two-level space mapping,” *IET Microwaves, Ant. Prop.*, vol. 9, no. 7, pp. 618–626, 2015.

APPENDICES

APPENDIX 1 STATISTICAL ANALYSIS OF MOEA

In this appendix, statistical analysis of the MOEA algorithm has been performed for the benchmark designs of Sections 4.5.2, 4.5.3 and 4.5.4. The Pareto sets have been obtained for 30 runs of the algorithm within five different regions of the search space and for different number of iterations I ($I = 10, 20, \dots, 100$). The MOEA population size is set to 500. The algorithm performance is expressed in terms of the average distance, the average standard deviation and the worst case peak distance from the average Pareto front. Each of the aforementioned figures is calculated with respect to the objective F_1 . One should reiterate that MOEA is executed on the RSA model and thus, regardless the number of R_s evaluations, the cost of its operation is negligible with respect to other steps of multi-objective optimization procedure considered in this work.

The first benchmark antenna is the UWB monocone with three variables (cf. Section 4.5.2). The results of statistical analysis gathered in Table A.1 indicate that the influence of the number of iterations on MOEA performance is low. As expected, the quality measures obtained in reduced spaces are noticeably better than ones from X_I . The results of statistical analysis for $I = 50$ iterations of the algorithm are shown in Figure A.1 It should be noted that fluctuations of the obtained Pareto fronts are negligible.

The analysis results (see Table A.2) obtained for a six-variable UWB dipole antenna (cf. Section 4.5.3) indicate that variations of quality factors for more than 20 iterations of the algorithm are small. Again, the results obtained within the reduced regions of the design space are significantly better than the results in the initial one.

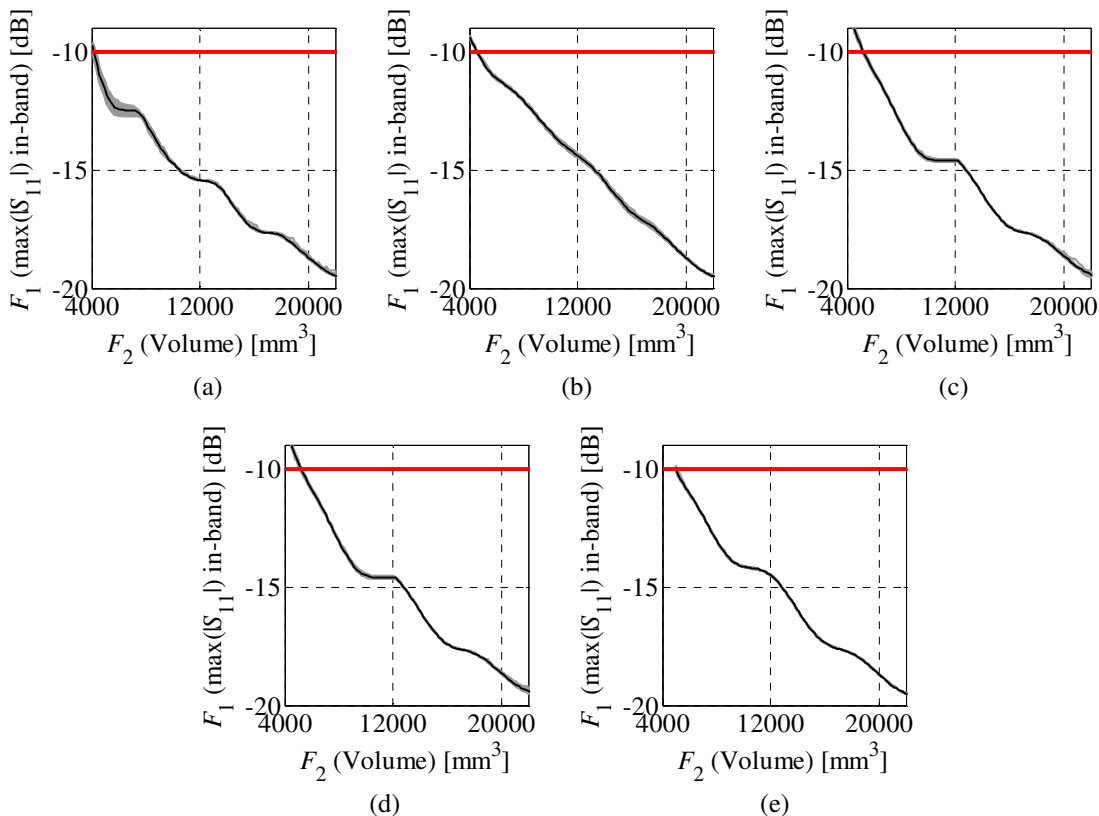


Figure A.1: The Pareto-optimal sets obtained for 30 runs of MOEA (gray lines) and the average value (black line). Results generated within: (a) initial space X_I ; and the following reduced spaces: (b) X_D (cf. Section 4.3.1); (c) X_S (cf. Section 4.3.2); (d) X_{S_r} (cf. Section 4.3.5); and (e) X_R (cf. Section 4.3.3). Note negligible discrepancies between the individual MOEA runs (especially within refined spaces), which are insignificant from the engineering point of view. The results are similar because antenna of Section 4.5.2 is described by only three adjustable parameters.

TABLE A.1: MOEA ALGORITHM PERFORMANCE FOR THREE-VARIABLE DESIGN ($N = 500$)

Design Space		Average Distance from the Mean Pareto Front					Average Standard Deviation from the Mean Pareto Front					Worst Case peak Distance from the Mean Pareto Front				
		X_I	X_D	X_S	X_{S_r}	X_R	X_I	X_D	X_S	X_{S_r}	X_R	X_I	X_D	X_S	X_{S_r}	X_R
Number of Iterations	10	0.26	0.14	0.05	0.05	0.02	0.21	0.10	0.05	0.05	0.02	1.60	1.02	0.36	0.36	0.22
	20	0.10	0.06	0.04	0.03	0.01	0.10	0.05	0.04	0.03	0.02	1.01	0.65	0.32	0.31	0.23
	30	0.08	0.05	0.03	0.03	0.01	0.09	0.04	0.03	0.03	0.02	0.73	0.42	0.32	0.25	0.29
	40	0.06	0.03	0.02	0.02	0.01	0.07	0.02	0.02	0.02	0.01	0.76	0.28	0.21	0.21	0.17
	50	0.04	0.03	0.02	0.02	0.01	0.06	0.02	0.02	0.03	0.01	0.49	0.22	0.44	0.25	0.18
	60	0.05	0.03	0.02	0.02	0.01	0.06	0.02	0.02	0.02	0.01	0.59	0.20	0.24	0.31	0.27
	70	0.05	0.02	0.02	0.02	0.01	0.06	0.02	0.02	0.02	0.01	0.61	0.24	0.22	0.23	0.25
	80	0.04	0.02	0.02	0.02	0.01	0.05	0.02	0.02	0.02	0.01	0.38	0.14	0.32	0.35	0.18
	90	0.03	0.02	0.02	0.01	0.01	0.04	0.02	0.02	0.02	0.01	0.38	0.13	0.20	0.17	0.14
	100	0.03	0.02	0.01	0.01	0.01	0.04	0.01	0.01	0.02	0.01	0.36	0.12	0.21	0.25	0.12

The Pareto-optimal sets obtained for 30 runs of MOEA with $I = 50$ are shown in Figure A.2. It should be noted that fluctuations of the Pareto fronts vary noticeably in the search spaces reduced using different algorithms. Moreover, increased variations of the results around the corners of the Pareto fronts occur in Figure A.2(b)-(d). The reason is that the extreme Pareto designs reside on the corners of 6-dimensional reduced search spaces X_D , X_S and X_{S_r} . Consequently, exploration capability of MOEA close to these extreme solutions is limited. In Figure A.2(e), however, the effect is significantly reduced because the extreme designs are allocated on the faces of the rotated search space X_R which allows for better exploration of their surroundings.

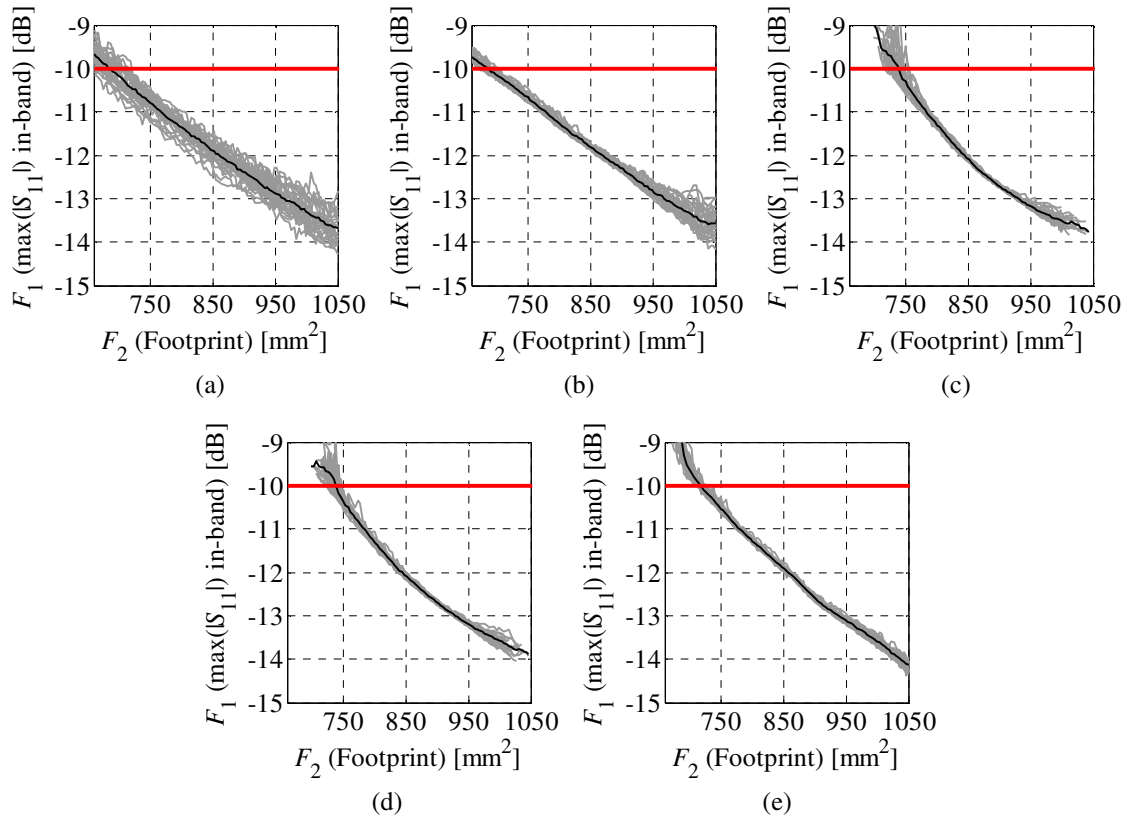


Figure A.2: The Pareto-optimal sets obtained for 30 runs of MOEA (gray lines) and the average value (black line). Results generated within: (a) initial space X_I ; and the following reduced spaces: (b) X_D ; (c) X_S ; (d) X_{S_r} ; and (e) X_R . The largest discrepancies between obtained Pareto sets are observed within the initial search space; however, they are negligible from the engineering point of view.

The last benchmark design is a 9-variable UWB monopole antenna of Section 4.5.4. The results of statistical analysis are gathered in Table A.3. Again, for more than 20 iterations the quality factors of the algorithm operation are similar, especially for the reduced search spaces. The performance of the algorithm within the reduced spaces is also significantly better as compared to X_I . The Pareto-optimal sets generated for 30 runs of MOEA with $I = 50$ are shown in Figure A.3. The largest fluctuations of the Pareto fronts can be observed within the initial space, however, the discrepancies are still below 1 dB and thus negligible from the engineering point of view. Increased fluctuations of the Pareto fronts in Figure A.3(b)-(d) are due to the same reasons as described for the dipole antenna.

TABLE A.2: MOEA ALGORITHM PERFORMANCE FOR SIX-VARIABLE DESIGN ($N = 500$)

Design Space	Average Distance from the Mean Pareto Front					Average Standard Deviation from the Mean Pareto Front					Worst Case peak Distance from the Mean Pareto Front					
	X_I	X_D	X_S	X_{S_r}	X_R	X_I	X_D	X_S	X_{S_r}	X_R	X_I	X_D	X_S	X_{S_r}	X_R	
Number of Iterations	10	0.69	0.35	0.14	0.13	0.09	0.36	0.23	0.13	0.12	0.08	2.82	4.17	2.06	1.53	0.92
	20	0.53	0.33	0.11	0.12	0.07	0.32	0.22	0.11	0.12	0.08	2.34	1.36	1.23	1.28	1.08
	30	0.33	0.16	0.09	0.09	0.07	0.22	0.14	0.08	0.09	0.08	2.09	0.92	0.89	1.00	1.03
	40	0.25	0.14	0.09	0.08	0.06	0.16	0.12	0.10	0.08	0.07	1.35	0.98	1.14	0.89	1.26
	50	0.19	0.08	0.08	0.07	0.06	0.12	0.08	0.10	0.08	0.08	0.98	0.72	1.07	1.20	1.02
	60	0.16	0.08	0.06	0.06	0.06	0.11	0.07	0.08	0.07	0.08	0.75	0.74	1.03	1.15	0.90
	70	0.16	0.07	0.05	0.05	0.06	0.11	0.06	0.07	0.07	0.08	0.74	0.51	0.88	1.05	1.06
	80	0.16	0.06	0.05	0.05	0.05	0.11	0.05	0.06	0.06	0.07	0.74	0.48	0.73	0.73	0.80
	90	0.16	0.06	0.04	0.05	0.05	0.11	0.05	0.05	0.06	0.06	0.85	0.47	0.90	0.92	0.95
	100	0.17	0.05	0.05	0.05	0.04	0.11	0.04	0.05	0.06	0.05	0.85	0.37	0.96	1.05	0.81

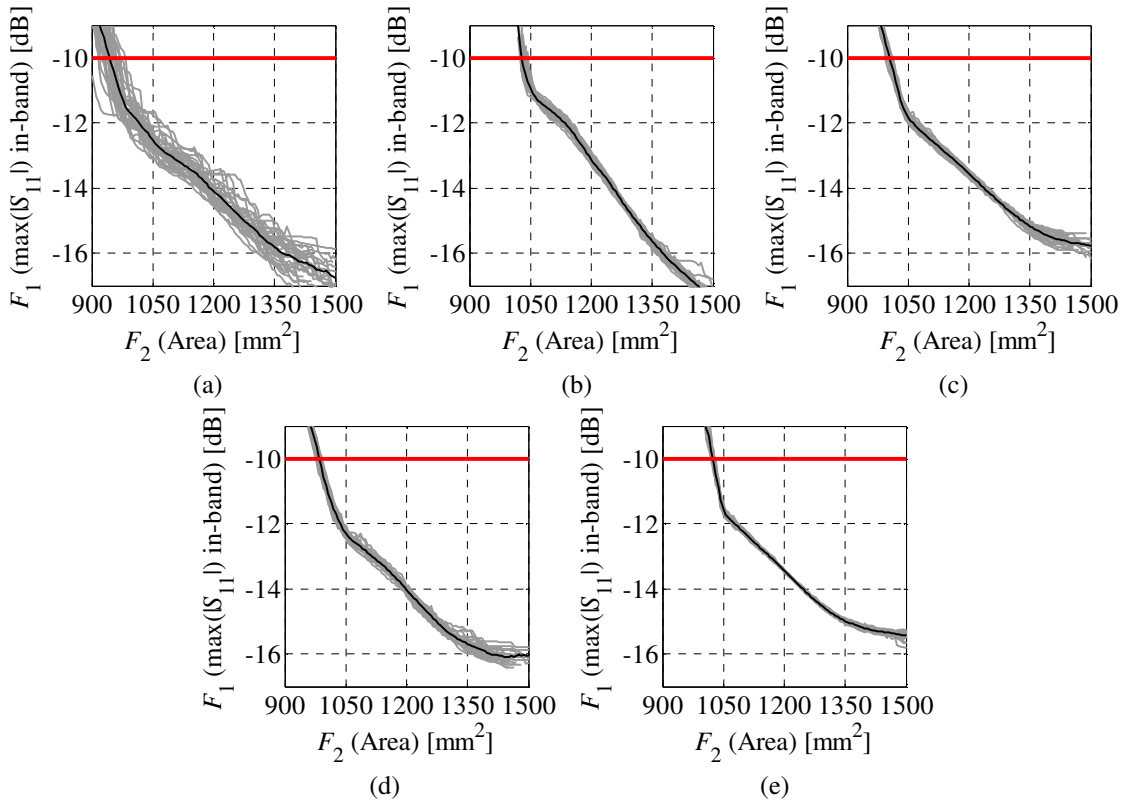


Figure A.3: The Pareto-optimal sets obtained for 30 runs of MOEA (gray lines) and the mean value (black line). Results of the analysis from: (a) initial space X_I ; and the following reduced spaces: (b) X_D ; (c) X_S ; (d) X_{S_r} ; and (e) X_R . The largest discrepancies between obtained Pareto sets are observed within the initial search space. Pareto fronts in (b)-(d) exhibit notably smaller discrepancies because their corresponding design spaces are narrower. The increased discrepancies between fronts can be observed in the vicinity of their extreme values.

TABLE A.3: MOEA ALGORITHM PERFORMANCE FOR NINE-VARIABLE DESIGN ($N = 500$)

		Average Distance from the Mean Pareto Front					Average Standard Deviation from the Mean Pareto Front					Worst Case peak Distance from the Mean Pareto Front				
		X_I	X_D	X_S	X_{Sr}	X_R	X_I	X_D	X_S	X_{Sr}	X_R	X_I	X_D	X_S	X_{Sr}	X_R
Number of Iterations	Design Space															
	10	0.46	0.25	0.13	0.21	0.07	0.36	0.17	0.13	0.15	0.07	3.44	1.62	1.31	1.34	1.26
	20	0.34	0.17	0.11	0.16	0.06	0.27	0.12	0.09	0.13	0.06	3.29	1.61	0.76	1.08	0.78
	30	0.32	0.12	0.09	0.14	0.06	0.26	0.10	0.08	0.11	0.05	1.97	1.68	0.96	1.01	0.65
	40	0.33	0.11	0.09	0.11	0.05	0.25	0.09	0.07	0.09	0.05	2.72	1.62	0.61	0.59	0.76
	50	0.33	0.10	0.09	0.11	0.04	0.26	0.08	0.07	0.08	0.05	2.61	1.58	0.86	0.70	0.73
	60	0.31	0.09	0.08	0.12	0.05	0.24	0.07	0.07	0.09	0.05	3.32	0.93	0.52	0.67	0.61
	70	0.28	0.09	0.08	0.12	0.05	0.22	0.08	0.06	0.09	0.05	1.69	1.09	0.47	0.83	0.67
	80	0.29	0.09	0.09	0.12	0.04	0.23	0.08	0.07	0.10	0.05	1.91	1.18	0.55	0.98	0.67
	90	0.30	0.09	0.08	0.12	0.04	0.25	0.08	0.07	0.10	0.04	1.94	1.57	0.65	0.67	0.56
100	0.26	0.10	0.09	0.12	0.04	0.21	0.08	0.07	0.10	0.04	1.98	1.03	0.54	0.73	0.56	

ABOUT THE AUTHOR

Adrian Bekasiewicz was born in Gdansk on January 7th, 1987. He graduated from the Faculty of Electronics, Telecommunications and Informatics at the Gdansk University of Technology, Poland. In September 2011 he defended his MSc thesis entitled *PBG structures in planar circuits miniaturization procedure* (final grade: A). In October 2011, he began PhD studies at the same faculty.

Between October 2013 and January 2014, he did a research internship at the Engineering Optimization and Modeling Center (EOMC), Reykjavik University, Iceland. The internship was funded by European Social Fund. In August 2014, he has joined EOMC where he worked as a research associate until December 2015. Between January 2016 and April 2016 he was on another research internship at EOMC (funded as a part of the ETIUDA research project that he was awarded in 2014).

During his PhD studies Mr. Bekasiewicz has participated in five research projects financed by the Polish Ministry of Science and Higher Education (one project), the National Science Center (NCN; two projects held at Gdansk University of Technology and one at Medical University of Gdansk), and the Icelandic Research Fund (RANNIS; one project). Furthermore, he is involved in the RANNIS infrastructure project aimed at construction of the anechoic chamber for antenna measurements at Reykjavik University.

Adrian Bekasiewicz is an active reviewer for many ISI-ranked journals (including leading journals in the area of antenna engineering such as IEEE Antennas and Wireless Propagation Letters, IEEE Transactions on Wireless Communications, IET Microwaves Antennas & Propagation, International Journal of Antennas and Propagation, but also related to CAD, numerical modeling and optimization, e.g., International Journal of Numerical Modelling: Electronic Networks, Devices and Fields, Engineering Computations). He was also member of the program committee for the International Conference on Computational Science (since 2015).

During his academic career, he was awarded several times for his research achievements. In 2011, he won the best paper award at the National Conference on Electronics. In 2012, he obtained distinction from the Dean of the Faculty of Electronics Telecommunications and Informatics for outstanding MSc thesis. In the same year, he received the first prize funded by AP/AES/MTT joint chapter of Polish IEEE section for the best MSc thesis in the field of microwave/antenna techniques and radio-location systems. In 2015, he won (together with prof. Slawomir Koziel) the best paper award (third prize) at the IEEE Loughborough Antennas and Propagation Conference. In 2016, he won the best paper award (first prize) at the International Conference on Microwaves, Radar and Wireless Communications.

Mr. Bekasiewicz is a co-author of 143 publications including 47 ISI-ranked papers, 7 chapters in books published by Springer, 84 peer-reviewed conference articles, and 4 works in domestic journals. He is also a co-author of a monograph *Multi-Objective Design of Antennas Using Surrogate Models*, to be published by World Scientific (currently in production). Majority of his publications are in an area of microwave and antenna engineering. However, he is also co-author of papers in the area of chemistry (one ISI publication), aerospace engineering (one book chapter and four conference papers) and hydrodynamics (three conference papers). It should be noted that 40 of his publications are directly related to multi-objective optimization of microwave/antenna structures. His current H-index, according to Google Scholar, Scopus, and Web of Knowledge, is 8, 6, and 6, respectively.